

Lagrangian Computations of Radiating Fire Plumes

by

Issam Adnan Lakkis

Submitted to the Department of Mechanical Engineering
in partial fulfillment of the requirements for the degree of

Doctor of Philosophy in Mechanical Engineering

at the

MASSACHUSETTS INSTITUTE OF TECHNOLOGY

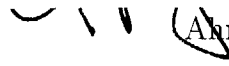
June 2000

© Massachusetts Institute of Technology 2000. All rights reserved.

Author

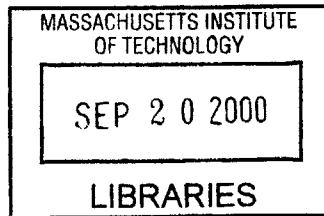
Department of Mechanical Engineering
February 10, 2000

Certified by

 Ahmed F. Ghoniem
Professor
Thesis Supervisor

Accepted by

Ain Sonin
Chairman, Department Committee on Graduate Students



ENG

لَقَدْ كَفَرَ

To my parents, sisters, and brothers who always had faith in me.

Lagrangian Computations of Radiating Fire Plumes

by

Issam Adnan Lakkis

Submitted to the Department of Mechanical Engineering
on February 10, 2000, in partial fulfillment of the
requirements for the degree of
Doctor of Philosophy in Mechanical Engineering

Abstract

Modeling and simulation of fires are useful in determining their impact on nearby and distant objects, quantifying their environmental impact, improving fire suppression techniques, etc. Fires, essentially naturally aspirated combustion phenomena, are buoyancy driven diffusion flames in which the fuel supply rate is governed by the burn rate itself. It has been observed experimentally that the complex interaction between the flow, transport process and chemistry in a fire leads to large scale “puffing”; an unsteady phenomenon manifested in the periodic ejection of bellowing smoke. The complexity of the phenomenon defies analytical treatment except at the very coarse grain level essentially using similarity principles. Numerical solutions based on ensemble averaging/closure and flow-combustion interaction models are encumbered by uncertainty and unproven hypotheses. A viable alternative is a numerical simulation of the unsteady governing equations with sufficient resolution to capture the important scales. In this work, contributions to a grid-free Lagrangian approach to simulate numerically fire plumes are suggested. The physical model incorporates unsteady buoyancy dynamics, transport of heat and mass by diffusion and convection, radiative transport of heat, and a single-step, infinite-rate chemical reaction with exothermic heat release. The numerical approach is based on the vortex method in which the unsteady conservation equations of vorticity, chemical species and energy are solved using a set of moving computational elements carrying time dependent quantities. A compatible approach is proposed to solve the radiative transport equations. Simulations of an axisymmetric plume are used to identify the dynamic mechanisms leading to “puffing”, the processes which govern entrainment into the rising unsteady plume, burn rate, and overall observable quantities such as the flame height, radiation flux, etc.

Thesis Supervisor: Ahmed F. Ghoniem
Title: Professor

Acknowledgments

I thank my advisor Professor Ahmed Ghoniem for his guidance, support, and understanding over the past six years. I also thank Professors Borivoji Mikic and Jack Howard for accepting to serve on my committee and for helping make the last year a smooth ride.

My thanks go to Shankar Subramaniam for his friendship, help, and patience in answering an endless stream of questions.

My thanks also go to my friends Nadine Alameh, Omar Baba, Louay Bazzi, Mariam Chahin, Ahmed Doughan, Mona Fawaz, Adrin Gharakhani, Jean-Pierre Hathout, Karim Hussein, Yamila Hussein, Samer Jabbour, Ali Jouzou, Issa Kaakour, Ziad Kanaan, Hisham Kassab, Fadi Karameh, Issam Kaysi, Dina Katabi, Lucy McCauley, Youssef Marzouk, Saadeddine Mneimneh, Amr Muhammad, Bilal Mughal, Richard Rabbat, Farhan Rama, Maysa Sabah, Khalil Sardouk, Nasser Sharara, Alan Shihadeh, Mary Taylor, and Rabih Zbib.

I thank Professors Nesreen Ghaddar and Fadl Moukalled of the American University of Beirut for promoting in me the interest and challenge to pursue my Ph.D. at MIT.

I thank the National Institute of Standards and Technology, Sandia National Laboratory, the Air force Office of Scientific Research, and the Department of Energy for sponsoring and supporting this work. Special thanks to Drs. James Strickland and Louis Gritzo.

I thank Professor Ain Sonin and Leslie Regan for their advice.

Contents

1	Introduction	19
1.1	Experimental work	21
1.1.1	Puffing	22
1.1.2	Intermittency and flame height	22
1.1.3	Entrainment	23
1.1.4	Radiation	23
1.2	Analytical models	24
1.3	Numerical methods	25
1.4	Objectives and tasks	26
1.5	Vortex methods	27
1.5.1	Convection	27
1.5.2	Diffusion	27
1.5.3	Generation	29
1.6	Grid-free modeling of radiative transport	29
1.6.1	The method of spherical harmonics	30
1.6.2	The discrete ordinates method	30
1.6.3	The zonal method	30
1.6.4	The Monte Carlo method	31
1.7	Roadmap	31
2	Governing Equations	32
2.1	Conservation equations	32
2.1.1	Thermodynamic properties	35
2.1.2	Laws of chemical reaction	35

2.1.3	Boundary conditions	35
2.2	Conservation of mass	36
2.3	Conservation of momentum	36
2.4	Conservation of energy	36
2.5	Combustion	37
2.5.1	Chemical reaction	37
2.5.2	Conservation of species	37
2.5.3	Rate of reaction and heat release	38
2.5.4	Equation of state	39
2.6	Density effects	39
2.7	Dimensionless form of the governing equations	41
2.8	The vorticity equation	43
2.9	Shvab-Zel'dovich formulation	44
2.10	Infinite rate chemistry	46
2.11	Rate of change of material integrals	46
2.12	Summary	47
3	The Vortex Method	48
3.1	Introduction	48
3.2	The vortex method	49
3.3	Discretization of the vorticity field	50
3.3.1	points	50
3.3.2	blobs	51
3.4	Vorticity transport	51
3.4.1	Convection	52
3.4.2	Diffusion	53
3.4.3	Generation	54
3.5	Velocity Field: Helmholtz Decomposition	56
3.5.1	Potential velocity component	56
3.5.2	Rotational velocity component	56
3.5.3	Expansion velocity component	57
3.6	Convergence and accuracy	58

3.6.1	Convergence	58
3.6.2	Accuracy	59
3.7	Summary	61
4	Scalar Transport	62
4.1	Discretization of the scalar field	62
4.2	Scalar transport	63
4.2.1	convection	63
4.2.2	diffusion	63
4.2.3	generation	64
4.3	The transport element method	64
4.4	Discussion	66
4.4.1	Advantages	66
4.4.2	Disadvantages	66
5	Diffusion	68
5.1	Background	68
5.2	The redistribution method	68
5.3	Core function	69
5.4	Core spreading	70
5.5	The smoothed redistribution method	71
5.5.1	diffusion stage	72
5.5.2	redistribution stage	73
5.6	The redistribution equations	73
5.7	Various diffusion lengths	75
5.8	Diffusion of the scalar	76
5.9	Treatment near the axis of symmetry	78
5.10	Scalar gradients	79
5.11	Remarks	79
5.12	Accuracy	80
6	Convection	81
6.1	Vortical velocity component	82

6.1.1	Velocity of a point vortex	83
6.1.2	Velocity of a vortex blob	84
6.2	Expansion velocity	87
6.2.1	Expansion of a point source	89
6.2.2	Expansion of a vortex blob	89
6.3	Numerical Algorithm	90
6.3.1	Strang splitting	90
6.3.2	Solving the convection-generation step	92
6.3.3	Numerical algorithm	92
7	Radiation	94
7.1	Radiation in a Gray Non-Scattering Medium	94
7.2	The Discrete Source Method	96
7.3	Solution for a Spherical Element	98
7.4	Solution for an Axisymmetric Element	98
7.4.1	Thin Ring Approximation	98
7.5	Treatment of large absorption coefficient	100
7.6	Solution inside the core	101
7.7	Extension to Cartesian Coordinates	102
7.8	Example I	103
7.8.1	Convergence	106
7.9	Example II	107
7.10	Conclusion	111
8	Computations of Isothermal Buoyant Plumes	113
8.1	Introduction	113
8.2	Numerical Parameters and assumptions	115
8.3	Results and discussion	116
8.3.1	Effect of pool diameter	117
8.3.2	Effect of Reynolds number	119
8.3.3	Effect of outflow velocity	120

9	Computation of Fire Plumes	122
9.1	Introduction	122
9.2	Assumptions	124
9.3	Governing Equations	125
9.3.1	Boundary conditions	126
9.4	The vortex method	127
9.5	Example	128
9.5.1	The early stages and the mushroom	129
9.5.2	Time dependent structure of the plume	130
9.5.3	Puffing frequency	133
9.5.4	Radial temperature profiles	134
9.5.5	Average flame height	134
9.5.6	Velocity field	135
9.5.7	Entrainment	136
9.6	Conclusions	136
10	Solutions Using the Smoothed Redistribution Method	152
10.1	Stokes flow	152
10.1.1	Vorticity and scalar	154
10.1.2	Scalar gradient	160
10.1.3	Number of elements	161
10.2	Vortex ring	166
10.2.1	Vorticity and scalar	168
10.2.2	Convergence and accuracy	171
10.2.3	Number of elements	182
11	Solutions Using the Discrete Source Method	188
11.1	Assumptions	188
11.2	Governing equations	189
11.3	Parameters	189
11.4	Initial conditions	189
11.5	Boundary conditions	191
11.6	Numerical parameters	191

11.7 Results and discussion	191
11.7.1 Vorticity	191
11.7.2 Scalars	195
11.7.3 Convergence	199
11.8 The role of radiation	200
11.9 Conclusion	201
12 Conclusion	206

List of Figures

1-1	Diagram.	20
4-1	Discretization of material layer into elements.	65
5-1	Schematic	72
6-1	Convergence properties of the self induced velocity of a vortex blob.	85
6-2	Self induced velocity.	86
6-3	Comparison of numerical and exact radial profiles (at $z = 0$) of axial velocity component for $r_o = 5$ and $r_o = 21$	87
6-4	Convergence properties of the radial component of the expansion velocity at the center of a blob.	91
6-5	Comparison of numerical and exact radial profiles (at $z = 0$) of radial expansion velocity component at the center of the element for $r_o = 5$ and $r_o = 21$	91
6-6	Numerical algorithm.	93
7-1	Schematic.	95
7-2	Decomposing the participating medium into computational elements.	97
7-3	Ring in polar cylindrical coordinates.	99
7-4	Irradiance due to a thin ring with small a	100
7-5	Ring and sphere solutions for large a	101
7-6	G_{self} for both a ring and a sphere as a function of $a\delta$	102
7-7	Exact vs. approximate solutions of G for $a = 1, 10$ and 100	103
7-8	Schematic for example I.	104
7-9	Exact vs. approximate solutions of G for $a = 1, 10$ and 100	105
7-10	Exact vs. approximate solutions of G for $a = 1, \delta = 0.01, 0.02, 0.04, 0.08, 0.1$	106

7-11	Exact vs. approximate solution of G for $\alpha = 5, \delta = 0.01, 0.02, 0.04, 0.08, 0.1$.	107
7-12	Schematic for example II.	108
7-13	Species distributions of 1-D diffusion flame.	108
7-14	Dependence of the Plank-mean absorption coefficient on temperature [91].	109
7-15	Temperature and absorption coefficient distribution of the 1-D flame.	110
7-16	Temperature and absorption coefficient distributions used in Example II.	110
7-17	Radiation source distribution for Example II.	111
8-1	Schematic.	115
8-2	frequency	117
8-3	Dependence of pulsation frequency on pool diameter.	118
8-4	Dependence of Strouhal number on Froude number, $Re = \text{constant}$.	119
8-5	Impact of reducing the pool diameter.	121
8-6	Dependence of Strouhal number on Reynolds number, $Fr = \text{constant}$.	121
9-1	Schematic.	123
9-2	Typical cycle showing the computational elements at four times. Color denotes temperature. Major ticks with 0.5 spacing.	137
9-3	Product mass fraction distribution at four times. Major ticks with 0.5 spacing.	138
9-4	Vorticity distribution at four times. Major ticks with 0.5 spacing.	139
9-5	Density distribution at four times. Major ticks with 0.5 spacing.	140
9-6	Fuel mass fraction distribution at four times. Major ticks with 0.5 spacing.	141
9-7	Upper figure: radial velocity component history at a point located at $(r, z) = (0.4, 0.8)$. Lower figure: the power spectrum density vs. frequency.	142
9-8	Strouhal vs. Froude number.	143
9-9	Radial temperature profiles.	144
9-10	Average distributions of velocity, temperature, fuel and product mass fractions. Major ticks with 0.5 spacing.	145
9-11	Average flame height versus dimensionless heat released obtained from reference [103].	146
9-12	The instantaneous velocity field near the pool at $t = 45.368$ and $t = 47.386$. Major ticks with 0.5 spacing.	147
9-13	Average velocity field. Color denotes speed.	148

9-14	Velocity field at pool base of a 7.1 cm toluene fire obtained from reference [101].	149
9-15	Mass entrained as a function elevation. Delichatsios' correlation [26] is also shown.	150
9-16	Comparison of present numerical results concerning entrainment mass flow-rates with experimental data[103] and Delichatsios' correlation[26].	151
10-1	Vorticity contours at $\tau = 0.2$ for $\Delta\tau = 0.018, 0.0045, 0.001125$ and 0.0005 . Solid lines are exact solution. Dash lines are numerical solution. Contour levels are 0.01, 0.04, 0.1, 0.2, and 0.3	156
10-2	Scalar contours at $\tau = 0.2$ for $\Delta\tau = 0.018, 0.0045, 0.001125$ and 0.0005 . Solid lines are exact solution. Dash lines are numerical solution. Contour levels are 0.01, 0.05, 0.15, 0.3, and 0.45	157
10-3	Global error versus time step. Core size is constant $\sigma = \sqrt{8 \times 0.0005}$. Circles denote vorticity. Squares denote scalar.	158
10-4	Global error versus time step. Overlap ratio is constant $\sigma/h = 2$. Circles denote vorticity. Squares denote scalar.	158
10-5	Total circulation. Solid line is exact solution. Symbols are numerical solution: $\Delta\tau = 0.00025$: black circles, $\Delta\tau = 0.0005$: grey circles, and $\Delta\tau = 0.001$: empty circles.	159
10-6	Global error versus overlap ratio. Time step is constant $\Delta\tau = 0.0005$. Circles denote vorticity. Squares denote scalar.	160
10-7	Upper figure: radial vorticity profile at $z = 0, \tau = 0.2$. Lower figure: axial vorticity profile at $r = 1, \tau = 0.2$. Solid lines are exact solution. Symbols are numerical solution.	162
10-8	Upper figure: radial scalar profile at $z = 0, \tau = 0.2$. Lower figure: axial vorticity profile at $r = 0, \tau = 0.2$. Solid lines are exact solution. Symbols are numerical solution.	163
10-9	Radial and axial components of scalar gradient at $\tau = 0.2, \Delta\tau = 0.0005$. Solid lines are exact solution. Dashed lines are numerical solution. Contour levels for radial component are -0.33, -0.25, -0.15, -0.05 and 0.01. Contour levels for axial component are -0.38, -0.25, -0.1, 0.1, 0.25, and 0.38.	164

10-10	Radial and axial components of scalar gradient at $\tau = 0.2$, $\Delta\tau = 0.0005$, $\delta = 3.5h$ and $\delta = 5h$. Solid lines are exact solution. Dashed lines are numerical solution. Contour levels for radial component are -0.33, -0.25, -0.15, -0.05 and 0.01. Contour levels for axial component are -0.38, -0.25, -0.1, 0.1, 0.25, and 0.38.	165
10-11	Number of elements as a function of time step.	167
10-12	Number of elements as function of overlap ratio. $\Delta\tau = 0.0005$	167
10-13	Initial elements distribution.	168
10-14	Computational elements distribution at different times.	169
10-15	Scalar contours overlaid on top of vorticity colored distribution. Scalar contours (inwards) are 0.03, 0.1, 0.2, 0.3, 0.45, 0.6, 0.9, 1.2, and 1.45.	170
10-16	Upper figure: total circulation. Lower figure: mean axial position. Solid line is exact solution. Symbols are numerical solution: $\Delta\tau = 0.0005$: black circles, $\Delta\tau = 0.001$: grey circles, and $\Delta\tau = 0.002$: empty circles.	172
10-17	Upper figure: error in impulse. Lower figure: mean axial expansion. Solid line is exact solution. Symbols are numerical solution: $\Delta\tau = 0.0005$: black circles, $\Delta\tau = 0.001$: grey circles, and $\Delta\tau = 0.002$: empty circles.	173
10-18	Upper figure: error in total energy. Lower figure: mean axial position. Solid line is exact solution. Symbols are numerical solution: $\Delta\tau = 0.0005$: black circles, $\Delta\tau = 0.001$: grey circles, and $\Delta\tau = 0.002$: empty circles.	174
10-19	Upper figure: mean radial expansion. Lower figure: mean axial expansion. Solid line is exact solution. Symbols are numerical solution: $\Delta\tau = 0.0005$: black circles, $\Delta\tau = 0.001$: grey circles, and $\Delta\tau = 0.002$: empty circles.	175
10-20	Vorticity (upper) and scalar (lower) contours at $\tau = 0.2$ for $\Delta\tau = 0.0005$, 0.002, and 0.01. Core size and core expansion fraction are fixed.	178
10-21	Global error as a function of overlap ratio. Core size and core expansion fraction are fixed. Vorticity: filled circles. Scalar: empty circles.	179
10-22	Vorticity (upper) and scalar (lower) contours at $\tau = 0.2$ for $\Delta\tau = 0.0005$, 0.001, and 0.002. Overlap ratio and core expansion fraction are fixed.	180
10-23	Global error as a function of core size. Overlap ratio and core expansion fraction are fixed. Vorticity: filled circles. Scalar: empty circles.	181

10-24	Vorticity (upper) and scalar (lower) contours at $\tau = 0.2$ for $\sigma_f/h_0 = 1, 2,$ and 3.535. Core expansion fraction is fixed.	183
10-25	Global error as a function of overlap ratio. Core expansion fraction is fixed. Vorticity: filled circles. Scalar: empty circles.	184
10-26	Vorticity (upper) and scalar (lower) contours at $\tau = 0.2$ for $x = 0.02, 0.1,$ and 0.5. Final core size and initial element spacing are fixed.	185
10-27	Global error as a function of core expansion fraction. Final core size and initial element spacing are fixed. Vorticity: filled circles. Scalar: empty circles.	186
10-28	Number of elements as a function of time. Solid line: $\Delta\tau = 0.0005$, dash-dot line: $\Delta\tau = 0.001$, and dashed line: $\Delta\tau = 0.002$	187
11-1	Initial species radial distribution at $z = 0$	190
11-2	Initial elements distribution. Mixture fraction contours: 0.01, 0.1, 0.5, & 0.9.	190
11-3	Vorticity contours at $\tau = 0.005$. Dashed contours (blue outwards): -1.4, -1, -0.5 & -0.1. Solid contours (red inwards): 0, 0.1, 0.5, 1 & 1.4. Temperature distribution is also shown.	192
11-4	Vorticity contours at $\tau = 0.05, 0.1, 0.15,$ and 0.2. Dashed contours (blue outwards): -2.5, -1.5, -0.5 & -0.1. Solid contours (red inwards): 0.1, 0.5, 1.5 & 3.	193
11-5	Total circulation versus time for $\Delta\tau = 0.0005$	194
11-6	Fuel contours at $\tau = 0.05, 0.1, 0.15,$ and 0.2. Contour values (inwards): 0.01, 0.05, 0.1, 0.2, 0.5, 0.8.	196
11-7	Temperature contours at $\tau = 0.05, 0.1, 0.15,$ and 0.2. Contour values (in- wards): 1.1, 1.3, 1.7, 2.35 & 3.	197
11-8	Vorticity contours at $\tau = 0.2$: -2.5, -1.5, -0.5, -0.1, 0.1, 0.5, 1.5, & 3. Solid line: $\Delta\tau = 0.0005$. Dash-dot-dot line: $\Delta\tau = 0.001$. Dash-dot line: $\Delta\tau =$ 0.002. Dashed line: $\Delta\tau = 0.005$	198
11-9	Scalar contours at $\tau = 0.2$: 0.00025, 0.001, 0.0025 & 0.0045. Solid line: $\Delta\tau = 0.0005$. Dash-dot-dot line: $\Delta\tau = 0.001$. Dash-dot line: $\Delta\tau = 0.002$. Dashed line: $\Delta\tau = 0.005$	198
11-10	L-2 norm of error in vorticity and mixture fraction as a function of time step.	199
11-11	Number of elements versus time for $\Delta\tau = 0.0005$	200

11-12	Vorticity distribution for the radiating case at $\tau = 0.05, 0.1, 0.15,$ and 0.2 . Dashed contours (blue outwards): $-2.5, -1.5, -0.5$ and -0.1 . Solid contours (red inwards): $0.1, 0.5, 1.5$ and 3	202
11-13	Temperature distribution for the radiating case at $\tau = 0.05, 0.1, 0.15,$ and 0.2 . Contour values (inwards): $1.1, 1.3, 1.5, 1.9, 2.35,$ and 3	203
11-14	Total positive, negative, and net circulation as function of time with and without radiation. Symbols denote the case with radiation.	204
11-15	Ratio of thermal energy loss to energy generated by chemical reaction as a function of time. The maximum fuel mass fraction is also presented.	205

List of Tables

- 2.1 notation 33
- 2.2 notation 34

- 8.1 Parameter values used in numerical simulation. 116
- 8.2 Comparison between current study and the experiment done by Hamins et al. 120

- 10.1 Parameters. 176

Chapter 1

Introduction

Fires result in human, environmental, and economic losses. Minimization of these losses has mainly been empirically based. Fire science, being a relatively young subject, is gaining more interest in recent years due to its clear benefits. According to the study conducted by Shaenman[81], a total annual savings of \$5-9 billion could be traced to the National Institute of Standards and Technology program, costing less than \$9 million per year. Fire science extends beyond the combustion process itself to include study of their effects. According to Cox[23], “fire is such a complex subject that its study forces together many otherwise disparate specialisms. The subject of fire science includes contributions from structural engineers, behavioural psychologists, toxicologists and statisticians.” Among the objectives of fire science are determining the impact of fires on nearby and distant objects, predicting their growth and propagation, quantifying their environmental impact, improving fire suppression techniques, etc. According to the International Standards Organization[74], fire is defined as:

- (i) A process of combustion characterized by the emission of heat accompanied by smoke or flame, or both.
- (ii) Combustion spreading uncontrolled in time and space.

The subject of this thesis is numerical modeling and simulation of fires. Fires differ from human controlled combustion processes in three major aspects: (1) They are uncontrolled in the sense that the rate of fuel supply is determined by the positive feedback of heat (dominated by thermal radiation) from the products of the fire. (2) They are buoyancy driven and naturally aspirated. (3) They are diffusion flames where mixing of fuel with air

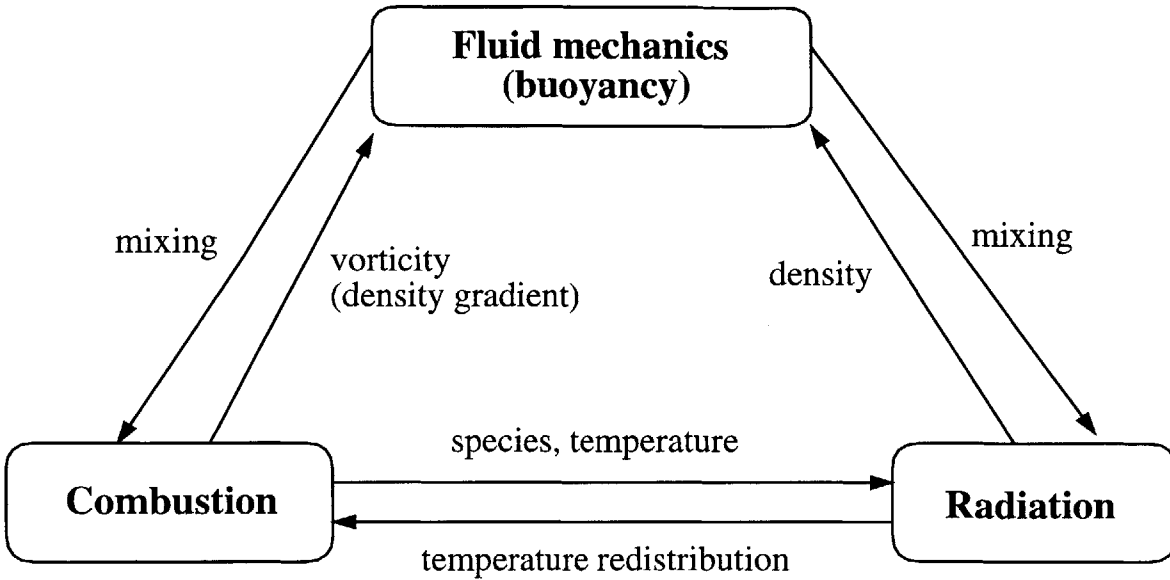


Figure 1-1: Diagram.

is controlled by buoyancy dominated convection which, along with stoichiometry, results in inefficient combustion in the form of long flames. This inefficiency results in large volumes of hot products that contain large quantities of soot particles due to the inefficient partial oxidation of fuel. Thermal radiation from these large exposed combustion volumes may ignite potential fuel and thus increase the possibility of fire spreading, especially in enclosures [23].

Natural fires are characterized by $Fr < 1$, where the Froude number, $Fr \equiv u^2/gD$, represents the ratio of inertial to buoyant forces. Fire flows are predominantly turbulent. The corresponding length scales vary between the Kolmogorov scale, of the order of few millimeters, and the fuel dimension or plume width, associated with large eddies. Based on the corresponding turbulence Reynolds number, fires tend to be at the lower end of fully turbulent flows.

Diffusion flames, including fires, are controlled by diffusion rather than chemical reaction. For fires, typical diffusion time scale is of the order of few seconds, whereas chemical time scales are in the range 10^{-5} - 10^{-6} s. This justifies for the assumptions of local equilibrium and infinite rate chemistry. It has been observed experimentally that fire plumes exhibit large scale unsteady motion in the form of “smoke” puffs which are shed periodically within a pool diameter above the fuel pool. These products of combustion form as a result of the complex interaction of buoyant fluid dynamics, heat and mass transport via convec-

tion and diffusion, radiative heat transport, and complex hydrocarbon oxidation chemistry (Figure 1). Contrary to most other combustion processes, the fuel supply rate in a fire, governed by the evaporation/sublimation or pyrolysis, is determined by the heat flux back to the pool, with a significant contribution from radiation. Radiation also contributes to the loss of a significant fraction of the heat released within the fire. The release of heat within the plume also generates strong buoyancy currents which determine the rate of air entrainment towards the fuel pool. Mixing within the plume is driven by the shear layers which form along the plume boundaries, and their role in enhancing the diffusion controlled fluxes of heat and mass along the stretched material interfaces. Clearly, a physical model designed to simulate fire dynamics must account for the unsteady interactions among these processes, namely buoyancy, convection and diffusive transport, radiation, and chemistry.

This chapter is organized as follows. Experimental observations are discussed first followed by analytical methods. Next, comparison between grid-based and grid-free numerical methods is discussed. The objectives are then stated. An overview of vortex methods follows. Numerical methods for solving radiative transfer are then described. Finally, a roadmap of the thesis is laid out.

1.1 Experimental work

Experimental study of pool fires has been conducted over wide ranges of parameters [41, 12, 103, 102] for the purpose of determining the dependence of the burn rate, the flame height, the heat release rate and radiative flux on the size of the pool and the fuel characteristics. These experimental studies have shown that most fires possess strong dynamics, characterized by the shedding of large burning structures, often referred to as puffing. These structures depend strongly on the pool diameter and weakly on the fuel type, and their formation is believed to impact the entrainment and hence the burning rate and products' composition.

The following sections summarize some of the important experimental observations, covering the unsteady behavior of the fire in terms of the puffing frequency, intermittency and flame height, air entrainment, and radiative heat loss.

1.1.1 Puffing

The dependence of the puffing frequency on the fuel pool diameter and fuel type has been compiled experimentally (see Hamins et al [41].) The puffing frequency, f , represented in the form of a Strouhal number $St = fD/w_0$, has been described by $St \propto Fr^{-m}$, where the Froude number, $Fr = w_0^2/gD$ with $m = 0.38$ and 0.57 for non-reacting plumes and fire plumes, respectively. The fuel source diameter is D , the fuel outflow speed from the source is w_0 , and the gravitational acceleration is g . The dependence of the Strouhal number on the Froude number has later been derived by Delichatsios[27] using dimensional analysis.

Despite several attempts to determine the mechanism leading to puffing and predict its characteristics, e.g. the phenomenological analysis by Weckman[98] based on assuming the presence of a vortex near the pool outside the diffusion flame, the modeling by Bejans[7] based on the theory of buckling of inviscid flows, the linear stability analysis of diffusion flames conducted by Lingens et al[64] which showed that instability of this flow close to the fuel source is absolute, etc., a comprehensive approach for predicting the puffing frequency and explaining mechanistically the processes leading to the unsteadiness is not yet available.

1.1.2 Intermittency and flame height

The intermittency, I , defined as the fraction of time during which at least part of the flame lies above a horizontal plane located at a specified elevation, Z , above the fuel source, and the flame height, Z_f , defined as the height at which $I = 0.5$, have been studied experimentally [103, 68]. The extent of intermittency, normalized by the average flame height, was shown to increase with the fuel source diameter.

Data on flame heights is available for wide ranges of fuels and burner diameters[45, 104, 100, 57]. Correlations[45, 8, 9, 44, 43], obtained from fitting the experimental data, relate the average flame height, normalized by the fuel source diameter, to the dimensionless heat release rate $Q_D^* = \dot{Q}_f / \rho_\infty C_{p\infty} T_\infty \sqrt{gD} D^2$, where \dot{Q}_f , ρ_∞ , $C_{p\infty}$, and T_∞ are the heat release rate in the fire, the ambient density, ambient temperature, and the constant pressure specific heat respectively. This correlation shows two distinct regions where the flame height scales differently: $Z_f/D \propto Q_D^{*2/3}$ for $Q_D^* < 1$ and $Z_f/D \propto Q_D^{*2/5}$ for $Q_D^* > 1$.

1.1.3 Entrainment

Entrainment, while driven by the fire dynamics, determines the burn rate, and hence must be quantified accurately in a fire model. However, current entrainment correlations which are based on experimental results suffer from a large scatter. Results obtained by Thomas et al[89] differ by up to 50% from those obtained by Delichatsios[28] and about 35% from those obtained from Caltech[13]. This large scatter is attributed to the differences in the definition of entrainment utilized in connection with different measurement techniques, and the difficulties facing experimental measurements.

One technique is based on experimental measurements of density and velocity at different locations to estimate total mass flux in the plume[103]. However, measuring simultaneously the instantaneous profiles of temperature and velocity is difficult because physical probes with fast time response often can not survive the high temperature environment of the plume. Another technique, which uses the Ricou and Spalding apparatus[78], is based on regulating the air supply to a fire-surrounding hood until the pressure differential across the hood vanishes. This technique is a poor choice when measuring entrainment close to the pool surface due to its sensitivity to flame oscillations. Furthermore, the selection of the diameter of the circular opening at the top of the surrounding box is critical to this technique as it affects the flow in the neighborhood of the fire. A third method which uses the hood technique[13] suffers its own shortcomings as well, especially if determining the mass flux in the plume is required.

Recently, a theoretical model for predicting entrainment rates based on prior knowledge of heat release and vorticity distributions within the plume has been suggested by Zhou et al.[102]. However, measurements of these quantities in fires have been most challenging due to the lack of accurate instruments for direct measurement of vorticity, and errors associated with available instruments used for indirect measurements.

1.1.4 Radiation

Experimental work focused on measuring the ratio of the total energy lost by radiation to the total heat released for a variety of fuels and a range of burner diameters. This ratio was found to be roughly independent of the burner diameter and to depend strongly on the fuel. Its values vary from 0.25 for methane flames[10, 75] to as large as 0.5 for acetylene

flames. These results reveal the significance of radiation in studying fire dynamics and its impact on its surroundings. However, measurements of the instantaneous radiative flux are not available.

Clearly radiation is one of the primary mechanisms for the supply of heat to the fuel pool and the loss of heat from the plume. Radiative flux depends non-linearly on the instantaneous composition of the combustion products, their optical properties, and the temperature. Therefore, prediction of the radiative flux within the fire and to surrounding objects requires accurate knowledge of distribution of these quantities.

1.2 Analytical models

Algebraic models, limited to estimating the average velocity and temperature fields for the nonreacting buoyant plume rising above the top of a fire, have been developed. In the point source model[80, 71], the plume is assumed to rise from an equivalent point source, which allows determination of similarity solution; a reasonable description of the flow far above the source. The solution is obtained using the integral form of the conservation equations along with the following assumptions: (1) Gaussian radial profiles of vertical velocity and temperature, (2) Boussinesq approximation, and (3) entrainment rate per unit height is proportional to the ambient density, the centerline velocity, and the scale of the width of the plume at that elevation[71].

The point source properties, the elevation and the initial enthalpy and momentum fluxes, however, have to be determined such that the far-field characteristics of the point source plume asymptotically approach those of the real plume above the top of the fire. Although the enthalpy flux must be equal to that produced by the fire, the equivalent point source elevation (effective origin) and the initial momentum flux are not so easily determined and one must rely on correlations based on experimental data[13, 44] to determine the offset of the effective origin from the real origin by matching the initial mass flux.

Incorporation of unsteadiness into the point source model is limited to steady input of buoyant fluid at the source[95] and allowing the top of the plume to rise to accommodate the entrained flow.

1.3 Numerical methods

Experimental observations showed that the fire flow-field is characterized by the shedding of large burning structures above the pool. These structures are thought to contain regions of high vorticity, which control the entrainment of air into the reacting zone, and hence mixing and burning rate. These observations suggest that accurate representation of vorticity is a primary requirement of numerical computation of this flow. The numerical approach we choose to compute the flow field is the vortex method (in axisymmetric coordinates.) Vortex methods may be classified as grid-free, Lagrangian, vorticity based, and conservative.

Vortex methods have been successfully used to investigate the evolution of vortex sheets [18, 83, 35], high Reynolds number wakes [86, 15], three dimensional problems [53, 67, 33, 2], non-reacting buoyant plumes[36], reacting flows in shear layers [84], co-axial jets [65], and fires [59, 36].

In these methods, convection is simulated by transporting conserved quantities such as circulation along particles' trajectories. Vortex methods differ from conventional grid-based methods in various ways. Vortex methods requires elements in regions of non-zero vorticity only, hence endowing the method with spatial adaptivity and maintained numerical resolution. The Lagrangian aspect of vortex methods avoids the introduction of numerical diffusion induced by the discretization of convective derivatives on a fixed grid. This advantage is especially important when "high Reynolds number" flows are considered, where numerical dissipation might destroy the small scale features of the flow produced by the convection processes. Further, conventional numerical methods require special treatment of the far-field boundary conditions for flows in unbounded domains. These conditions are naturally satisfied in the vortex method by using the proper Green's function of the Poisson's equation relating the velocity to the vorticity. An overview of vortex methods can be found in [19, 34, 63].

While grid-based numerical methods are highly developed, vortex methods are still under development, especially for complex flows such as combustion. Some of the challenges in simulating reacting flows using a vortex method include incorporating the effects of *variable diffusion properties*, the dynamic impact of *large heat release*, and *radiative heat transfer*. For the problem at hand, some development in the numerical algorithm has been made and some assumptions had to be enforced regarding the unresolved problems. These are

described next.

1.4 Objectives and tasks

The objectives of this work are

- to develop a grid-free Lagrangian computational tool (based on the vortex method) for the numerical simulation of fire plumes in an axisymmetric domain, in which **buoyancy**, **combustion**, and **radiation** are incorporated, and
- to utilize this tool to reveal mechanisms in fire dynamics such as puffing, entrainment, flame height, etc.

Meeting the above objectives requires carrying out the following tasks:

1. Formulate an accurate vortex method in an axisymmetric domain. This includes determining an axisymmetric “adaptive” core function, development and implementation of an accurate diffusion algorithm, and extending the method to transport a reacting scalar field.
2. Extending the formulation to account for nonlinear source terms in variable density radiating flows.
3. Solve the energy equation with the radiation source term. This presents a significant challenge on two levels. First, the evaluation of the radiation source term, which involves a volume integral of the black body radiation attenuated by the radiation kernel, in a grid-free manner (to be compatible with the grid-free form of the rest of the scheme). Second, coupling the solution of the vorticity transport equation and the energy equation.
4. Using simulation results to investigate fire dynamics leading to the experimentally observed phenomenon of puffing and intermittency in flame height, dependence of the average fire properties on pool and fuel characteristics, and the origin of the entrainment mechanism.

1.5 Vortex methods

In the vortex methods, the equations governing conservation of vorticity, energy, and species are numerically solved via operator splitting. The stability and convergence properties are discussed in chapter 3. The splitting results in the requirement to solve three processes separately. These processes are convection, diffusion, and generation. Next, we discuss briefly the various methods currently used to solve each substep.

1.5.1 Convection

In the convection step, the elements, carrying conserved quantities, are convected according to the velocity field. The velocity field is determined using Biot-Savart summation[3] over all the elements. The direct summation is an expensive process where the computational cost is of the order of N^2 , where N is the number of elements. For the purpose of reducing the cost, fast methods[38] were developed with a cost of the order of $N \log N$.

1.5.2 Diffusion

Grid-free Lagrangian numerical modeling of diffusion involves solving the diffusion equation on an irregular distribution of vortices. Some of the current methods for diffusion modeling are random walk, core spreading, diffusion velocity, particle strength exchange, and redistribution method.

Random walk method

Proposed by Chorin[17], the random walk method is applied by giving the positions of vortices random displacements of, a process which spreads out vorticity similar to diffusion. The solution of random walk method converges to that of the Navier-Stokes as the number of elements increases. The random walk method is simple to use and conserves the total circulation. However, the random walk method suffers from several drawbacks. First, it does not conserve the mean position of vorticity. Second, it leads to noisy solutions. The performance of the method improves for larger number of elements resulting in an increase in the overall computational cost of a simulation.

Core spreading method

The core spreading method[63] solves the diffusion equations by associating for each element a basis function with a core radius that expands in time. The core function, based on the Green's function of the diffusion equation, solves the diffusion equation accurately. However, as the elements expand in time, the convection process becomes inaccurate, as proved by Greengard. Rossi proposed splitting the elements into smaller vortices in a symmetrical fashion, which reduces the error due to convection but on the expense on an exponential increase in the number of elements.

Diffusion velocity method

The diffusion velocity method[37, 73, 52] is based on simulating diffusion as a part of the convection process. This is done by determination of an artificial "diffusion" velocity derived by absorbing the diffusion term in the convection term in the vorticity equation. The diffusion velocity method has the following disadvantages: the diffusion velocity may become infinite in regions of vanishing vorticity or large vorticity gradients. Further the method is not divergence free and requires an large number of vortices for accurate simulation.

Particle strength exchange method (PSE)

The PSE method[77, 16, 22, 25] is based on determination of the circulations of the elements in time by approximating the diffusion operator by an integral operator, and discretizing the latter using the particles positions as quadrature points. The PSE method requires large overlap as a condition for accuracy resulting in a large number of elements. Further the method requires periodic remeshing to maintain accuracy leading the interpolation errors.

Redistribution method

The redistribution method[86] simulates diffusion by transferring fractions of the circulation of the element to be diffused to neighboring elements. The fractions are obtained by solving a linear system of equations based on conserving various moments of vorticity. The redistribution method however is based on a point representation of the vorticity field making it difficult to recover the pointwise vorticity field. In practice, the vorticity field is recovered by determination the appropriate core radius by trial and error.

1.5.3 Generation

The source terms are the baroclinic vorticity generation in the vorticity equation, rate of reaction in the species conservation equation, and heat of reaction and the divergence of the radiative heat flux in the energy equation. The source term is in general a function of the pointwise distribution of vorticity, temperature, species, and their gradients. Since the quantities transported by the elements are integral quantities, then the pointwise source term distribution has to be cast into these transported quantities. One way of performing this task is to calculate the circulation by integrating vorticity over physical area, assuming uniform distribution within physical area[85]. Another way is to determine the circulations by solving a linear system obtained by evaluating the vorticity representation equation at the elements locations. Methods for solving the linear system are discussed by Marshall and Grant[66].

1.6 Grid-free modeling of radiative transport

Radiative transport in a participating medium transforms the energy equation into an integro-differential equation. In combustion problems, the temperature gradients are so steep that the region where the radiative flux, which is proportional to the fourth power of temperature, is significant only in a small subset of the entire flow domain. Especially when utilizing a grid-free scheme to perform the convective-diffusive-reactive simulations, it is desirable to develop a compatible scheme which does not require a grid to compute the radiative flux and its divergence (needed in the energy equation.) We have developed the discrete-source method[58] in which the radiative flux and irradiance are computed by summing over a collection of radiating elements distributed over the region of high temperature. In an axisymmetric domain, the irradiance and radiative flux, being triple integrals of the radiation kernel over the elemental volume, are reduced to double integrals which are then approximated by single integrals that are evaluated semi-analytically.

Methods currently used to solve radiative transfer include the method of spherical harmonics, the discrete ordinates method, the zonal method, and the Monte Carlo method. A brief description of these methods is presented next.

1.6.1 The method of spherical harmonics

The method of spherical harmonics[51, 55, 24, 72] transforms the equations of transfer into a set of simultaneous partial differential equations. The method has the following disadvantage, lower-order approximations are only accurate in optically thick media, whereas for higher-order approximations accuracy improves slightly with a rapid increase in mathematical complexity. The method of spherical harmonics is based on decoupling direction and location by expressing the intensity as a two-dimensional Fourier series. The expression in the summation is a product of a position-dependent coefficient and a spherical harmonic which is direction-dependent. Exploiting the orthogonality properties of spherical harmonics, the equation of radiative heat transfer is convoluted with these functions to yield an infinite system of coupled partial differential equations in the unknown position-dependent coefficients. The infinite series is truncated retaining retaining N terms, where N is the order of the method.

1.6.2 The discrete ordinates method

First proposed by Chandrasekhar[14], the discrete ordinates method[93, 94, 30, 31] also transforms the equation of transfer into a set of partial differential equations. It differs from the method of spherical harmonics in that the directional variation of the intensity is discretized over a finite set of discrete directions spanning the total solid angle. Thus, the method may be thought of as a finite difference approximation of the directional dependence of the equation of transfer.

1.6.3 The zonal method

In the zonal method[46, 47], the medium is subdivided into a finite number of isothermal volumes and surface area zones. Energy balance is then performed for the radiative exchange between each two zones, leading to a linear system with the temperature or heat flux as the unknown. The method requires calculation of "exchange areas"[61] between each two zones. Evaluation of these exchange factors is a difficult and expensive process.

1.6.4 The Monte Carlo method

The Monte Carlo method[32, 49, 48, 97] is a statistical method in which the history of a statistically meaningful random sample of photons is traced from their point of emission to their points of absorption. As the complexity of the problem increases, the Monte Carlo method requires less computational effort and less complex formulation than conventional methods. However, it is subject to statistical error

1.7 Roadmap

This thesis may be divided into two parts: numerical development and application. The development part is covered in chapters 2 through 7 as follows: the governing equations are stated in chapter 2. Vortex methods are discussed in chapter 3 followed by scalar transport in chapter 4. Diffusion, convection and radiation modeling are discussed in chapters 5, 6, and 7 respectively. The application part covers chapters 8 through 11 as follows: Isothermal and reacting plumes are discussed in chapters 8 and 9 respectively. Examples of stokes flow, vortex ring, reacting fuel ring, and reacting radiating fuel ring are discussed in chapter 10 and 11. Conclusion and future work are stated in chapter 12.

Chapter 2

Governing Equations

In this chapter, the conservation equations governing the flow of a multicomponent reacting mixture of ideal gases in an axisymmetric domain are presented. The equations governing conservation of mass, momentum, and energy are described in sections 2.2, 2.3, and 2.4 respectively, along with the underlying assumptions. In section 2.5, the species conservation equation is presented, along with the chemical reaction and expressions for the rate of reaction and heat release. Density effects in large heat release buoyant flows in unbounded domains are discussed in section 2.6. The dimensionless form of the governing equations is presented in section 2.7. In section 2.8, the equation governing vorticity transport is presented. The Shvab-Zel'dovich formulation, used to eliminate the reaction source terms in the energy and species conservation equations, is presented in section 2.9. The special case of infinite rate chemical reaction is discussed in section 2.10. Expressions for the rates of change of material integrals of scalar and vector quantities are shown in section 2.11. The symbols appearing in the equations are described in Table 2.1.

2.1 Conservation equations

The laws of conservation for a multicomponent reacting mixture[99, 3] of ideal gases are:

1. Conservation of mass (continuity).
2. Conservation of momentum (Newton's second law).
3. Conservation of energy (first law of thermodynamics).

Symbol	Description
a	acceleration
A	the frequency factor in the Arrhenius expression
B	a constant in the frequency factor (A)
c_p	Specific heat of the mixture at constant pressure
D	mass diffusion coefficient
D_{ij}	binary mass diffusion coefficient for the pair or species i and j
E_a	activation energy for the reaction
\mathbf{g}	gravity, $\mathbf{g} \equiv -g\hat{\mathbf{z}}$, where g is gravitational acceleration
h_i^0	heat of formation per unit mass for species i
k	specific reaction rate constant
M_i	molecular mass of species i
M_i	average molecular mass of the mixture
N_s	total number of chemical species present
p	thermodynamic pressure
\mathbf{q}_r	radiative heat flux
\mathbf{r}	position vector in axisymmetric coordinates; $\mathbf{r} \equiv r\hat{\mathbf{r}} + z\hat{\mathbf{z}}$
r	radial coordinate
R^0	universal gas constant
\tilde{s}	mixture fraction
T	temperature
t	time
\mathbf{u}	velocity vector (u_r, u_z)
u_r	radial velocity component
u_z	axial velocity component
U	reference velocity
X_i	mole fraction of species i
Y_i	mass fraction of species i
z	axial coordinate
α	thermal diffusivity $\alpha = \lambda/\rho c_p$
β	exponent determining the temperature dependence of the frequency factor for the reaction
Γ	circulation
λ	thermal conductivity
μ	coefficient of (shear) viscosity
ν	kinematic viscosity $\nu = \mu/\rho$
$\boldsymbol{\omega}$	vorticity vector
ω	vorticity
ϕ	fuel to air mass fraction fraction
ρ	density
θ	coordinate in azimuthal direction
Θ	rate of heat generation per unit volume due to chemical reaction
ν	(mole) stoichiometric coefficient
ϖ_i	reaction rate
\mathcal{X}	chemical symbol for a species

Table 2.1: notation

Symbol	Description
<i>subscripts</i>	
i	refers to i th species ($i = 1, \dots, N_s$)
f	fuel
o	oxidizer
p	product
d	diluent
0	refers to free stream conditions
sz	refers to a Shvab-Zel'dovich conserved scalar
<i>superscripts</i>	
*	denotes a dimensionless variable
$'$	refers to reactants
$''$	refers to products
<i>accents</i>	
$\hat{\cdot}$	denotes a unit vector
<i>operators</i>	
$\nabla \mathbf{v}$	gradient of vector \mathbf{v}
$D\mathbf{v}/Dt$	the convective (material) derivative; $D\mathbf{v}/Dt = \partial\mathbf{v}/\partial t + (\mathbf{u} \cdot \nabla)\mathbf{v}$
$\nabla \times \mathbf{v}$	curl of vector \mathbf{v}
$\nabla \cdot \mathbf{v}$	divergence of vector \mathbf{v}
<i>dimensionless numbers</i>	
Le	Lewis number, $Le \equiv \alpha/\mathcal{D}$
Pe	Peclet number, $Pe \equiv r_0 U/\alpha$
Pr	Prandtl number, $Pr \equiv \nu/\alpha$
Re	Reynolds number, $Re \equiv r_0 U/\nu$

Table 2.2: notation

4. Conservation of species.

The unknowns are the velocity \mathbf{u} , the thermodynamic pressure p , the absolute temperature T , the species concentrations X_i , $i = 1, N_s$, where N_s is the number of species. The knowns are the chemical equilibrium constants, reaction rates, heats of formation, and boundary condition for \mathbf{u} , p , and T .

2.1.1 Thermodynamic properties

The conservation equations also contain the thermodynamic properties: density ρ , enthalpy h (or internal energy e), and the transport properties μ , λ , \mathcal{D}_{ij} . Assuming thermodynamic equilibrium, these properties are uniquely determined by the pressure and temperature. Thus the system is completed by assuming knowledge of the state relations

$$\chi = \chi(p, T) \quad (2.1)$$

where χ denotes any of the properties ρ , h , μ , λ , and \mathcal{D}_{ij} . The state relation for density[82] in differential form is

$$\frac{d\rho}{\rho} = -\beta dT + \kappa dp, \quad (2.2)$$

where for an ideal gas, the coefficient of thermal expansion, β , and the isothermal compressibility, κ , are given by

$$\beta \equiv -\frac{1}{\rho} \left(\frac{\partial \rho}{\partial T} \right)_p = \frac{1}{T}, \text{ and } \kappa \equiv \frac{1}{\rho} \left(\frac{\partial \rho}{\partial p} \right)_T = \frac{1}{p}. \quad (2.3)$$

2.1.2 Laws of chemical reaction

Determination of the source terms in the energy and species conservation equations requires modeling of the rate of reaction and knowledge of chemical-equilibrium constants and heats of formation.

2.1.3 Boundary conditions

The boundary conditions for \mathbf{u} , p , T , and X_i must be specified for a particular problem.

2.2 Conservation of mass

The equation of continuity is

$$\frac{D\rho}{Dt} + \rho \nabla \cdot \mathbf{u} = 0 \quad (2.4)$$

where ∇ is the gradient operator and D/Dt is the material derivative ($\frac{D}{Dt} \equiv \frac{\partial}{\partial t} + \mathbf{u} \cdot \nabla$); the time derivative following the motion of the fluid.

2.3 Conservation of momentum

Assuming that

1. the fluid is Newtonian,
2. the fluid is in thermodynamic equilibrium,
3. the only body force is gravity, \mathbf{g} ,
4. the coefficient of viscosity, μ , is constant, and
5. the effect of bulk viscosity is negligible,

the momentum equation is

$$\rho \frac{D\mathbf{u}}{Dt} = \rho \mathbf{g} - \nabla p + \mu \nabla^2 \mathbf{u} \quad (2.5)$$

2.4 Conservation of energy

Assuming that

1. the reversible compression component due to equilibrium pressure is negligible,
2. the irreversible expansion component, due to departure of mean normal stress from equilibrium pressure, is negligible, and
3. the dissipation of mechanical energy into heat, due to the interaction of deviatoric stress component with the non-isotropic strain component, is negligible,
4. the Dufour heat flux¹ is negligible,

¹the component of heat flux due to the concentration gradients of the chemical species.

the energy equation is

$$\rho c_p \frac{DT}{Dt} = \nabla \cdot (\lambda \nabla T) + \Theta - \nabla \cdot \mathbf{q}_r, \quad (2.6)$$

where Θ is a source term corresponding to the rate of generation of energy per unit volume of a material element due to external agents or chemical reaction, and $-\nabla \cdot \mathbf{q}_r$ is the source term due to radiative transport; \mathbf{q}_r is the radiation heat flux.

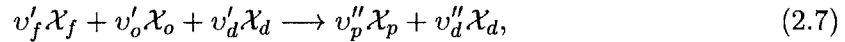
2.5 Combustion

In addition to the conservation equations of mass, momentum, and energy, combustion formulation characterizing flow of a viscous, heat-conducting mixture of diffusing, reacting gases entails

1. description of chemical reactions among the species,
2. development of the mass conservation for each species, and
3. development of the relevant source term in the energy equation due to these chemical reactions.

2.5.1 Chemical reaction

The chemical reaction, assumed single-step and irreversible, accounts for consumption of reactants, fuel (f) and oxidant (o), in the presence of a diluent (d), and production of products (p) according to



where v'_i and v''_i are the stoichiometric coefficients for species i , appearing as a reactant and as a product, respectively; $i = f, o, d, p$. The stoichiometric coefficients specify the molecular proportions in which the reactants participate. The chemical symbol for species i is denoted by \mathcal{X}_i .

2.5.2 Conservation of species

Consider the individual components of the mixture, denoting the density of the i -component by ρY_i , where Y is the mass fraction and $i = 1, \dots, N_s$. Assuming that

1. the binary diffusion coefficients of all pairs of species are equal, $\mathcal{D} \equiv \mathcal{D}_{ij}$,
2. the pressure gradient diffusion² is negligible, and
3. the Soret effect³ is negligible,

then the equation governing conservation of chemical species is

$$\rho \frac{DY_i}{Dt} = \nabla \cdot (\rho \mathcal{D} \nabla Y_i) + \dot{\rho}_i. \quad (2.8)$$

The mass production rate per unit volume of the i th component, $\dot{\rho}_i$, may be expressed as

$$\dot{\rho}_i = M_i v_i \varpi, \quad (2.9)$$

where M_i is the molecular mass of the i th component, $M_i v_i$ is the mass stoichiometric coefficient; $v_i = v_i'' - v_i'$, and ϖ is the reaction rate. Thus the conservation equation for species i is

$$\rho \frac{DY_i}{Dt} = \nabla \cdot (\rho \mathcal{D} \nabla Y_i) + M_i v_i \varpi. \quad (2.10)$$

2.5.3 Rate of reaction and heat release

The reaction rate is proportional to the product of the concentrations of the reactants,

$$\varpi = k(T) \prod_{i=1}^{N_s} \left(\frac{X_i p}{R^0 T} \right)^{v_i'} \quad (2.11)$$

where X_i is the mole fraction of species i , and $k(T)$, the specific reaction rate constant, is given empirically by the Arrhenius expression

$$k = A e^{-E_a/R^0 T}, \quad (2.12)$$

where R^0 is the universal gas constant, E_a is the activation energy, and A is the frequency factor given by the approximation

$$A = B T^\beta \quad (2.13)$$

²contribution of pressure gradient to concentration gradients when the mass fractions differ from the mole fractions.

³The contribution of thermal diffusion to concentration gradients.

where B and β are constants, $0 \leq \beta \leq 1$.

The heat release Θ is

$$\Theta = - \sum_i^N \dot{\rho}_i h_i^0 \quad (2.14)$$

where h_i^0 heat of formation per unit mass for species i . If the reaction is exothermic and the heat of reaction of the fuel (h_f^0) is large compared to that of all other species, then the heat release may be expressed as

$$\Theta = M_f v_f' h_f^0 \varpi. \quad (2.15)$$

2.5.4 Equation of state

The ideal gas equation of state, relating the density to the temperature, is

$$p = \frac{\rho R^0 T}{M}, \quad (2.16)$$

where the average molar mass, M , is given by

$$M = \frac{1}{\sum_{i=1}^{N_s} Y_i / M_i}. \quad (2.17)$$

The mole fraction is related to the mass fraction via

$$X_i = Y_i \frac{M}{M_i}. \quad (2.18)$$

2.6 Density effects

In this section, we discuss the effects of density variation on the momentum and energy conservation equations, and the sources of change in density. The discussion will be focused on flows involving large heat release in a unbounded domain in the presence of gravity.

In natural convection, a local change of density is the agency that initiates motion. Therefore, ρ must be allowed to vary in the expression for the gravitational force, $\mathbf{f} = \rho \mathbf{g}$, even if it is treated as a constant parameter elsewhere. Further, in the presence of gravity, spatial variation in density will result in nonuniform acceleration. Therefore, ρ must be allowed to vary in the term $\rho D\mathbf{u}/Dt$.

There are three ways to change the density of a given fluid particle: (1) isentropic compression, (2) viscous dissipation, and (3) heating by conduction or radiation ⁴. Isentropic compression is important in high speed flows, and in sound waves propagating in either liquids or gases, viscous dissipation is important in high-speed gas bearings and in supersonic boundary layers, and heating by conduction or radiation is important in fires and in boundary layers on very hot or cold bodies. Dimensional analysis of the problem of free convection over a flat plate leads to the dimensionless numbers gz/a^2 , $(\Delta T/T)(gz/a^2)$, and $\Delta T/T$ reflecting the relative importance of (1), (2), and (3) with respect to the divergence of the velocity, respectively. Obviously for operating conditions of fires, $gz/a^2 \ll 1$ and $(\Delta T/T)(gz/a^2) \ll 1$, leaving heating by conduction or radiation as the dominant source of density variation. For a fire of elevation 5 meters with a maximum relative temperature change of 5, the values are 0.0004, 0.002, and 5 respectively.

The term anelastic flow[82] implies that the density of a particle varies only as a result of isobaric thermal expansion, so that equation 2.2 is approximated by

$$\frac{D\rho}{Dt} \cong -\rho\beta\frac{DT}{Dt} \quad (2.19)$$

Together with the continuity and energy equation, equations 2.19 yield the result

$$\nabla \cdot \mathbf{u} + \frac{\rho\beta}{c_p}\nabla \cdot \mathbf{q} = 0 \quad (2.20)$$

The effect of the anelastic approximation is to remove the acoustic phenomena from theoretical consideration, while still allowing an accurate accounting for the buoyancy and inertial effects of variable density, the modification of viscous forces and heat conduction by the variation of transport properties, and the velocity induced by moderately slow expansion or contraction of the fluid particles.

For a thermally perfect gas ($\beta T = 1$), equation 2.19 becomes

$$\frac{D(\rho T)}{Dt} = 0 \quad (2.21)$$

This thermodynamic conclusion does not imply, however, that the pressure is absolutely uniform. Pressure gradients may be large enough to be important in momentum balance, but

⁴viscous dissipation and heating by conduction or radiation are usually accompanied by thermal expansion

simultaneously small enough to have no significant influence on the variations of density or temperature. So, assuming anelastic flow of a thermally perfect gas, the continuity equation reduces to

$$\nabla \cdot (P\mathbf{u} + (1 - \gamma^{-1})(\lambda\nabla T - \mathbf{q}_r)) = 0, \quad (2.22)$$

and the equation of state is approximated as

$$\rho T = P \text{ a constant}, \quad (2.23)$$

where $\gamma = c_p/c_v$ and the value of P is determined by the initial state of the fluid. For unbounded domains, $P = p_0$; the farfield pressure.

2.7 Dimensionless form of the governing equations

Using the reference length⁵ r_0 , reference circulation⁶ $\Gamma_0 \equiv r_0\sqrt{gr_0}$, reference velocity $U \equiv \Gamma_0/r_0$, reference time⁷ $t_0 \equiv r_0/U$, and other properties at freestream conditions $p_0, \rho_0, T_0, M_0, \mu_0, k_0, \mathcal{D}_0$, the dimensionless variables, denoted by asterisks, are as follows:

$$\mathbf{r}^* = \frac{\mathbf{r}}{r_0}, \quad \nabla^* = r_0 \nabla \quad (2.24)$$

$$\mathbf{u}^* = \frac{\mathbf{u}}{U} \quad (2.25)$$

$$t^* = \frac{t}{r_0/U} \quad (2.26)$$

$$T^* = \frac{T}{T_0} \quad (2.27)$$

$$\rho^* = \frac{\rho}{\rho_0} \quad (2.28)$$

⁵pool radius in the fire problem; initial radial location for the vortex ring problem.

⁶for the vortex ring problem, Γ_0 is the initial circulation.

⁷Oscillatory effects which are intrinsic to the flow pattern, such as the shedding of vortices in a buoyant plume, are not fundamental external parameters but are part of the solution to the flow problem. Thus the Strouhal number of the plume vortices is uniquely determined by the flow.

$$M_i^* = \frac{M_i}{M_0} \quad (2.29)$$

$$p^* = \frac{p + \rho_0 g z - p_0}{\rho_0 U^2} \quad (2.30)$$

$$\mu^* = \frac{\mu}{\mu_0}, \quad \lambda^* = \frac{\lambda}{\lambda_0}, \quad c_p^* = \frac{c_p}{c_{p0}}, \quad \mathcal{D}^* = \frac{\mathcal{D}}{\mathcal{D}_0} \quad (2.31)$$

$$Q_f^* = \frac{h_f^0}{c_{p0} T_0} \quad (2.32)$$

$$\varpi_f^* = \frac{r_0}{\rho_0 U} M_f v'_f \varpi \quad (2.33)$$

$$(\nabla \cdot \mathbf{q}_r)^* = \frac{r_0}{\rho_0 c_{p0} T_0 U} \nabla \cdot \mathbf{q}_r \quad (2.34)$$

After omitting the asterisks, the conservation equations, in their dimensionless form, are described as

Conservation of mass:

$$\frac{D\rho}{Dt} + \rho \nabla \cdot \mathbf{u} = 0 \quad (2.35)$$

Conservation of momentum:

$$\rho \frac{D\mathbf{u}}{Dt} = -\nabla p + \frac{1}{Re_0} \mu \nabla^2 \mathbf{u} + (1 - \rho) \hat{\mathbf{z}} \quad (2.36)$$

Conservation of energy:

$$\rho c_p \frac{DT}{Dt} = \frac{1}{Pe_0} \nabla \cdot (\lambda \nabla T) + Q_f \varpi_f - \nabla \cdot \mathbf{q}_r \quad (2.37)$$

Conservation of species

$$\rho \frac{DY_i}{Dt} = \frac{1}{Le_0 Pe_0} \nabla \cdot (\rho D \nabla Y_i) + \Lambda_i \varpi_f, \quad i = 1, \dots, N_s \quad (2.38)$$

Ideal Gas equation of state:

$$\frac{\rho T}{M} = 1 \quad (2.39)$$

where $\Lambda_f = -1$, $\Lambda_o = -(M_o v'_o)/(M_f v'_f) \equiv -\phi$, $\Lambda_p = (M_p v'_p)/(M_f v'_f) \equiv 1 + \phi$, and $\Lambda_d = 0$. The Reynolds, Prandtl, Peclet, and Lewis numbers are respectively

$$Re_0 = \frac{Ur_0}{\nu_0} \quad (2.40)$$

$$Pr_0 = \frac{\nu_0}{\alpha_0}, \quad \alpha_0 = \frac{\lambda_0}{\rho_0 c_{p0}} \quad (2.41)$$

$$Pe_0 = \frac{r_0 U}{\alpha_0} = Re_0 Pr_0 \quad (2.42)$$

$$Le_0 = \frac{\alpha_0}{\mathcal{D}_0} \quad (2.43)$$

2.8 The vorticity equation

The vorticity vector is defined as the curl of the velocity,

$$\boldsymbol{\omega} = \nabla \times \mathbf{u}. \quad (2.44)$$

In axisymmetric coordinates, the vorticity vector points in the azimuthal direction, $\hat{\boldsymbol{\theta}}$, and is given by

$$\boldsymbol{\omega} \equiv \omega \hat{\boldsymbol{\theta}} \equiv \left(\frac{\partial u_r}{\partial z} - \frac{\partial u_z}{\partial r} \right) \hat{\boldsymbol{\theta}} \quad (2.45)$$

The vorticity equation[20], obtained by taking the curl of the momentum equation 2.5 and using the continuity equation 2.4, may be described as

$$\frac{D\boldsymbol{\omega}}{Dt} = ((\boldsymbol{\omega} \cdot \nabla)\mathbf{u} - \boldsymbol{\omega}(\nabla \cdot \mathbf{u})) + \left(\frac{\nabla \rho}{\rho} \right) \times \left(\mathbf{g} - \frac{D\mathbf{u}}{Dt} \right) + \nu \nabla^2 \boldsymbol{\omega} \quad (2.46)$$

Noting that the reference vorticity is

$$\boldsymbol{\omega}^* = \frac{\boldsymbol{\omega}}{\sqrt{gr_0}/r_0}, \quad (2.47)$$

the vorticity equation, in dimensionless form, after omitting the asterisks, is given by

$$\frac{D\boldsymbol{\omega}}{Dt} = ((\boldsymbol{\omega} \cdot \nabla)\mathbf{u} - \boldsymbol{\omega}(\nabla \cdot \mathbf{u})) + \frac{\nabla\rho}{\rho} \times \left(-\hat{\mathbf{z}} - \frac{D\mathbf{u}}{Dt}\right) + \frac{\nu}{Re_0} \nabla^2 \boldsymbol{\omega} \quad (2.48)$$

Noting that $\boldsymbol{\omega} \cdot \nabla \mathbf{u} = (\omega u_r/r)\hat{\theta}$, then

$$\frac{D\omega}{Dt} = \left(\frac{u_r}{r} - \nabla \cdot \mathbf{u}\right)\omega + \frac{1}{\rho} \left(a_z \frac{\partial\rho}{\partial r} - a_r \frac{\partial\rho}{\partial z}\right) + \frac{\nu}{Re_0} \left(\nabla^2 \omega - \frac{\omega}{r^2}\right) \quad (2.49)$$

where

$$a_r = -\frac{Du_r}{Dt} \quad (2.50)$$

$$a_z = -1 - \frac{Du_z}{Dt} \quad (2.51)$$

Assuming that $\rho T/M = 1$, and that μ is constant, then

$$\frac{D\omega}{Dt} = \left(\frac{u_r}{r} - \nabla \cdot \mathbf{u}\right)\omega - \frac{1}{\tilde{T}} \left(a_z \frac{\partial\tilde{T}}{\partial r} - a_r \frac{\partial\tilde{T}}{\partial z}\right) + \frac{\tilde{T}}{Re_0} \left(\nabla^2 \omega - \frac{\omega}{r^2}\right) \quad (2.52)$$

where $\tilde{T} = T/M$.

2.9 Shvab-Zel'dovich formulation

The energy and species conservation equations are complicated by the presence of source terms. These "reactive scalars" equations can be simplified using the Shvab-Zel'dovich (S-Z) variables[99]. These variables are constructed from combinations of the primitive scalars such that their transport equations do not contain the source terms. Define the following S-Z variables:

$$\eta_{sz} = Y_o - \phi Y_f \quad (2.53)$$

$$\gamma_{sz} = T - \frac{Q_f}{1 + \phi} Y_p \quad (2.54)$$

$$\delta_{sz} = Y_d \quad (2.55)$$

Then, the S-Z scalar transport equation are obtained from algebraic manipulations of equations (2.37) and (2.38) as follows:

$$\rho \frac{D\eta_{sz}}{Dt} = \frac{1}{Pe_0} \nabla \cdot \left(\rho \frac{\mathcal{D}}{Le_0} \nabla \eta_{sz} \right) \quad (2.56)$$

$$\rho \frac{D\gamma_{sz}}{Dt} = \frac{1}{Pe_0} \nabla \cdot \left(\lambda \nabla T - \rho \frac{\mathcal{D}}{Le_0} \nabla \left(\frac{Q_f}{1+\phi} Y_p \right) \right) \quad (2.57)$$

$$\rho \frac{D\delta_{sz}}{Dt} = \frac{1}{Pe_0} \nabla \cdot \left(\rho \frac{\mathcal{D}}{Le_0} \nabla \delta_{sz} \right) \quad (2.58)$$

Assuming that

$$Le \equiv \frac{\alpha}{\mathcal{D}} = 1, \quad (2.59)$$

the Shvab-Zel'dovich scalar transport equation have the following general form:

$$\rho \frac{D\tilde{s}}{Dt} = \frac{1}{Pe_0} \nabla^2 \tilde{s} \quad (2.60)$$

where \tilde{s} is a S-Z variable. Moreover, if all these variables can be normalized such that the resulting normalized variables have the boundary conditions, then equation (2.60) can be solved once for all the S-Z variables. The S-Z variables imposes some limitations on the problem. This is because a necessary condition for obtaining the reduced equation 2.60 is that the mass diffusion coefficients must be the same for all the species and the Lewis number must be unity.

Now define the following normalized S-Z variable; the mixture fraction

$$s = \frac{\tilde{s} - \tilde{s}_{o,0}}{\tilde{s}_{f,0} - \tilde{s}_{o,0}} \quad (2.61)$$

for $\tilde{s} = \eta_{sz}, \gamma_{sz}$, and δ_{sz} , where the subscripts $o,0$ and $f,0$ refer to the boundary conditions on the fuel side and oxidizer side of reaction, respectively. The normalized form of the S-Z scalar transport equation becomes:

$$\rho \frac{ds}{dt} = \frac{1}{Pe_0} \nabla^2 s \quad (2.62)$$

with the following boundary conditions: $s = 1$ on the fuel side, and 0 on the oxidizer side. The normalized equation has the characteristic that its boundary conditions are the same for $\tilde{s} = \eta_{sz}, \gamma_{sz}$, and δ_{sz} . Once s is obtained, η_{sz}, γ_{sz} , and δ_{sz} are obtained from equation 2.61.

2.10 Infinite rate chemistry

The number of scalars is $N_s + 1$ (N_s species and T). Solving equation (2.62) provides us with $N_s - 1$ linear equations (2.53, 2.54, 2.55). Another equation is the identity

$$Y_f + Y_o + Y_p + Y_d = 1. \quad (2.63)$$

Obviously, an additional equations is required to solve for the scalars. If the chemical reaction rate is assumed to be infinite, then, according to equation 2.11, $Y_f^{u_f} Y_o^{v_o} = 0$, i.e. the fuel and oxidizer do not co-exist, and the reaction occurs across an infinitely thin interface characterized by

$$\eta_{sz,F} = 0 \quad (2.64)$$

The fuel and oxidizer mass fractions are then determined as follows

$$\begin{aligned} Y_f = 0, Y_o = \eta_{sz} & \quad \text{if } \eta_{sz} > 0 \\ Y_f = -\eta_{sz}/\phi, Y_o = 0 & \quad \text{if } \eta_{sz} < 0 \end{aligned} \quad (2.65)$$

The average molecular mass is independent of the sign of η_{sz} and is given by

$$M = \left(\frac{1}{M_p} + \left(\frac{1}{M_o} - \frac{1}{M_p} \right) \eta_{sz} + \left(\frac{1}{M_d} - \frac{1}{M_p} \right) Y_d \right)^{-1} \quad (2.66)$$

where

$$M_p = \frac{M_f M_o (1 + \phi)}{M_o + \phi M_f} \quad (2.67)$$

2.11 Rate of change of material integrals

An area or volume integral of some quantity along the path which moves with the fluid and consists always of the same fluid particles is a material integral. Material integrals are needed to represent the total amount of some quantity associated with a given body of

fluid, and their rates of change with respect to time are also relevant. The rates of change of area and volume material integrals[3] of a quantity θ are respectively

$$\frac{d}{dt} \int_{\delta A} \theta dA = \int_{\delta A} \frac{D\theta}{Dt} dA + \int_{\delta A} \theta \left(\nabla \cdot \mathbf{u} - \frac{u_r}{r} \right) dA \quad (2.68)$$

and

$$\frac{d}{dt} \int_{\delta V} \theta dV = \int_{\delta V} \frac{D\theta}{Dt} dV + \int_{\delta V} \theta (\nabla \cdot \mathbf{u}) dV. \quad (2.69)$$

if $\theta = \omega$, then

$$\frac{d}{dt} \int_{\delta A} \omega dA = \int_{\delta A} \frac{D\omega}{Dt} dA + \int_{\delta A} \omega \left(\nabla \cdot \mathbf{u} - \frac{u_r}{r} \right) dA \quad (2.70)$$

if $\theta = \rho T$, then with use of the continuity equation,

$$\frac{d}{dt} \int_{\delta V} \rho T dV = \int_{\delta V} \rho \frac{DT}{Dt} dV \quad (2.71)$$

if $\theta = \rho$, then

$$\frac{d}{dt} \int_{\delta V} \rho dV = 0 \quad (2.72)$$

2.12 Summary

In this chapter we presented the governing equations in dimensionless form. The underlying assumptions are stated in terms of their relevance to each equation. Development of the radiation source term in the energy equation is presented in chapter 7. In the next chapter, the vortex method is discussed, whereas the numerical implementation is left for a later stage.

Chapter 3

The Vortex Method

In this chapter, we review the vortex method in an axisymmetric domain and summarize its advantages.

3.1 Introduction

In an inviscid flow without external forces, according to Kelvin's circulation theorem[3, 20], the circulation around a contour moving with the flow is invariant in time. Then, by Stokes' theorem, the flux of vorticity across a surface moving with the fluid is constant in time:

$$\Gamma_{C(t)} = \int_{C(t)} \mathbf{u} \cdot d\mathbf{s} = \int_{A(t)} \boldsymbol{\omega} \cdot d\mathbf{A} \quad (3.1)$$

where \mathbf{u} is velocity and $A(t)$ is a surface whose boundary is an oriented contour $C(t)$. In two dimensional inviscid flows vorticity is convected by the velocity field. Thus, viewing inviscid fluid dynamics in terms of elements of vorticity which induce motion on each other is mathematically correct and often very convenient. This observation constitutes the basis of the vortex method; a Lagrangian numerical method in which the computational elements, carrying vorticity, follow the motion in the fluid.

A large class of fluid problems involves flows that are characterized by small regions of vorticity imbedded in an otherwise irrotational fluid. Examples include jets, vortex sheets, wakes, buoyant plumes, and fires. Generation of vorticity may be due to an imposed velocity differential at a boundary (jets, vortex sheets), or due to an external body force acting on a region of non-zero density gradient (buoyant plumes and fires), or at boundaries such as

flow over a cylinder (separation - wake).

Vortex methods have the following advantages:

1. computational elements exist only in regions of nonzero vorticity; these constitute small portions of the flow field, which results in savings in computational time.
2. they are grid-free and thus more suited to problems involving flow around complicated geometries.
3. they are adaptive; since vorticity follows motion, numerical resolution is maintained.
4. no direct discretization of the spatial velocity gradients is needed; this avoids introduction of numerical diffusion and possible destruction of small scale features in high Reynolds number flows.
5. they satisfy far field boundary conditions in unbounded domains; grid based methods are forced to use a computational domain of finite size.

3.2 The vortex method

The approach we choose to compute the fire plume flow field is simulation using the vortex method. Vortex methods have been successfully used to investigate the evolution of vortex sheets [18, 83, 35], high Reynolds number wakes [86, 15], three dimensional problems [54, 67, 33, 2], reacting flows in shear layers [84, 85], and co-axial jets [65].

Vortex methods simulate flows of this type by discretizing the vorticity field into vortex elements and convecting these elements in a Lagrangian reference frame. The required local velocities are computed as the solution to a Poisson equation for the stream function, often in terms of a Green's function or Biot-Savart integration. As the vortex elements move with the flow, the vorticity field is then updated by integrating the vorticity transport equation in time, and so on. An overview of vortex methods can be found in [19, 34, 63]. The vorticity equation, equation 2.52, is discussed in section 2.3.

An additional contribution to the velocity field is the potential component which is imposed by satisfying the boundary conditions. Furthermore, In the case of low Mach number compressible flows, compressibility enters into the picture in terms of accounting for density variation in the above formulation. Spatial density gradients contribute to the

destruction or creation of vorticity, whereas temporal variation adds an expansion component to the velocity field, which is required to satisfy continuity. The decomposition of the velocity field into a rotational, potential and an expansion component, called the Helmholtz decomposition, will be discussed in section 2.5.

3.3 Discretization of the vorticity field

The vorticity field is modeled as a collection of vortex elements initially discretizing an initial vorticity distribution, such as the case of a non-reacting jet, or distributed initially in the region of non-zero density gradients, such as the interface between the fuel and oxidizer in a diffusion flame. The vorticity field can be written as a sum of functions of small support[19],

$$\omega \cong \sum_{i=1}^N \omega_i(\mathbf{r}). \quad (3.2)$$

The support of a function ω_i is the neighborhood where it does not vanish.

A special, useful choice of functions $\omega_i(\mathbf{r})$ is

$$\omega_i = \Gamma_i \phi_\delta(\mathbf{r} - \mathbf{r}_i), \quad (3.3)$$

$$\phi_\delta = \frac{1}{\delta^2} \phi\left(\frac{\mathbf{r}}{\delta}\right), \quad \delta \text{ small}, \quad (3.4)$$

where Γ_i are the coefficients and ϕ is a smooth function such that

$$\int \phi dr dz = 1. \quad (3.5)$$

3.3.1 points

A special case is representation of the vorticity field using a collection of N point vortices. In this case, $\phi_\delta = \delta(\mathbf{r}) = \text{Dirac delta function}$, and

$$\omega(\mathbf{r}, t) = \sum_{i=1}^N \Gamma_i \delta(\mathbf{r} - \mathbf{r}_i(t)), \quad (3.6)$$

This representation is numerically problematic due to the following reasons:

1. reconstruction of the vorticity field is not possible unless a smoothing function is em-

ployed. The size of the smoothing function, not known a priori, is usually determined by trial and error.

2. determination of the velocities at the location of the points is not possible due to the singularities associated with Dirac delta functions. Again, a smoothing function has to be introduced.

3.3.2 blobs

An alternative is to use vortices with finite cores (vortex blobs) with a specified vorticity distribution within the vortex known as the smoothing or core function. For a collection of vortex blobs, the vorticity field is approximated by

$$\omega_\delta(\mathbf{r}, t) = \sum_{i=1}^N \Gamma_i \phi_\delta(\mathbf{r}, \mathbf{r}_i), \quad (3.7)$$

where the core function ϕ_δ is characterized by core of size δ and Γ_i is the circulation of element i located at \mathbf{r}_i . The smoothed or approximated vorticity can be related to the exact vorticity via the convolution

$$\omega_\delta(\mathbf{r}, t) = \int \phi_\delta(\mathbf{r}, \mathbf{r}') \omega(\mathbf{r}', t) d\mathbf{r}' \equiv \phi_\delta * \omega \quad (3.8)$$

3.4 Vorticity transport

In this section, vorticity transport using a collection of Lagrangian computational element is discussed. For a specified form of the core functions, determination of the vorticity field, discretized according to equation 3.7, requires knowledge of the locations, cores, and circulations of the computational elements. The locations are obtained by integrating the velocity field in time. Knowledge of the core size and its role will be clear in chapter 5. The circulations of the computational elements are obtained by integrating the vorticity equation over the elements areas.

Recall that the equation governing the transport of vorticity, presented in section 2.8, is

$$\frac{D\omega}{Dt} - \left(\frac{u_r}{r} - \nabla \cdot \mathbf{u} \right) \omega = \frac{1}{\rho} \left(a_z \frac{\partial \rho}{\partial r} - a_r \frac{\partial \rho}{\partial z} \right) + \frac{\nu}{Re_0} \left(\nabla^2 \omega - \frac{\omega}{r^2} \right) \quad (3.9)$$

where

$$a_r = -\frac{Du_r}{Dt} \quad (3.10)$$

$$a_z = -1 - \frac{Du_z}{Dt} \quad (3.11)$$

The vorticity equation 3.9 updates the circulations of the computational element that are used to calculate the velocity field. The baroclinic and buoyancy terms, expressed as the first term of equation 3.9, contribute to the creation and destruction of vorticity. Further, the diffusion term, expressed as the second term of equation 3.9, corresponds both to molecular diffusion that changes the vorticity distribution and to decay of the vorticity near the axis of symmetry. The diffusion term differs from the corresponding term in two dimensional cartesian coordinates in the sense that the later is responsible only for vorticity redistribution without affecting its conservation. This will be discussed further when the numerical implementation of diffusion is laid out in the following chapter.

The vorticity equation is solved in three steps: convection, diffusion, and generation. These steps are described below and the details of their numerical implementation are discussed in chapters 4 (diffusion) and 5 (convection).

3.4.1 Convection

In this step, we solve the equation

$$\frac{D\omega}{Dt} - \left(\frac{u_r}{r} - \nabla \cdot \mathbf{u} \right) \omega = 0 \quad (3.12)$$

for a material element with vorticity $\omega(\mathbf{r})$. Integrating over the area of the element, then, using equation (2.65), we get

$$\frac{d\Gamma}{dt} = 0, \quad (3.13)$$

where the circulation is given by

$$\Gamma \equiv \int_A \omega dA. \quad (3.14)$$

The computational elements are transported in time according to

$$\frac{d\Gamma_i}{dt} = 0 \quad (3.15)$$

and

$$\frac{d\mathbf{r}_i}{dt} = \mathbf{u}_i \quad (3.16)$$

where \mathbf{r}_i is the location of a computational element of circulation Γ_i and its velocity \mathbf{u}_i is obtained from the Helmholtz decomposition, discussed in section 2.5. In this step the assumptions have been made that computational elements retain their shape and they move according to the velocities of their centers.

3.4.2 Diffusion

In the diffusion step, the computational elements are assumed stationary. Diffusion of vorticity is then governed by the equation

$$\frac{\partial\omega}{\partial t} = \frac{1}{Re_0} \left(\nabla^2\omega - \frac{\omega}{r^2} \right), \quad (3.17)$$

where the kinematic viscosity is assumed to be constant. Recall that the objective is to solve for $(\mathbf{r}_i, \Gamma_i, \delta_i)$ ¹ such that the vorticity representation (equation 3.7) approximates the solution of equation 3.17. This will be the topic of chapter 5.

Of special interest is the Green's function of equation 3.17. The Green's function, which is the solution for an initial point source of vorticity located at (r_0, z_0) of the form

$$\omega_0 \equiv \omega(r, z, t = 0) = \delta(r - r_0)\delta(z - z_0)\delta(t), \quad (3.18)$$

is

$$\omega(r, z, t) = \frac{2\pi r_0}{(4\pi\nu t)^{3/2}} e^{-\frac{r^2+r_0^2+(z-z_0)^2}{4\nu t}} I_1\left(\frac{rr_0}{2\nu t}\right), \quad (3.19)$$

where $\nu = 1/Re$, δ is the Dirac delta function, and I_1 is the modified Bessel function of the

¹Even though the elements locations are fixed in this step, new elements may be introduced.

second kind of order one. The circulation, as a function of time, is given by

$$\Gamma(t) \equiv \int_{-\infty}^{\infty} \int_0^{\infty} \omega dr dz = \left(1 - e^{-\frac{r_0^2}{4\nu t}}\right). \quad (3.20)$$

Unlike the case of diffusion of point vortex in cartesian coordinates where the circulation is conserved, the circulation in axisymmetric diffusion is not conserved. Due to radial symmetry, the circulation decay in time proceeds at a larger rate the closer the point vortex is to the axis of symmetry.

The Green's function given by equation 3.19 provides the basis for diffusion by core expansion and serves as a candidate smoothing function.

3.4.3 Generation

In this step, the vorticity is updated according to

$$\frac{\partial \omega}{\partial t} = \frac{1}{\rho} \left(a_z \frac{\partial \rho}{\partial r} - a_r \frac{\partial \rho}{\partial z} \right) \quad (3.21)$$

where

$$a_r = -\frac{Du_r}{Dt} \quad (3.22)$$

$$a_z = -1 - \frac{Du_z}{Dt} \quad (3.23)$$

According to the above equation, vorticity is generated (or destroyed) if the flow accelerates (or decelerates) in a direction of a non-zero density (temperature) gradient. The spatial gradients of the density are obtained using the scalar-transport method described in chapter 4. The acceleration terms are usually determined by first order backward Euler differentiation of the velocity.

For convenience, let's express equation 3.21 as

$$\frac{\partial \omega}{\partial t} = \Theta(\mathbf{r}) \quad (3.24)$$

Again, the objective is determine the elements circulations such that the vorticity representation (equation 3.7) approximates the solution of equation 3.24. Using the vorticity

representation 3.7 we get

$$\sum_{i=1}^N \phi_{\delta}(\mathbf{r}, \mathbf{r}_i) \frac{\partial \Gamma_i(t)}{\partial t} = \Theta(\mathbf{r}) \quad (3.25)$$

Approximating the time derivative using a first order forward Euler discretization, we get

$$\sum_{i=1}^N \Delta \Gamma_i \phi_{\delta}(\mathbf{r}, \mathbf{r}_i) = \Delta t \Theta(\mathbf{r}) \quad (3.26)$$

where $\Delta \Gamma_i \equiv \Gamma_i(t + \Delta t) - \Gamma_i(t)$. One way to solve equation 3.26 is to satisfy it at a specified set of points, more specifically at the centers of the elements. This leads to the linear system

$$\sum_{i=1}^N \Delta \Gamma_i \phi_{\delta}(\mathbf{r}_j, \mathbf{r}_i) = \Delta t \Theta(\mathbf{r}_j) \text{ for } j = 1, \dots, N. \quad (3.27)$$

The coefficient matrix $\phi_{\delta}(\mathbf{r}_j, \mathbf{r}_i)$ is, in general, ill conditioned (interpolation matrix), such that the solution with a fairly smooth source field ($\Theta(\mathbf{r})$) leads to large variations in circulations of nearby elements. An alternative to solving system 3.27 directly, the iterative scheme proposed by Marshall and Grant[66] is used to obtain a smooth fit to the source field. In this scheme, it is temporarily assumed that surrounding each element j , there exists a set of elements $Q(j)$ for which the elements amplitudes are nearly the same as that at element j . The set $Q(j)$ contains the elements that are within a characteristic distance, δ^* , selected to be the core size δ . Letting $P(j)$ denotes the complement of $Q(j)$, i.e. the set of elements that are located at distance more that δ^* from element j , the linear system 3.27 is approximated by

$$\Delta \Gamma_j^{(m+1)} \sum_{i \in Q(j)} \phi_{\delta}(\mathbf{r}_j, \mathbf{r}_i) + \sum_{i \in P(j)} \Delta \Gamma_i^{(m)} \phi_{\delta}(\mathbf{r}_j, \mathbf{r}_i) = \Delta t \Theta(\mathbf{r}_j) \text{ for } j = 1, \dots, N. \quad (3.28)$$

where m is the iteration index. Thus, given the amplitude values at iteration m , the amplitudes at level $m + 1$ may be obtained according to

$$\Delta \Gamma_j^{(m+1)} = \frac{\Delta t \Theta(\mathbf{r}_j) - \sum_{i \in P(j)} \Delta \Gamma_i^{(m)} \phi_{\delta}(\mathbf{r}_j, \mathbf{r}_i)}{\sum_{i \in Q(j)} \phi_{\delta}(\mathbf{r}_j, \mathbf{r}_i)} \text{ for } j = 1, \dots, N. \quad (3.29)$$

The set $Q(j)$ typically includes 8-10 elements. Convergence is usually reached within about 5-8 iterations where the maximum relative change in element amplitudes is less than 10^{-6} . This method is fast and accurate for large values of N .

3.5 Velocity Field: Helmholtz Decomposition

The velocity field is needed to update the vortex element position, \mathbf{r} , governed by equation 3.16. The velocity field is expressed in terms of its components using the Helmholtz decomposition[3]:

$$\mathbf{u} = \mathbf{u}_P + \mathbf{u}_\omega + \mathbf{u}_e \quad (3.30)$$

where \mathbf{u}_P , \mathbf{u}_ω , and \mathbf{u}_e are the potential, vortical, and volumetric expansion components of the velocity, respectively.

3.5.1 Potential velocity component

The potential velocity is obtained from the velocity potential Φ_P according to

$$\mathbf{u}_P = \nabla\Phi_P, \quad (3.31)$$

where the velocity potential Φ_P satisfies the Laplace equation

$$\nabla^2\Phi_P = 0 \quad (3.32)$$

subject to the boundary condition

$$\frac{\partial\Phi_P}{\partial n} = -(\mathbf{u}_\omega + \mathbf{u}_e) \cdot \mathbf{n} \quad (3.33)$$

at the solid boundaries.

3.5.2 Rotational velocity component

The velocity induced by the vorticity field is obtained by taking the curl of the stream function Ψ_ω ,

$$\mathbf{u}_\omega = \nabla \times \Psi_\omega, \quad (3.34)$$

where the stream function satisfies the Poisson equation

$$\nabla^2\Psi_\omega = -\omega. \quad (3.35)$$

3.5.3 Expansion velocity component

The velocity field induced by volumetric expansion is obtained from its potential Φ_e , according to

$$\mathbf{u}_e = \nabla \Phi_e, \quad (3.36)$$

where the velocity potential satisfies the Poisson equation with the local time variation of the density as the source

$$\nabla^2 \Phi_e = -\frac{1}{\rho} \frac{D\rho}{Dt}. \quad (3.37)$$

Denote \mathbf{G}_ω and G_e as the Green's functions of the Poisson equations 3.37 and 3.35, the expansion and vortical velocity component are then given by the convolutions

$$\mathbf{u}_\omega = \mathbf{K}_\omega * \omega \equiv \int \mathbf{K}_\omega(\mathbf{r}; \mathbf{r}') \omega(\mathbf{r}', t) d\mathbf{r} \quad (3.38)$$

and

$$\mathbf{u}_e = \mathbf{K}_e * \varrho \equiv \int \mathbf{K}_e(\mathbf{r}; \mathbf{r}') \varrho(\mathbf{r}', t) d\mathbf{r} \quad (3.39)$$

where $\varrho = -\frac{1}{\rho} \frac{D\rho}{Dt}$,

$$\mathbf{K}_\omega = \nabla \times \mathbf{G}_\omega, \quad (3.40)$$

and

$$\mathbf{K}_e = \nabla G_e. \quad (3.41)$$

Using the vortex blob representation, equation 3.7, then the vortical and expansion velocity components are approximated by

$$\mathbf{u}_\omega^n = \sum_{i=1}^N \Gamma_i \mathbf{K}_{\sigma, \omega}(\mathbf{r}; \mathbf{r}_i) \quad (3.42)$$

and

$$\mathbf{u}_e^n = \sum_{i=1}^N \Gamma_i^\varrho \mathbf{K}_{\sigma, \varrho}(\mathbf{r}; \mathbf{r}_i), \quad (3.43)$$

where the superscript n refers to numerical solution, and

$$\mathbf{K}_{\sigma, \omega} = \mathbf{K}_\omega * \phi_\delta \quad (3.44)$$

and

$$\mathbf{K}_{\sigma,\varrho} = \mathbf{K}_{\varrho} * \phi_{\delta,\varrho}. \quad (3.45)$$

Selection of the core functions is performed and discussed in chapter 4. Expressions for the kernels $\mathbf{K}_{\sigma,\omega}$ and $\mathbf{K}_{\sigma,\varrho}$ and subsequently numerical tools to evaluate the velocity will be developed in chapter 5.

3.6 Convergence and accuracy

Two questions arise. The first one relates to the error involved in splitting the vorticity equation into three steps and its convergence characteristics. The second question relates to the accuracy of the vortex method in terms of blob representation of the vorticity field and numerical evaluation of the convolution integrals relevant to the velocity field.

3.6.1 Convergence

We shall state results obtained by Beale and Majda[4] for the rates of convergence for viscous splitting of the Navier stokes equations governing an unbounded incompressible flow in two dimensions. Define the solution operators of Euler's equations ($E(t)$) and the heat equation ($H(t)$) such that

$$E(t)v_0 = v(t), \quad \text{where} \quad (3.46)$$

$$v_t + v \cdot \nabla v + \nabla p = 0 \quad (3.47)$$

$$\nabla \cdot v = 0, \quad v(0) = v_0 \quad (3.48)$$

and

$$H(t)w_0 = w(t), \quad \text{where} \quad (3.49)$$

$$w_t = \nu \nabla^2 w, \quad w(0) = w_0. \quad (3.50)$$

The viscous splitting algorithm, which is the underlying basis for the random vortex method, is given by the approximation

$$\tilde{u}_n = (H(\Delta t)E(\Delta t))^n u_0, \quad (3.51)$$

where u is the velocity and n denoted the numerical solution at time $n\Delta t$. Another algorithm (Strang) with an improved rate of convergence is

$$u_n = (H(\Delta t/2)E(\Delta t)H(\Delta t/2))^n u_0. \quad (3.52)$$

For an arbitrarily large time T and a fixed nonnegative integer s , convergence rates for viscous splitting using the two algorithms 3.51 and 3.52 are²

$$\max_{0 \leq n\Delta t \leq T} |u(n\Delta t) - \tilde{u}_n|_s \leq C_1 \nu \Delta t, \quad (3.53)$$

$$\max_{0 \leq n\Delta t \leq T} |u(n\Delta t) - u_n|_s \leq C_2 \nu \Delta t^2, \quad (3.54)$$

where the constants C_i , $i = 1, 2$ are independent of ν and depend only on $|u_0|_{s+\sigma}$, T , and $|\nabla \times u_0|_{L^1}$. Thus simulating the effects of viscosity through splitting algorithms can significantly improve the quality of the approximate solution even for small viscosity.

3.6.2 Accuracy

In conventional methods, errors in finite difference integrations produce numerical viscosity (and dispersion). The error in vortex methods, however, has a different structure, because there is no differencing of the advection terms in space. A summary of the results available in the literature[19, 40, 6, 5] are presented in this section. The results were obtained for a two dimensional incompressible unbounded flows. The following two observations can be made:

- The error in the vortex methods is primarily due to the error in the evaluation of the convolution integrals 3.42 , and
- accuracy depends on the smoothness of the flow, the initial approximation of vorticity, and on the choice of the the smoothing function ϕ and its properties.

Define the error in the particle trajectory to be

$$e_i(t) = \mathbf{r}_i(\mathbf{r}_i^0, t) - \tilde{\mathbf{r}}_i(\mathbf{r}_i^0, t) \quad (3.55)$$

² $|\cdot|_s$ is the L^2 -Sobolev norm of order s of a given function. $u \in H^s$ when $|u|_s < \infty$.

where \mathbf{r}_i and $\tilde{\mathbf{r}}_i$ are the exact and numerical positions of particle i , and the superscript 0 denotes initial conditions. Then the error in the velocity³ is given by:

$$\dot{e} = \frac{de}{dt} = \dot{\mathbf{r}} - \mathbf{u}(\tilde{\mathbf{r}}) = e_m + e_d + e_s \quad (3.56)$$

with

$$e_m = \int K(\mathbf{r}, \mathbf{r}') \omega(\mathbf{r}') d\mathbf{r}' - \int K_\sigma(\mathbf{r}, \mathbf{r}') \omega(\mathbf{r}') d\mathbf{r}' \quad (3.57)$$

$$e_d = \int K_\sigma(\mathbf{r}, \mathbf{r}') \omega(\mathbf{r}') d\mathbf{r}' - \sum_j \Gamma_j K_\sigma(\mathbf{r}, \mathbf{r}_j) \quad (3.58)$$

$$e_s = \sum_j \Gamma_j K_\sigma(\mathbf{r}, \mathbf{r}_j) - \sum_j \Gamma_j K_\sigma(\tilde{\mathbf{r}}_i, \tilde{\mathbf{r}}_j) \quad (3.59)$$

where e_m is the smoothing error due to replacing K with K_σ , e_d is the discretization error which results from the replacement of the integral by a sum, and e_s is the “stability error” which arises because the sum is evaluated at the computed rather than the exact locations of the blobs. The stability error, e_s , can be bounded in such a way that the over-all error is bounded by a constant times ($\|e_d\| + \|e_m\|$); thus

$$\|\text{error}\|_{L^1} \leq \text{constant} \cdot \left[\sigma^p + \left(\frac{h}{\sigma} \right)^L \sigma \right] \quad (3.60)$$

where the first term on the right hand side of the inequality is the smoothness error. The order of the core function is p ; the number of vanishing moments, i.e.

$$\int \mathbf{r}^m \phi(\mathbf{r}) d\mathbf{r} = 0, \text{ for } m = 1, \dots, p-1. \quad (3.61)$$

$$\text{or } \hat{\phi}(k) = 1 - O(k^p) \quad (3.62)$$

The moments conditions 3.61 are the guidelines for constructing core function of arbitrary order p . The second term is the discretization error, where L is the smoothness of ϕ ; the number of derivatives, and h is a measure of the elements spacing. If L is large enough, such as the case of a nearly uniform grid⁴, one can choose $h/\sigma < 1$ (thus making the blobs overlap) so that the error in the trajectories of the blobs is close to $O(h^p)$. However, the error in the blob methods does grow in time. One factor in this growth is the growing irregularity

³we omit the subscript i for brevity

⁴For sufficiently smooth integrands, the trapezoidal rule is of high order accuracy.

of the blob distribution and the resulting growth in the derivatives that enter the error in the trapezoidal rule. In general, the local strain field may distort the particles locations resulting in the violation of the overlap condition in some regions. Perlman[76] proved that if σ was chosen to be close to h accuracy is lost in relatively short time, and suggested that σ should increase with time. Since the discretization error decreases as σ increases and the smoothing error increases with σ , a large value of σ can be chosen to preserve the accuracy over a fixed time interval. An alternative remedy is periodic remeshing onto a uniform grid or a grid correction procedure as in the PSE [21]. Remeshing is performed by conserving the circulation as well as the linear and angular momentum of the vorticity field.

3.7 Summary

In this chapter, we argued that the vortex-element method is a convenient approach towards numerically simulating the axisymmetric fire plume problem. Its advantages over other methods based on velocity-pressure considerations have been pointed out. The basic components of the vortex method, its convergence and accuracy have been presented. The details of the numerical implementation of the vortex-element method will be discussed in chapters 5 and 6, where we present the solution of the vorticity diffusion equation as well as the various components of the velocity field. Scalar transport is discussed next.

Chapter 4

Scalar Transport

The equation governing scalar transport is

$$\rho \frac{Ds}{Dt} = \frac{1}{Pe_0} \nabla^2 s + \Theta \quad (4.1)$$

where s is a scalar that can be a Shvab-Zel'dovich variable or any of the primitive scalars such as species mass fraction or temperature, and Θ is a source term either due to finite rate chemical reaction or radiative transport or both.

4.1 Discretization of the scalar field

Analogous to the discrete representation of the vorticity field, equation 3.7, the scalar field is approximated by

$$s_\delta(\mathbf{r}, t) = \sum_{i=1}^N \frac{E_i}{r_i} \phi_\delta(\mathbf{r}, \mathbf{r}_i) \quad (4.2)$$

where the core function ϕ_δ , characterized by core of size δ , does not necessarily have the same form as that utilized in vorticity transport, and E_i is the energy of element i located at \mathbf{r}_i . Recalling that the core function has the general form

$$\phi_\delta = \frac{1}{\delta^2} \phi\left(\frac{\mathbf{r}}{\delta}\right), \quad (4.3)$$

the smooth function ϕ satisfies in this case the condition

$$\int \phi r dr dz = 1 \quad (4.4)$$

4.2 Scalar transport

Scalar transport involves determination of the locations, cores, and energies of the computational elements such that the discrete scalar field representation given by equation 4.2 provides an approximate solution to equation 4.1. The equation governing scalar transport is solved in three substeps: convection, diffusion, and generation.

For convenience, we write the scalar transport equation as

$$\frac{Ds}{Dt} + s\nabla \cdot \mathbf{u} = \frac{1}{\rho Pe_0} \nabla^2 s + \frac{1}{\rho} \Theta + s\nabla \cdot \mathbf{u}. \quad (4.5)$$

4.2.1 convection

In this step, we solve the equation

$$\frac{Ds}{Dt} + s\nabla \cdot \mathbf{u} = 0 \quad (4.6)$$

for a material element. Integrating over the volume of the element, and using equation 2.66, we get

$$\frac{dE_i}{dt} = 0 \quad (4.7)$$

where the energy is given by

$$E \equiv \int_A s r dr dz, \quad (4.8)$$

where A is the cross sectional area of the element.

4.2.2 diffusion

In this step, the diffusion equation

$$\frac{\partial s}{\partial t} = \frac{1}{\rho Pe_0} \nabla^2 s \quad (4.9)$$

is solved. Numerical implementation is presented in chapter 5.

We present the Green's function of the diffusion for the case of uniform density,

$$\frac{\partial s}{\partial t} = \frac{1}{Pe_0} \nabla^2 s. \quad (4.10)$$

The Green's function, which is the solution for an initial scalar source located at (r_0, z_0) of the form

$$s_0 \equiv s(r, z, t = 0) = \delta(r - r_0)\delta(z - z_0)\delta(t), \quad (4.11)$$

is given by

$$s(r, z, t) = \frac{2\pi}{(4\pi\alpha t)^{3/2}} e^{-\frac{r^2+r_0^2+(z-z_0)^2}{4\alpha t}} I_0\left(\frac{rr_0}{2\alpha t}\right) \quad (4.12)$$

where $\alpha = 1/Pe_0$ and I_0 is the modified Bessel function of the first kind of order zero.

4.2.3 generation

In this section, the scalar is updated according to

$$\frac{\partial s}{\partial t} = \frac{1}{\rho} \left(\Theta - s \frac{D\rho}{Dt} \right). \quad (4.13)$$

This equation is solved in the same way the vorticity generation equation is solved in section 3.4.3.

4.3 The transport element method

An alternative to transporting the scalar is to transport the scalar gradient. The transport element method[34, 85, 56, 35] solves the scalar transport equation, with initial conditions $s(\mathbf{r}(t=0), t=0) = s_0(\mathbf{r}_0)$ by transporting the scalar gradient \mathbf{g}_s , $\mathbf{g}_s \equiv \nabla s$. Similar to the vorticity, scalar gradients exist over a small subset of the domain, and evolve around regions of strong shear, or mixing. The idea behind the method is to transport the gradients field, \mathbf{g}_s , from which the scalar field can be recovered by solving the Poisson equation¹:

$$\nabla^2 s = \nabla \cdot \mathbf{g}_s \quad (4.14)$$

Once the gradient field is obtained, the scalar field is recovered by convoluting $\nabla \cdot \mathbf{g}_s$ with the Green's function of Poisson's equation according to

$$s(\mathbf{r}, t) = \int \nabla \cdot \mathbf{g}_s(\mathbf{r}', t) G(\mathbf{r}, \mathbf{r}') d\mathbf{r}' \quad (4.15)$$

¹The scalar field need not be recovered unless it is needed, such as the case with the finite rate chemical reaction and radiative transport

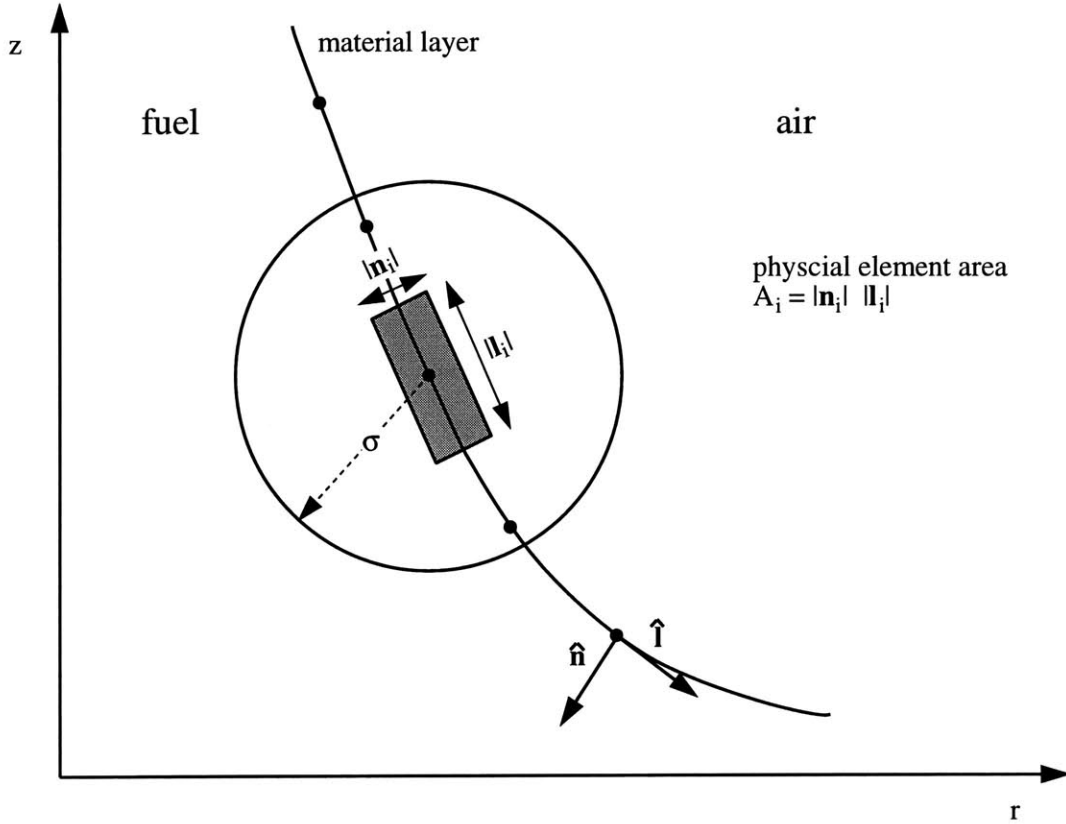


Figure 4-1: Discretization of material layer into elements.

integrating by parts, and noting that the product of the green's function and the gradient vanishes at infinity and at the axis of symmetry, then

$$s(\mathbf{r}, t) = - \int \mathbf{g}_s(\mathbf{r}', t) \cdot \nabla G(\mathbf{r}, \mathbf{r}') d\mathbf{r}' \quad (4.16)$$

The equation governing the scalar gradient is obtained by taking the gradient of equation 4.1

$$\frac{d\mathbf{g}_s}{dt} = -\mathbf{g}_s \cdot \nabla \mathbf{u} - \mathbf{g}_s \times \boldsymbol{\omega} + \frac{1}{Pe_0} \nabla^2 \mathbf{g}_s \quad (4.17)$$

Attempts to integrate equation 4.17 proved problematic. A successful alternative is the conservative approach, in which the magnitude and direction of \mathbf{g}_s are transported separately.

If the material lines are chosen to coincide with isoscalar lines, then for a material elements i , the equation

$$\mathbf{g}_{s,i} = |\mathbf{g}_{s,i}| \hat{\mathbf{n}}, \quad (4.18)$$

follows from the definition of the gradient, where $\hat{\mathbf{n}}$ is the unit normal vector in the direction

normal to the material line oriented along unit vector $\hat{\mathbf{l}}$, $\hat{\mathbf{l}} \cdot \hat{\mathbf{n}} = 0$, see Figure 4-1. For flows with variable density, the equation describing the magnitude of the gradient across a material element and the product of the density (ρ_i) and the length of the element ($|\mathbf{l}_i|$) are similar, so that

$$\frac{|\mathbf{g}_{s,i}|}{\rho_i |\mathbf{l}_i|} = \frac{|\mathbf{g}_{s,i}^0|}{\rho_i^0 |\mathbf{l}_i^0|} \quad (4.19)$$

where the superscript 0 denotes initial conditions. The initial gradient, $|\mathbf{g}_{s,i}^0|$, may be related to the initial scalar differential across the element by $|\mathbf{g}_{s,i}^0| = \Delta s_i^0 / |\mathbf{n}_i^0|$, where $|\mathbf{n}_i^0|$ is the initial thickness of element i . The evolution of the length and orientation of a material element is numerically implemented by transporting its endpoints. Thus, for an element i , the scalar gradient is given by

$$\mathbf{g}_{s,i} \equiv \mathbf{g}_s(\mathbf{r}_i, t) = \frac{\Delta s_i^0}{\rho_i^0 A_i^0} \rho_i |\mathbf{l}_i| \hat{\mathbf{n}}_i \quad (4.20)$$

Numerical solution of Poisson's equation is discussed in chapter 6.

4.4 Discussion

We note the advantages and disadvantages of the transport element method.

4.4.1 Advantages

1. like the vorticity, gradients of the scalar exist in small regions of the domain. Computational elements are concentrated in these regions.
2. For computations where the scalar field is not needed, transporting the gradient is computationally cheap.
3. Recovering the scalar field can be recovered by solving the Poisson equation 4.14.

4.4.2 Disadvantages

1. The transport element method requires connectivity of each layer at all times. This puts restrictions on diffusion modeling. One way to model diffusion of scalar gradients is core spreading. The core spreading method is discussed in the next chapter.

-
2. The number of elements can become large inside vortical structures due to the spinning of the material layer. This requires refinement of the time step to provide sufficient resolution for regions of strong gradients.

Chapter 5

Diffusion

5.1 Background

Fundamental to the vortex element method is the representation of the vorticity field. As discussed in section 3.3, this is mainly done in two ways: point vortices and vortex blobs. Each of the two methods has its advantages and disadvantages. In general, representing the vorticity field by a system of point vortices is numerically problematic, due to the singularity at the location of the vortices. As an alternative, investigators have used vortices with finite cores (vortex blobs) in their simulations with a specified vorticity distribution¹ within the vortex. The core size, σ , can be thought of as measure of the region of influence associated with a certain element. The objective of this core function is to provide smooth solutions near or at the element locations. Selection of core function, its advantages, and estimates of the smoothing and discretization errors are discussed in section 5.3.

For a deep understanding of the roles of vortex points and vortex blobs, it is essential to understand how the properties of each of these two representations are manifested in numerical solution of diffusion and convection separately.

5.2 The redistribution method

Solving the diffusion equation using a collection of point vortices is possible. The redistribution method[86, 87] accounts for diffusion by distributing fractions of the element circulation to neighboring elements. This is done by solving a linear system derived from conserving as

¹known as core function or basis function

much moments of vorticity necessary for the order of accuracy required. A positive solution of the system imposes the requirement that the neighborhood of the element ($R_d \sim \sqrt{16\nu\sigma t}$) should be represented by elements with an average spacing of ($h \sim \sqrt{8\nu\Delta t}$), which necessitates the injection of new elements to fill the gaps². The error involved in the distribution method is of the order of the time step Δt . The redistribution method is accurate and efficient for problems where the pointwise vorticity distribution is not needed in the course of a numerical simulation. If the pointwise vorticity is needed, however, the redistribution method has to utilize a smoothing function to reconstruct the vorticity field, and the size of the core radius is not known a priori and has to be determined by trial and error. Thus, for problems where pointwise values of vorticity are needed, such as the case when there is vorticity generation, the redistribution method cannot be used in its original format and has to be extended to allow for a systematic way of recovering vorticity accurately.

Evaluation of the elements velocities in the convection step is faced with arising singularities when using point vortices. In this case desingularization is required and a core must be introduced in the convection step. Evaluating the stream function requires summation of the contributions over all elements, with an average spacing h . The contribution of each element is obtained by convoluting the core function with the Green's function of the Poisson equation governing the stream function. The discretization error involved in this process is of the order of $O(h^L/\sigma^L)$, where L is the smoothness of the core function.

In this work, we propose to extend the redistribution method for a vortex blob representation of the vorticity field. The method has the advantages that in addition to its capability to recover the vorticity field, it provides the flexibility of controlling the core size. On the other hand, using vortex blobs to solve the diffusion equation introduces a smoothing error associated with order of the core function used, in addition to the discretization error associated with convection.

5.3 Core function

The use of a core function yields a smooth vorticity field and results in a bounded induced velocity field. The core function has to satisfy the following conditions: conservation (equation 5.3), it should allow representation of the field to a certain degree of accuracy (moments

²This turns out to have an advantage in solving the convection part.

conditions 2.61) , and it should be smooth³ enough, $L \gg 1$.

It is convenient to select a core function that satisfies identically the viscous part of the vorticity transport equation for a viscous fluid. For a point vortex, the solution of the vorticity diffusion equation is given by equation 3.19. In this case, the spread of vorticity due to diffusion is $\sqrt{4\nu t}$. Thus, it seems reasonable to construct a core function with a core size σ that spreads in time accordingly. Indeed, it can be shown that a core function of the form

$$\phi_\sigma(\mathbf{r}; \mathbf{r}_o, t) = C \frac{2\pi r_0}{\pi^{3/2} \sigma^3} e^{-\frac{(r-r_0)^2 + (z-z_0)^2}{\sigma^2}} e^{-\frac{2rr_0}{\sigma^2}} I_1\left(\frac{2rr_0}{\sigma^2}\right) \quad (5.1)$$

with a core that expands in time according to

$$\frac{d(\sigma^2)}{dt} = 4\nu \quad \text{or} \quad \sigma^2 = \sigma_0^2 + 4\nu t \quad (5.2)$$

satisfies the vorticity diffusion equation exactly, where $\sigma_0 = \sigma(t = 0)$. The constant C , introduced to satisfy the conservation condition

$$\int_{-\infty}^{\infty} \int_0^{\infty} \phi_\sigma(\mathbf{r}; \mathbf{r}_o, t) dr dz = 1, \quad (5.3)$$

is given by

$$C = \frac{1}{1 - e^{-r_0^2/\sigma^2}}. \quad (5.4)$$

The vorticity distribution given by equation 3.19 assumes that the element has undergone diffusion over a period of $\sigma^2/4\nu$ and consequently its circulation has decayed by a factor of $(1 - e^{-r_0^2/\sigma^2})$. Thus, initially the core function should be scaled by the factor C . Using the moment conditions, given by equation 3.61, it can be shown that the core function 5.1 is second order accurate, i.e. $p = 1$.

Equation 5.2 is the basis of the core spreading method for diffusion.

5.4 Core spreading

Using the core function given by equation 5.1 produces a smoothing error of the order σ^2 . Obviously this puts a constraint on the allowable size of the core. On the other hand, in assigning a core size for the vorticity distribution in a certain element, it is assumed that the

³to be L -times differentiable.

core retains the same shape for all times and that it moves with the center of the element. If the overlap is such that $\sigma < h$, then this assumption applies to the material contained within the element. In physical terms, expanding the core according to equation 5.2 introduces error because this element may suffer considerable strain in realistic flows. Even though the initial vorticity may be set up such that $\sigma_0 > h_0$, the strain will push elements apart at longer times especially for relatively high Reynolds numbers, despite the fact that the core size increases at the rate given by equation 5.2. Notice that the core expands at a rate of $4\Delta t/Re$ per convection time step Δt . In this respect, Greengard[39] showed that even though vorticity is correctly diffused, it is incorrectly convected. Greengard proved that the core spreading algorithm converges to a system of equations different from the Navier-Stokes equations. Thus core spreading suffers from an increasing smoothing error at a rate of the order of νt from one side, and a possibly increasing discretization error of the order of $\sigma (h/\sigma)^L$. The remedy is to keep σ bounded and to maintain overlap at all times, with a preferable element distribution closest to that of a uniform grid.

5.5 The smoothed redistribution method

As seen from the previous discussion, the core size σ and the overlap σ/h are the critical convergence parameter for a vortex method. Thus, it is necessary that the cores do not grow too large and that overlap be maintained at all times. Realizing that core expansion spreads the vorticity in accordance to the diffusion equation, limiting the size of the core does not serve this purpose anymore and hence resorting to a different way of spreading the vorticity is a must. The method we use to solve the diffusion equation is the Smoothed Redistribution Method. Implementing the diffusion step for a certain element involves transferring fractions of its circulation to its neighboring elements. The equations governing the redistribution of circulation are obtained from conserving the zeroth, first, and second moments of vorticity. A schematic of the redistribution procedure is shown in the Figure 5-1, where the element to be diffused, located at (r_0, z_0) , has circulation Γ_0 and core size σ_0 . It is convenient to separate the process into two stages. In the first stage, the expansion stage, the element undergoes core expansion and circulation decay. The core of the element expands such that $\sigma_0(\Delta t)^2 = \sigma_0^2 + 4\nu\Delta t$, where Δt is the time step, and its circulation decays according to $\Gamma_0(\Delta t) = \Gamma_0 \left(1 - e^{-r_0^2/(\sigma_0^2 + 4\nu\Delta t)}\right) / \left(1 - e^{-r_0^2/\sigma_0^2}\right)$. In the redistribution stage, the objective

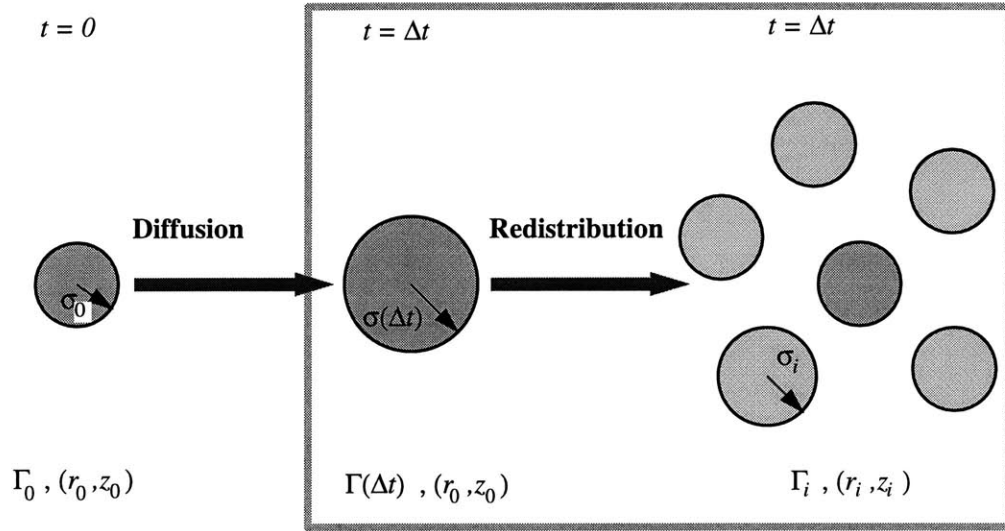


Figure 5-1: Schematic

is to replace element $(\Gamma_0(\Delta t), r_0, z_0, \sigma(\Delta t))$ with neighboring elements $(\Gamma_i, r_i, z_i, \sigma_i)$.

5.5.1 diffusion stage

The objective is to diffuse an element using core expansion over a time step of Δt with initial condition $(\Gamma_0, r_0, z_0, \sigma_0)$ at $t=0$ and vorticity distribution

$$\omega_0(\mathbf{r}; \mathbf{r}_0) = \frac{\Gamma_0}{1 - e^{-r_0^2/\sigma_0^2}} \frac{2r_0}{\pi^{1/2}\sigma_0^3} e^{-\frac{(r-r_0)^2+(z-z_0)^2}{\sigma_0^2}} e^{-\frac{2rr_0}{\sigma_0^2}} I_1\left(\frac{2rr_0}{\sigma_0^2}\right). \quad (5.5)$$

At time $t = \Delta t$, the core expands yielding a vorticity distribution of the form

$$\omega_{\Delta t}(\mathbf{r}; \mathbf{r}_0) = \frac{\Gamma_0}{1 - e^{-r_0^2/\sigma^2}} \frac{2r_0}{\pi^{1/2}\sigma^3} e^{-\frac{(r-r_0)^2+(z-z_0)^2}{\sigma^2}} e^{-\frac{2rr_0}{\sigma^2}} I_1\left(\frac{2rr_0}{\sigma^2}\right), \quad (5.6)$$

where

$$\sigma^2 \equiv \sigma_{\Delta t}^2 = \sigma_0^2 + 4\nu\Delta t. \quad (5.7)$$

Thus, the circulation at $t = \Delta t$ is

$$\Gamma_{\Delta t} \equiv \int_{-\infty}^{\infty} \int_0^{\infty} \omega_{\Delta t}(\mathbf{r}; \mathbf{r}_0) dr dz = \Gamma_0 \frac{1 - e^{-r_0^2/\sigma^2}}{1 - e^{-r_0^2/\sigma_0^2}}. \quad (5.8)$$

The vorticity distribution may be written in the alternative form

$$\omega_{\Delta t}(\mathbf{r}; \mathbf{r}_o) = \frac{\Gamma_{\Delta t}}{1 - e^{-r_o^2/\sigma^2}} \frac{2r_o}{\pi^{1/2}\sigma^3} e^{-\frac{(r-r_o)^2+(z-z_o)^2}{\sigma^2}} e^{-\frac{2rr_o}{\sigma^2}} I_1\left(\frac{2rr_o}{\sigma^2}\right). \quad (5.9)$$

5.5.2 redistribution stage

In the redistribution stage, the diffused element $(\Gamma_{\Delta t}, r_o, z_o, \sigma_{\Delta t})$ is to be replaced by a set of N neighboring elements characterized by $(\Gamma_i, r_i, z_i, \sigma_i)$ for $i = 1, N$. The vorticity distribution for element i is

$$\omega_i(\mathbf{r}; \mathbf{r}_i) = \frac{\Gamma_i}{1 - e^{-r_i^2/\sigma_i^2}} \frac{2r_i}{\pi^{1/2}\sigma_i^3} e^{-\frac{(r-r_i)^2+(z-z_i)^2}{\sigma_i^2}} e^{-\frac{2rr_i}{\sigma_i^2}} I_1\left(\frac{2rr_i}{\sigma_i^2}\right). \quad (5.10)$$

A condition on this process is that the neighbors core sizes σ_i are specified a priori, and thus are input to the redistribution process. Further, the neighbors locations are mainly inherited from the previous time step. Conditions for creating new neighbors will be explained in the following section. Thus, the problem reduces to determining the fraction of $\Gamma_{\Delta t}$ that goes to element i , i.e. Γ_i . The redistribution process is constrained by conserved quantities, namely the moments of vorticity. We choose to conserve the zeroth, first and second moments of vorticity:

$$\sum_{i=1}^N \int_{-\infty}^{\infty} \int_{-\infty}^{\infty} \mathbf{r}^n \omega_i(\mathbf{r}; \mathbf{r}_i) dr dz = \int_{-\infty}^{\infty} \int_{-\infty}^{\infty} \mathbf{r}^n \omega_{\Delta t}(\mathbf{r}; \mathbf{r}_o) dr dz, \quad (5.11)$$

for $n = 0, 1, 2$. Conservation of higher moments is not expected to lead to improvement in accuracy since the error is limited by the smoothness error of the second order core utilized.

5.6 The redistribution equations

Carrying out the various integrals in equation 5.11, and defining fraction f_i as

$$f_i = \frac{\Gamma_i}{\Gamma_{\Delta t}}, \quad (5.12)$$

the following equations may be obtained:

Zeroth moment (conservation of circulation)

$$\sum_{i=1}^N f_i = 1. \quad (5.13)$$

First r moment

$$\sum_{i=1}^N f_i \frac{r_i^2 e^{-\frac{r_i^2}{2\sigma_i^2}} \left(I_0 \left(\frac{r_i^2}{2\sigma_i^2} \right) + I_1 \left(\frac{r_i^2}{2\sigma_i^2} \right) \right)}{\sigma_i \left(1 - e^{-r_i^2/\sigma_i^2} \right)} = \frac{r_0^2 e^{-\frac{r_0^2}{2\sigma^2}} \left(I_0 \left(\frac{r_0^2}{2\sigma^2} \right) + I_1 \left(\frac{r_0^2}{2\sigma^2} \right) \right)}{\sigma \left(1 - e^{-r_0^2/\sigma^2} \right)} \quad (5.14)$$

where I_1 and I_0 are modified Bessel functions of first kind of orders 0 and 1 respectively.

First z moment (mean axial position)

$$\sum_{i=1}^N f_i z_i = z_0. \quad (5.15)$$

Second r moment (radial impulse)

$$\sum_{i=1}^N f_i \frac{r_i^2}{\left(1 - e^{-r_i^2/\sigma_i^2} \right)} = \frac{r_0^2}{\left(1 - e^{-r_0^2/\sigma^2} \right)}. \quad (5.16)$$

Second z moment (axial impulse)

$$\sum_{i=1}^N f_i \left(z_i^2 + \frac{1}{2} \sigma_i^2 \right) = \left(z_0 + \frac{1}{2} \sigma^2 \right). \quad (5.17)$$

Cross rz moment

$$\sum_{i=1}^N f_i \frac{r_i^2 z_i e^{-\frac{r_i^2}{2\sigma_i^2}} \left(I_0 \left(\frac{r_i^2}{2\sigma_i^2} \right) + I_1 \left(\frac{r_i^2}{2\sigma_i^2} \right) \right)}{\sigma_i \left(1 - e^{-r_i^2/\sigma_i^2} \right)} = \frac{r_0^2 z_0 e^{-\frac{r_0^2}{2\sigma^2}} \left(I_0 \left(\frac{r_0^2}{2\sigma^2} \right) + I_1 \left(\frac{r_0^2}{2\sigma^2} \right) \right)}{\sigma \left(1 - e^{-r_0^2/\sigma^2} \right)}. \quad (5.18)$$

Recall that $\sigma^2 = \sigma_0^2 + 4\nu\Delta t$ and $\Gamma_{\Delta t} = \Gamma_0(1 - e^{-r_0^2/\sigma^2})/(1 - e^{-r_0^2/\sigma_0^2})$.

It is recommended that positive fractions are only allowed, since negative fractions represent diffusion in the opposite direction, which is not physically plausible. Equations 5.13 -5.18 can be cast in a linear system of the form

$$\mathbf{A}\mathbf{f} = \mathbf{b} \quad \text{subject to } \mathbf{f} > \mathbf{0}, \quad (5.19)$$

where the coefficient matrix \mathbf{A} has $M = 6$ rows and N columns, the solution vector \mathbf{f} consists of N fractions corresponding to N elements, and the right hand sides compose vector \mathbf{b} of size M . A necessary (but not sufficient) condition for the system to be solvable

is that the number of neighbors has to satisfy

$$N \geq M. \tag{5.20}$$

This condition is justified physically by the fact that away from the axis, the linear system can be solved with a configuration if 6 neighbors uniformly distributed on a circle of radius h around the element to be diffused, where h , the elements spacing, is a typical diffusion length of $O(\sqrt{\nu\Delta t})$. To establish the sufficient condition, we proceed with a physical observation. In general, the distribution of elements is distorted by convection possibly creating gaps of size larger than h^2 . In this case, diffusion into these gaps is not possible, since there are no neighbors to receive fractions. This problem is solved by filling the gaps with new elements and consequently condition 5.20 is always satisfied and the system 5.19 is solvable. Injection of new elements is done one element at a time on a circle of radius h around the element to be diffused. The element is selected from a prescribed set of candidates, distributed evenly on the circle, in such a way that the distance to the closest neighbor is maximized over all candidates.

Discussion of the relevant size of diffusion length, in addition to selection of the “neighborhood radius”, which determines what elements are involved in the redistribution process, will be presented in the next section.

The linear system 5.20 is solved using the non-negative least squares method[62]. Usually, the L^2 norm of the error is selected to be less than 10^{-6} . Notice that for elements close to the axis of symmetry, some of the equations are singular. Treatment of diffusion of elements close to the axis of symmetry is discussed in section 4.9.

5.7 Various diffusion lengths

In the implementation of the diffusion scheme discussed thus far, it is crucial to decide on various length scales related to diffusion and discuss their relevance. For this reason, the following parameters are defined:

- Element spacing h : The element spacing h reflects the diffusion length of the diffusion process. If the core were to expand to account for diffusion, the expansion over time step Δt is $\sqrt{4\nu\Delta t}$. Thus it is expected that for a neighboring element to receive a

fraction of the circulation of the element to be diffused, then distance between the two elements, h , must be of the order of $\sqrt{4\nu\Delta t}$. Numerical experiments yielded an optimal value of $h = \sqrt{8\nu\Delta t}$.

- Neighborhood radius R : The neighborhood radius associated with a certain element is the radius within which all elements are considered as neighbors, and thus candidates to receive fractions of the circulation. Noting that in the $2D$ cartesian case, the core radius may be mathematically described as the standard deviation of a normal distribution of vorticity representing the core function, it convenient to choose the neighborhood radius to be twice the standard deviation, the location at which the function decays to less that 1% of its value. Thus a typical value for the neighborhood radius is $R \sim \sqrt{16\nu\Delta t}$.
- Core radius σ : The core radius represents the extent of the basis function for vorticity. Thus, within the core, satisfactory vorticity discretization requires at least the presence of few neighborhood elements, otherwise the convolution suffers. For smooth flows, we select σ to be of the order of R . For flows that experience large strain , a more conservative core size should be selected to maintain overlap especially at longer times.

5.8 Diffusion of the scalar

The equation governing the diffusion of the scalar is

$$\frac{\partial s}{\partial t} = \alpha \left(\frac{\partial^2 s}{\partial r^2} + \frac{1}{r} \frac{\partial s}{\partial r} + \frac{\partial^2 s}{\partial z^2} \right) \quad (5.21)$$

The scalar core function and the expansion equation are, respectively,

$$\phi(\mathbf{r}; \mathbf{r}_o, t) = \frac{2\pi}{\pi^{3/2}\sigma^3} e^{-\frac{r^2+r_o^2+(z-z_o)^2}{\sigma^2}} I_o \left(\frac{2rr_o}{\sigma^2} \right) \quad (5.22)$$

and

$$\frac{d(\sigma^2)}{dt} = 4\alpha. \quad (5.23)$$

It should be noted that the conserved quantity⁴ in this case is rs , such that

$$\int_{-\infty}^{\infty} \int_0^{\infty} \phi(\mathbf{r}; \mathbf{r}_o, t) r dr dz = 1. \quad (5.24)$$

Consequently, conservation of moments of the scalar is governed by

$$\sum_{i=1}^N \int_{-\infty}^{\infty} \int_0^{\infty} \mathbf{r}^n s_i(\mathbf{r}; \mathbf{r}_i) r dr dz = \int_{-\infty}^{\infty} \int_0^{\infty} \mathbf{r}^n s_{\Delta t}(\mathbf{r}; \mathbf{r}_0) r dr dz \quad \text{for } n \leq 2. \quad (5.25)$$

Defining $f_i = E_i/E_o$, and assuming that $\alpha = \nu$, the corresponding redistribution equations in discretized form would then be

Zeroth moment (conservation of energy)

$$\sum_{i=1}^N f_i = 1. \quad (5.26)$$

First r moment

$$\sum_{i=1}^N f_i \frac{e^{-\frac{r_i^2}{2\sigma_i^2}} \left((r_i^2 + \sigma_i^2) I_0 \left(\frac{r_i^2}{2\sigma_i^2} \right) + r_i^2 I_1 \left(\frac{r_i^2}{2\sigma_i^2} \right) \right)}{\sigma_i} = \frac{e^{-\frac{r_0^2}{2\sigma^2}} \left((r_0^2 + \sigma_0^2) I_0 \left(\frac{r_0^2}{2\sigma^2} \right) + r_0^2 I_1 \left(\frac{r_0^2}{2\sigma^2} \right) \right)}{\sigma}. \quad (5.27)$$

First z moment

$$\sum_{i=1}^N f_i z_i = z_0. \quad (5.28)$$

Second r moment

$$\sum_{i=1}^N f_i (r_i^2 + \sigma_i^2) = r_0^2 + \sigma^2. \quad (5.29)$$

Second z moment

$$\sum_{i=1}^N f_i \left(z_i^2 + \frac{1}{2} \sigma_i^2 \right) = \left(z_0^2 + \frac{1}{2} \sigma^2 \right). \quad (5.30)$$

Cross rz moment

$$\sum_{i=1}^N f_i \frac{z_i e^{-\frac{r_i^2}{2\sigma_i^2}} \left((r_i^2 + \sigma_i^2) I_0 \left(\frac{r_i^2}{2\sigma_i^2} \right) + r_i^2 I_1 \left(\frac{r_i^2}{2\sigma_i^2} \right) \right)}{\sigma_i} = \frac{z_0 e^{-\frac{r_0^2}{2\sigma^2}} \left((r_0^2 + \sigma_0^2) I_0 \left(\frac{r_0^2}{2\sigma^2} \right) + r_0^2 I_1 \left(\frac{r_0^2}{2\sigma^2} \right) \right)}{\sigma}. \quad (5.31)$$

⁴If s represents temperature, the conserved quantity is the thermal energy of the element.

5.9 Treatment near the axis of symmetry

If an element is close to the axis, then it is possible to simplify the various equations by expanding the circulation decay equation and the moment equations in Taylor series of r_0 around zero. To order of $(r_0/\sigma_0)^2$, we get

Circulation decay

$$\Gamma_{\Delta t} = \Gamma_0 \frac{\sigma_0^2}{\sigma^2} \left(1 + \frac{1}{2} \left(\frac{r_0}{\sigma_0} \right)^2 - \left(\frac{r_0}{\sigma} \right)^2 \right) \quad (5.32)$$

Zeroth moment (conservation of circulation)

$$\sum_{i=1}^N f_i = 1. \quad (5.33)$$

First r moment

$$\sum_{i=1}^N f_i \left(\sigma_i + \frac{C}{2} \frac{r_i^2}{\sigma_i^2} \right) = \sigma + \frac{C}{2} \frac{r_0^2}{\sigma^2} \quad (5.34)$$

First z moment

$$\sum_{i=1}^N f_i z_i = z_0. \quad (5.35)$$

Second r moment

$$\sum_{i=1}^N f_i \left(\sigma_i^2 + C r_i^2 \right) = \sigma^2 + C r_0^2 \quad (5.36)$$

Second z moment

$$\sum_{i=1}^N f_i \left(z_i^2 + \frac{1}{2} \sigma_i^2 \right) = \left(z_0 + \frac{1}{2} \sigma^2 \right). \quad (5.37)$$

Cross rz moment

$$\sum_{i=1}^N f_i z_i \left(\sigma_i + \frac{C}{2} \frac{r_i^2}{\sigma_i^2} \right) = z_0 \left(\sigma + \frac{C}{2} \frac{r_0^2}{\sigma^2} \right) \quad (5.38)$$

where $C = 1$ for the scalar and $1/2$ for the vorticity. Since the core is second order, this special treatment can be applied to elements of $r_0 < \sigma_0$ with error of order of σ_0^2 . Numerical experiments showed that solving the system 5.20 with the moment equations 5.13-5.18 is problematic for $r_0 < h/2$. In this case, using the approximate moment equations 5.33-5.38 proved to be stable and accurate.

5.10 Scalar gradients

The scalar gradient is required to calculate the baroclinic term in the vorticity equation. The scalar at location \mathbf{r} is obtained by the summation

$$s(\mathbf{r}) = \sum_{i=1}^N E_i \phi_{s,\sigma}(\mathbf{r}; \mathbf{r}_i). \quad (5.39)$$

Thus the scalar gradient may be obtained as

$$\nabla s(\mathbf{r}) = \sum_{i=1}^N E_i \nabla \phi_{s,\sigma}(\mathbf{r}; \mathbf{r}_i) \quad (5.40)$$

where $\nabla \phi_{s,\sigma}(\mathbf{r}, \mathbf{r}_i) = \frac{\partial}{\partial r} \phi_{s,\sigma}(\mathbf{r}, \mathbf{r}_i) \hat{\mathbf{r}} + \frac{\partial}{\partial z} \phi_{s,\sigma}(\mathbf{r}, \mathbf{r}_i) \hat{\mathbf{z}}$ and

$$\frac{\partial}{\partial r} \phi_{s,\sigma}(\mathbf{r}, \mathbf{r}_i) = -\frac{4E_i}{\pi^{1/2}\sigma_i^5} e^{-\frac{r^2+r_i^2+(z-z_i)^2}{\sigma_i^2}} \left[r I_0\left(\frac{2rr_i}{\sigma_i^2}\right) - r_i I_1\left(\frac{2rr_i}{\sigma_i^2}\right) \right] \quad (5.41)$$

$$\frac{\partial}{\partial z} \phi_{s,\sigma}(\mathbf{r}, \mathbf{r}_i) = -\frac{4E_i}{\pi^{1/2}\sigma_i^5} (z - z_i) e^{-\frac{r^2+r_i^2+(z-z_i)^2}{\sigma_i^2}} I_0\left(\frac{2rr_i}{\sigma_i^2}\right) \quad (5.42)$$

5.11 Remarks

We make the following remarks:

1. The circulation is not conserved in the half plane $0 \leq r < \infty, -\infty < z < \infty$, whereas the energy is. Both the circulation and energy are conserved in full plane $-\infty < r < \infty, -\infty < z < \infty$.
2. Since the axial behavior of the scalar and vorticity core functions is the same, the corresponding moment equations are the same. The radial moment equations are different, however. The overall impulse of the energy increases at a rate of $4\nu t$, whereas the overall impulse of the circulation decays at the same rate as the circulation.

5.12 Accuracy

Following on the discussions of sections 2.6.2 and 4.4, the following advantages of the smooth redistribution method are stated:

1. By incorporation of a smoothing function, recovery of pointwise vorticity and scalar fields is possible. The core function is second order accurate.
2. The method offers control on the spatial as well as the temporal values of the core size, thus allowing local balancing of the smoothing and discretization errors. This balancing can be done by deciding on the smallest core radius such the overlap $\sigma = ch$ is maintained, where h may be thought of as the average local elements spacing, an indication of local diffusion rate.
3. The introduction of new elements is done in way to promote the uniformity (or smoothness, i.e. larger L) of the flow, which has a significant impact on reducing the discretization error.

Chapter 6

Convection

The flow, represented as a collection of vortex elements, moves in time according to $d\mathbf{r}/dt = \mathbf{u}$, where \mathbf{r} is the position and \mathbf{u} is the velocity. Thus determination of the velocity field is required to transport the vortex elements (or the vorticity field) in time. The velocity field satisfies the mass conservation equation, the circulation equation¹, and the boundary conditions: zero flow normal to solid boundaries, $\mathbf{u} \cdot \hat{\mathbf{n}}$, and a prescribed velocity at the pool base, $\mathbf{u}(0 \leq r \leq r_0, z = 0)$, where $\hat{\mathbf{n}}$ is the unit vector normal to a solid boundary. Solving this system of partial differential equations can be facilitated through the use of Helmholtz decomposition. The Helmholtz decomposition[3], discussed briefly in chapter 3, expresses the velocity into its various components according to

$$\mathbf{u} = \mathbf{u}_\omega + \mathbf{u}_e + \mathbf{u}_P, \quad (6.1)$$

where \mathbf{u}_ω , \mathbf{u}_e , and \mathbf{u}_P are the vortical, expansion, and potential components of the velocity, respectively. The problem reduces to solving the Poisson equation relevant to each component.

In this chapter, we will present the formulation for establishing the velocity field. The vortical component is discussed first. Then, we present the solution for the expansion component. Finally, we put the convection part in perspective in the overall picture of the vortex method and more specifically we briefly discuss the scheme used to integrate the velocity in time to update the elements positions.

¹or the momentum equation, alternatively.

6.1 Vortical velocity component

The vortical velocity component satisfies the continuity equation of an incompressible fluid in an unbounded domain²

$$\nabla \cdot \mathbf{u}_\omega = 0. \quad (6.2)$$

A vector potential $\boldsymbol{\psi}(\mathbf{r}, t) = \psi(\mathbf{r}, t)\hat{\boldsymbol{\theta}}$, also called the stream function, may then be defined according to

$$\nabla \times \boldsymbol{\psi} \equiv \mathbf{u}_\omega \quad (6.3)$$

or

$$\mathbf{u}_\omega \equiv (u_{\omega,r}, u_{\omega,z}) = \left(-\frac{1}{r} \frac{\partial \psi}{\partial z}, \frac{1}{r} \frac{\partial \psi}{\partial r} \right), \quad (6.4)$$

where $\hat{\boldsymbol{\theta}}$ is the unit vector in the azimuthal direction. Using equation 6.3 and the definition of vorticity, the stream function can be shown to satisfy the Poisson equation

$$\nabla^2 \left(\frac{\psi}{r} \right) = -\omega, \quad (6.5)$$

where ω is the vorticity field.

Using the Green's function method, equation 6.5 can be solved to obtain ψ as the convolution

$$\psi(\mathbf{r}, t) = \int_{-\infty}^{\infty} \int_0^{\infty} G(\mathbf{r}; \mathbf{r}') \omega(\mathbf{r}', t) dr' dz'. \quad (6.6)$$

The Green function is the solution of equation 6.5 for a Dirac delta vorticity distribution, $\delta(r - r') \delta(z - z')$, and may be obtained using Fourier/Hankel transform as

$$G(r, r', z - z') = \frac{1}{2\pi} (r_1 + r_2) [K(\lambda) - E(\lambda)], \quad (6.7)$$

where $r_1^2 \equiv (r + r')^2 + (z - z')^2$, $r_2^2 \equiv (r - r')^2 + (z - z')^2$, $\lambda \equiv (r_2 - r_1) / (r_2 + r_1)$, and K and E are respectively the complete elliptic integrals of the first and second kind.

The vortical velocity $\mathbf{u}_\omega (u_{\omega,r}, u_{\omega,z})$, obtained from equation 6.4, is

$$u_{\omega,r} = -\frac{1}{r} \int_{-\infty}^{\infty} \int_0^{\infty} \frac{\partial}{\partial z} G(r, r', z - z') \omega(\mathbf{r}', t) dr' dz', \quad (6.8)$$

²The vortical velocity component is solenoidal.

$$u_{\omega,z} = \frac{1}{r} \int_{-\infty}^{\infty} \int_0^{\infty} \frac{\partial}{\partial r} G(r, r', z - z') \omega(\mathbf{r}', t) dr' dz' \quad (6.9)$$

where

$$\frac{\partial}{\partial z} G(r, r', z - z') = \frac{1}{2\pi} \left\{ (z - z') \frac{r_1 + r_2}{r_1 r_2} \left[K(\lambda) - \frac{E(\lambda)}{2} \left(\frac{r_1}{r_2} + \frac{r_2}{r_1} \right) \right] \right\} \quad (6.10)$$

and

$$\frac{\partial}{\partial r} G(r, r', z - z') = \frac{1}{2\pi} \left\{ \left(\frac{r - r'}{r_1} + \frac{r + r'}{r_2} \right) K(\lambda) - \frac{r_1 + r_2}{2} E(\lambda) \left(\frac{r - r'}{r_1^2} + \frac{r + r'}{r_2^2} \right) \right\}. \quad (6.11)$$

6.1.1 Velocity of a point vortex

If the vorticity field is represented by N point vortices, then

$$\omega(\mathbf{r}', t) = \sum_{i=1}^N \Gamma_i \delta(r' - r_i) \delta(z' - z_i). \quad (6.12)$$

The corresponding velocity field is given by

$$u_{\omega,r} = -\frac{1}{2\pi r} \sum_{i=1}^N \Gamma_i \left\{ (z - z_i) \frac{r_1 + r_2}{r_1 r_2} \left[K(\lambda) - \frac{E(\lambda)}{2} \left(\frac{r_1}{r_2} + \frac{r_2}{r_1} \right) \right] \right\}, \quad (6.13)$$

$$u_{\omega,z} = \frac{1}{2\pi r} \sum_{i=1}^N \Gamma_i \left\{ \left(\frac{r - r_i}{r_1} + \frac{r + r_i}{r_2} \right) K(\lambda) - \frac{r_1 + r_2}{2} E(\lambda) \left(\frac{r - r_i}{r_1^2} + \frac{r + r_i}{r_2^2} \right) \right\}, \quad (6.14)$$

where $r_1^2 \equiv (r + r_i)^2 + (z - z_i)^2$, $r_2^2 \equiv (r - r_i)^2 + (z - z_i)^2$, and $\lambda \equiv (r_2 - r_1) / (r_2 + r_1)$.

The point vortex solution is singular at the locations of the points, and desingularization has to be employed if the vorticity field is represented by point vortices. The point vortex solution, however, provides an approximation for the far field solution due to a vortex blob with a core function of compact support, such as the one given by equation 6.16. More specifically, for thin elements, i.e. for $\sigma_i/r_i \ll 1$, or for locations far from the element, i.e. for $(r - r_i)^2 + (z - z_i)^2 \gg \sigma_i^2$, representing the blob by a point vortex located at its center and carrying the same circulation provides a good approximation. This advantage will be instrumental in deciding on the appropriate ranges of the variables for construction of the tables for vortex blobs, as discussed below.

6.1.2 Velocity of a vortex blob

As discussed in Chapters 2 and 3, the vortex element method is based on the representation of the vorticity field by a collection of elements according to

$$\omega(\mathbf{r}', t) = \sum_{i=1}^N \Gamma_i \phi_\sigma(\mathbf{r}'; \mathbf{r}_i), \quad (6.15)$$

where ϕ_σ is the core function characterized by core radius σ . In the previous chapter, we showed that diffusion of a vortex element can be modeled by redistributing the necessary fractions of circulation to neighboring elements. The core function, selected to satisfy the viscous part of the vorticity equation, is

$$\phi_\sigma(\mathbf{r}', \mathbf{r}_i) = \frac{1}{1 - e^{-r_i^2/\sigma_i^2}} \frac{2r_i}{\pi^{1/2}\sigma_i^3} e^{-\frac{(r'-r_i)^2+(z'-z_i)^2}{\sigma_i^2}} e^{-\frac{2r'r_i}{\sigma_i^2}} I_1\left(\frac{2r'r_i}{\sigma_i^2}\right). \quad (6.16)$$

Substituting equations 6.15 and 6.16 into equations 6.8 and (6.9 results in the following expressions for the vortical velocity

$$u_{\omega,r} = -\frac{1}{r} \sum_{i=1}^N \int_{-\infty}^{\infty} \int_0^{\infty} \Gamma_i \frac{\partial}{\partial z} G(r, r', z - z') \phi_\sigma(r', r_i, z' - z_i) dr' dz', \quad (6.17)$$

$$u_{\omega,z} = \frac{1}{r} \sum_{i=1}^N \int_{-\infty}^{\infty} \int_0^{\infty} \Gamma_i \frac{\partial}{\partial r} G(r, r', z - z') \phi_\sigma(r', r_i, z' - z_i) dr' dz'. \quad (6.18)$$

The double integrals in equations 6.17 and 6.18 are complicated and no closed form solution is attainable. Note that the variables into the two integrals are $r, r_i, z - z_i$ and σ_i . Normalizing by the core radius σ_i reduces the dimensions to three, namely $r/\sigma_i, r_i/\sigma_i$, and $(z - z_i)/\sigma_i$. We propose to solve the double integrals numerically for appropriate ranges of these variables and store the results in the form of a three dimensional table.

Numerical integration and convergence

Numerical integration of equations 6.17 and 6.18 was performed using the trapezoidal rule. The domain used is a square of size 5σ centered at the element. At the edge of the integration domain, the core function decays to less than $10^{-8}\%$ of its maximum value. The convergence characteristics obey those of the trapezoidal rule. Figure 6-1 shows the relative percent error in the self induced velocity as a function of r_o/σ , where r_o is the radius of the element and

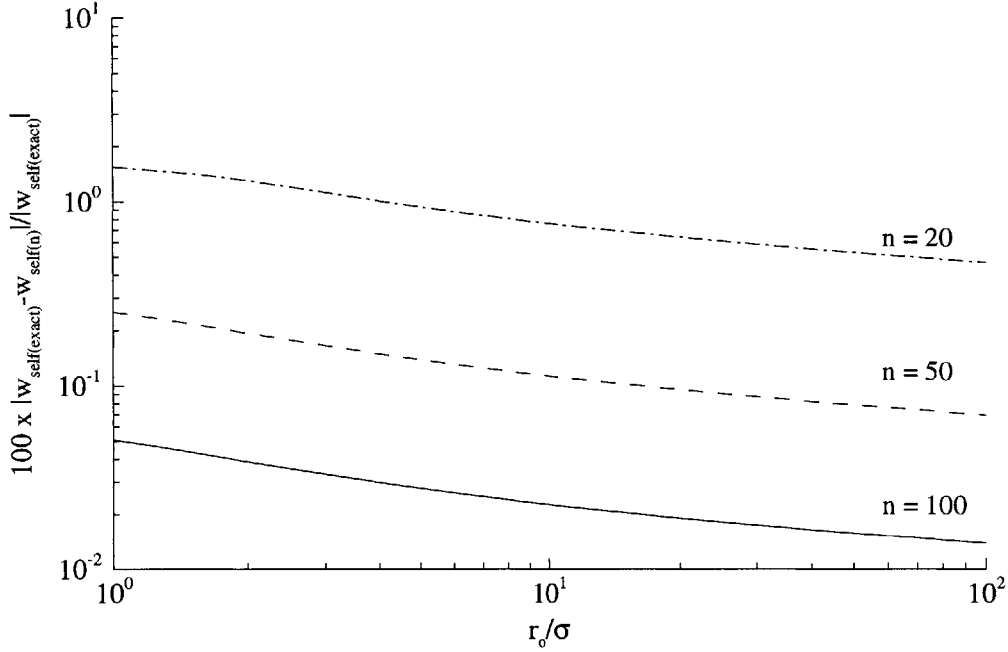


Figure 6-1: Convergence properties of the self induced velocity of a vortex blob.

σ is the core size. As the grid size increases from 20×20 to 50×50 to 100×100 , the error decreases by the square of the ratio of the grid sizes. The reference grid size is 200×200 . The grid size used in constructing the tables is 100×100 , corresponding to less than 1% relative error.

Using the numerical integration method described above, the vortical velocity components were evaluated for the following ranges:

- Element radius: $0 \leq r_o/\sigma \leq 20$, with spacing of 0.2.
- Solution grid: $r_o/\sigma - 5 \leq r/\sigma \leq r_o/\sigma + 5$ and $0 \leq (z - z_o)/\sigma \leq 5$.

We expect that outside these ranges, the point vortex solution should provide a good approximation of the solution. It should be noted that evaluating the velocity in the neighborhood of the center for elements where $r_o/\sigma > 20$ requires desingularization. This is implemented in using the following expressions for r_1 and r_2

$$r_1^2 \equiv (r + r_o)^2 + (z - z_o)^2 + 0.56\sigma^2 \quad (6.19)$$

$$r_2^2 \equiv (r - r_o)^2 + (z - z_o)^2 + 0.56\sigma^2 \quad (6.20)$$

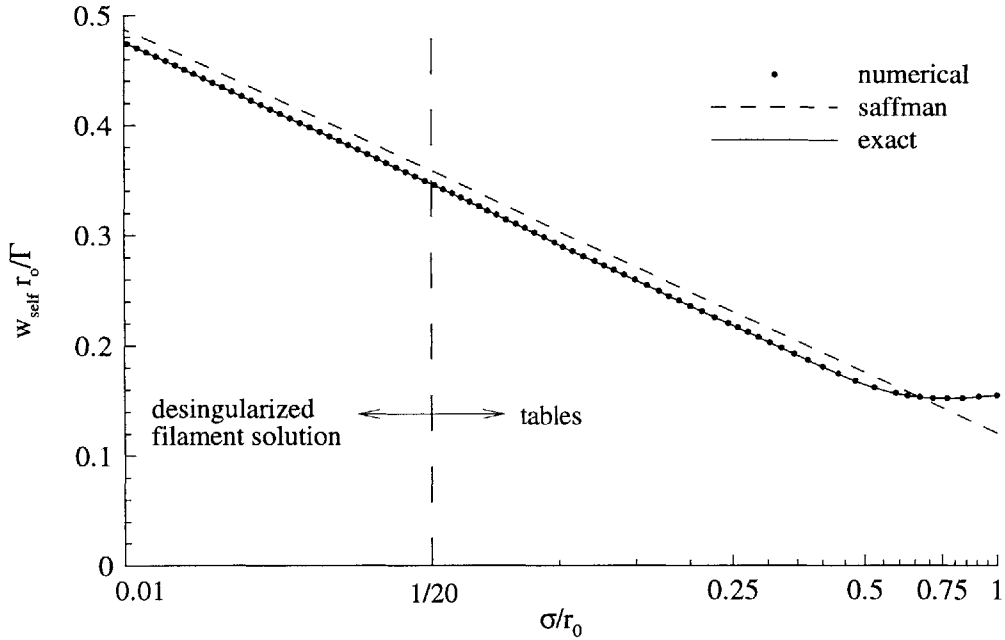


Figure 6-2: Self induced velocity.

The desingularization constant, obtained by matching the desingularized solution a converged numerical solution, applies to all values of r_o/σ . This is confirmed in Figure 6-2, where the self induced velocity is presented over the range $1 \leq r_o/\sigma \leq 100$. The exact³ solution is plotted along with the numerical solution (tables + point vortex solution). Saffman's[79] expression of the self induced velocity for a thin ring, given by

$$w_{self} = \frac{\Gamma_0}{4\pi r_0} \left(\log \left(\frac{8r_0}{\sigma} \right) - 0.558 \right), \quad (6.21)$$

is also presented. The deviation of the solution obtained by Saffman for large σ/r_0 is due to the error involving in the approximation.

Figure 6-3 shows the performance of the numerical solution in terms of radial profiles of the axial vortical velocity component through the center of the element. The exact and numerical values are plotted for two element radii, $r_o = 5$ and $r_o = 21$, over a range of 10 around the element center. Dimensions are normalized by the core radius σ . The case of $r_o = 5$ corresponds either to interpolation using the tables for $|r - r_o| < 5$ or to the

³Numerically obtained using a 200×200 grid.

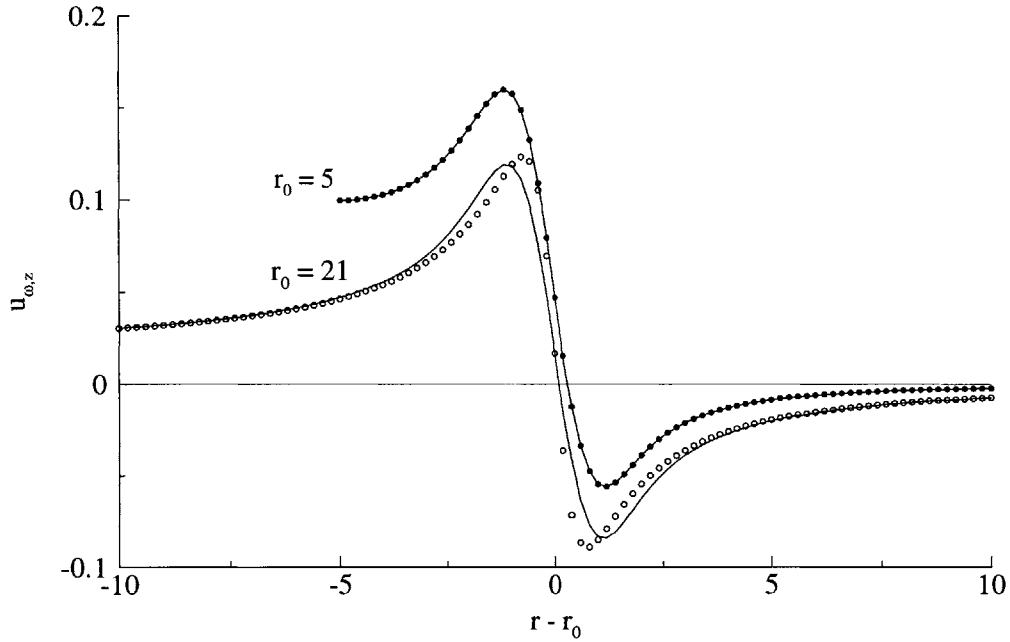


Figure 6-3: Comparison of numerical and exact radial profiles (at $z = 0$) of axial velocity component for $r_o = 5$ and $r_o = 21$.

desingularized point vortex solution for $|r - r_o| > 5$. The other case, $r_o = 21$, corresponds to a range outside those of the tables and the desingularized point vortex solution is used throughout. The error due to this approximation in the vicinity of the element center is not expected to produce significant errors when evaluating the velocity induced by a large number of elements.

6.2 Expansion velocity

The expansion velocity component satisfies the mass conservation equation for an irrotational compressible flow given by

$$\nabla \cdot \mathbf{u}_e = -\frac{1}{\rho} \frac{D\rho}{Dt}. \quad (6.22)$$

This gives rise to the scalar potential, Φ , defined as

$$\nabla\Phi \equiv \mathbf{u}_e, \quad (6.23)$$

or

$$\mathbf{u}_e \equiv (u_{e,r}, u_{e,z}) = \left(\frac{\partial \Phi}{\partial z}, \frac{\partial \Phi}{\partial z} \right). \quad (6.24)$$

Using equations 6.22 and 6.23, the Poisson equation governing the potential is obtained as

$$\nabla^2 \Phi = -\varrho, \quad (6.25)$$

where $\varrho = (1/\rho) D\rho/Dt$. The potential is then obtained as the convolution

$$\Phi(\mathbf{r}, t) = \int_{-\infty}^{\infty} \int_0^{\infty} G(\mathbf{r}; \mathbf{r}') \varrho(\mathbf{r}', t) dr' dz', \quad (6.26)$$

where the Green function, G , defined as the solution of equation 6.25 for a Dirac delta scalar distribution, $\delta(r - r') \delta(z - z')$, is given as

$$G(r, r', z - z') = \frac{2}{\pi} \frac{r_o}{(r_1 + r_2)} K(\lambda), \quad (6.27)$$

where $r_1^2 \equiv (r + r')^2 + (z - z')^2$, $r_2^2 \equiv (r - r')^2 + (z - z')^2$, $\lambda \equiv (r_2 - r_1) / (r_2 + r_1)$, and K is the complete elliptic integrals of the first kind.

The expansion velocity $\mathbf{u}_e(u_{e,r}, u_{e,z})$, obtained from equation 6.24, is

$$u_{e,r} = \int_{-\infty}^{\infty} \int_0^{\infty} \frac{\partial}{\partial r} G(r, r', z - z') \varrho(\mathbf{r}', t) dr' dz', \quad (6.28)$$

$$u_{e,z} = \int_{-\infty}^{\infty} \int_0^{\infty} \frac{\partial}{\partial z} G(r, r', z - z') \varrho(\mathbf{r}', t) dr' dz', \quad (6.29)$$

where

$$\frac{\partial}{\partial r} G(r, r', z - z') = \frac{1}{2\pi r} \left\{ \left(\frac{r - r'}{r_1} - \frac{r + r'}{r_2} \right) K(\lambda) + \frac{r_1 + r_2}{2} \left(\frac{r + r'}{r_2^2} - \frac{r - r'}{r_1^2} \right) E(\lambda) \right\} \quad (6.30)$$

and

$$\frac{\partial}{\partial z} G(r, r', z - z') = \frac{2}{\pi} \left\{ \frac{r'(z - z')}{r_1 r_2} \left[\frac{1}{r_1 + r_2} K(\lambda) - \frac{1}{2} \frac{r_1 + r_2}{r_1 r_2} E(\lambda) \right] \right\}. \quad (6.31)$$

6.2.1 Expansion of a point source

If the expansion field, ϱ , is represented by a system of point sources, then

$$\varrho(\mathbf{r}', t) = \sum_{i=1}^N E_i \delta(r' - r_i) \delta(z' - z_i), \quad (6.32)$$

where E_i is the strength of the element. The corresponding expansion velocity is given by

$$u_{e,r} = \frac{1}{2\pi r} \sum_{i=1}^N E_i \left\{ \left(\frac{r-r'}{r_1} - \frac{r+r'}{r_2} \right) K(\lambda) + \frac{r_1+r_2}{2} \left(\frac{r+r'}{r_2^2} - \frac{r-r'}{r_1^2} \right) E(\lambda) \right\}, \quad (6.33)$$

and

$$u_{e,z} = \frac{2}{\pi} \sum_{i=1}^N E_i \left\{ \frac{r'(z-z')}{r_1 r_2} \left[\frac{1}{r_1+r_2} K(\lambda) - \frac{1}{2} \frac{r_1+r_2}{r_1 r_2} E(\lambda) \right] \right\}, \quad (6.34)$$

where $r_1^2 \equiv (r+r_i)^2 + (z-z_i)^2$, $r_2^2 \equiv (r-r_i)^2 + (z-z_i)^2$, and $\lambda \equiv (r_2 - r_1) / (r_2 + r_1)$.

6.2.2 Expansion of a vortex blob

Representation of the scalar field by a collection of elements is according to

$$\varrho(\mathbf{r}', t) = \sum_{i=1}^N E_i \phi_\sigma(\mathbf{r}', \mathbf{r}_i), \quad (6.35)$$

where ϕ_σ is the core function characterized by core radius σ . The core function used is the scalar core function developed for scalar diffusion discussed in the previous chapter,

$$\phi_\sigma(\mathbf{r}', \mathbf{r}_i) = \frac{2\pi}{\pi^{3/2} \sigma_i^3} e^{-\frac{r'^2 + r_i^2 + (z' - z_i)^2}{\sigma_i^2}} I_0 \left(\frac{2r' r_i}{\sigma_i^2} \right) \quad (6.36)$$

Substituting equations 6.35 and 6.36 in equations 6.28 and 6.29 results in the following expressions for the expansion velocity

$$u_{e,r} = \sum_{i=1}^N \int_{-\infty}^{\infty} \int_0^{\infty} E_i \frac{\partial}{\partial r} G(r, r', z - z') \phi_\sigma(r', r_i, z' - z_i) dr' dz', \quad (6.37)$$

$$u_{e,z} = \sum_{i=1}^N \int_{-\infty}^{\infty} \int_0^{\infty} E_i \frac{\partial}{\partial z} G(r, r', z - z') \phi_\sigma(r', r_i, z' - z_i) dr' dz', \quad (6.38)$$

where the gradient of the Green function G is given by equation 6.30 and 6.31.

Numerical integration and convergence

Numerical integration of equations 6.37 and 6.38 is conducted in a similar fashion to that of the vortical velocity, and the results were stored in a three dimensional table. In Figure 6-4, the radial component of the expansion velocity at the center of an element for $0.01 \leq \sigma/r_0 \leq 1$, evaluated using the tables or the point solution, is compared to a converged numerical solution, referred to as the exact solution in the figure. As the elements gets closer to the axis, the magnitude of the radial component of the expansion velocity at the center of the element decreases. This is due to symmetry at the axis, where the radial velocity is zero. Figure 6-5 shows the performance of the numerical solution in terms of radial profiles of the radial expansion velocity component through the center of the element. The exact and numerical solutions are plotted for two element radii, $r_0 = 5$ and $r_0 = 21$, over a range of 10 around the element center. Dimensions are normalized by the core radius σ . The case of $r_o = 5$ corresponds either to interpolation using the tables for $|r - r_o| < 5$ or to the desingularized point vortex solution for $|r - r_o| > 5$. The other case, $r_o = 21$, corresponds to a range outside those of the tables and the desingularized point vortex solution is used throughout. The error due to this approximation in the vicinity of the element center is not expected to produce significant errors when evaluating the velocity induced by a large number of elements.

6.3 Numerical Algorithm

6.3.1 Strang splitting

Solving the vorticity and energy equations is done using the Strang splitting algorithm, discussed in section 3.6.1,

$$\mathbf{u}_n = (H(\Delta t/2)\mathcal{E}(\Delta t)H(\Delta t/2))\mathbf{u}_{n-1} \quad (6.39)$$

where \mathbf{u} is the velocity, n denoted solution at time $n\Delta t$, $\mathcal{E}(t)$ and $H(t)$ are the solution operators of Euler's equation and the heat equation respectively.

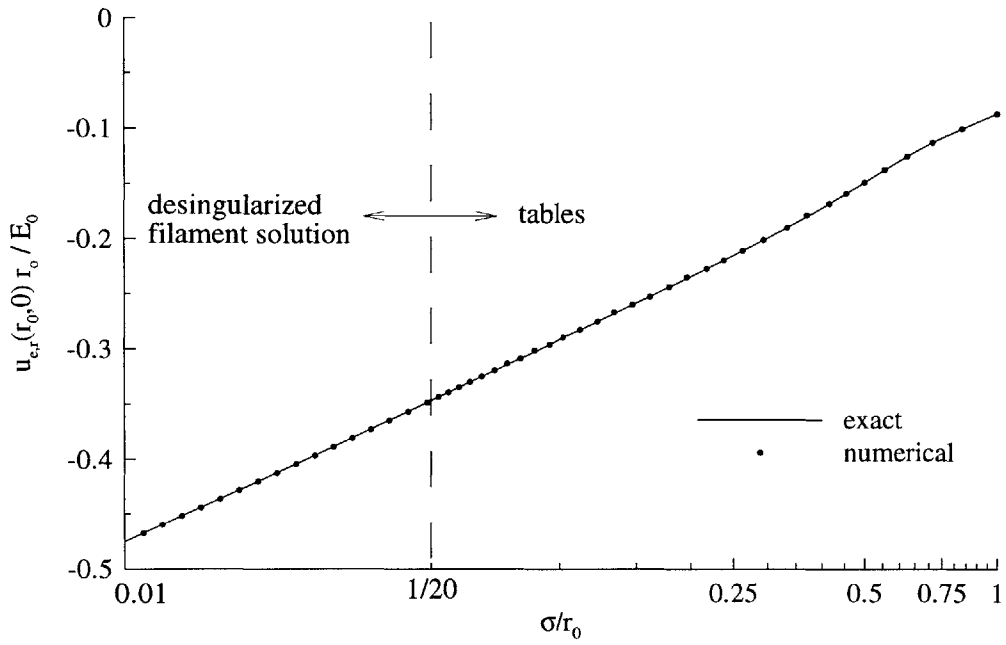


Figure 6-4: Convergence properties of the radial component of the expansion velocity at the center of a blob.

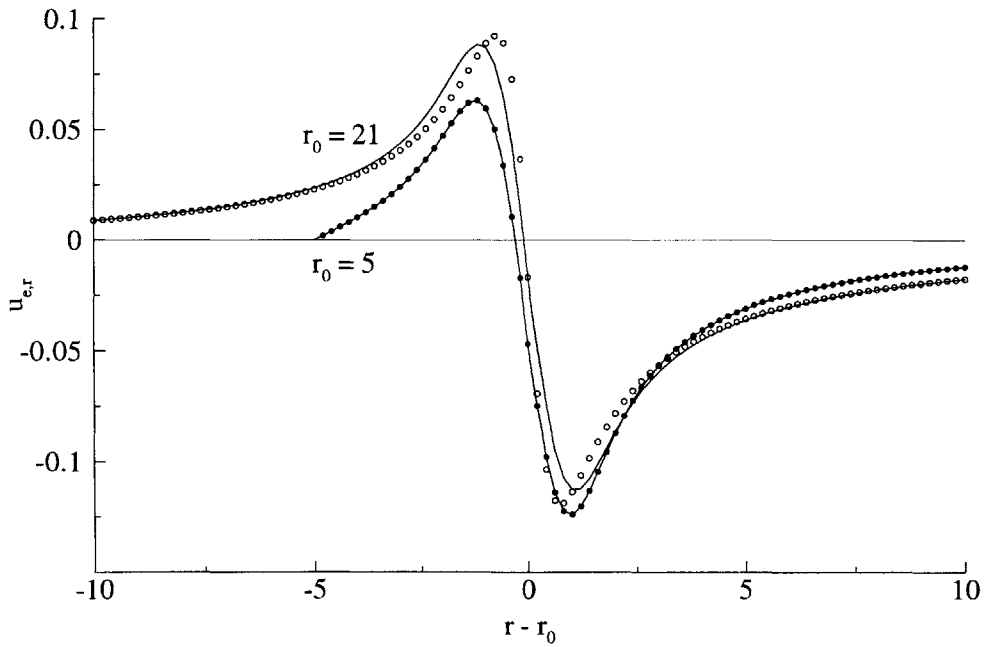


Figure 6-5: Comparison of numerical and exact radial profiles (at $z = 0$) of radial expansion velocity component at the center of the element for $r_o = 5$ and $r_o = 21$.

6.3.2 Solving the convection-generation step

The convection-generation step may be represented by

$$\frac{dy}{dt} = f(t, y) \quad (6.40)$$

where y denotes element location \mathbf{r} , circulation Γ , and energy E . Correspondingly $f(t, \mathbf{r}) = \mathbf{u}$, $f(t, \Gamma) = \Gamma_g$, and $f(t, E) = Eg$, where Γ_g and Eg represent the source terms for the circulation and energy respectively. Equation 6.40 is solved numerically using a second order Runge-Kutta method[1]:

$$y_{n+1} = y_n + \frac{\Delta t}{2}(f_1 + f_2) + O(\Delta t^3) \quad (6.41)$$

$$f_1 = f(t_n, y_n) \quad (6.42)$$

$$f_2 = f(t_n + \Delta t, y_n + f_1) \quad (6.43)$$

6.3.3 Numerical algorithm

Incorporation of Strang (viscous) splitting and second order Runge-Kutta integration in time into the vortex method may be done according to the algorithm shown in Figure 6-6.

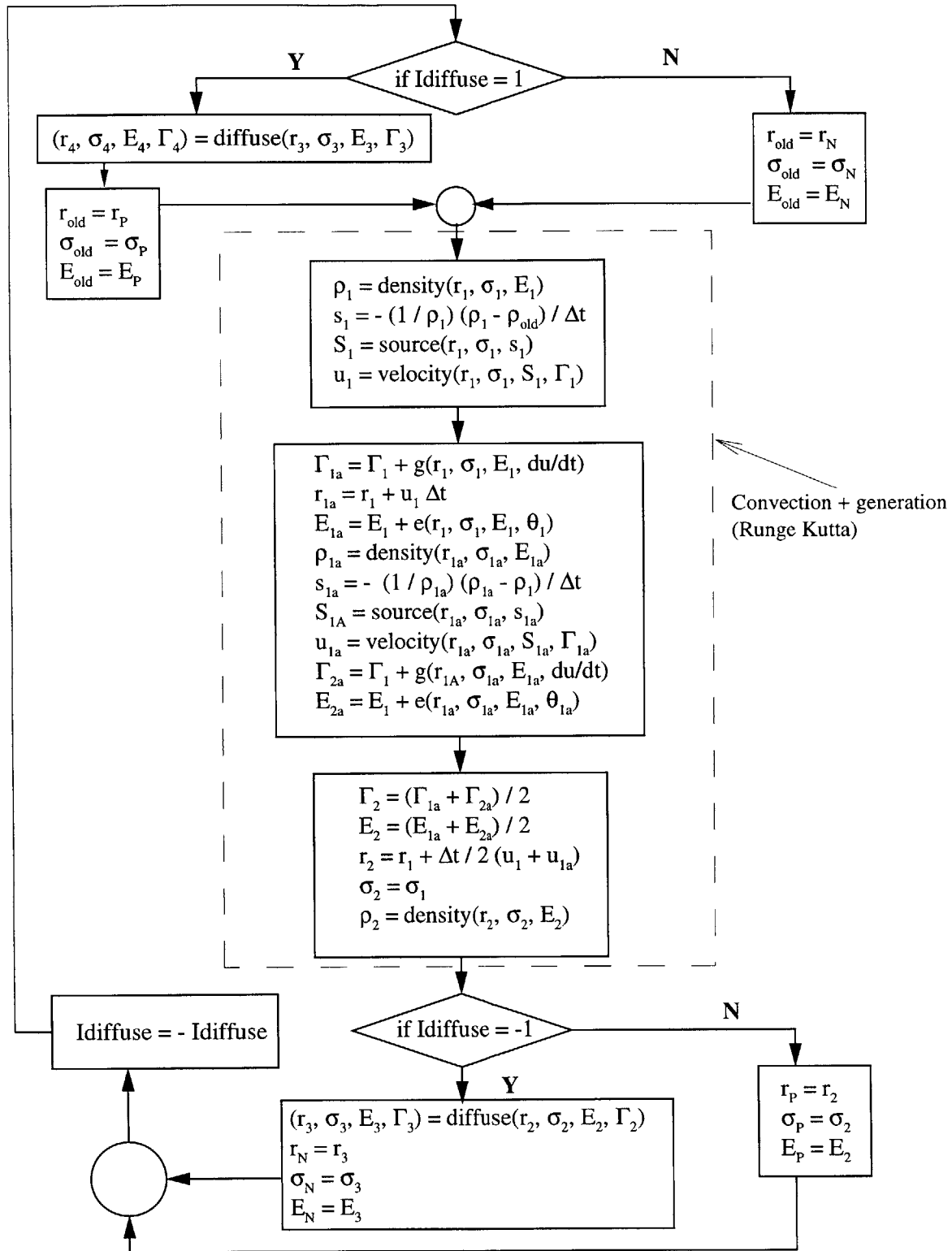


Figure 6-6: Numerical algorithm.

Chapter 7

Radiation

Radiative transport in a participating medium transforms the energy equation into an integro-differential equation which must be solved if radiation is considered as an important mechanism of heat transfer in a convective-diffusive-reactive environment. In most cases, especially in combustion problems, the temperature gradients are so steep that the region where the radiative flux, which is proportional to the fourth power of temperature, is significant in a small subset of the entire flow domain. Especially when utilizing a grid-free Lagrangian scheme to perform the convective-diffusive-reactive simulations, it is desirable to develop a compatible scheme which does not require a grid to perform the computations of the radiative flux and its divergence (needed in the energy equation.) We have developed the discrete source method in which the radiative flux and irradiance are computed by summing over a collection of radiating elements distributed over the region of high temperature. In an axisymmetric domain, the irradiance and radiative flux, both are triple integrals of the radiation kernel over the elemental volume, are reduced to double integrals which are then approximated by single integrals that are evaluated semi-analytically. We demonstrate the accuracy of the scheme by comparing the results with direct numerical evaluation of the original integrals for cases relevant to combustion problems.

7.1 Radiation in a Gray Non-Scattering Medium

For a gray non-scattering medium, the specific intensity $I(\mathbf{r}, \hat{s})$, the energy transfer rate per unit area per unit solid angle, of a radiation field at the point \mathbf{r} in the direction \hat{s} is given

by[70]

$$I(\mathbf{r}, \hat{\mathbf{s}}) = I(\mathbf{r}'_{\Sigma}) e^{-\int_0^s a(s'') ds''} + \int_0^s i_b(\mathbf{r}', \hat{\mathbf{s}}) e^{-\int_{s'}^s a(s'') ds''} a(s') ds', \quad (7.1)$$

where a is the absorption coefficient. The black body intensity, i_b , is given by $i_b = \sigma T^4/\pi$, where σ is the Stefan-Boltzmann constant (the refractive index of the medium is assumed to be unity). The source and target are defined by vectors \mathbf{r} and \mathbf{r}' respectively, and $\mathbf{s} = s\hat{\mathbf{s}}$ is the coordinate along the ray emanating from \mathbf{r}'_{Σ} at the boundary (Σ) and passing through target \mathbf{r} , see Figure 7-1. The outer integration in the second term of the right-hand side of equation 7.1 is along \mathbf{s} from a point $s' = 0$ at the boundary to the target point $s' = s$ inside the medium.

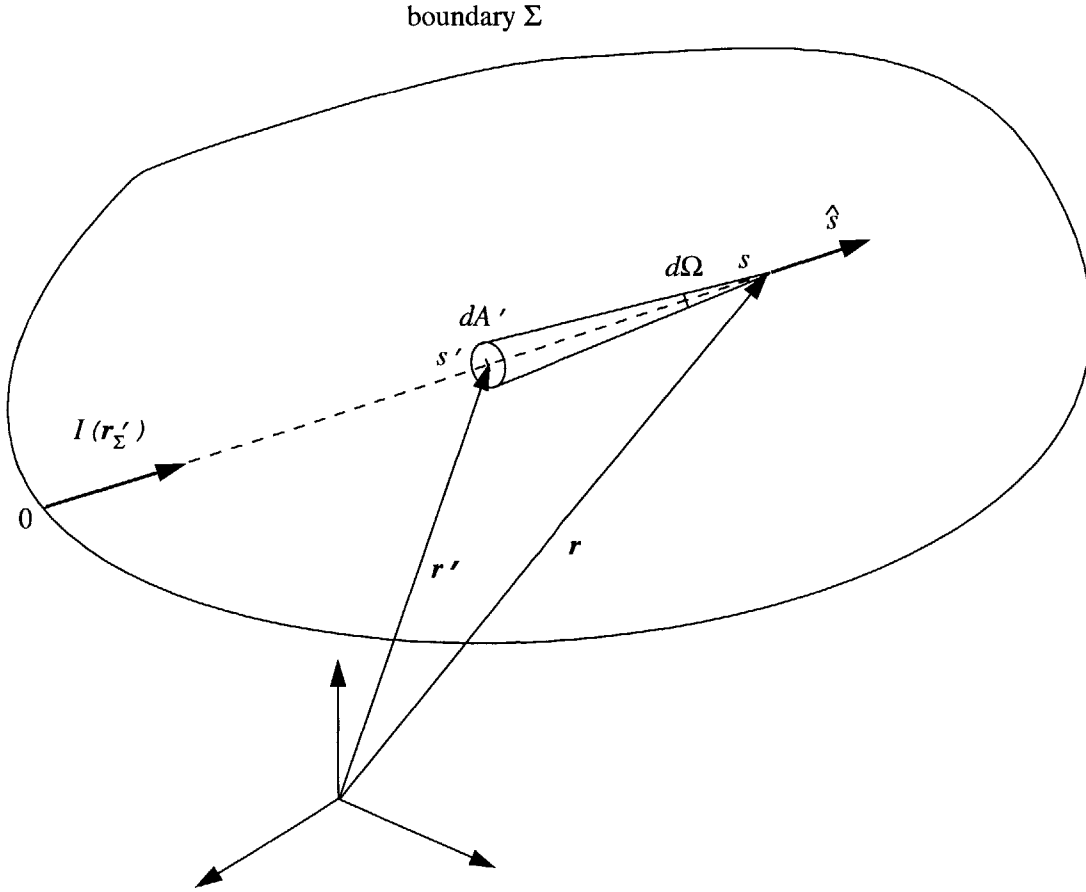


Figure 7-1: Schematic.

The total radiative heat flux vector is the intensity integrated over all solid angles Ω

$$\mathbf{q}(\mathbf{r}) = \int_{4\pi} I(\mathbf{r}, \hat{\mathbf{s}}) \hat{\mathbf{s}} d\Omega, \quad (7.2)$$

where the solid angle $d\Omega = dA'/|\mathbf{r} - \mathbf{r}'|^2$ and the unit vector $\hat{s} = (\mathbf{r} - \mathbf{r}')/|\mathbf{r} - \mathbf{r}'|$.

The divergence of the heat flux, the negative of which is the radiation source term in the energy equation, is given by

$$\nabla \cdot \mathbf{q}(\mathbf{r}) = a(\mathbf{r}) (4\pi i_b(\mathbf{r}) - G(\mathbf{r})), \quad (7.3)$$

where G , the irradiance, is given by

$$G(\mathbf{r}) = \int_{4\pi} I(\mathbf{r}, \hat{s}) d\Omega. \quad (7.4)$$

Assuming that the incident intensity crossing the boundary is zero, the irradiance is expressed as[88]

$$G(\mathbf{r}) = \int_V a(\mathbf{r}') i_b(\mathbf{r}') \frac{e^{-\int_{s'}^s a(s'') ds''}}{|\mathbf{r} - \mathbf{r}'|^2} dV(\mathbf{r}'). \quad (7.5)$$

7.2 The Discrete Source Method

Our objective is to simulate radiative transport using a grid free scheme compatible with the vortex method. To meet this objective, we propose the Discrete Source Method. This method enables the calculation of the heat flux and its divergence, induced by a collection of computational elements that discretize the temperature field. The solution is presented in terms of a "Biot-Savart" summation over the computational elements decomposing the domain.

If a volume V is selected to be large enough such that it is surrounded by a cold medium, Figure 7-2, the incident intensity crossing the boundary can be neglected, and the irradiance is given by equation 7.5.

Decomposing volume V into N elemental volumes, and assuming that the temperature T_j and absorption coefficient a_j are uniform within each element, $j = 1, N$, then the irradiance may be expressed in the following discretized form,

$$G(\mathbf{r}) \simeq \sum_{j=1}^N G_j(\mathbf{r}), \quad (7.6)$$

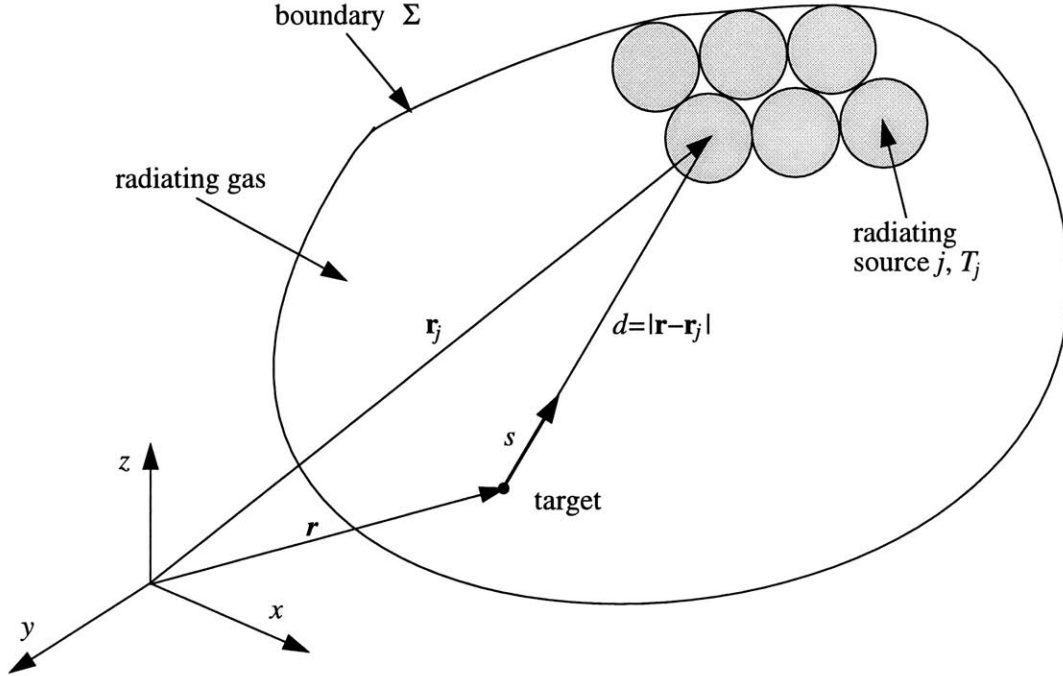


Figure 7-2: Decomposing the participating medium into computational elements.

where $G_j(\mathbf{r})$ is the irradiance induced by computational element j ,

$$G_j(\mathbf{r}) \simeq a_j i_{b_j} \int_{V_j} \frac{e^{-\bar{a}_j |\mathbf{r} - \mathbf{r}'|}}{|\mathbf{r} - \mathbf{r}'|^2} dV(\mathbf{r}'), \quad (7.7)$$

where \bar{a}_j , defined as the "effective attenuation coefficient", is given by

$$\bar{a}_j = \frac{\int_0^{|\mathbf{r} - \mathbf{r}_j|} a(s) ds}{|\mathbf{r} - \mathbf{r}_j|}. \quad (7.8)$$

The effective attenuation coefficient is obtained by assuming that $|\mathbf{r} - \mathbf{r}'| \simeq |\mathbf{r} - \mathbf{r}_j|$ in evaluating the inner integral of equation 7.5. This approximation, justified by selecting small enough computational elements, simplifies computing the integral considerably. For a source-target configuration, the effective attenuation coefficient is calculated once, according to equation 7.8, and is then used as a constant in the triple integral 7.7.

7.3 Solution for a Spherical Element

Consider a spherical radiative source of radius r_0 and absorption coefficient a . The irradiance at distance r from the center of the sphere is given by[90]

$$\frac{G_{r \leq r_0}}{4\pi i_b} = \frac{a}{\bar{a}} + \frac{a}{4r} (r^2 - r_0^2) \Delta E - \frac{1}{2} e^{-\bar{a}r_0} \left(\sinh(\bar{a}r) \left(\frac{ar_0}{\bar{a}r} + \frac{a}{\bar{a}^2 r} \right) + \frac{a}{\bar{a}} \cosh(\bar{a}r) \right), \quad (7.9)$$

$$\frac{G_{r > r_0}}{4\pi i_b} = \frac{a}{4r} (r^2 - r_0^2) \Delta E + \frac{1}{2} e^{-\bar{a}r} \left(\sinh(\bar{a}r_0) \left(\frac{a}{\bar{a}} - \frac{a}{\bar{a}^2 r} \right) + \frac{ar_0}{\bar{a}r} \cosh(\bar{a}r_0) \right), \quad (7.10)$$

where $\Delta E = Ei_1(\bar{a}(r+r_0)) - Ei_1(\bar{a}|r-r_0|)$, $Ei_1(x) = \int_1^\infty e^{-xt} t^{-1} dt$ is the exponential integral, and $\bar{a} = \int_0^r a(s) ds/r$. Of special interest is the "self-induced" irradiance, defined as the irradiance at the center of the sphere. The self-induced irradiance is given by

$$\frac{G_{\text{self sphere}}}{4\pi i_b} = 1 - e^{-ar_0}. \quad (7.11)$$

7.4 Solution for an Axisymmetric Element

Consider a ring of radius r_0 , cross-section radius δ , blackbody intensity i_b , and absorption coefficient a , as shown in Figure 7-3.

In polar-cylindrical coordinates (s, θ, ψ) , the irradiance at location $\mathbf{r}(r, 0, z)$ is

$$G(\mathbf{r}) = ai_b \int_0^{2\pi} \int_0^{2\pi} \int_0^\delta K_G(\mathbf{r}, \mathbf{r}') s(r_0 + s \cos \theta) ds d\theta d\psi, \quad (7.12)$$

where

$$K_G(\mathbf{r}, \mathbf{r}') = \frac{e^{-\bar{a}\sqrt{s^2 - 2s(z \sin \theta - (r_0 - r \cos \psi) \cos \theta) - 2rr_0 \cos \psi + d^2}}}{s^2 - 2s(z \sin \theta - (r_0 - r \cos \psi) \cos \theta) - 2rr_0 \cos \psi + d^2}, \quad (7.13)$$

$d^2 = r^2 + z^2 + r_0^2$, and $\bar{a} = \int_0^{|\mathbf{r}-\mathbf{r}'|} a(s) ds/|\mathbf{r}-\mathbf{r}'|$.

7.4.1 Thin Ring Approximation

For the case of a thin ring, characterized by $s/r_0 \leq \delta/r_0 \ll 1$, and if the effective attenuation coefficient is such that $\bar{a}\delta < 1$ (optically-thin), an approximation is obtained by expanding the integrand of integral 7.12 in Taylor series in s around zero to second order.

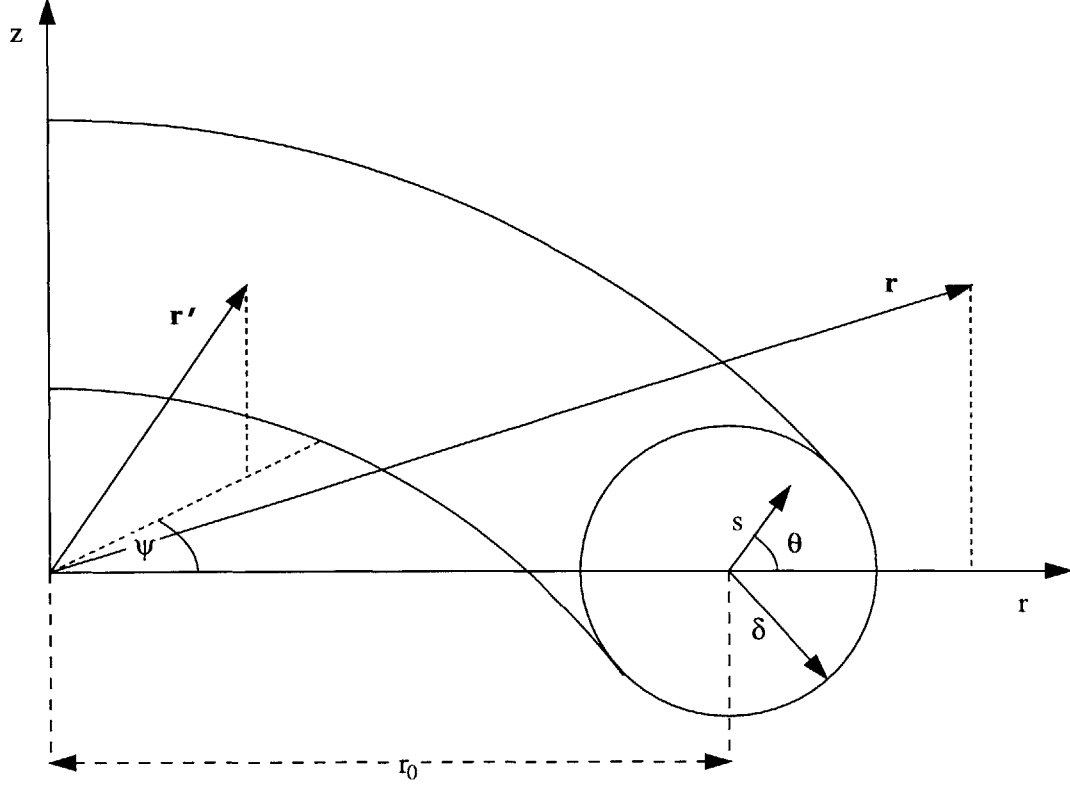


Figure 7-3: Ring in polar cylindrical coordinates.

The irradiance is then approximated by

$$G(\mathbf{r}) = 4ai_b \int_0^{2\pi} \int_0^{2\pi} \int_0^{\delta} \left(\frac{e^{-\bar{a}\lambda\sqrt{1-\kappa^2\cos^2\beta}}}{\lambda^2(1-\kappa^2\cos^2\beta)} sr_0 + O((\bar{a}s)^2) \right) ds d\theta d\beta, \quad (7.14)$$

where $\lambda^2 = (r + r_0)^2 + z^2$, $\kappa^2 = 4rr_0/\lambda^2$, and $\psi = 2\beta$. Integrating in s and θ directions leads to

$$G(\mathbf{r}) = i_b \frac{4\pi\delta^2 r_0}{\lambda^2} f(\alpha, \kappa) + O((\bar{a}\delta)^3), \quad (7.15)$$

where $\alpha = \bar{a}\lambda$ and

$$f(\alpha, \kappa) = \int_0^{\pi/2} \frac{e^{-\alpha\sqrt{1-\kappa^2\cos^2\beta}}}{1-\kappa^2\cos^2\beta} d\beta. \quad (7.16)$$

The thin ring approximation provides a "good" approximation of the heat flux and its divergence away from the core for values of \bar{a} satisfying $\bar{a}\delta < 1$. This is clearly observed in Figure 7-4, where radial profiles of the irradiance at two elevations are presented for a thin ring with the following parameters: $r_0 = 1, a = 1, \delta = 0.02$. Inside the core, however, this approximation diverges, and it is singular at the center of the core ($\kappa = 1$). In the following

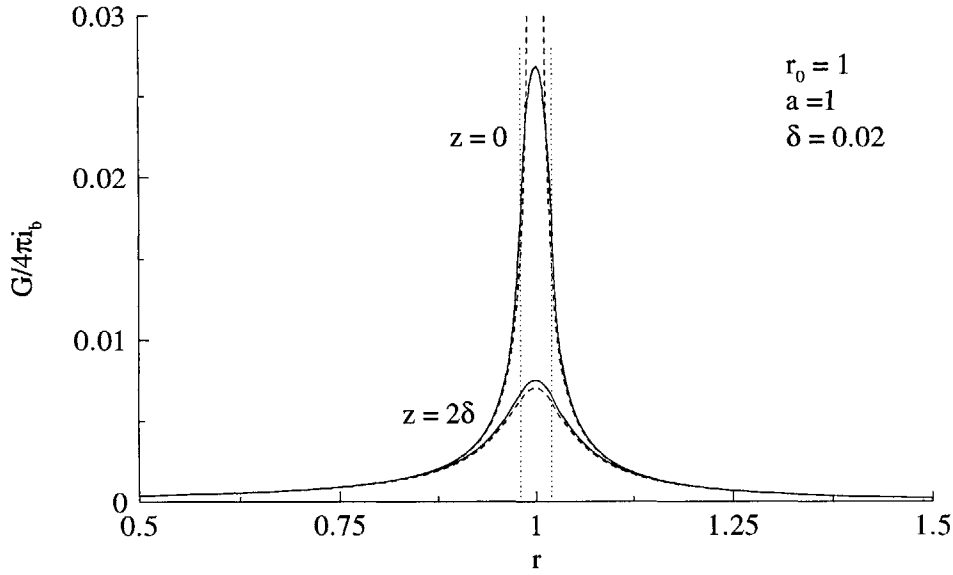


Figure 7-4: Irradiance due to a thin ring with small a

two sections, approximate solutions for G for large values of \bar{a} and/or inside the core are presented.

We note that desingularization of the integrand of equation 7.16 proved ineffective, especially for large values of the effective attenuation coefficient \bar{a} . The reason is that small perturbations in this integrand get magnified due to the "exponentiation effect" of \bar{a} . For example, consider the case where $a\delta = 5$. Here, the kernel of G is negligible at the edge of the core, and the sole contribution at the center of the element is due to the element itself. In this case, we require better than just killing the singularity for an accurate representation of the radiation field. The solution to this problem is presented in the next section.

7.5 Treatment of large absorption coefficient

For large \bar{a} , the integral decays fast and the contribution of sources with $\bar{a}\delta \gg 1$ is in their immediate vicinity. Thus, it is convenient, under the condition $\bar{a}\delta > 1$, to approximate G by its value corresponding to a spherical element centered at r_0 with a radius δ .

To show the usefulness of the sphere solution, equations 7.9 and 7.10, for rings with $\bar{a}\delta > 1$, radial profiles of irradiance due to a ring with $r_0 = 1, \delta = 0.02, a = 100$ are

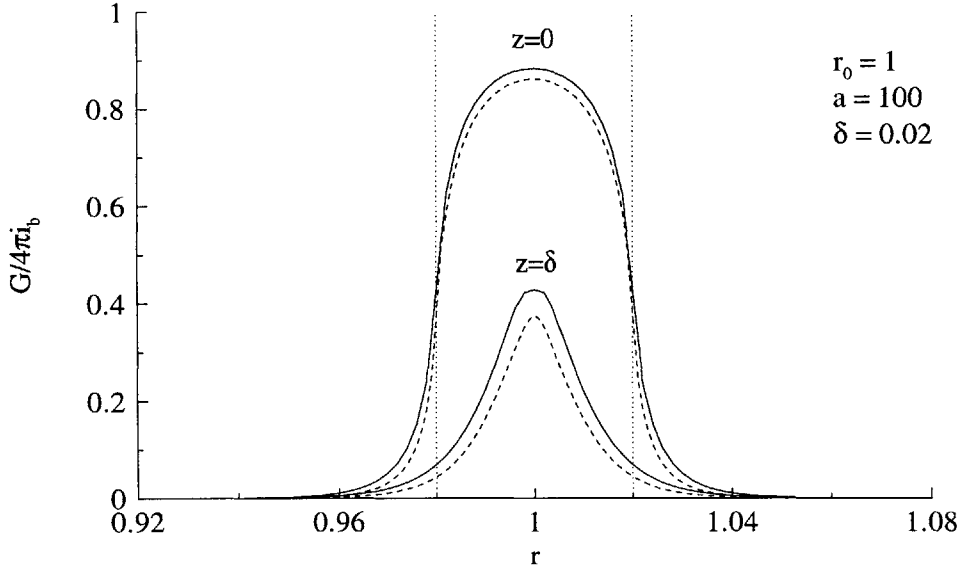


Figure 7-5: Ring and sphere solutions for large a

presented in Figure 7-5 along with those obtained for a sphere located at $r_0 = 1$ and of radius $\delta = 0.02$. The two profiles show good agreement.

7.6 Solution inside the core

The solution outside the core of an optically-thin computational ring has been presented in section 4.1. Further, an approximation of the solution for an optically-thick ring was proposed in the previous section. In this section, we propose an approximation inside the core of an optically-thin ring using a scaling of the spherical element solution to match the induced irradiance at the center of the element. According to equation 7.12, the self induced irradiance is given by

$$G_{\text{self ring}} = \frac{a}{\pi} \int_0^{\pi/2} \int_0^{2\pi} \int_0^{\delta} \frac{e^{-a\sqrt{s^2 + 4\sin^2\beta(s\cos\theta + 1)}}}{s^2 + 4\sin^2\beta(s\cos\theta + 1)} s(1 + s\cos\theta) ds d\theta d\beta, \quad (7.17)$$

where s , a , and δ/r_0 , are non-dimensionalized by r_0 , and $G_{\text{self ring}} = G(r_0, 0)/(4\pi i_b)$. Integral 7.17 was calculated numerically for the ranges of $\delta \in [0.01, 1]$ and $a \in [0, 100]$. The solution is presented in Figure 7-6, showing that $\ln(G_{\text{self ring}})$ is a linear function of $\ln(a\delta)$ for $\ln(a\delta) \leq -3$, while it approaches the optically-thick limit non-linearly for $\ln(a\delta) > -3$. In the same

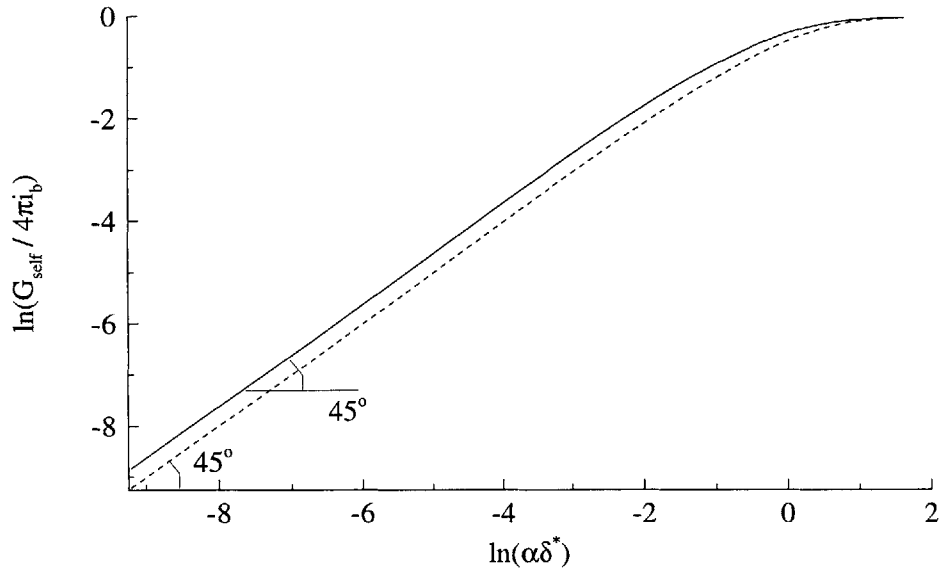


Figure 7-6: G_{self} for both a ring and a sphere as a function of $a\delta$.

figure, the value for a spherical element is presented.

Knowing the value of the self induced irradiance, and observing that as $a\delta$ increases the solution for G approaches that for a spherical element, the solutions for an optically-thick ring ($a\delta > 1$), or inside the core of an optically-thin ring ($a\delta < 1$) are approximated by the corresponding spherical element solution scaled by the ratio of the ring self-induced irradiance to the sphere self-induced irradiance, i.e.

$$G = \frac{G_{\text{self ring}}}{G_{\text{self sphere}}} G_{\text{sphere}} \quad \text{for } a\delta > 1 \text{ or } a\delta < 1 \text{ and } s < \delta. \quad (7.18)$$

Recall that the solution outside the core of an optically-thin ring is given by the thin ring approximation, equation 7.15, discussed in section 7.4.1.

Using the model just laid out, approximate vs. exact calculations of the radial profiles of G at various elevations are presented in Figure 7-7 for values of a of 1,10 and 100 respectively.

7.7 Extension to Cartesian Coordinates

In three dimensional Cartesian coordinates, the medium may be decomposed into spherical computational elements. The solution due to sphere is given by equations 7.9 and 7.10. For

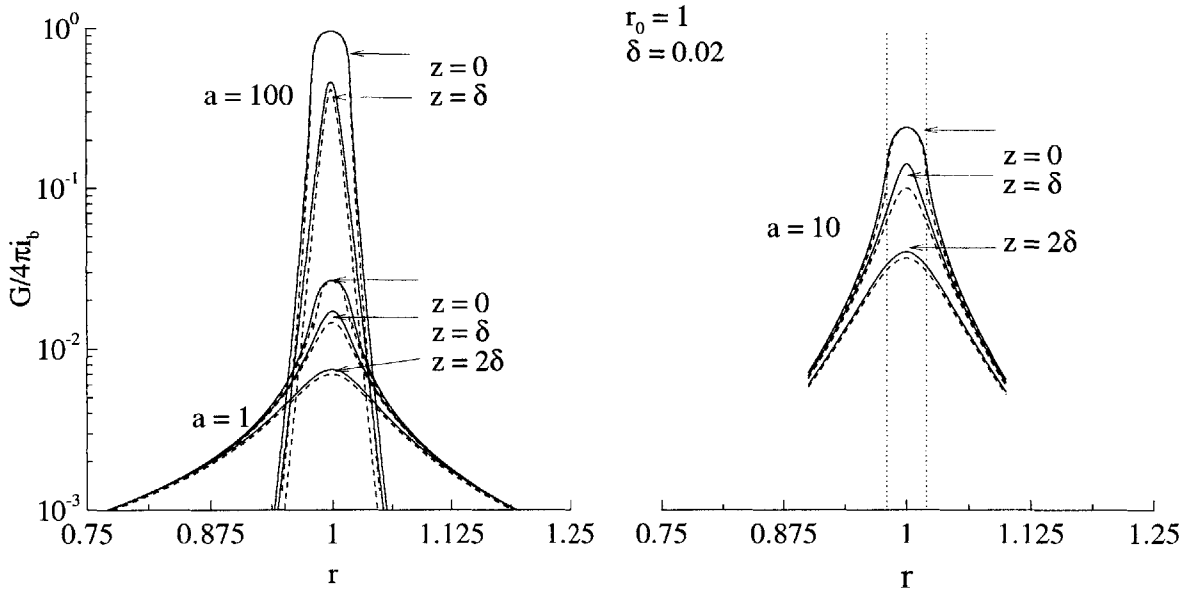


Figure 7-7: Exact vs. approximate solutions of G for $a = 1, 10$ and 100 .

two dimensional rectangular geometries, the computational elements are infinite circular cylinders. The irradiance due to a infinite cylinder[42] of radius r_0 and absorption coefficient a at radial location r is given by

$$\frac{G_{r \leq r_0}}{4\pi i_b} = ar_0 \int_1^\infty \frac{I_1(\bar{a}yr_0)K_0(\bar{a}yr)}{y} dy \quad (7.19)$$

$$\frac{G_{r \geq r_0}}{4\pi i_b} = ar_0 \int_1^\infty \frac{\rho I_1(\bar{a}yr)K_0(\bar{a}yr) + I_0(\bar{a}yr)(\rho K_1(\bar{a}yr) - K_1(\bar{a}yr_0))}{y} dy \quad (7.20)$$

where I and K are the modified Bessel functions of first and second kind respectively, $\rho = r/r_0$, and \bar{a} is the "effective attenuation coefficient" given by equation 7.8.

7.8 Example I

To validate our model and check its accuracy, we use the following example in which the absorption coefficient is assumed to be constant throughout the domain.

We consider a ring with square cross section, as shown in Figure 7-8, with radius $r_0 = 1$ and side $w = 1$. The objective is to compare the irradiance calculated using the model with that computed using exact numerical integration. The comparison is done in terms of radial

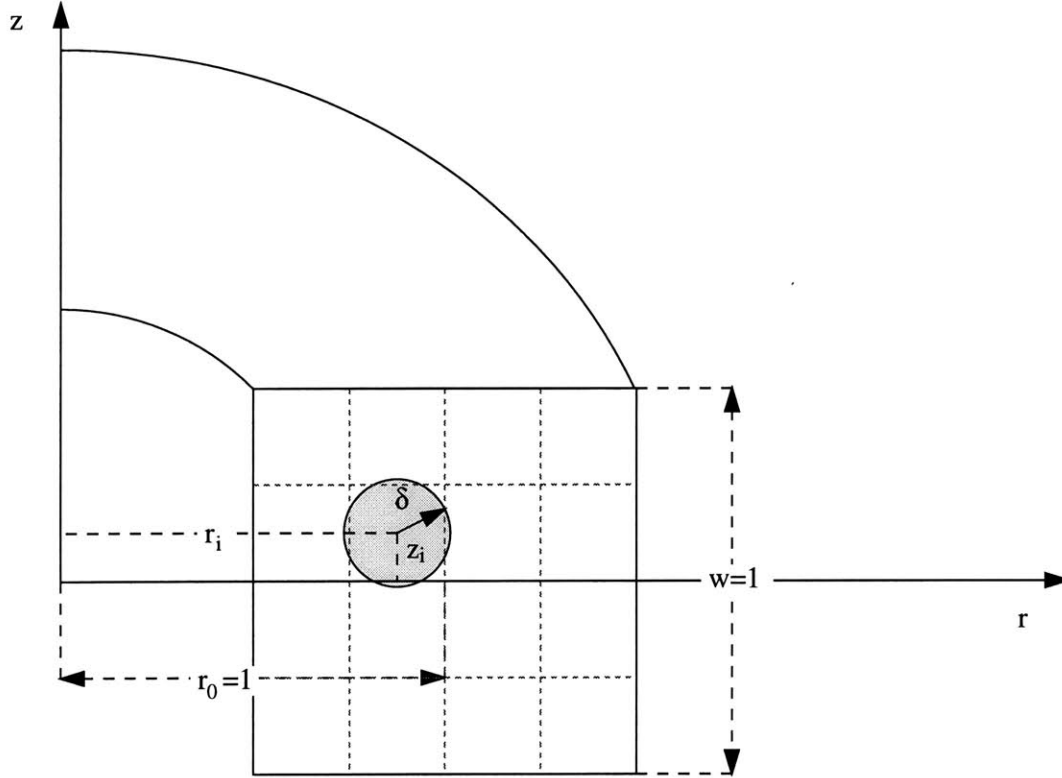


Figure 7-8: Schematic for example I.

profiles of G passing through the center of the domain for three values of the absorption coefficient: $a = 1, 10$, and 100 .

The mesh used to perform the numerical integration was tested for each case to obtain a mesh independent solution. As expected from the nature of the kernel, the number of points in each dimension required for an accurate solution is proportional to a , the reason being the steeper gradients due to the exponential term. For $a = 1$, for example, we use a $100 \times 100 \times 100$ mesh. To cut down the cost, we used a cutoff distance to alleviate computing the contribution of those points of the domain that are at a distance d from the target point such that $ad = 6$.

Implementation of our model demands discretizing the domain into N computational element that are essentially rings characterized by a radius r_i and core radius $\delta_i, i = 1, N$. The rings are constructed by discretizing the domain using a rectangular mesh, and representing each cell by a ring located at the center of the cell with a core radius selected such that the thermal energy of the cell is conserved. We are interested in values of δ that are typical to a those used in flow and/or combustion calculations. We choose $\delta_i = 0.02$, i.e.

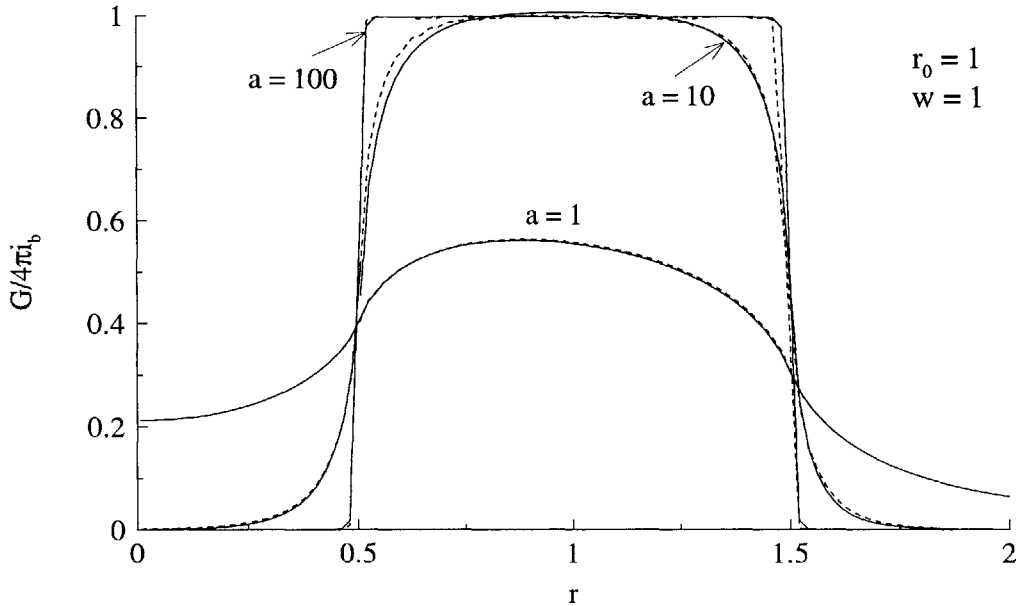


Figure 7-9: Exact vs. approximate solutions of G for $a = 1, 10$ and 100 .

we use 50×50 rings for all the cases (independent of a). The use of cutoff distance is also implemented in these computations.

The results are presented in Figure 7-9 where the irradiance normalized by the black body intensity is plotted versus the radial location r . For the case of $a = 1$, the value of G on the z -axis is non-zero which is due to low attenuation ($a = 1$) experienced by the intensity in a certain direction. Due to the same reason, the maximum value of G occurs on the side of the domain that is closer to the axis, where the azimuthal distribution of the domain has a significant contribution. This would not be the case for higher values of a , as seen in Figure 7-9. In this case, the domain is optically thick and the attenuation is large leading to a fast decay in the vicinity of the domain. This explains the sharp rise (drop) in the value of G around $r = 0.5$ (1.5). The behavior is even more obvious in the case of the optically thick limit where $a = 100$. In this case, the irradiance has a top-hat profile, where no intensity escapes the domain. Obviously, for the three cases, the model compares satisfactorily with the exact solution.

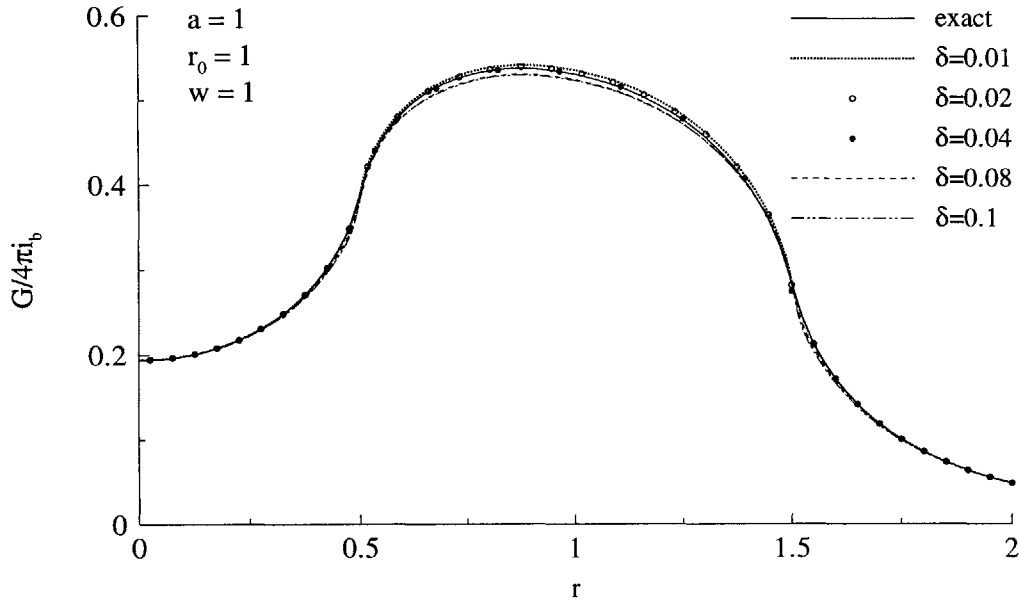


Figure 7-10: Exact vs. approximate solutions of G for $a = 1, \delta = 0.01, 0.02, 0.04, 0.08, 0.1$.

7.8.1 Convergence

The accuracy of the discrete source method depends on the "optical core radius" of the computational element, i.e. $\bar{a}\delta$. According to the model, accuracy is expected to improve as $\bar{a}\delta$ departs from unity, i.e. $\bar{a}\delta \ll 1$ or $\bar{a}\delta \gg 1$. On the other hand accuracy is expected to be least when $\bar{a}\delta \sim 1$. To prove that the model behaves as expected, we solve for the irradiance induced by the isothermal ring of square cross section, see Figure 7-8 for the schematic. The results are presented in Figures 7-10 and 7-11, corresponding to values of a of 1 and 5 respectively. In Figure 7-10, where $a = 1$, radial profiles of the irradiance at $z = 0$ are plotted for different core sizes of the computational elements. Numerical results shows a satisfactory agreement with the exact solution for all selected values of δ . This behavior is expected since $a\delta \ll 1$ for all selected core sizes. Departure of the numerical solution from the exact solution, however, shows in Figure 7-11, where $a = 5$, as the core size increases ($\delta = 0.08, 0.1$ for example). In this case, the optical core radius $a\delta$ is of the order of unity ($a\delta = 0.4, 0.5$). Convergence to the exact solution occurs as δ decreases, which corresponds to $a\delta \ll 1$.

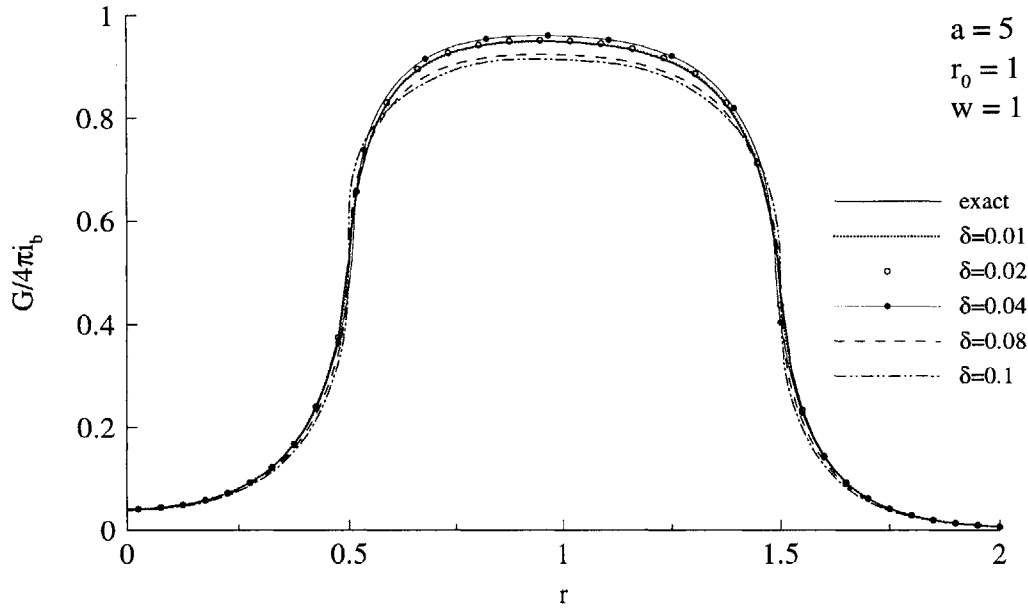


Figure 7-11: Exact vs. approximate solution of G for $a = 5, \delta = 0.01, 0.02, 0.04, 0.08, 0.1$.

7.9 Example II

Even though the example presented above provides the validation required for the suggested model, it was based on the assumption that the absorption coefficient is uniform in space and that the volume of gas considered has a uniform temperature that is higher than that of the cold surrounding. A more realistic example would obviously be that of a medium associated with a temperature distribution within and correspondingly variable absorption coefficient. Here we consider methane fuel ring, Figure 7-12, that is reacting with the atmosphere.

The objective is to determine the radiation source distribution. The reaction is assumed to be single-step and to proceed at an infinite rate: $CH_4 + 2(O_2 + 3.76N_2) \rightarrow CO_2 + 2H_2O + 7.52N_2$. Based on a one dimensional model, the corresponding species distributions are shown in Figure 7-13.

The absorption coefficient is obtained according to the following equation[70]:

$$a(T) = \sum_{f,o,p,d} a_{p,i}(T)p_i \quad (7.21)$$

where i corresponds to a species, and $a_{p,i}$ is the Plank-mean absorption coefficient of species

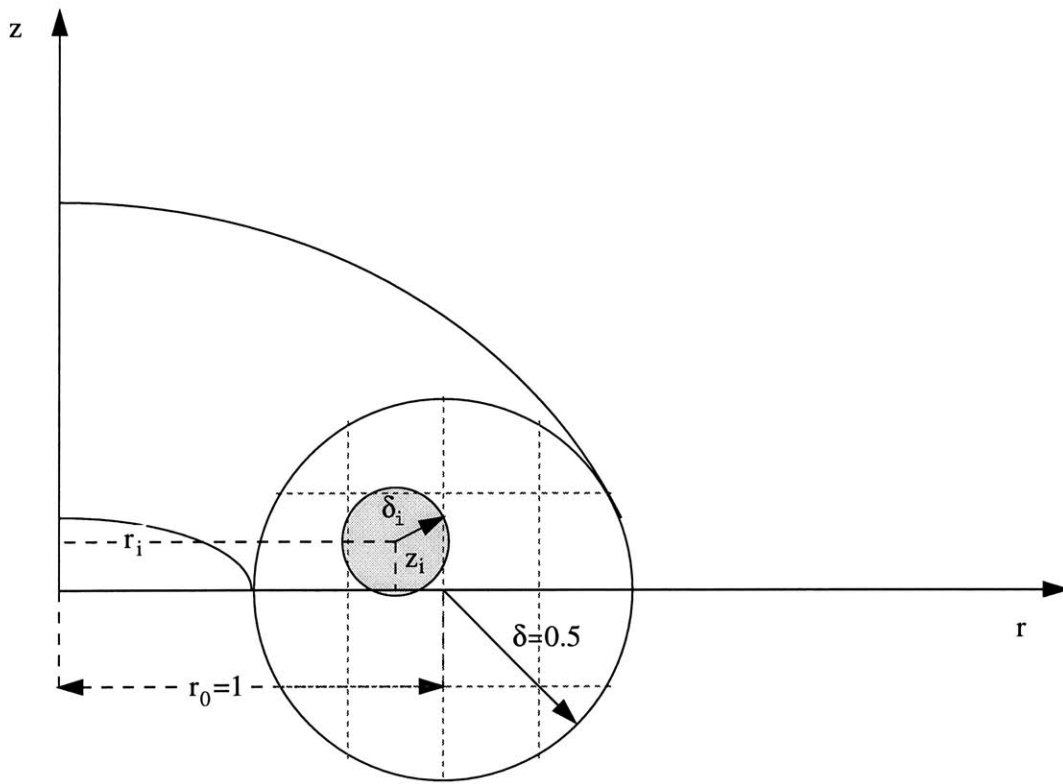


Figure 7-12: Schematic for example II.

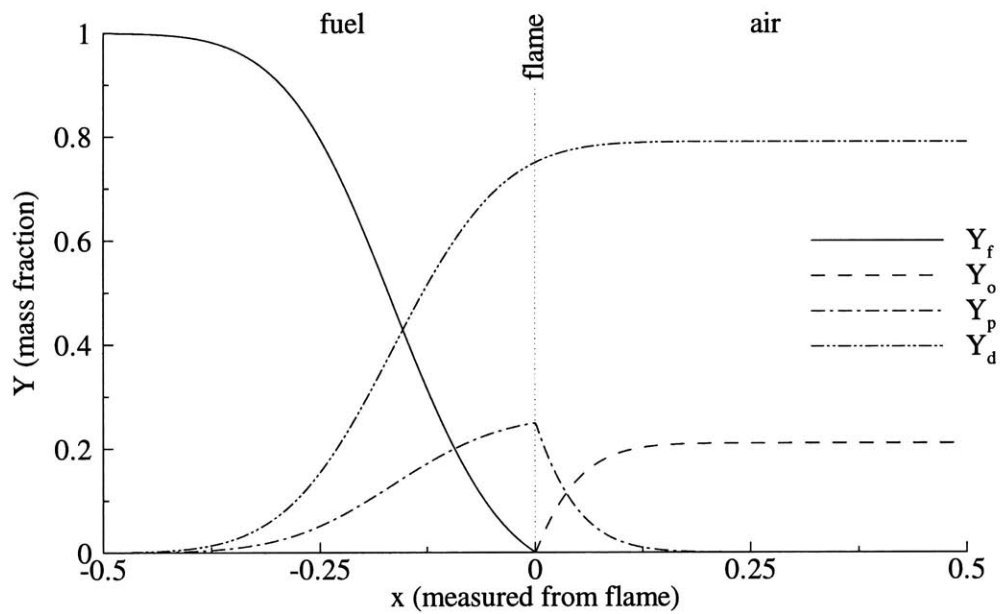


Figure 7-13: Species distributions of 1-D diffusion flame.

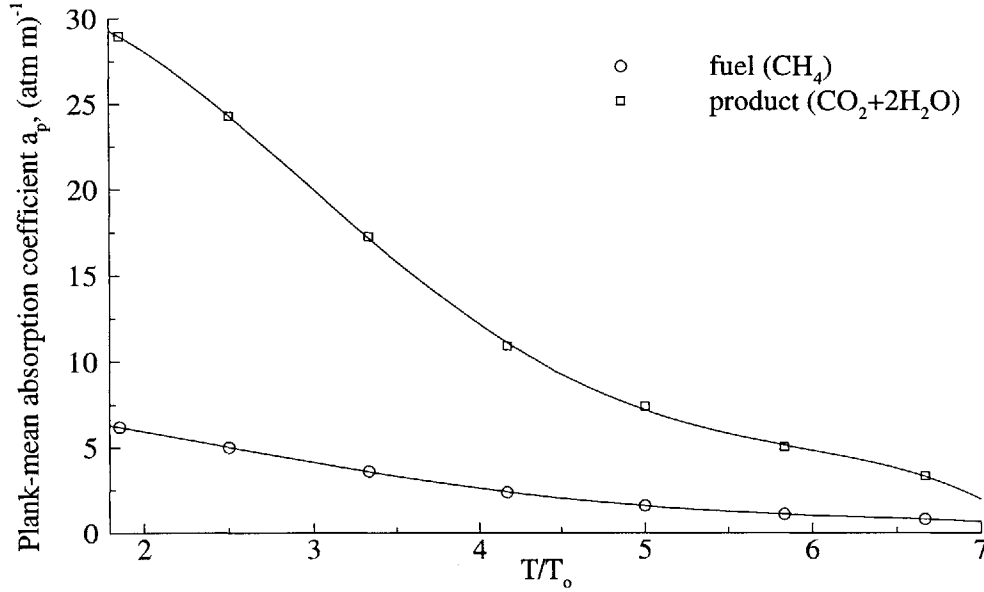


Figure 7-14: Dependence of the Plank-mean absorption coefficient on temperature [91].

i , and p_i is the partial pressure of the species. The Plank-mean absorption coefficient is defined as

$$a \equiv \frac{\int_0^\infty i_{b\eta} a_\eta d\eta}{\int_0^\infty i_{b\eta} d\eta} \quad (7.22)$$

where η is the wavenumber, $i_{b\eta}$ is the Plank function, and a_η is the spectral absorption coefficient.

The temperature dependence of a_p for the various species, obtained using narrow band averaged values for the absorption coefficient[91], is presented in Figure 7-14. The absorption coefficient of air is negligible for the range of temperature we are interested in.

The temperature and absorption coefficient distributions we select for our example are presented in Figure 7-16. These distributions are based on the 1-D distributions.

The exact solution for the divergence of the heat flux is based on direct numerical integration of equation 7.5. The numerical parameters were selected along the same lines discussed in Example I. In obtaining the discrete source method solution, three sizes of computational elements were used: $\delta = 0.01, 0.02$ and 0.04 . As mentioned before, the effective attenuation coefficient was obtained using equation 7.8. The results are presented in Figure 7-17. The solutions obtained using the discrete source method agree well with

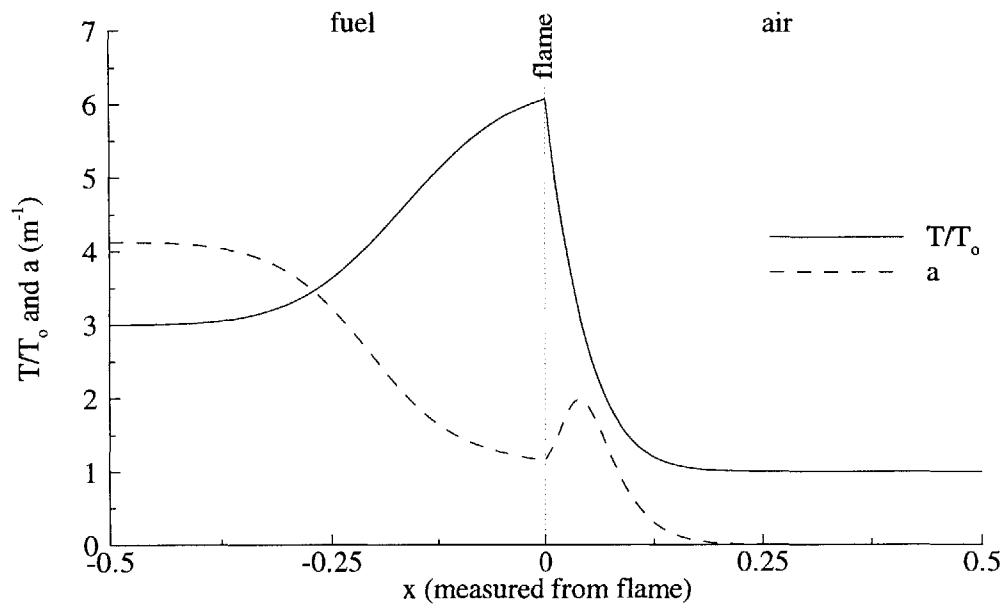


Figure 7-15: Temperature and absorption coefficient distribution of the 1-D flame.

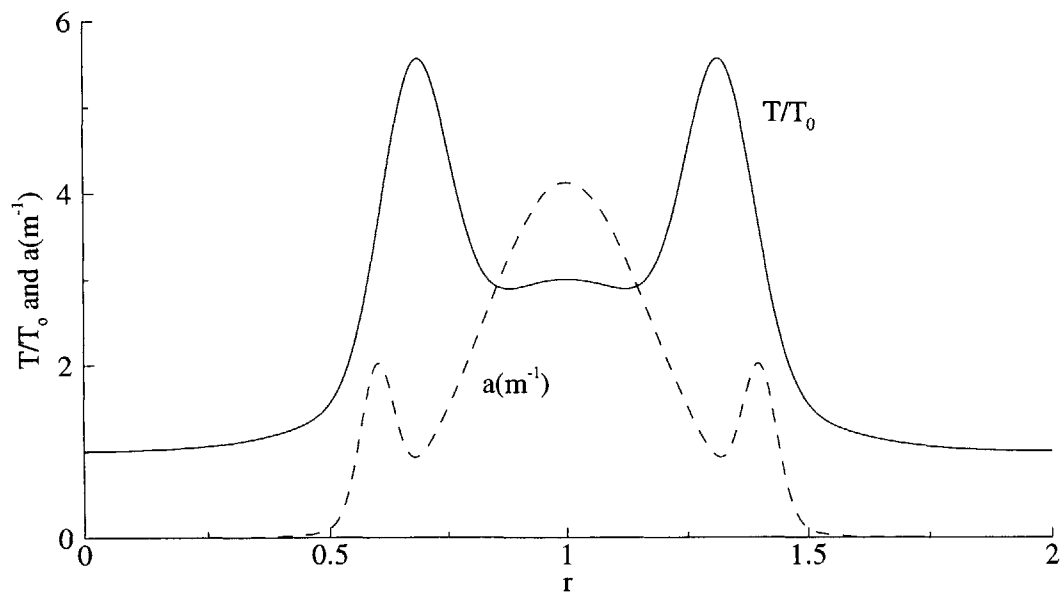


Figure 7-16: Temperature and absorption coefficient distributions used in Example II.

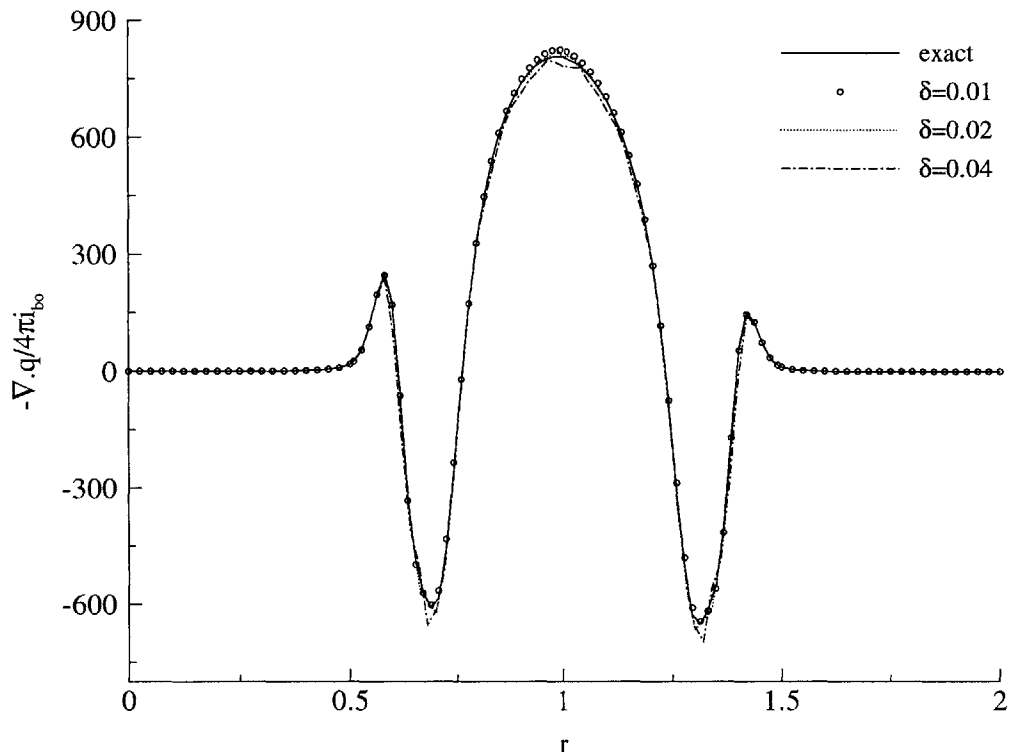


Figure 7-17: Radiation source distribution for Example II.

the exact solution for the element sizes used. The slight deviation for the case of $\delta = 0.04$ is due to assumption involved in evaluating the effective attenuation coefficient, i.e. when evaluating the inner integral of equation 7.5, we assume that the source element is represented by its center ($s' = 0$).

7.10 Conclusion

A grid-free Lagrangian scheme for calculating the radiative source term in the energy equation has been presented. The Discrete Source Method is compatible with the vortex and transport element methods. The solution is presented in terms of "Biot-Savart" summation over a collection of elements discretizing the domain. The field induced by each element is expressed in two forms depending on the "optical thickness" of the element, and the fields can be obtained from analytical expressions or a tabulated integral in two dimensions. In three dimensions, only analytical expressions are used, equations 7.9 and 7.10. An attrac-

tive feature of the method is the use of the concept of "effective attenuation coefficient" which proved to be a useful tool of analysis.

Chapter 8

Computations of Isothermal Buoyant Plumes

Abstract

Numerical investigation of the pulsation frequency of an axisymmetric isothermal buoyant plume was conducted for various ranges of pool diameter, initial velocity, and Reynolds number¹. The effect of pool diameter on the pulsation frequency was shown to match the experimental data in the literature over the corresponding pool diameter ranges. A similar correlation has been obtained for the Strouhal number as a function of the inverse Froude number, for a Froude number range of 5×10^{-5} to 0.27. The effects of the Reynolds number on the puffing frequency has also been investigated for a Reynolds number range of 50 to 700. No vortical structures formation was observed for low values of Reynolds number, when the flow is laminar. However, periodic shedding of vortical structures has been observed once the transition to turbulence is established for higher values of Reynolds number, and the corresponding variation of the puffing frequency was found to be small. Finally, the effect of initial velocity was investigated for various pool diameters. The critical velocity needed to initiate pulsation was shown to decrease significantly as the pool diameter increases. The influence of the initial velocity on the pulsation frequency for a certain pool diameter was proven to be weak for low values of Froude number.

8.1 Introduction

The periodic motion observed near the surface of an axisymmetric pool fire has recently gained much attention and has been investigated experimentally, theoretically, and analyzed dimensionally. It has been related to the formation of large scale vortical structures whose size is of the order of the pool diameter, and is believed to affect the rate of entrainment of

¹based on pool diameter and buoyancy characteristic velocity.

ambient air into the combustion zone. As a result, the periodic shedding of these structures influences the downstream behavior of the flame in terms of the combustion efficiency, the flame height fluctuations, and the radiation field which is essential in determining the fuel velocity at the pool surface.

The objective of this study is to investigate numerically the effect of the pool diameter and the initial fuel velocity on the pulsation frequency for a non-reacting buoyant plume, and comparing the numerical results obtained with experiments. The numerical method used is the vortex element method described in Chapter 3. The transport element method, discussed in section 3.3, is used for scalar transport. The core spreading method is used for diffusion. For the case of an isothermal plume, the scalar transported is the inverse of the density, $1/\rho$, governed by

$$\frac{D}{Dt} \left(\frac{1}{\rho} \right) = \frac{1}{ReSc} \nabla^2 \left(\frac{1}{\rho} \right) \quad (8.1)$$

where the Schmidt number is $Sc = \nu/\mathcal{D}$, ν is the kinematic viscosity and \mathcal{D} is the mass transport coefficient²

Experimental studies have been conducted by many investigators for both the reacting and the non-reacting cases, and various visualization and measurement techniques have been used to collect data on the time dependent flow. For the reacting case, these studies have shown that the puffing frequency, f , depends strongly on the pool diameter, D , according to $f \sim D^{-0.5}$, for a wide range of pool diameter and fuel type, as shown in Figure 1a, leading to the conclusion that this correlation arises mostly from the fluid mechanics of the problem rather than the combustion chemistry. This observation has been suggested by Weckman et al.[98], and has been proven experimentally by Cetegen et al.[11], and Hamins et al.[41]. The latter covered a wider range of pool diameters, and showed that the puffing frequency and the pool diameter follow the above relation. They also showed that the Strouhal number, $St = fD/V_0$, where V_0 is the outward fuel velocity at the pool surface, is related to the Froude number, $Fr = V_0/\sqrt{gD}$, where g is the gravitational acceleration, for both the reacting and non-reacting cases over a wide range of Fr , according to the relation $St \sim 1/Fr^m$, where $m = 0.57$ for the reacting case, and $m = 0.38$ for the non-reacting case, as shown in Figure 1b. The importance of the Strouhal and Froude numbers

²Equivalently, we could have assumed air rising at a high temperature, $\rho_f T_f = \rho_0 T_0$, in which case the energy equation leads to a similar equation, with $1/RePr$ instead of $1/ReSc$. However, unlike the isothermal case, there is volumetric expansion in this alternative formulation.

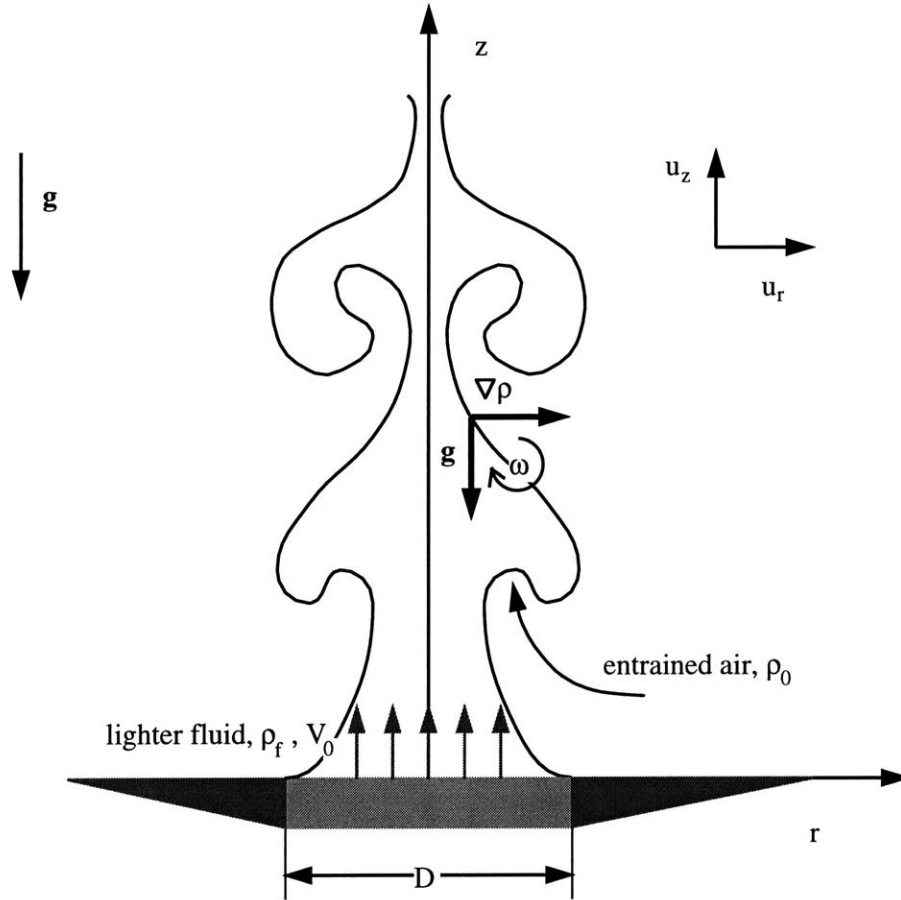


Figure 8-1: Schematic.

have been investigated by Emori and Saito[29] in their dimensional analysis of the puffing frequency of pool fires. It has further been shown by Hamins et al.[41] that the burner exit fuel velocity has a small but finite influence on the puffing frequency, with this influence being negligible for some diameters, provided that the exit velocity is larger than the critical velocity required to initiate pulsation for a certain pool diameter.

The nature of organized vortical structures in reacting and non-reacting buoyant plumes and the associated driving mechanism have not been fully investigated yet. This will be discussed in the next chapter.

8.2 Numerical Parameters and assumptions

A schematic of the plume is shown in Figure 8-1. We consider the rise of a lighter fluid (or fuel of density ρ_f) into the atmosphere (of density ρ_0). The flow is assumed axisymmetric and isothermal. Both the lighter fluid and air are assumed ideal gases, with constant and

equal mass transport coefficients and kinematic viscosities. It is assumed further that the Schmidt number is unity.

The numerical parameters are selected as follows: the spatial discretization, $h = 0.02$, the time step, $\Delta t = 0.02$, the initial core radius, $\sigma_0 = 1.3h$, and the number of material lines, $n_L = 1$. The most restricting is representing the scalar gradient and the vorticity by a single material line. However, for the numerical measurement of the pulsation frequency, it proved to be enough. For all the cases, the number of time steps was 5000, over which the velocity history shows the formation of a considerable number of vortical structures for unbiased estimation of the pulsation frequency.

The cases investigated, shown in table 8.1, cover wide ranges of pool diameter, Froude number, and Reynolds number. The air to fuel density ratio was kept constant for all cases, $\rho_0/\rho_f = 7.075$. Notice that a necessary condition for buoyancy to dominate the inertia is $Fr < 1$.

Data set	D (m)	V_0 (m/s)	ν (m^2/s)	Fr	Re
1	0.01 – 50	0.1627	$4.47 \times 10^{-6} - 1.5811$	$0.27 - 5.4 \times 10^{-5}$	700
2†	0.01 – 0.1	0.3	0.0001414	0.9184 – 0.09184	22.135 – 700
3	1	0.5146	0.0626 – 0.00447	0.027	50 – 700
4†	0.025	0.05 – 0.4	0.0001414	0.01 – 0.653	87.5
5†	0.05	0.0005 – 0.5	0.0001414	$5.1 \times 10^{-7} - 0.51$	247.48

† Kinematic viscosity corresponds to Helium.

Table 8.1: Parameter values used in numerical simulation.

8.3 Results and discussion

The time history of the horizontal velocity component at a specific location is used to estimate the frequency of oscillation which corresponds to that of the vortical structure formation. The location³ selected was at $r = 0.4D$ and $z = 0.8D$. The frequency is obtained using the “Welch” method of power spectrum estimations. This method involves the application of Fourier transform with smoothing and averaging so that more reliable spectral estimates can be obtained. The frequency associated with a certain velocity history is shown as a plot of the power spectral density ($(m/s)^2/Hz$) versus the frequency (Hz), with the area

³Experiments show that vortical structure forms within a pool diameter above the pool base

under each peak representing the energy of the signal. A typical power spectrum is shown in Figure 8-2, where the dominant frequency is 7 Hz because it is associated with the highest energy.

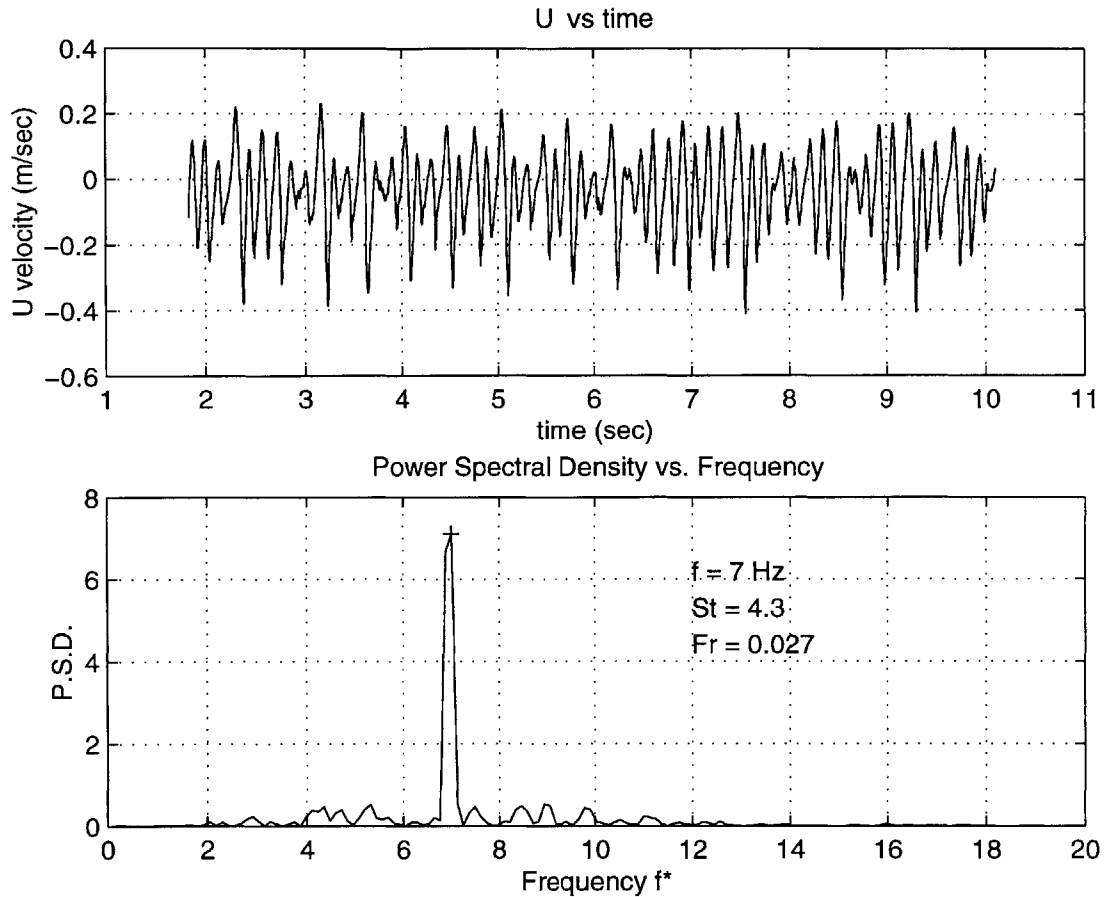


Figure 8-2: frequency

8.3.1 Effect of pool diameter

In data set 1, the Froude number was varied by varying the diameter while keeping the outflow velocity constant. The Reynolds number is kept constant by varying the kinematic viscosity accordingly. Figure 8-3 shows log-log plot of the pulsation frequency against the pool diameter. A strong dependence is apparent and a power fit yields $f \sim D^{-0.7}$,

represented by the dashed line. Experiments were conducted by Hamins et al.[3] for an isothermal buoyant stream of helium for diameters = 0.025, 0.035, 0.05, 0.075, and 0.1 m with Froude number in the range of 10⁻³ - 1 and Reynolds number based on V_0 in the range of 1 - 100. These experiments yielded a Strouhal-Froude number relation in the form:

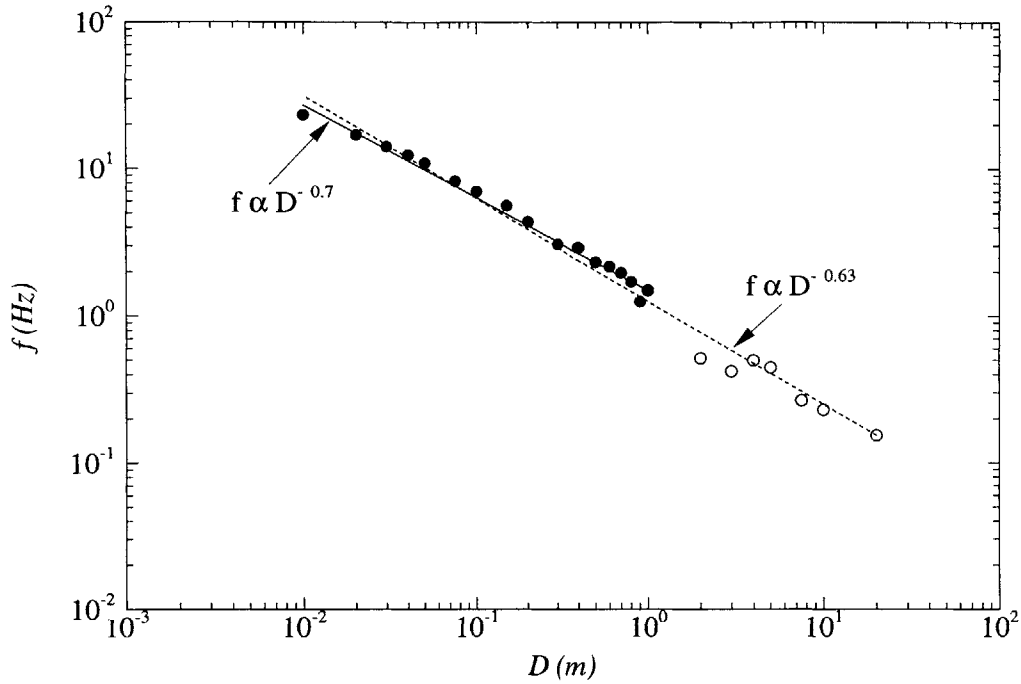


Figure 8-3: Dependence of pulsation frequency on pool diameter.

$St \sim Fr^{-0.38}$, corresponding to a frequency-diameter relation of $f \sim D^{-0.62}$. Restricting the diameter range to 0.01 - 1 m yields the correlation $f \sim D^{-0.63}$, represented by the solid line in figure 8-3.

Figure 8-4 displays a plot of the Strouhal number against the inverse of Froude number, with a power law fit of $St \sim Fr^{-0.37}$ for the diameter range mentioned. A simple comparison between the current results and the experimental measurements of Hamins et al.[41] is shown in table 8.2. The above comparison shows that at low Froude number, the pulsation frequency is strongly dependent on the pool diameter and the influence of other parameters such as Reynolds number, initial velocity, and fluid viscosity is weaker.

Data set 2 corresponds to varying the pool diameter, while keeping all other parameters constant. Thus reduction in the pool diameter reduces both the Froude and Reynolds numbers. Helium is the working fluid. The outflow velocity is 0.3 m/s. The diameter ranges from 0.01 - 0.1 m, and consequently the Reynolds number ranges from 22 to 700 and Froude number from 0.91 to 0.091. Thus, the condition for buoyancy to be dominant, $Fr \ll 1$, does not apply for all the above cases. The effect of this deviation is shown in

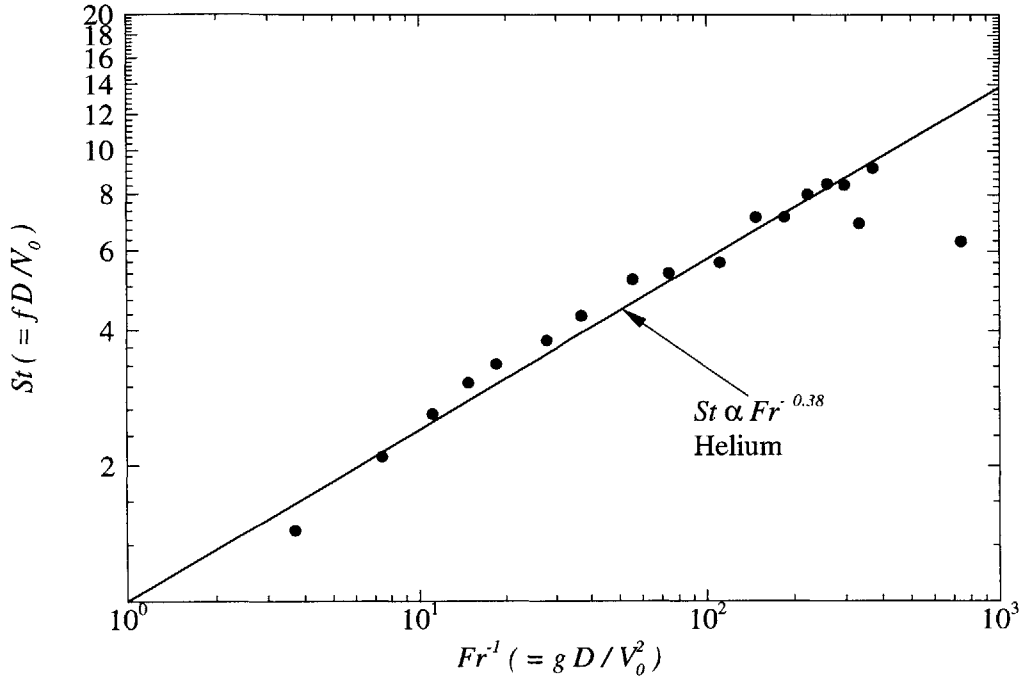


Figure 8-4: Dependence of Strouhal number on Froude number, $Re = \text{constant}$.

Figure 8-5, where the Strouhal number frequency is plotted against the Froude number, where the arrow along the dashed line indicates increase in Reynolds number and thus decrease in the momentum. The solid line and symbols represent data set 1. It is apparent that the two plots approach each other as D increases, or Fr decreases. For $D > 0.05$ m, or $Fr < 0.18$, the difference between the two curves is less than 15 % and reaches 5 % at $Fr = 0.091$. The considerable difference between the two curves for relatively high values of Froude number is expected since the fuel-air shear layer near the pool and the air entrainment mechanism become more dominated by the forced velocity field rather than buoyancy.

8.3.2 Effect of Reynolds number

In data set 3, for a diameter of 1 m and an initial velocity of 0.5146 m/s, Reynolds number, $Re = D\sqrt{gD}/\nu$ is varied from 50 to 700 by changing the kinematic viscosity. The corresponding value of the Froude number is 0.027. A plot of the Strouhal number against Reynolds number is shown in figure 8-6.

	Current Study	Hamins et al.
Working Fluid	arbitrary	Helium
Diameter range	0.01 - 1.0 m	0.025 - 0.1 m
$Re = D\sqrt{gD}/\nu$	700	87.5 - 700
$Re_{V_0} = DV_0/\nu$	36.37 - 363.7	1 - 100
Fr	$0.27 \times 10^{-2} - 0.27$	$10^{-3} - 1$
$f - D$ relation	$f \sim D^{-0.63}$	$f \sim D^{-0.62}$
$St - Fr$ relation	$St \sim Fr^{-0.37}$	$St \sim Fr^{-0.38}$

Table 8.2: Comparison between current study and the experiment done by Hamins et al.

For $Re < 225$, the flow is stable and no formation of vortical structures is observed. For $Re \sim 225$, vortical structures start to appear with the instability becoming stronger for higher values of Re . The Strouhal number for $Re \geq 400$ ranges from 4.0 to 4.2, indicating that the Reynolds number has a weak influence on the pulsation frequency once transition has been established.

8.3.3 Effect of outflow velocity

The effect of varying the outflow velocity on the periodic formation of the vortical structures has been investigated for $D = 0.025$, and 0.05 m corresponding to data sets 4 and 5 respectively. In either case, it was observed that there exists a critical outflow velocity, V_c , below which no instability was observed. For $D = 0.025$ m, $V_c = 0.2m/s$. For $D = 0.05m$, periodic shedding of vortical structures is observed for the entire velocity range. This implies that the critical velocity V_c is less than 0.0005 m/s. It can be concluded from the above that for relatively large pool diameters, the critical initial velocity required to initiate shedding of vortical structures is very small. The smaller the pool diameter is the larger is V_c .

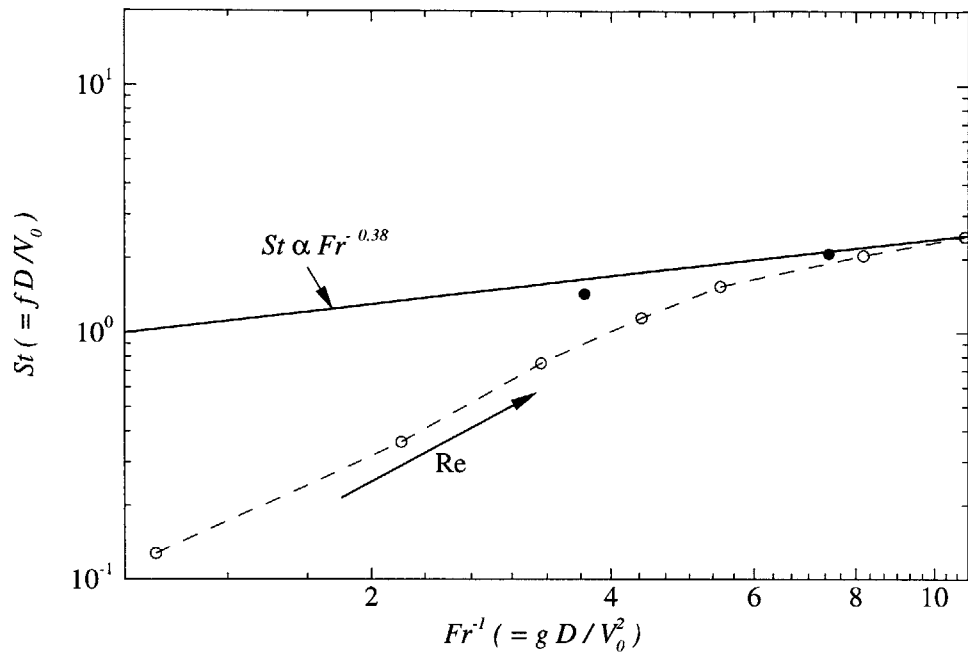


Figure 8-5: Impact of reducing the pool diameter.

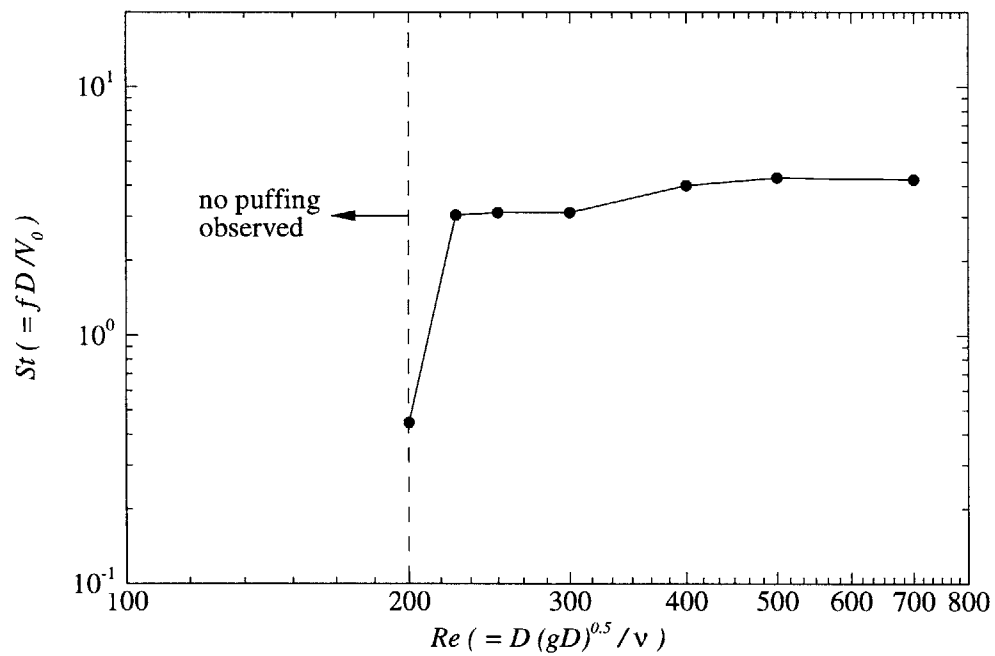


Figure 8-6: Dependence of Strouhal number on Reynolds number, $Fr = \text{constant}$.

Chapter 9

Computation of Fire Plumes

Abstract

In this chapter, numerical simulation of an axisymmetric fire plume is presented. A schematic is presented in Figure 9-1. The vortex method is used to compute the flow field, given the fuel velocity at the pool surface. The transport element method is used to transport the scalars. The chemical reaction is assumed to be infinitely fast and Shvab-Zel'dovich variables are used to reduce the combustion formulation to a single transport equation. Radiative transport is approximated by reducing the enthalpy of reaction. At the edge of the pool, computational elements, discretizing the mixture fraction gradient within the fuel-air interface, are injected with zero circulation. This assumption is based on the fact that a fire is buoyancy dominated; the Froude number is smaller than unity.

Numerical results show that the plume dynamics are dominated by the shedding of large vortical structures, of size of the order of the pool diameter, which originate within a pool diameter above the pool. Vorticity generation is mainly due to the interaction between radial density gradient and gravity. While the formation rate of vorticity is buoyancy dominated, the instability resembles that of the Kelvin-Helmholtz type. The structures appear to control the entrainment process, and burning occurs on their outer edges, with zones of high fuel concentration inside. The flame diffusion thickness, except for zones of intense strain close to the large eddies, increases gradually from the pool edge upwards. The fuel is pinched off the rising plume in large puffs as the entrained air reaches the plume centerline, causing the flame height to oscillate at the same frequency as the shed structures.

Numerical Predictions of the puffing frequency, averaging flame height and oscillations, and motion of the large structures are compared with experimental data.

9.1 Introduction

Large fires occur when a large supply of fuel which may be in the form of oil spill, an oil well, a dense forest, etc., is ignited. Besides their danger to human life and material, massive fires represent an environmental hazard, especially when they are induced for the purpose of cleaning up fuel spills or disposing of unwanted debris. In such cases, the composition of the combustion products, the soot concentration and the amount of unburned or partially

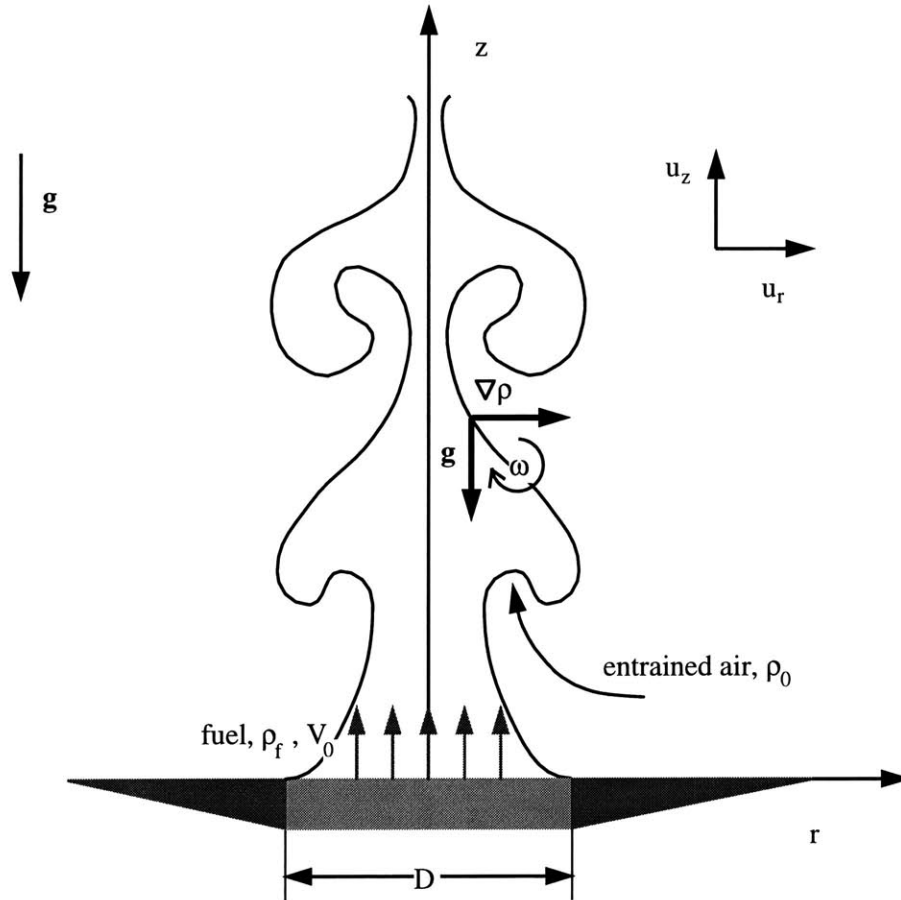


Figure 9-1: Schematic.

burned fuel injected into the atmosphere is of major concern. Since fires are naturally ventilated combustion phenomena, product formation in the reaction zone depends strongly on the local flow field established, and the amount of air entrained into the flame zone. Thus, the problem of determining the burning rate and the fire impact on the environment becomes strongly tied to determining the flow and combustion field in the neighborhood of the fuel pool.

Experimental investigation[41, 12, 103, 104] of laboratory fires, which maintain the characteristics of massive fires, has been conducted over a range of parameters for the purpose of investigating their dynamics and the factors determining the composition of their products. Experimental and numerical studies¹ [36, 60, 69] have shown that a large fire possesses persistent dynamics which can be characterized by the shedding of large burning structures near the pool. The formation of these structures is believed to impact

¹Including the present study.

the entrainment and hence the burning rate and products composition strongly.

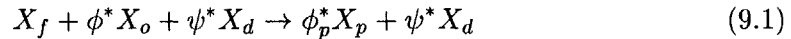
Due to the complexity involved in modeling these interactions, simplifications² are made in terms of modeling chemistry and accounting for radiative losses.

In the previous chapter, the flow in an isothermal plume was computed using the vortex method. Results of this formulation showed good agreement with experimental results on non-reacting plumes. In this chapter, combustion is introduced using an infinite rate formulation of the chemical reaction. The dynamic effects of combustion, including volumetric expansion and vorticity generation were also included in the formulation. To account for the effect of radiation, including heating the fuel pool and reducing the heat added to the plume, the enthalpy of reaction was reduced by 35% of its adiabatic value. In this chapter, we report on this infinite chemistry results of fire plume simulations, and focus on the entrainment field created by the formation of the large scale structures.

The chapter is organized as follows. Assumptions are stated in section 9.2. The governing equations are presented in section 9.3. The vortex-element method, the basis for computing the buoyant fluid mechanics, is discussed in Section 2. The transport-element method, which is used to compute the transport of non-reacting and reacting scalars, is presented in Section 3. An example is presented and analyzed in Section 4. Conclusions and suggestions for future work are summarized in Section 5.

9.2 Assumptions

- The fuel pool is circular and homogeneous, the surrounding is unbounded with no cross wind: the coordinates used are the axisymmetric cylindrical coordinates.
- The chemical reaction is assumed to be single-step and irreversible and to proceed at an infinite rate according to



where X is species, f stands for fuel, o for oxidizer, p for product, and d for diluent, and ϕ^* ($= n_o/n_f$) is the molar stoichiometric coefficient while ψ^* ($= n_d/n_f$) is the

²These simplifications will be stated later in this section.

diluent/oxidant molar fraction.

- Radiative loss is accounted for by reducing the the enthalpy of reaction by 35% of its adiabatic value.
- Lewis number for the various chemical species is equal to unity.
- Prandtl number is equal to unity.
- Low Mach number compressible flow.
- Reynolds number is constant.
- Non stratified atmosphere.
- The fuel outflow velocity at the pool surface is constant and small enough such that inertia is negligible compared to buoyancy.
- Baroclinic vorticity generation is ignored.

9.3 Governing Equations

The fire plume flow field is largely inviscid, turbulent and unsteady. Except for the ground, it is unbounded. Accordingly, and based on the assumptions stated above, the equations³ governing conservation of mass, momentum, energy, and chemical species, written in dimensionless form, are respectively:

$$\frac{D\rho}{Dt} + \rho \nabla \cdot \mathbf{u} = 0 \quad (9.2)$$

$$\frac{Du_r}{Dt} = -\frac{1}{\rho} \frac{\partial \rho}{\partial r} + \frac{1}{Re} \left(\nabla^2 u_r - \frac{u_r}{r^2} \right) \quad (9.3)$$

$$\frac{Du_z}{Dt} = -\frac{1}{\rho} \frac{\partial \rho}{\partial z} + \frac{1-\rho}{\rho} + \frac{1}{Re} \nabla^2 u_z \quad (9.4)$$

$$\frac{DT}{Dt} = \frac{1}{Pe} \nabla^2 T + Q \frac{W}{\rho} \quad (9.5)$$

³Presented for the sake of completion.

$$\frac{DY_k}{Dt} = \frac{1}{Le_k Pe} \nabla^2 Y_k + \Lambda_k \frac{W}{\rho} \quad (9.6)$$

where the velocity $\mathbf{u} = (u_r, u_z)$ is nondimensionalized with respect to $U = \sqrt{gD}$, g and D are the gravitational acceleration and the pool diameter, respectively. The Reynolds number is $Re = DU/\nu$, ν being the kinematic viscosity. The density, ρ , is nondimensionalized with respect to the ambient density ρ_0 . The difference between the local pressure and the atmospheric pressure, p , is nondimensionalized with respect to $\rho_0 g D$. The heat release is $Q = \Delta h_{r,f}/c_p T_0$, while $\Delta h_{r,f}$ and W are the enthalpy of reaction per unit of fuel mass and rate of reaction, respectively, Y_k is species mass fraction, $k = f, o, p$ and d . $\Lambda_f = -1$, $\Lambda_o = -\phi$, $\Lambda_p = 1 + \phi$, $\Lambda_d = 0$, ϕ and ψ are the mass stoichiometric coefficients of the oxidizer and diluent, respectively. The temperature, T , is nondimensionalized by the ambient temperature T_0 . The thermal diffusivity, Peclet and Lewis numbers are, respectively: $\alpha = \lambda/\rho c_p$, $Pe = DU/\alpha$, $Le_k = \alpha/D_{d,k}$, where λ is the thermal conductivity, c_p is the constant pressure specific heat, $D_{d,k}$ is the mass diffusion coefficient of species k . The ideal gas law in dimensionless form is given by: $\rho T = \bar{M}$, where $\bar{M} = 1/\sum_k (Y_k/M_k)$, M_k is molecular mass of species k , and \bar{M} is the average molecular mass. Variables are nondimensionalized with respect to values on the oxidizer side.

9.3.1 Boundary conditions

The boundary conditions are:

At infinity:

$$\omega_{\mathbf{r} \rightarrow \infty} = 0 \text{ and } s_{\mathbf{r} \rightarrow \infty} = s_0. \quad (9.7)$$

At axis of symmetry:

$$\omega_{r=0} = 0 \text{ and } \left(\frac{\partial s}{\partial r} \right)_{r=0} = 0. \quad (9.8)$$

At the ground, except for the pool, the normal velocity is zero; at the pool the velocity is prescribed:

$$u_z(z = 0, r > 1/2) = 0 \text{ and } u_z(z = 0, r < 1/2) = w_0 \quad (9.9)$$

Boundary conditions 9.7 and 9.8 are naturally satisfied since the core function used is the solution of the diffusion equation. Boundary condition 9.9 is satisfied by the treatment of the potential velocity component discussed in sections 3.5.1 and 6.3.

9.4 The vortex method

The equation governing the time evolution of the circulation of an element i , obtained by integrating the vorticity equation over the physical area of the element, A_i , is

$$\frac{D\Gamma_i}{Dt} = \frac{A_i}{\rho_i} \left[\left(1 + \frac{Du_z}{Dt} \right) \frac{\partial \rho}{\partial r} - \frac{Du_r}{Dt} \frac{\partial \rho}{\partial z} \right]_i + \frac{\delta A_i}{Re} \left(\nabla^2 \omega - \frac{\omega}{r^2} \right), \quad (9.10)$$

where the vorticity $\omega \equiv \nabla \times \mathbf{u} = \omega \hat{\boldsymbol{\theta}}$, $\hat{\boldsymbol{\theta}}$ being the unit vector in the azimuthal coordinate. It is assumed in equation 9.10 that the generation is uniform over the physical area of the element.

The circulation equation is solved in three steps: (i) convection, (ii) generation, and (iii) viscous diffusion. In the convection step, the elements are convected such that $d\Gamma_i/dt = 0$. In the generation step, the circulation of an element is updated according to equation 9.10 without the diffusion term. In the diffusion step the core spreading method, discussed in section 5.4, is used. The core function, assumed the same for both vorticity and scalar, is assumed to correspond to the Green's function of the diffusion equation in two dimensional Cartesian coordinates

$$\phi_\sigma(\mathbf{r}, \mathbf{r}_0) = \frac{1}{\pi\sigma^2} e^{-\frac{(r-r_0)^2 + (z-z_0)^2}{\sigma^2}}, \quad (9.11)$$

where σ is the core radius. The density and its gradients are obtained using the transport-element method described in section 4.3.

The vorticity field is modeled as a collection of vortex elements distributed along a number of layers initially placed at the interface between the fuel and oxidizer. These elements are transported in time according to $d\mathbf{r}/dt = \mathbf{u}$, where \mathbf{r} is the location of a computational element and the velocity \mathbf{u} is obtained from the Helmholtz decomposition discussed in chapter 6. Once the elements locations are found, the circulation is updated using equation (9.10).

The connectivity between the elements describing a layer, and the condition that the distance between neighboring elements must not exceed the core radius, are maintained by inserting elements whenever two neighboring elements move further apart due to stretching. The core overlap must always be maintained by choosing the core radius to be larger than the distance between neighboring elements to guarantee the smooth distribution of the computed vorticity field. Insertion of an element is performed such that circulation and

its first moment are conserved and that the distance separating neighboring elements is of the order of the initial spatial discretization [56, 35]. For an element at a certain location and of a length $|\mathbf{l}|$, the physical area A and the element thickness $|\mathbf{n}|$ are updated via the conservation of mass. In the case of buoyancy-driven plume, the initial circulation for all the elements is zero since inertia effects are negligible. The initial velocity field is the potential field induced by the outflow at the pool surface.

9.5 Example

The parameters for this example are:

1. the Froude number, $Fr = w_0^2/gD = 0.01$, where w_0 is axial velocity at pool surface,
2. the buoyancy-based Reynolds number is 700,
3. the mass stoichiometric ratio, $\phi = 4.0$,
4. the heat of reaction normalized by the initial temperature and specific heat, $Q = 70$.

The initial and boundary conditions are:

1. the fuel-air density and temperature ratios are: $\rho_f/\rho_0 = 0.1975$, $T_f/T_0 = 3.0$,
2. on the fuel side: $Y_f = 0.9$, $Y_o = 0.0$, $Y_p = 0.1$, and $Y_d = 0.0$,
3. on the air Side: $Y_f = 0.0$, $Y_o = 0.2$, $Y_p = 0.0$, and $Y_d = 0.8$.

The fuel considered is methane, and the molar masses are taken to correspond to methane-air mixture: $M_f = 16$, $M_o = 32$, $M_d = 28$, and $M_p = 26.62$. The heat of reaction is reduced from its adiabatic value to account for incomplete combustion and radiative losses, and the fuel temperature at the pool surface is taken to account for intense radiative heating of the evaporated methane.

The interface between the fuel and air is represented using 9 layers of elements. The average length of an element along a layer is 0.02 (nondimensionalized with respect to the pool diameter). The unsteady calculation proceeded with a time step of $\Delta t = 0.02$.

9.5.1 The early stages and the mushroom

During the transient stage between the onset of the simulation when the interface is horizontal and the time the flow reaches a stationary state, the interface between the fuel and air, i.e. the flame, rises to form the familiar mushroom cloud observed in buoyant flows. Although the rising horizontal interface is, in principle, Rayleigh-Taylor unstable, no sign of instability growth is observed and instead, it is convex towards the outside. On the other hand, the vertical surface of the plume, where the density gradient is perpendicular to gravity, is where all the vorticity is generated. The vertical vortex sheet, or sleeve since the flow is axisymmetric, rolls up close to the leading edge of the plume. Thus, the underlying flow leading to the formation of this mushroom is a strong vortex ring structure which forms at the leading edge of the rising plume. The ring forms as the vorticity generated along the rising interface spirals around a common center.

Vorticity is generated by the action of the gravity acting on the rising vertical interface[36]. Vorticity generation is best explained using equation 9.10. As mentioned before, the baroclinic term, corresponding to vorticity generation due to interaction between the density gradient and the hydrodynamic pressure gradient, was not included in the calculation so as to investigate the impact of the interaction between the density gradient and the gravity term. The baroclinic term is expected to play a secondary role to the gravity term.

The formation of the spiral appears to be due to the growth of an intrinsic instability along the vertical vortex layer of the Kelvin-Helmholtz type. There is another form of instability in this flow; it is the Rayleigh-Taylor instability of the initial horizontal interface between the fuel and air. As mentioned before, the mushroom appears to be a consequence of the action of the Kelvin-Helmholtz instabilities acting on the vertical vortex sheet. As the mushroom rises above the pool a distance of several pool diameters, the vertical interface rolls up again to forms new vortex rings near the pool. Eventually, the effect of the initial mushroom on the flow near the pool surface becomes negligibly weak (in the computations, as the entire mushroom passes through the exit boundary of the domain, which is located 5 – 6 plume diameters downstream, it is deleted). This starts the stationary state phase of the simulations.

As a time saving tool, we limit the vertical extent of the computational domain and delete the computational elements as they pass through this virtual boundary. The location of

this boundary is chosen such that it exceeds the expected average flame height. The later is estimated from experimental data which relates the normalized flame height to the quantity Q_D^* defined as $Q_D^* = \pi \rho_f Q Fr^{1/2} / 4$, which characterizes the overall Richardson number of this flow[103].

9.5.2 Time dependent structure of the plume

The flow eventually turns quasi-periodic with the regular formation of large vortical structures forming near the pool. The size of the vortical structures is of the order of the pool diameter. The frequency of formation of the vortical structures, known as the puffing frequency, has been investigated both experimentally[41, 12] and numerically[36, 60]. The dependence of the puffing frequency, f , represented in the form of a Strouhal Number, $St = fD/w_0$, on the Froude number has been shown to be reasonably described by $St = Fr^{-m}$, with $m = 0.38$ and 0.57 for non-reacting plumes and fire plumes, respectively[41]. Within the computational domain, at any moment in time, there are three or more large structures. While it is a rarely observed event, structures of different sizes and frequency are shed near the pool. Also, pairing between neighboring structures is observed, although infrequently.

Figure 9-2 shows a typical cycle of vortical structure formation in terms of locations of computational elements that coincide with the sharpest density and product mass fraction gradients, where a color code is used to indicate the local temperature. These layer of elements depict the reaction interface between fuel and air, which is convenient for representing diffusion flames. The figure shows both the linear and nonlinear stages of the growth of the instability mentioned before, the former is characterized by a downstream propagating wave with a growing amplitude, and the second starts as soon as the wave breaks and a spiral center is formed. The group velocity of the wave is non zero, and it appears to increase as the structure matures. The latter is due to the increase in the buoyancy as lighter products are formed inside these large structures. The figure confirms that the formation of the large structures is due to an instability which grows along the vorticity layer established by the plume buoyancy. The buoyancy is due in part to the initial buoyancy of the fuel plume and in part to the formation of hot products as the air and fuel mix and burn across the flame.

Figure 9-2 also shows the enormous stretch induced by the rollup of the vorticity layer which is experienced at locations between the large scales. The material initially contained between these layers is now pulled towards the rolling vortical structures. It also shows

the combustion enhancement within the large structures where higher temperatures are indicated. The large structures act as intense mixing zones within which the air they entrain is mixed with the fuel, and with fast chemistry, products are formed. Another interesting observation is the relative position of the flame with respect to the vorticity layer. As expected from stoichiometry, the flame is located on the air side of the vorticity layer since it needs more air to consume a certain amount of fuel. Similar observations are reported in reacting jet and shear layer experiments.

The results show that the vortical structures are responsible for air entrainment deep inside the rising fuel layer, leading to high product concentration within these structures. This is observed in Figure 9-3 where the product concentrations are shown to reach their maximum values around the outer edges of the evolving structures. These results indicate that while the products accumulate within the diffusion flame structure, the diffusion flame established between the rising fuel and air is convoluted by the evolving large vortical structures. The spiraling of the diffusion flame inside the structures is limited by the combined effects of volumetric expansion and vorticity generation, as observed in reacting shear layer results[84, 85]. Contrary to the latter, however, no pairing is observed, most likely due to the downstream (upward) acceleration of the eddies. Product concentration continues to increase inside the eddies until all the fuel is burnt.

The fact that the highest products concentration corresponds to regions of high vorticity is confirmed in Figure 9-4, where vorticity distribution is presented for the same cycle. The vorticity distribution in this figure is obtained by differentiating a grid-based velocity field which is recovered from the vortex elements. The establishment of a vertical vortex sheet due to the buoyancy generated torque is clear near the pool, and the first sign of the growing instability is also detectable at this stage. Vorticity continues to accumulate inside these structures as more burning takes place, and the core of maximum vorticity grows. The vortical core vertical acceleration is responsible for its elongation. Eventually, and as most of the fuel is burnt, vorticity generation and its accumulation inside the structures slow down and diffusion lowers the value of the maximum vorticity. Instead, vorticity is spread outwards over the area on the entrained fluid.

The density distribution depicted in Figure 9-5 shows that even before much burning has occurred, i.e., close to the pool, a sufficiently high rate of vorticity generation should be expected. This is because not only is methane density lower than that of air, methane

temperature rising from the pool is assumed to be higher than the ambient temperature due to the implicit effect of the radiative heat flux. This is taken as a boundary condition in this study since it has been shown to be true in many experimental measurements of different pool fires. It should also be mentioned that in our previous studies, we have shown that the similarity between isothermal plumes and fire plumes, over a relatively wide range of conditions stems from the similarity between the density fields in both cases[36]. Results in Figure 9-5 indeed shows this similarity.

The fuel concentration is depicted in Figure 9-6. Two interesting observations can be made here: (1) fuel concentration can reach zero instantaneously at some locations along the plume axis while its value is nonzero above these locations, and (2) the large structures are responsible for this penetration of the entrained air all the way to the plume axis. The figure also shows that the center of the large eddies is formed of fuel and products and that air entrainment towards these zones is relatively slow. It is worth mentioning here that while there is small fuel zones on the upper sides of the large eddies, there are large fuel zones on the lower side. This is consistent, while not conclusive, with the experimental observation that the higher soot concentration zones should be expected on the lower sides of the large eddies[92].

As mentioned before, the formation of the large structures is due to the growth of perturbation via the Kelvin-Helmholtz instability mechanism. The Kelvin-Helmholtz instability of nonreactive, homogeneous shear flow is of the convective type, i.e., it is a spatially growing instability, and its mechanism can not explain the evolution of self-excited oscillations. Linear stability analysis of diffusion flames has been conducted by Lingens et al.[56]. In their analysis, they found that the instability of this flow close to the burner rim is absolute; i.e. the flow exhibits a temporally growing instability mode of zero group velocity. Moreover, experiments on the effect of chemical reaction and heat release on the instability of a plane reactive shear layer showed that transition from convective to absolute instability occurs when the heat release is sufficiently large[50]. Thus, there is evidence that the instability observed in our simulations is an absolute linear instability of a diffusion flame separating two streams of different densities. On the other hand, the numerical results do not show a classical absolute instability since the waves appear to move while growing in amplitude. Clearly, the properties of the instability are not well understood yet, and more work is needed.

9.5.3 Puffing frequency

The above results, presented in terms of the distributions of the computational elements, the chemically active species, and vorticity, show that the most significant feature of the plume dynamics is the presence of time-dependent structures that determine the instantaneous structure of the fire. The characteristics of the periodic structures, in terms of their size, speed and frequency, observed for the cases investigated in our simulations are supported by experimental studies[96]. Periodic shedding of vortical structures whose size is of the order of magnitude of the pool diameter forming at nearly one pool diameter above the pool surface has been reported in experiments. The Strouhal number of this shedding, based on the buoyancy velocity and pool diameter, corresponding to the shedding frequency of the vortical structures for the case investigated is 2.8. This is obtained from the results shown in Figure 9-7 where the radial velocity component history at a point located at $(0.4D, 0.8D)$ above the pool surface and its Fourier transform are depicted. This result, along with cases investigated in our previous simulations, are shown in Figure 9-8, where the Strouhal number is plotted against the inverse of the square root of the Froude number. The straight lines shown in the figure represent the best fit obtained by Hamins et al.[41] for a large number of experiments.

As mentioned before, the puffing phenomenon is connected with the shedding of large vortical structures as the vorticity layer established by buoyancy rolls up due to a Kelvin-Helmholtz instability. The universal scaling law of this instability suggests that the instability properties are indeed intrinsic to the flow. While it has been hypothesized before that these flows could be linearly unstable, the actual observation of linearly growing waves along the vortex layer has not been reported before. In previous studies, we showed that similar phenomena are observable in isothermal plumes, and we used the similarity between the density fields established in both cases to explain the origin of the similarity. While it is tempting to discuss the phenomena as if it was a density interface instability, we iterate that all evidence confirms that it is a vortex layer instability. This can also be supported by the vorticity distribution contours shown in Figure 9-4 where it is clear that the roll up occurs following the establishment of a finite layer. We should also add that the dependence of the Strouhal number on the Froude number, the latter is a measure of the effect of buoyancy on this flow, is consistent with the fact that it is the properties of the vorticity layer, formed

by buoyancy, which determine the instability properties.

The speed of these vortical structures increase upwards, as can be seen from the results. Similar observations were made experimentally, and they are consistent with the generation of more light products as combustion proceeds within the large structures. Comparison between our predictions of the eddy-speed dependence on the vertical location and those obtained experimentally show good agreement.

9.5.4 Radial temperature profiles

A sample of the radial temperature profiles at different heights along the flame are shown in Figure 9.6. These profiles were obtained for a case for which $T_0 = 278K$ and $D = 5.7cm$. The profiles are reminiscent of diffusion flame temperature profiles in cases when the strain rate exerted on the flame is relatively low. A steep temperature drop is observed on both sides of the reaction front, with higher steepness on the air side. This is in qualitative agreement with corresponding temperature profiles obtained experimentally by Venkatesh et al.[101], presented in the same plot for a fire of $5.7cm$ pool diameter with 1-propanol as fuel. In our case, the fuel-air temperature ratio converges to a value of 3.0 at $r = D/2$, which is the ratio provided to the setup of the fuel-air interface as an initial condition. These profiles serve to show the extent of the flame structure within the fire zone, and to emphasize the significance of the high resolution achieved using the transport element method in capturing the evolving combustion field in the fire.

9.5.5 Average flame height

The observed flame height has been defined as the point above the pool where most of the fuel has burnt. Our simulations show that the flame height fluctuates around a plane nearly three diameters above the pool, as seen in the distribution of the instantaneous fuel mass fraction shown in Figure 9-6, and the averaged fuel mass fraction distribution presented in Figure 9-10. As mentioned before, flame fluctuations are due to the shedding of the large structures which tend to divide the evaporating fuel plume into segments and at times separate parcels of the plume from the rest. The flame height, Z_{fl}/D , has experimentally been correlated to the normalized heat of reaction Q_D^* according to the plot shown in Figure 9-11 which was compiled by Zukoski[103]. For our case, the flame height of $Z_{fl}/D = 3$, corresponding to $Q_D^* = 1.0$, is in good agreement with the experimental data.

Other average distributions are shown in Figure 9-10 as well. These include the products mass fraction, temperature and velocity. In all cases, the results obtained over a uniform grid were averaged over a large number of time steps which correspond to several large scale sheddings. The similarity between the products mass fraction and the temperature contours is due to our assumption that the Lewis number is unity. Another noteworthy observation is the average velocity distribution which shows a sharp increase in the value of the velocity within the flame zone and within a small vertical distance above the pool.

9.5.6 Velocity field

The instantaneous velocity fields at dimensionless times $t = 45.386$ and $t = 47.386$ are shown in Figure 9-12 to help shed some light on the properties of the entrainment field. The velocity on the air side indicates the entrainment of air by the vortical structures into the reacting zone. The entrainment velocity is maximum around the locations of the vortical structures shown in Figures 9-2 and 9-4 for the corresponding time instants. There, the instantaneous velocity field on the air side show downwards values and in some places air is driven away from the plume; a surprising result which has been confirmed by recent experimental results[101]. The fact that these values are all induced by the vortical structures forming along the plume edge explain these trends. The results also show the strong acceleration which coincides with the flame front. This acceleration is concomitant with the large drop in the density across the reaction front.

The average velocity field, depicted in Figure 9-10 and in larger scale in Figure 9-13, shows that the velocity rises to a maximum at an axial location of about two plume diameters and then falls. This behavior is expected, and is confirmed by experimental results, as the heat of reaction deposited within the zone of combustion lowers the density of the products and accelerates the flow, followed by a zone of nearly pure entrainment without measurable combustion which leads to lower temperatures and lower velocity. The ratio of the velocity of the air entrained into the flame zone at an axial location of $0.7D$ is about four times the velocity of the air entrained at the pool base. This agrees with corresponding values obtained by Zhou et al.[101] for a 7.1 cm toluene fire. Furthermore, the values of the velocity corresponding to a 7.1cm diameter pool ranges from ~ 6 cm/s on the air side at the pool base to 25 cm/s at $z \sim 0.7D$, which is in good agreement with the corresponding values obtained by Zhou et. al and shown in Figure 9-14.

9.5.7 Entrainment

Finally we use the average velocity field to compute the entrainment rate into the fire zone. The entrainment rate is defined as the mass flow rate of air entering the flame region at a well defined radius; $m_{ent} = \frac{d}{dz} \left(\int_0^R 2\pi\rho wr dr \right)$. Clearly the selection of the radius at which the integration is performed is crucial. Figure 9-15 shows the entrainment rate computed from our results for different choices of the radius R , normalized by the Froude number, the stoichiometric ratio and the fuel mass flow rate injected at the pool. On the same plane, we show the results from reference [101]. Plots showing a wide range of entrainment rates have been published in the literature[103], confirming the need for a precise definition of this important quantity. Finally, we show on Figure 9-16 a sample of this wide discrepancy in the experimental results, along with Delichatsios' correlation and our results.

9.6 Conclusions

Fire plume simulations show that the plume dynamics are dominated by the shedding of large vortical structures which originate in the vertical vorticity layer that forms above the pool. While the vorticity formation rate is buoyancy induced, the instability appears to be of a linear, Kelvin-Helmholtz type with accelerating group velocity. These structure govern the far field entrainment process, and burning occurs on their outer edges in the form of a gradually thickening diffusion flame. Within the large structures pockets of hot, high fuel concentration are observed. Fuel balls are "pinched" off the rising plume in the form of large puffs as the entrained air reaches the plume centerline causing the flame height to oscillate at the same frequency as the shed structures. Dynamic similarity between isothermal and intense fire plume is discussed in light of the density fields in both cases. Predictions of the puffing frequency, averaging flame height and oscillations, and motion of the large structures compare well with experimental data.

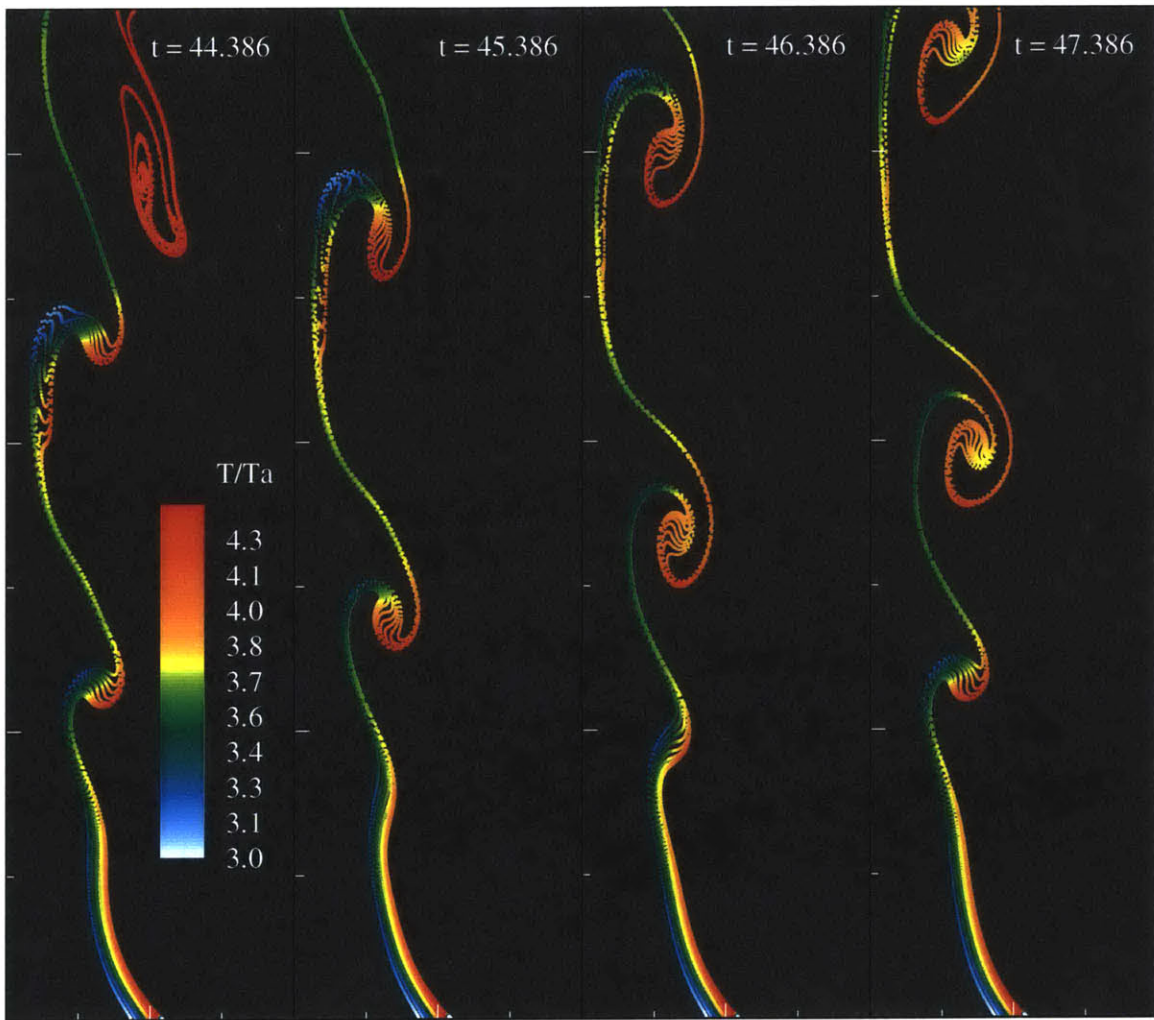


Figure 9-2: Typical cycle showing the computational elements at four times. Color denotes temperature. Major ticks with 0.5 spacing.

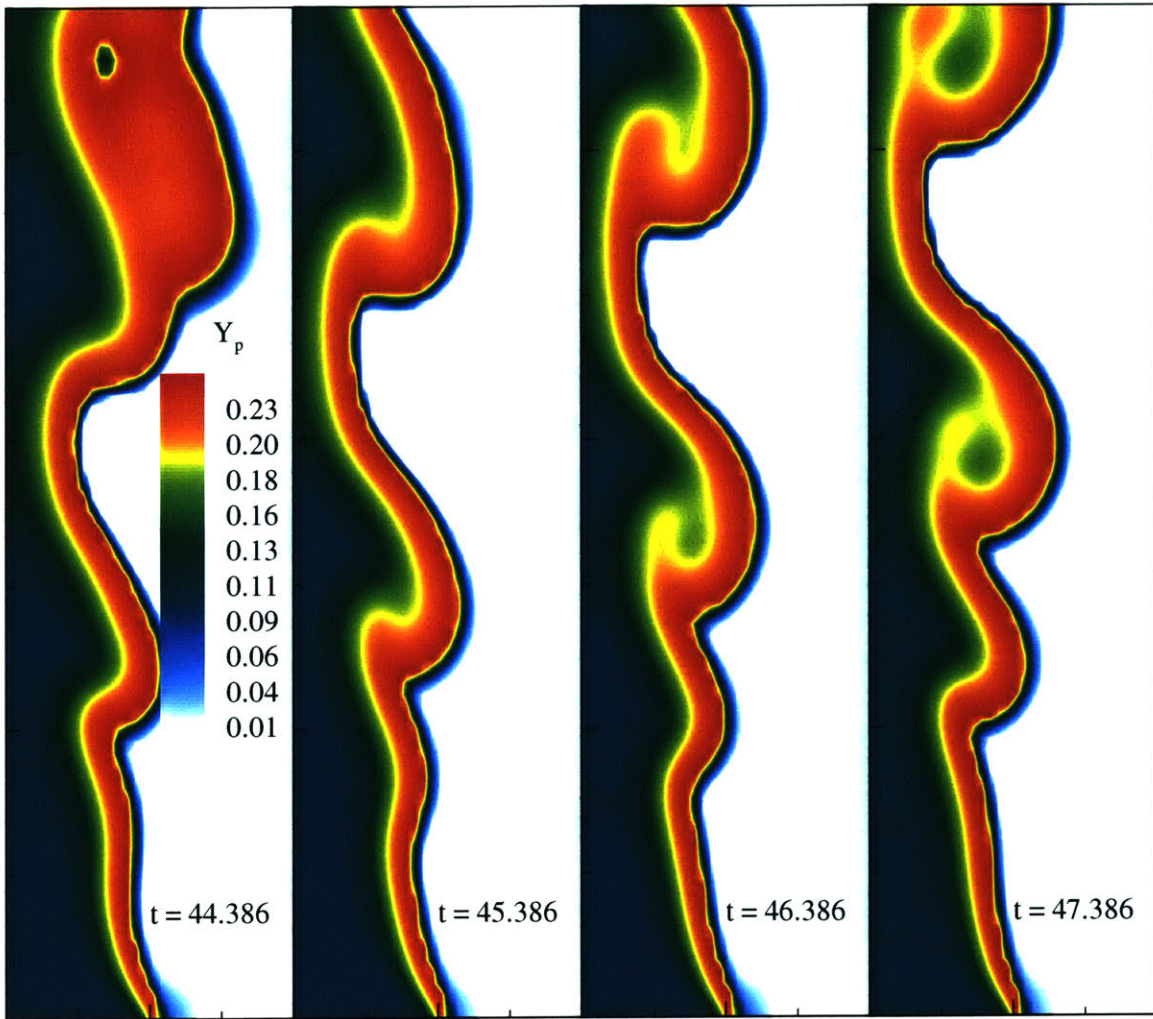


Figure 9-3: Product mass fraction distribution at four times. Major ticks with 0.5 spacing.

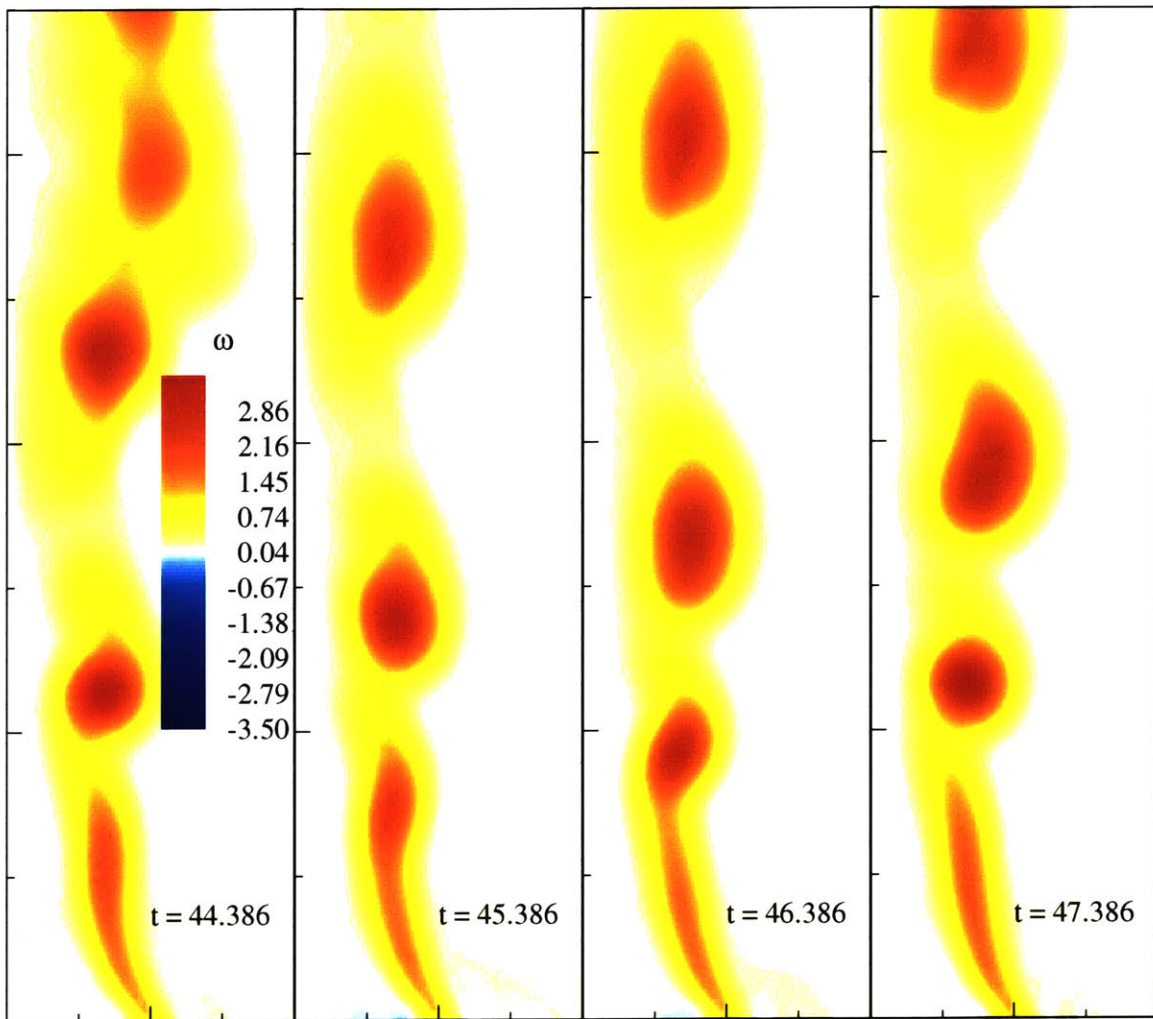


Figure 9-4: Vorticity distribution at four times. Major ticks with 0.5 spacing.

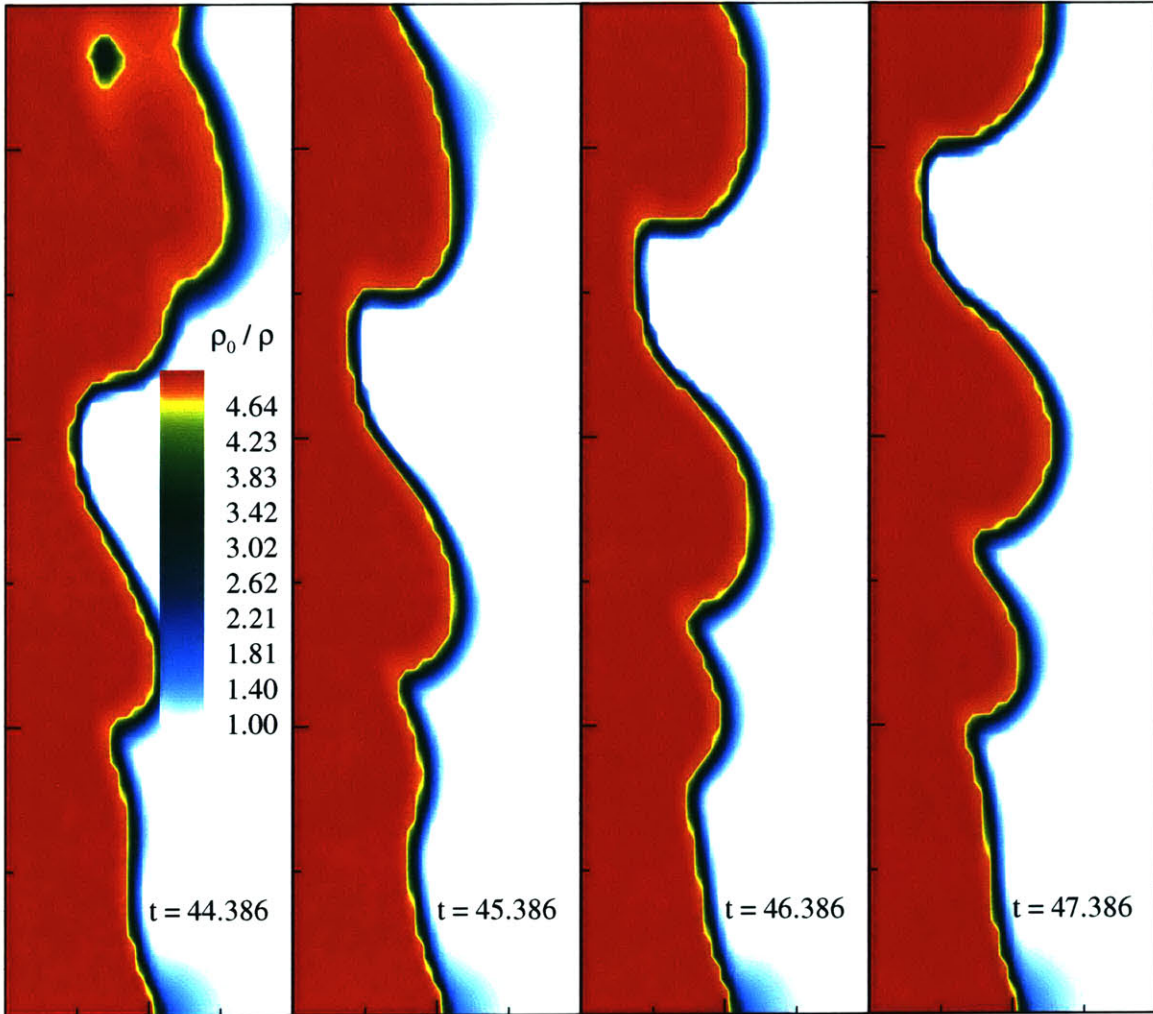


Figure 9-5: Density distribution at four times. Major ticks with 0.5 spacing.

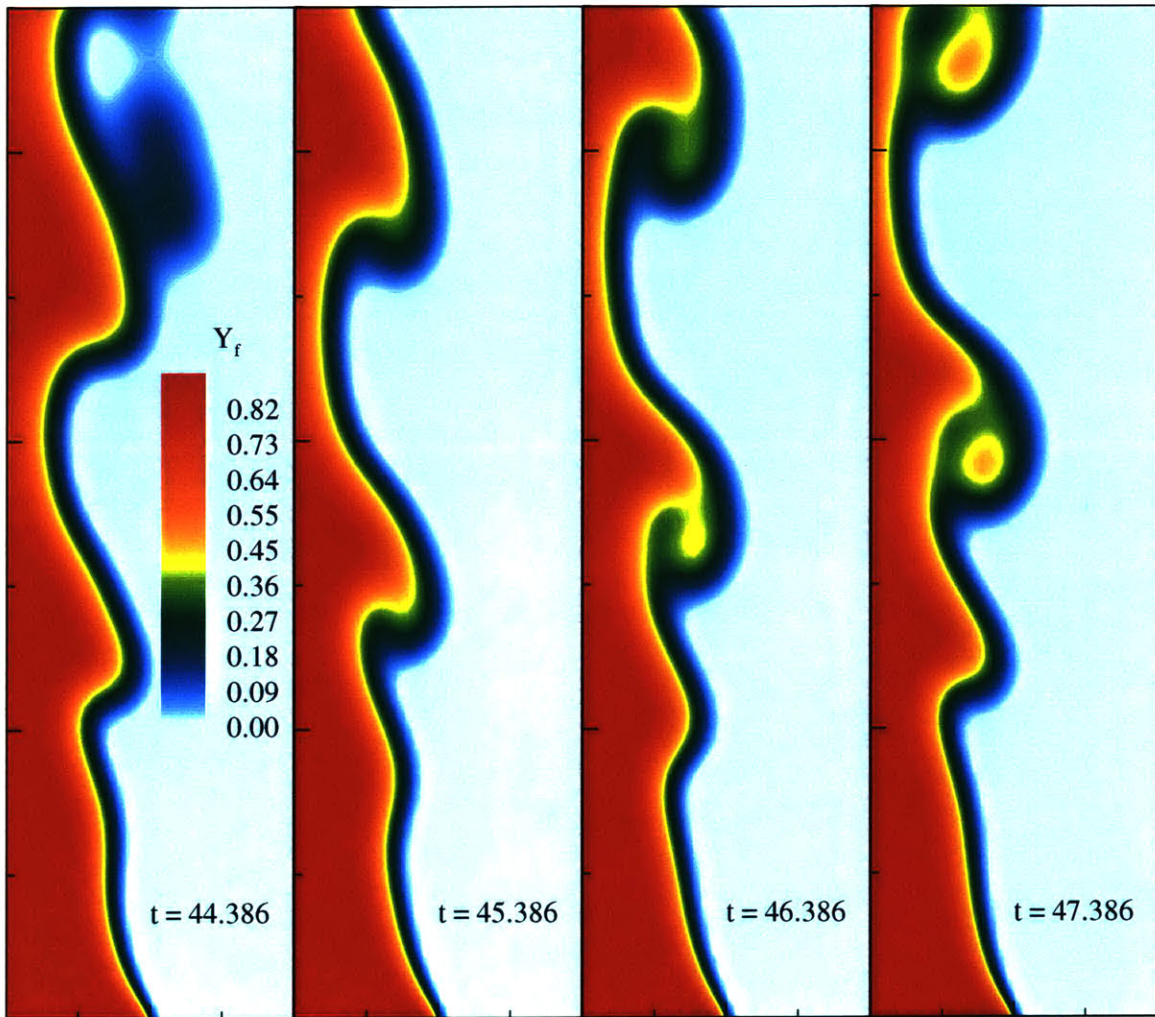


Figure 9-6: Fuel mass fraction distribution at four times. Major ticks with 0.5 spacing.

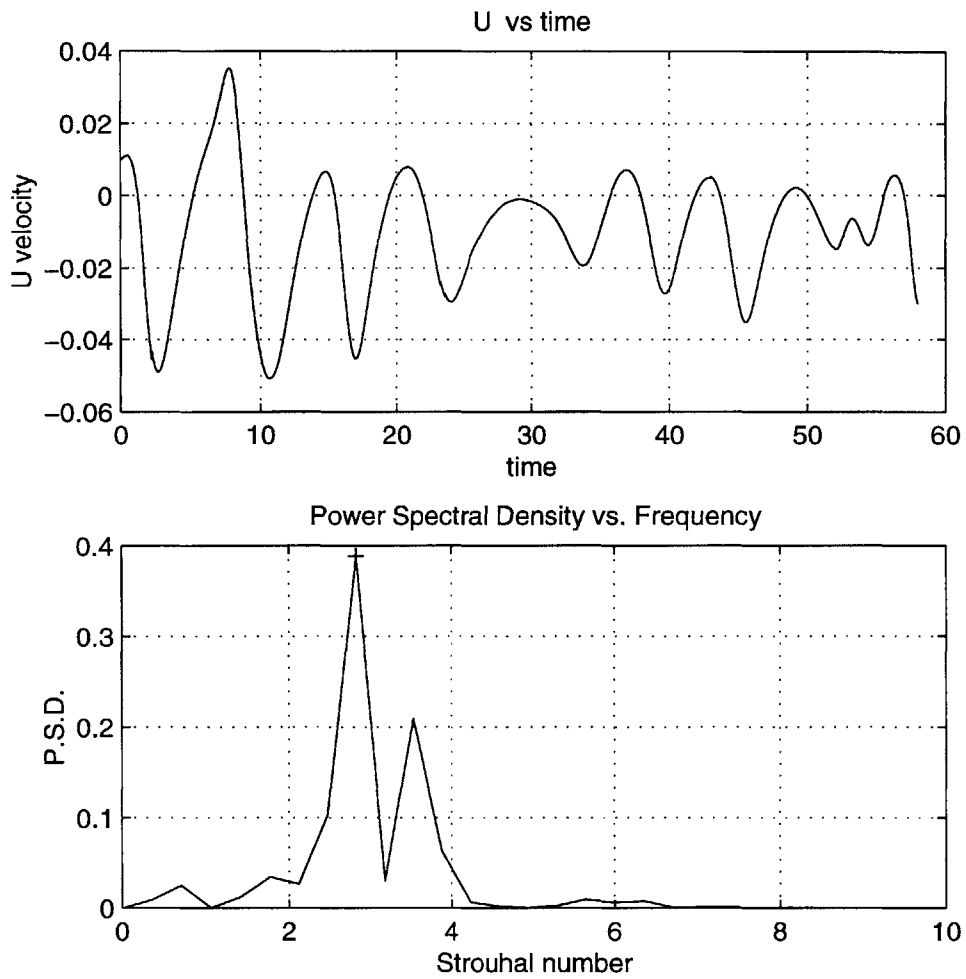


Figure 9-7: Upper figure: radial velocity component history at a point located at $(r, z) = (0.4, 0.8)$. Lower figure: the power spectrum density vs. frequency.

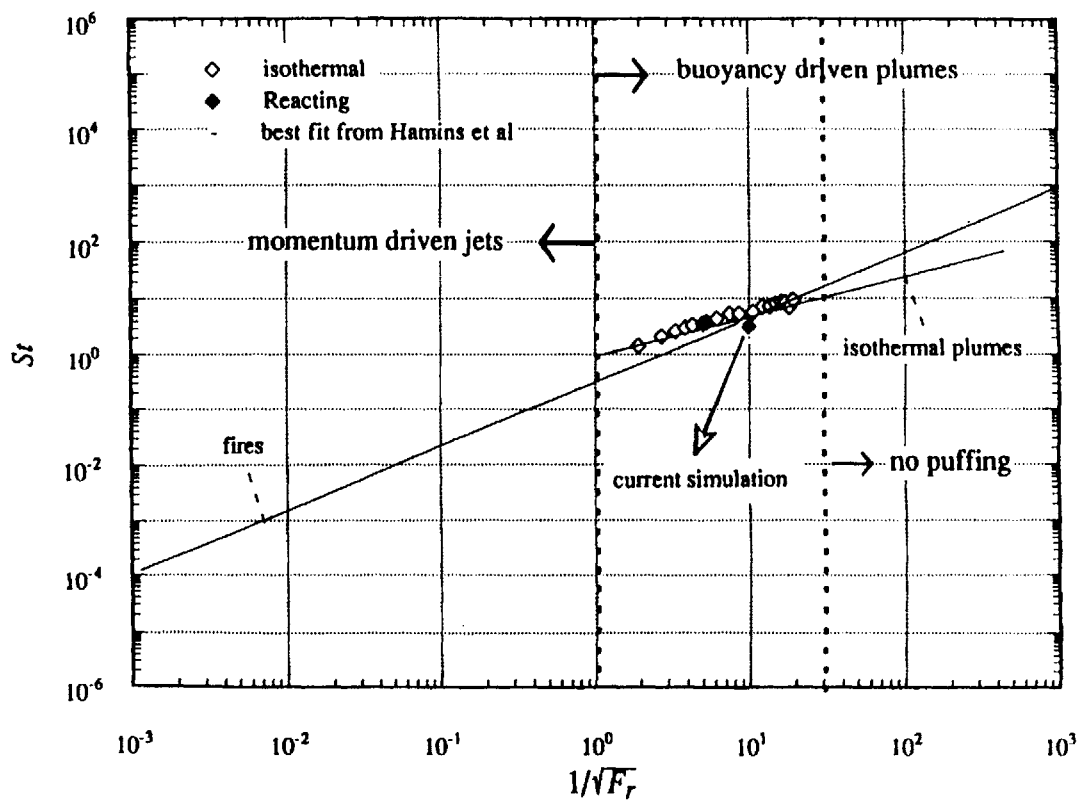


Figure 9-8: Strouhal vs. Froude number.

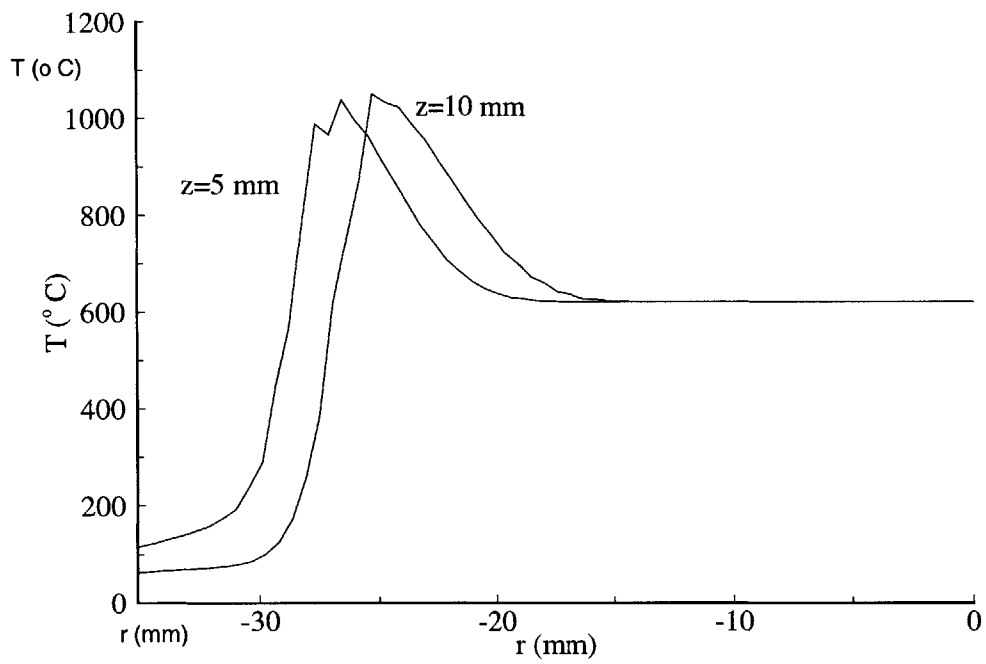


Figure 9-9: Radial temperature profiles.

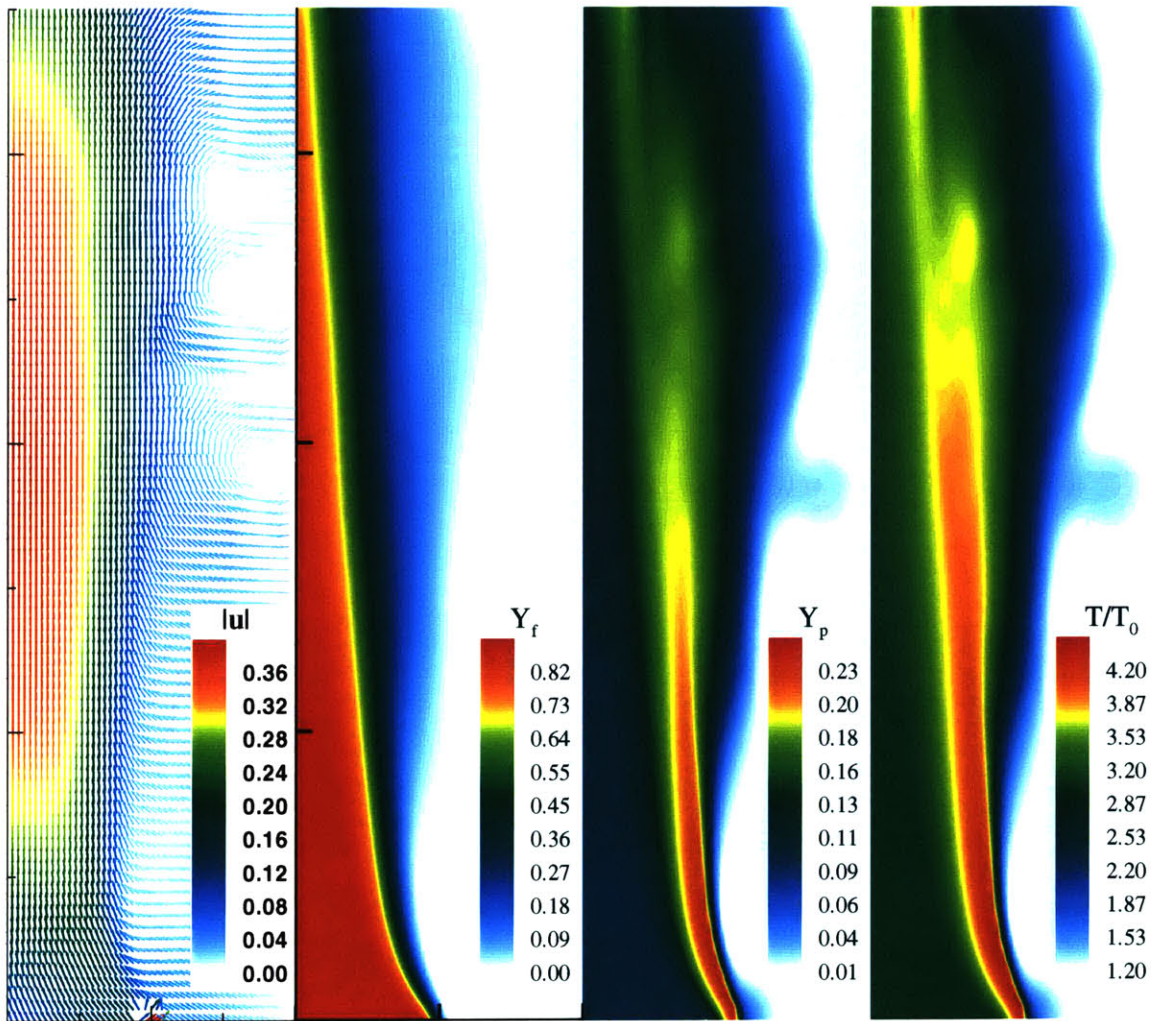


Figure 9-10: Average distributions of velocity, temperature, fuel and product mass fractions. Major ticks with 0.5 spacing.

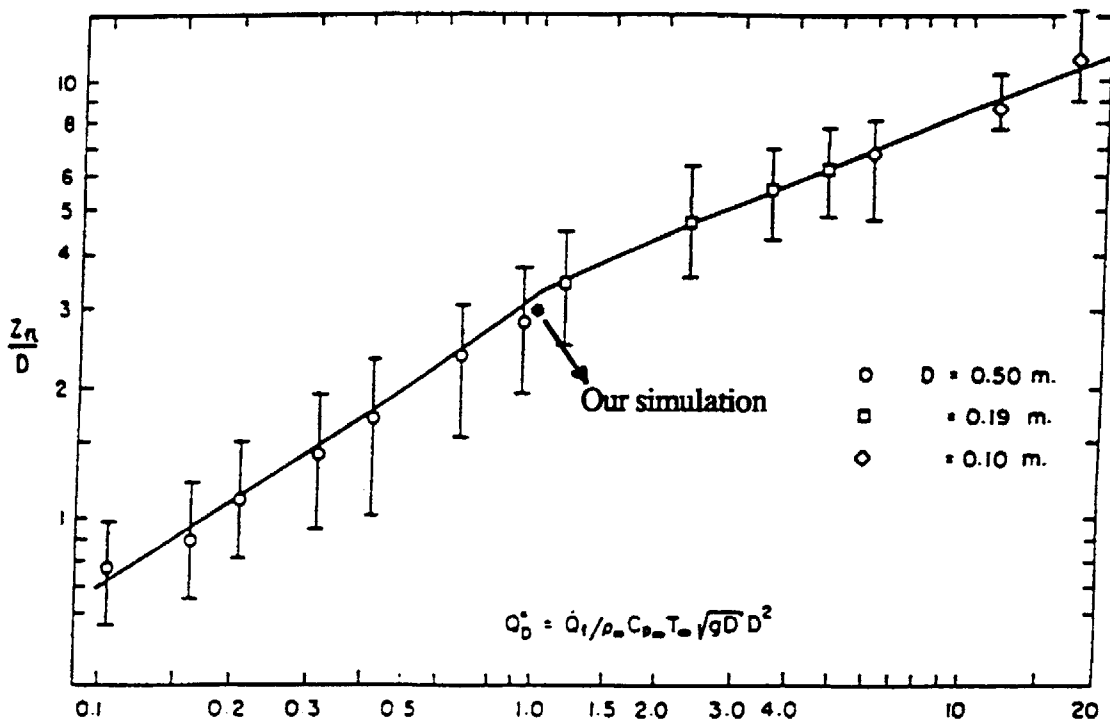


Figure 9-11: Average flame height versus dimensionless heat released obtained from Ref. [104].

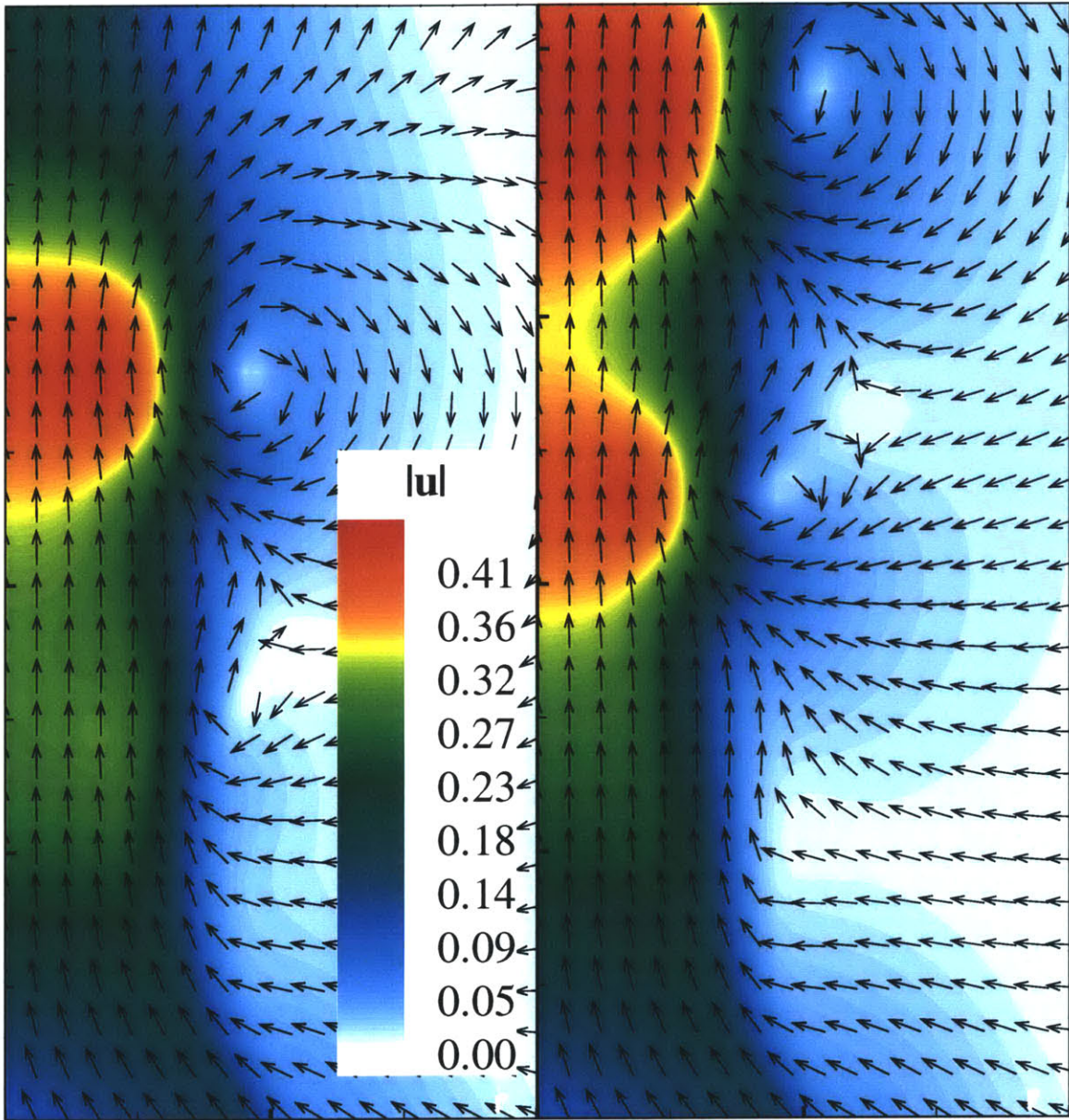


Figure 9-12: The instantaneous velocity field near the pool at $t = 45.368$ and $t = 47.386$. Major ticks with 0.5 spacing.

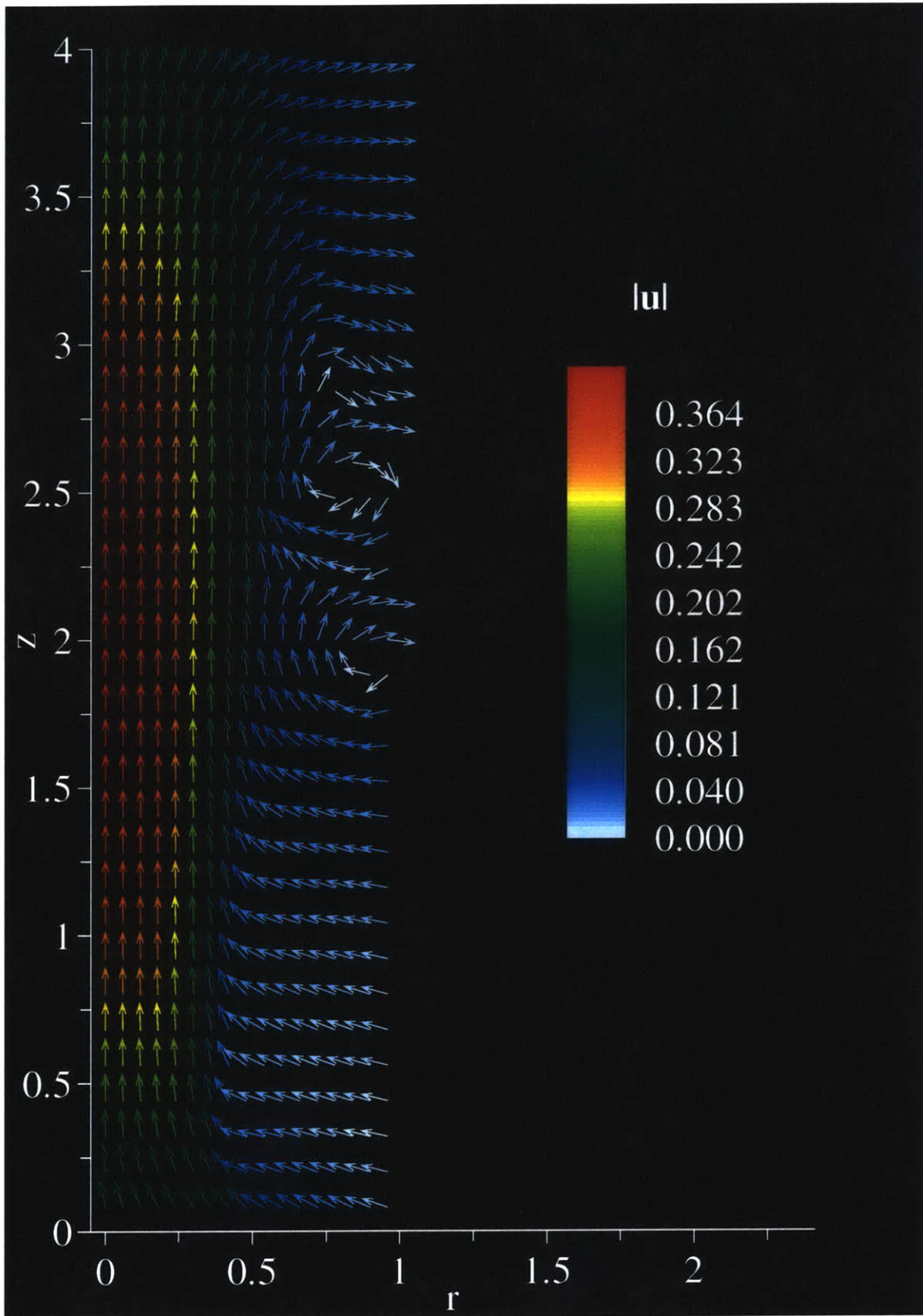


Figure 9-13: Average velocity field. Color denotes speed.

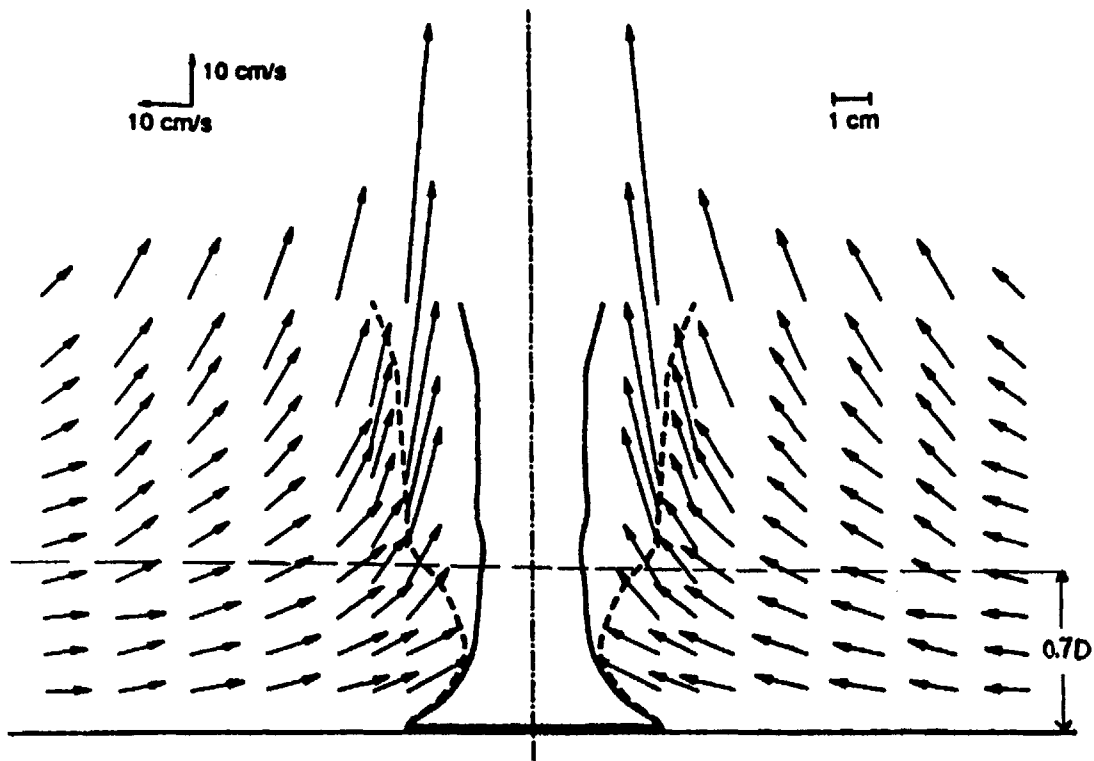


Figure 9-14: Velocity field at pool base of a 7.1 cm toluene fire obtained from reference [102].

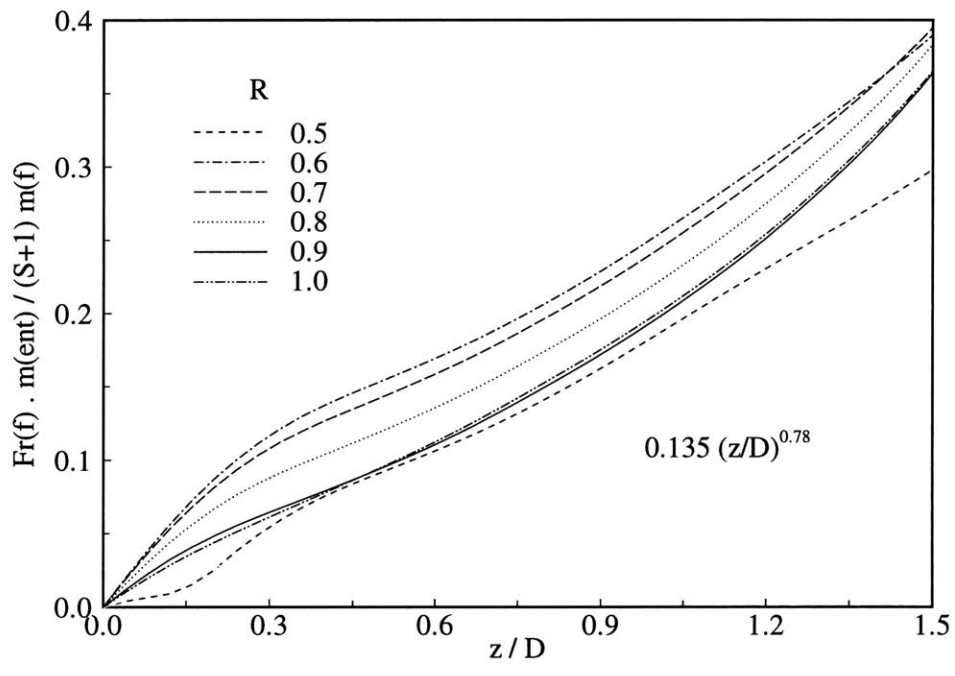


Figure 9-15: Mass entrained as a function elevation. Delichatsios' correlation [26] is also shown.

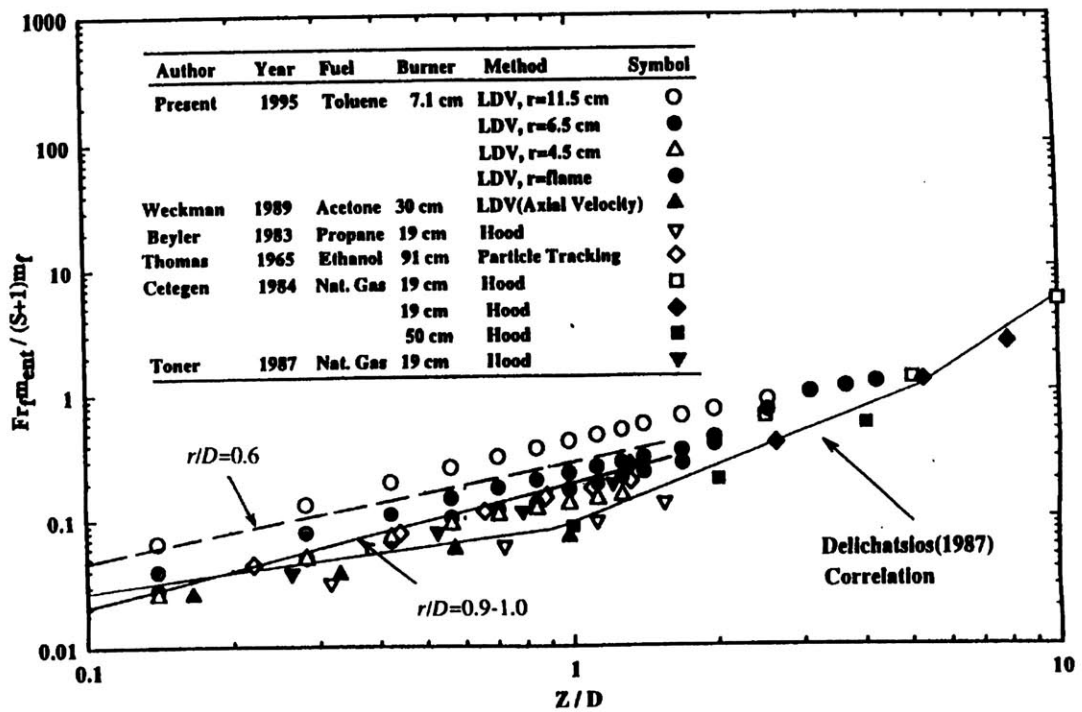


Figure 9-16: Comparison of present numerical results concerning entrainment mass flow-rates with experimental data[104] and Delichatsios' correlation[26].

Chapter 10

Solutions Using the Smoothed Redistribution Method

In chapter 10 and 11, numerical results for three problems of increasing complexity are presented. In this chapter, computations of Stokes flow and propagation of a vortex ring are considered. In the next chapter, combustion of a fuel patch with and without the role of radiative transfer is considered. The stokes flow problem involves solving the diffusion equation, and thus provides a basis for a convergence study of the smoothed redistribution method. The vortex ring problem, involving diffusion and convection, enables validation of the velocity tables, assessment of the convection accuracy for a smoothed discretization of the vorticity field, and the impact of the regularity of the distribution of elements imposed by the smoothed redistribution method. The problem of combustion of a fuel patch involves, in addition to convection and diffusion, coupling the vorticity and energy equations represented in generation of vorticity. This allows validation of the treatment of the source term, as well as the volumetric expansion velocity tables.

10.1 Stokes flow

To validate the smoothed redistribution method for diffusion, diffusion of a vortex ring carrying a passive scalar is considered. Using the initial circulation Γ_0 , energy E_0 , and radius, r_0 , the vorticity and scalar diffusion equations in dimensionless form are respectively

$$\frac{\partial \omega}{\partial t} = \frac{1}{Re} (\nabla^2 \omega - \frac{\omega}{r^2}) \quad (10.1)$$

and

$$\frac{\partial s}{\partial t} = \frac{1}{RePr} \nabla^2 s \quad (10.2)$$

where the Reynolds number is $Re = \Gamma_0/\nu$, the Prandtl number is $Pr = \nu/\alpha$, and ν and α are respectively the kinematic and thermal diffusivities. The Passive scalar is defined as $s = (T - T_\infty)/T_0$, where T_∞ corresponds to the farfield.

The initial conditions corresponds to a vortex ring located at $r_0 = 1$, $z_0 = 0$ with initial circulation $\Gamma_0 = 1$ and energy $E_0 = 1$. The Reynolds and Prandtl numbers are $Re = 50$ and $Pr = 1$ respectively. The redistribution length is selected to be $h = \sqrt{8\Delta\tau}$, where $\tau = \nu t$. The objective is to investigate the impact of the spatial resolution¹ $\Delta\tau$ (or h) and the ratio of core radius to elements' spacing (the overlap), σ/h . We present the following two sets of calculations:

1. Effect of spatial resolution: $0.00025 \leq \Delta\tau \leq 0.1$, $h = \sqrt{8\Delta\tau}$, $\sigma = 3h_0$, $h_0 = \sqrt{8\Delta\tau_0}$, $\Delta\tau_0 = 0.0005$.
2. Effect of spatial resolution with fixed overlap: $0.00025 \leq \Delta\tau \leq 0.02$, $h = \sqrt{8\Delta\tau}$, $\sigma = 2h$.
3. Effect of core size: $\Delta\tau = 0.0005$, $h = \sqrt{8\Delta\tau}$, $h \leq \sigma \leq 10h$.

The numerical results are compared to the exact solution in terms of contours and profiles of vorticity and scalar, as well as the time evolution of the global moments. The L_2 norm of the error on a uniform mesh is also presented. The exact solution of the diffusion equations 10.1 and 10.2 is

$$\phi_n = C_n \frac{2}{\pi^{1/2}\sigma^3} e^{-\frac{r^2+r_0^2+(z-z_0)^2}{\sigma^2}} I_n\left(\frac{2rr_0}{\sigma^2}\right) \quad (10.3)$$

where $n = 1$ corresponds to vorticity and $n = 0$ to scalar. The constants C_n are $C_1 = \Gamma_0 r_0 / (1 - e^{-r_0^2/\sigma_0^2})$ and $C_0 = 1$.

One way to measure the global error is to calculate the integral of the L_2 norm of the pointwise error. Numerically, the pointwise values are obtained on a uniform mesh of side

¹and thus the temporal resolution

6σ centered at the initial location, the global error is then determined by

$$|\epsilon|_{L_2} = \Delta\tau\Delta z \left(\sum_{i=1}^{N^2} (f_e(i) - f_n(i))^2 \right)^{1/2} \quad (10.4)$$

where f denotes vorticity or scalar. The subscripts e and n refer to exact and numerical solutions respectively. The uniform mesh is of size $\Delta\tau = \Delta z$ and dimension N^2 , where $N = N_\tau = N_z = 100$ has been used for all the cases discussed.

10.1.1 Vorticity and scalar

For a fixed core size, refining the spatial resolution results in a smoother and more accurate solution. This is shown in Figures 10-1 and 10-2 where the vorticity and scalar contours at $\tau = 0.2$ are respectively shown for time step values of $\Delta\tau = 0.018, 0.0045, 0.001125,$ and 0.0005 . The corresponding overlap values, σ/h , are also shown in the figures. For $\Delta\tau = 0.018$, where the core size is half the initial elements spacing, the numerical solution is noisy and characterized by oscillations around the exact solution. As the time step is reduced, and correspondingly the overlap ratio increased, the oscillations get more and more damped and the solution converges to the exact solution. For $\Delta\tau = 0.0005$, for example, the numerical solution is almost coincident with the exact solution. This behavior is expected since for values of $\sigma/h < 1$ there is not enough overlap resulting in oscillations with maxima at the elements locations. In the extreme case where the elements are Dirac delta functions, the solution is singular at these locations.

The corresponding error, as defined in equation 10.4, is shown in the log-log plot versus time step in Figure 10-3. The error may be correlated to h according to $|\epsilon|_{L_2} \propto h^{-2.19}$. The arrow on the plot indicated direction of increasing overlap ratio.

In order to confirm the argument that the overlap ratio is the key parameter for smoothness and accuracy of the solution, a set of simulations was conducted in which both the time step and the core size vary such that the overlap ratio is constant, $\sigma/h = 2$. The global error proved to be weakly dependent on the initial element spacing, as seen in Figure 10-4. The total circulation versus time, plotted in Figure 10-5, shows this weak dependence. This proves that error behavior experienced for the case of variable h and constant σ is predominantly due to the variation of the overlap ratio σ/h . This is further shown when the initial elements spacing is kept fixed, $h = \sqrt{8 \times 0.0005}$, and the overlap ratio σ/h is

varied by varying the core size σ . The error behavior in the case, shown in Figure 10-6, yields the correlation $|\epsilon|_{L_2} \propto (\sigma/h)^2$, similar to that obtained for the case of variable h and constant σ .

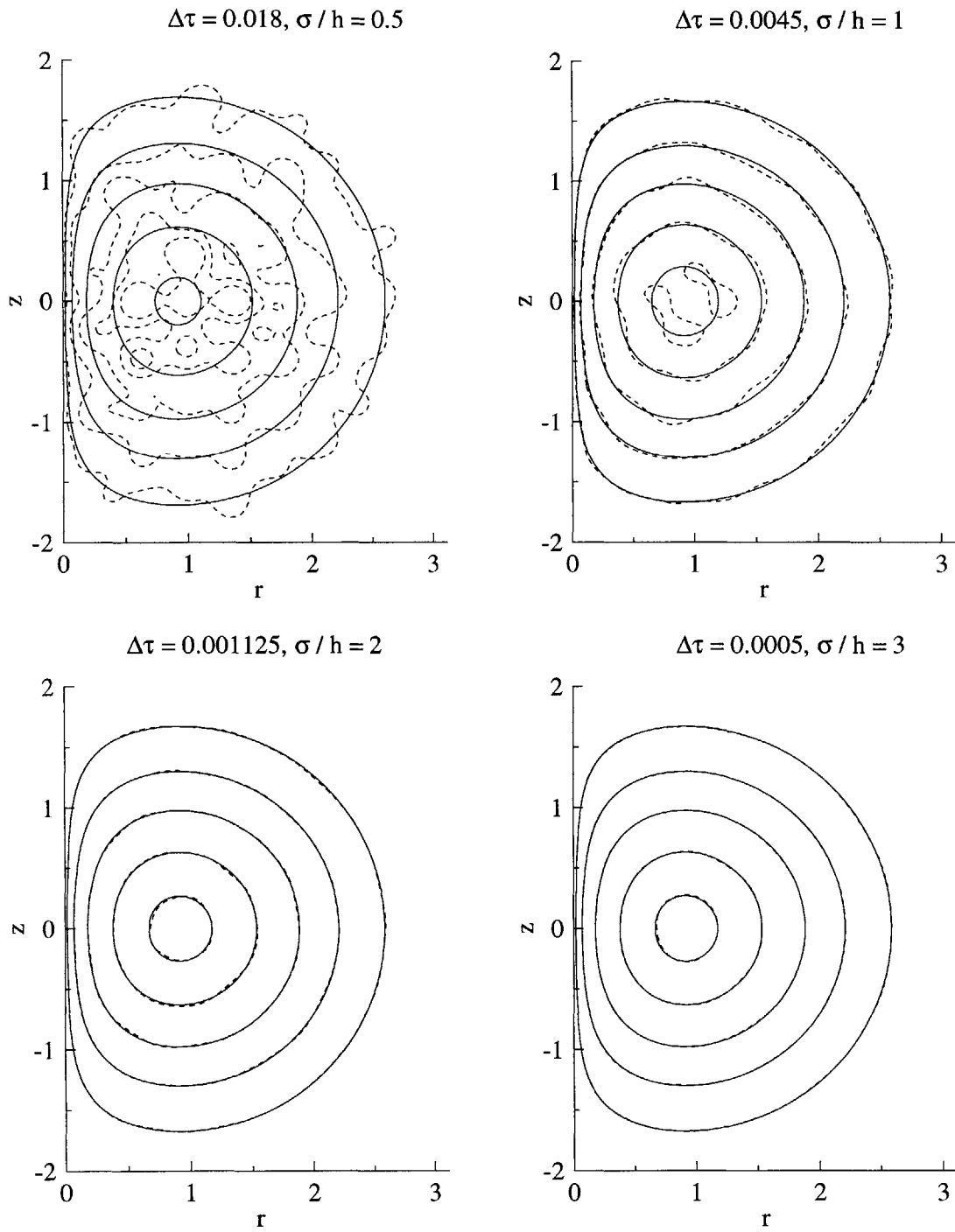


Figure 10-1: Vorticity contours at $\tau = 0.2$ for $\Delta\tau = 0.018, 0.0045, 0.001125$ and 0.0005 . Solid lines are exact solution. Dash lines are numerical solution. Contour levels are 0.01, 0.04, 0.1, 0.2, and 0.3

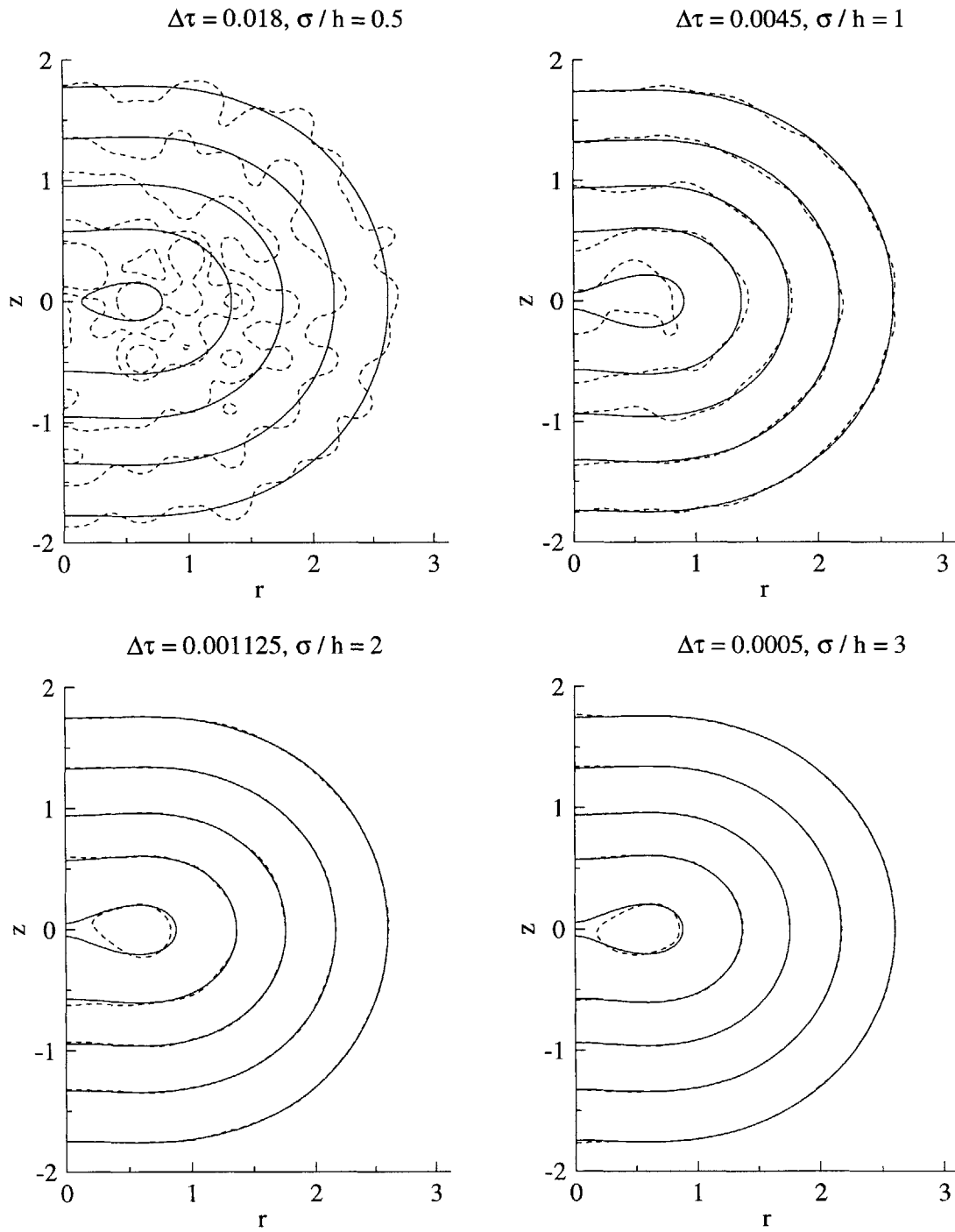


Figure 10-2: Scalar contours at $\tau = 0.2$ for $\Delta\tau = 0.018, 0.0045, 0.001125$ and 0.0005 . Solid lines are exact solution. Dash lines are numerical solution. Contour levels are 0.01, 0.05, 0.15, 0.3, and 0.45

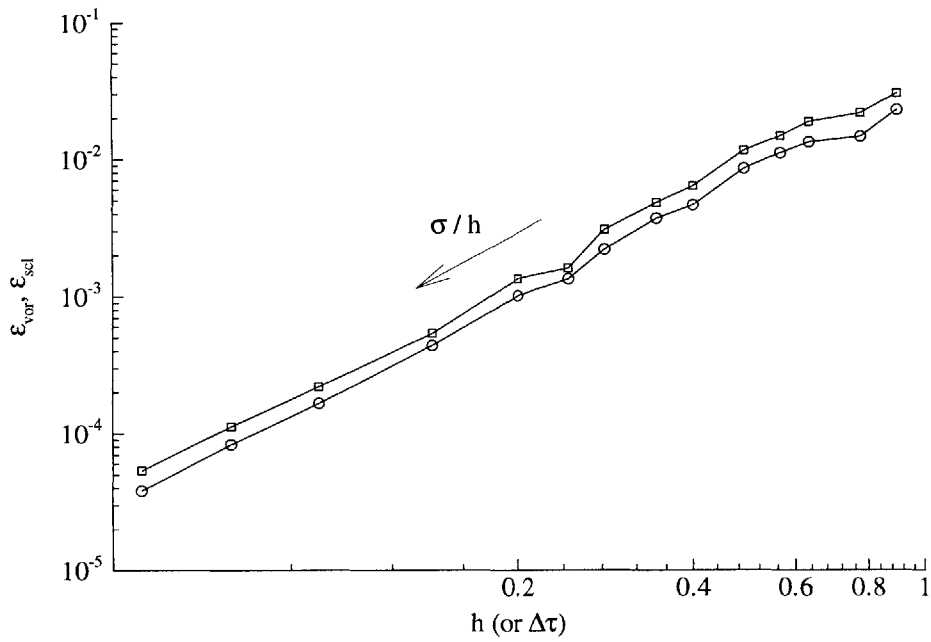


Figure 10-3: Global error versus time step. Core size is constant $\sigma = \sqrt{8 \times 0.0005}$. Circles denote vorticity. Squares denote scalar.

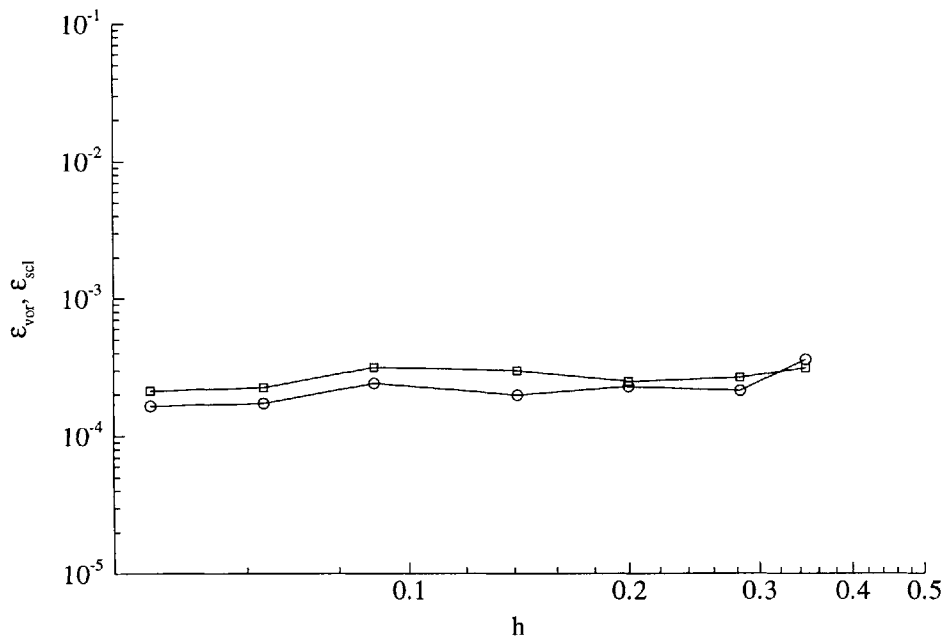


Figure 10-4: Global error versus time step. Overlap ratio is constant $\sigma/h = 2$. Circles denote vorticity. Squares denote scalar.

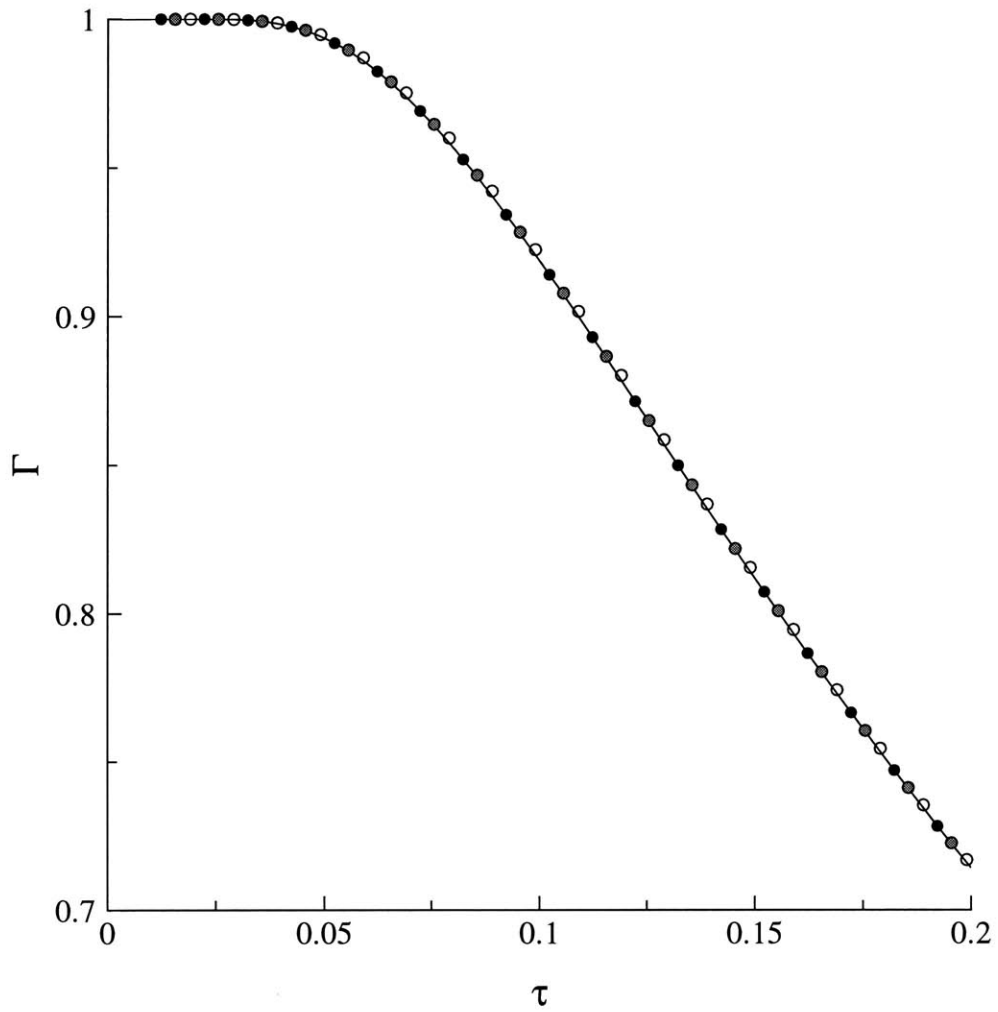


Figure 10-5: Total circulation. Solid line is exact solution. Symbols are numerical solution: $\Delta\tau = 0.00025$: black circles, $\Delta\tau = 0.0005$: grey circles, and $\Delta\tau = 0.001$: empty circles.

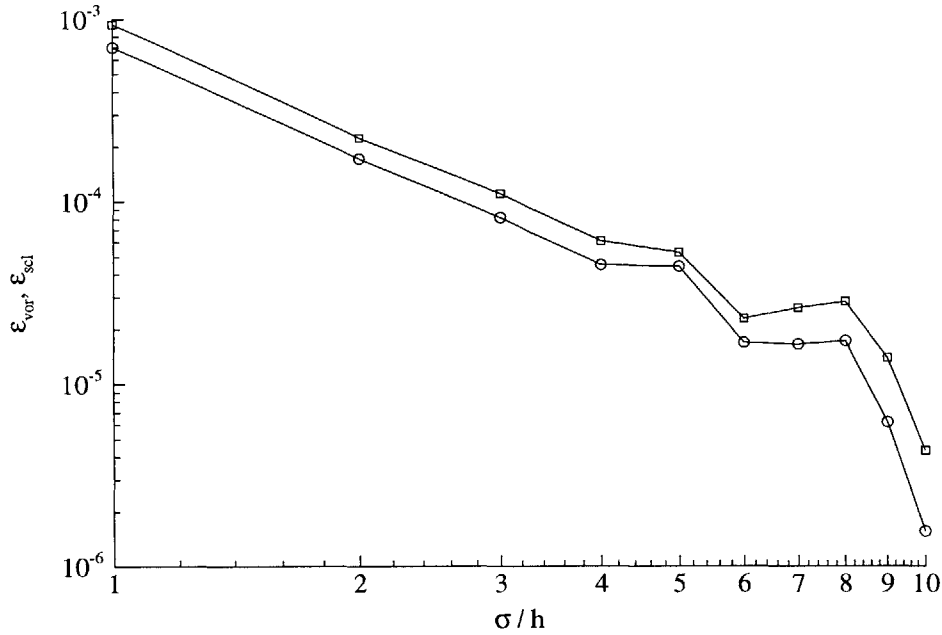


Figure 10-6: Global error versus overlap ratio. Time step is constant $\Delta\tau = 0.0005$. Circles denote vorticity. Squares denote scalar.

The impact of large overlap ratio is presented in terms of radial and axial profiles of vorticity and scalar shown in Figures 10-7 and 10-8 respectively, for overlap ratio $\sigma/h = 5$ and at time $\tau = 0.2$. The radial profiles are at $z = 0$. The axial vorticity profile is at $r = 1$ whereas the axial scalar profile is at $r = 0$. The numerical solution, denoted by the symbols, follows the exact solution closely.

10.1.2 Scalar gradient

In some problems, the scalar gradients may be required. This is the case in buoyant variable density flows, where the baroclinic and buoyant vorticity generation are functions of the density (or temperature) gradient. Thus accurate evaluation of the scalar gradient is a necessity. For the scalar gradient, the error incurred in the numerical solution of the scalar is magnified due to differentiation. Thus, it is expected that the scalar gradient numerical solution gets more accurate and less noisy as the overlap ratio increases, similar to the behavior of the scalar, but at a smaller rate. While the solution for the scalar at $\tau = 0.2$ is accurate for the case of $\sigma/h = 2$, as seen previously in Figure 10-2, the gradient solution is noisy and oscillatory. The radial and axial components of the scalar gradient are shown

in Figure 10-9. However, increasing the overlap further results in smoother and more accurate scalar gradients. This is clear in Figure 10-10 where the scalar gradient solutions are presented for $\sigma/h = 3.54$ and $\sigma/h = 5$.

10.1.3 Number of elements

The impact of resolution of the number of elements is presented in Figure 10-11. The plot shows that the number of elements is inversely proportional to the number of elements, i.e. $N \propto 1/\Delta\tau$. The size of the core, on the other hand, proved to have less influence on the number of elements. According to Figure 10-12, the number of elements decreases at a slow rate as the core size increases, except for very large cores, where the number of elements decreases rapidly.

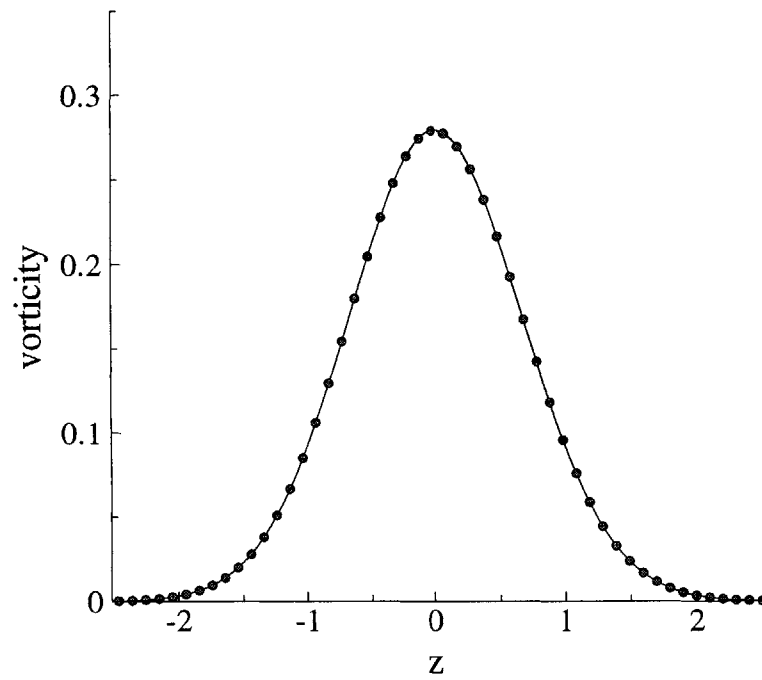
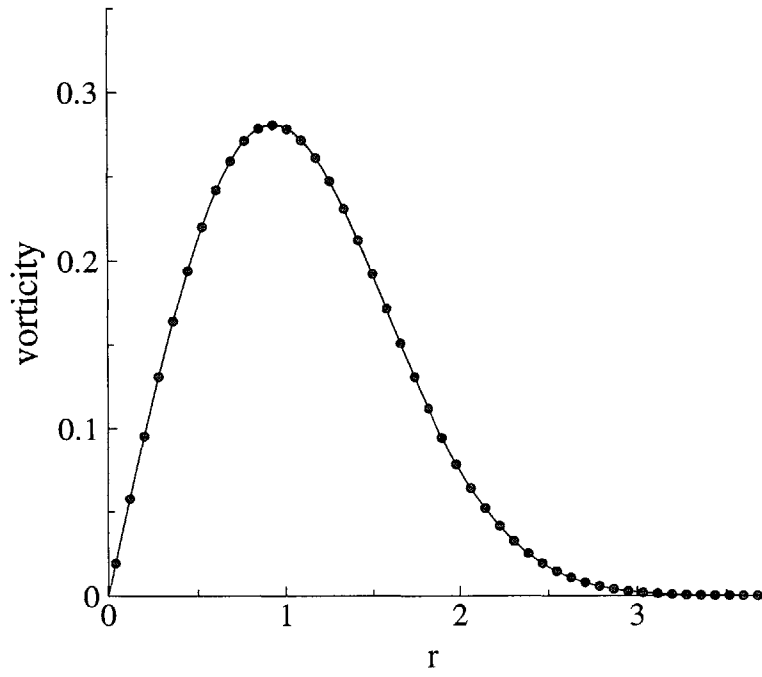


Figure 10-7: Upper figure: radial vorticity profile at $z = 0$, $\tau = 0.2$. Lower figure: axial vorticity profile at $r = 1$, $\tau = 0.2$. Solid lines are exact solution. Symbols are numerical solution.

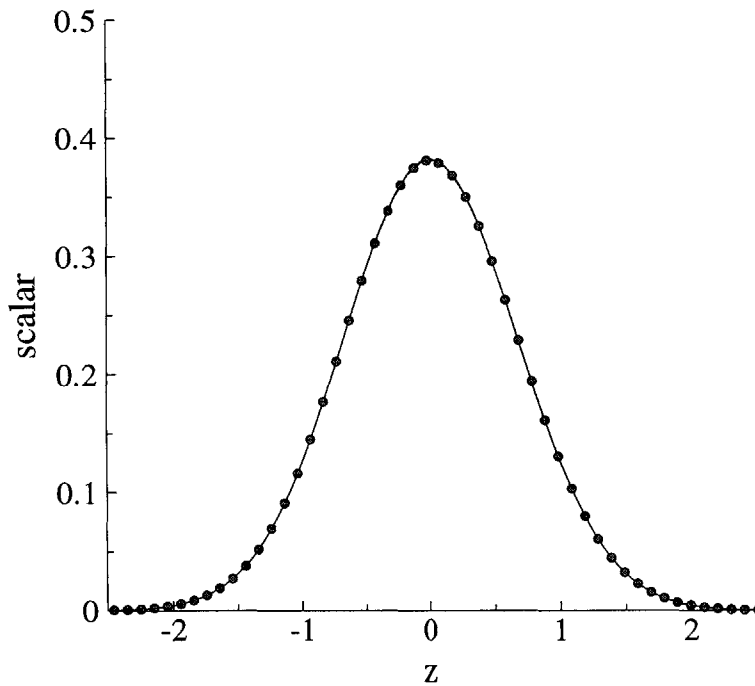
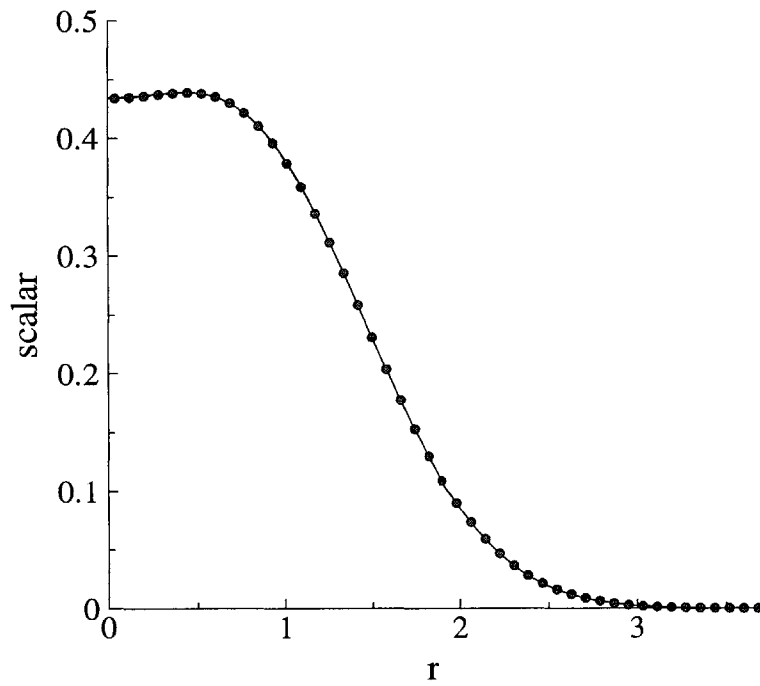


Figure 10-8: Upper figure: radial scalar profile at $z = 0$, $\tau = 0.2$. Lower figure: axial vorticity profile at $r = 0$, $\tau = 0.2$. Solid lines are exact solution. Symbols are numerical solution.

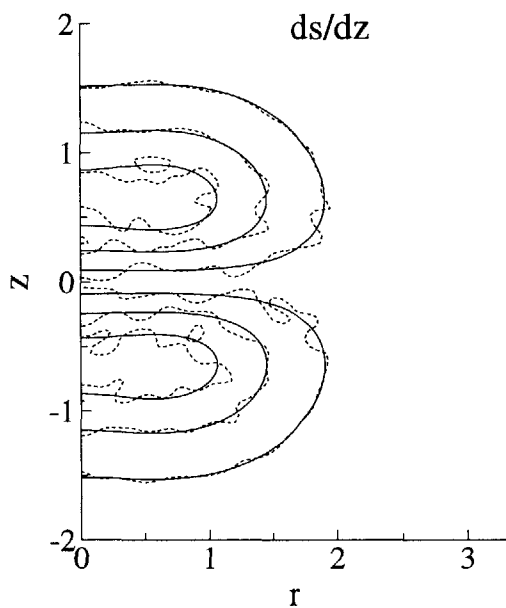
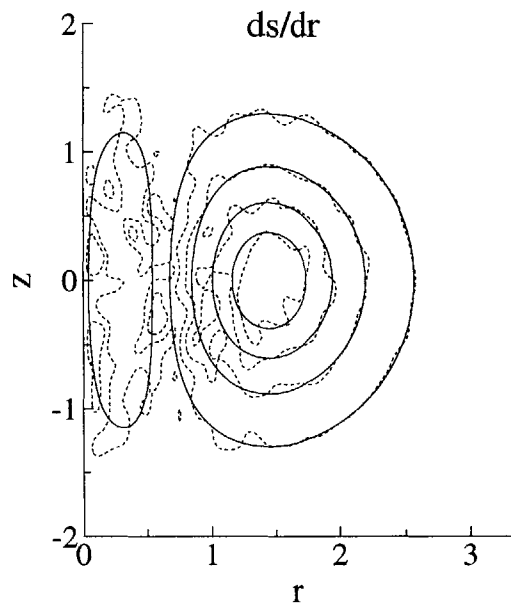


Figure 10-9: Radial and axial components of scalar gradient at $\tau = 0.2$, $\Delta\tau = 0.0005$. Solid lines are exact solution. Dashed lines are numerical gradient. Contour levels for radial component are -0.33, -0.25, -0.15, -0.05 and 0.01. Contour levels for axial component are -0.38, -0.25, -0.1, 0.1, 0.25, and 0.38.

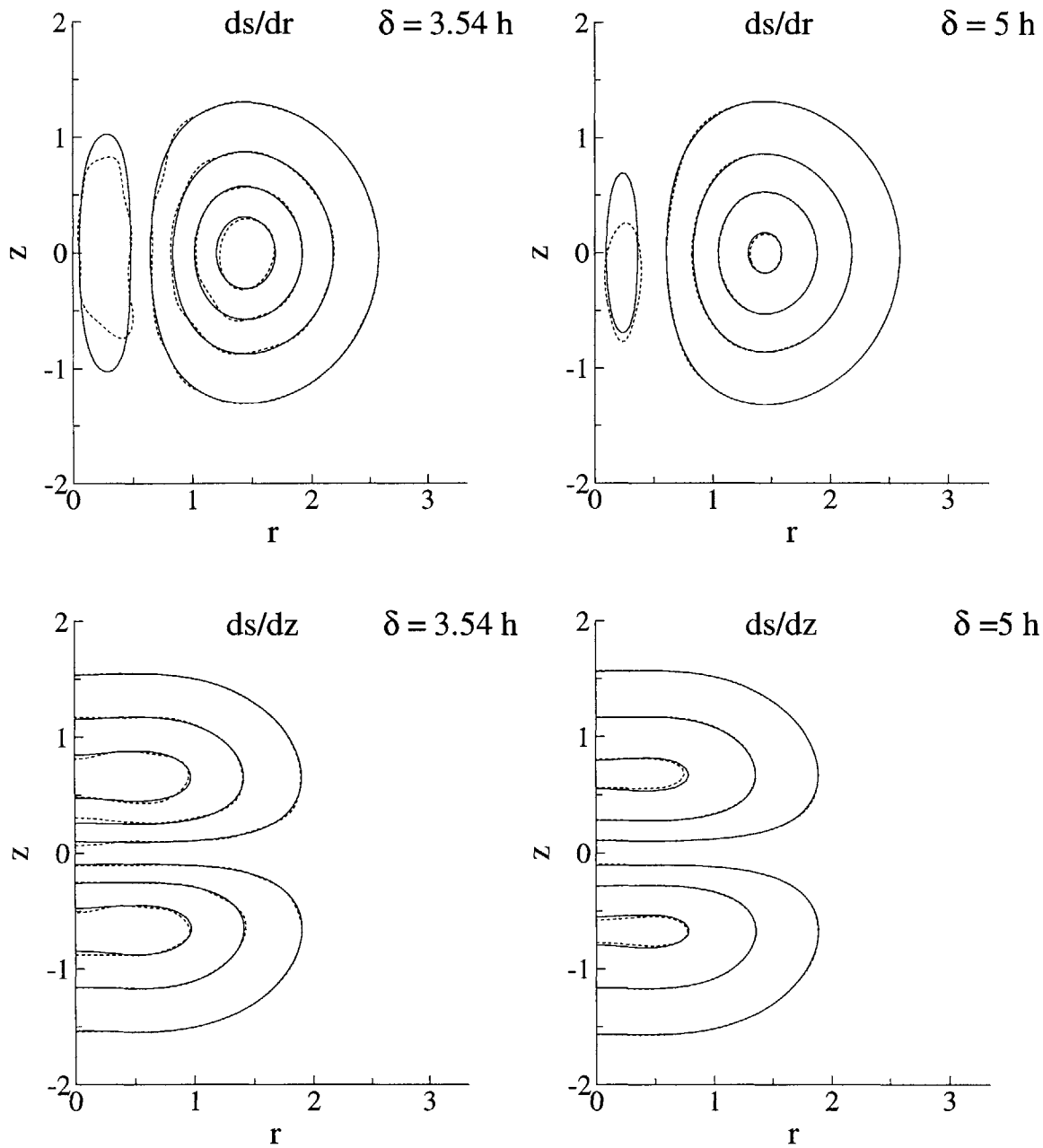


Figure 10-10: Radial and axial components of scalar gradient at $\tau = 0.2$, $\Delta\tau = 0.0005$, $\delta = 3.5h$ and $\delta = 5h$. Solid lines are exact solution. Dashed lines are numerical solution. Contour levels for radial component are -0.33, -0.25, -0.15, -0.05 and 0.01. Contour levels for axial component are -0.38, -0.25, -0.1, 0.1, 0.25, and 0.38.

10.2 Vortex ring

In this section, computation of the evolution of a vortex ring carrying a passive scalar is presented. Even though it is a relatively simple axisymmetric flow, it is fundamental to more complex flows such as jets and plumes. The domain is unbounded and the flow is incompressible. The governing equations are conservation of mass, momentum, and passive scalar, given respectively by

$$\nabla \cdot \mathbf{u} = 0, \quad (10.5)$$

$$\frac{D\mathbf{u}}{Dt} = -\frac{1}{\rho}\nabla p + \frac{1}{Re}\nabla^2\mathbf{u}, \quad (10.6)$$

and

$$\frac{Ds}{Dt} = \frac{1}{Re}\nabla^2 s. \quad (10.7)$$

Since there is no vorticity generation due to buoyancy or baroclinicity, solution of the vorticity equation involves only the convection and diffusion steps.

The initial conditions correspond to an axisymmetric point vortex, located at $r_0 = 1$ and $z_0 = 1$, that has diffused for a time $\tau_0 = 0.002$, where $\tau = t/Re$. The initial circulation and energy are $\Gamma_0 = 1$ and $E_0 = 1$ respectively. The Reynolds number is $Re \equiv \Gamma_0/\nu = 50$. The redistribution length is $h = \sqrt{8\Delta\tau}$. The initial distribution, shown in Figure 10-13, was obtained by diffusing a point vortex using the smoothed redistribution method with $\Delta\tau_0 = 0.0002$, $\sigma_0 = 0$. The initial vorticity and temperature distribution are almost two-dimensional Gaussians with core radius of $\sqrt{4\tau_0}$.

Since the initial core size is zero, overlap is attained by expanding the cores over a specified fraction of the diffusion time step, x . So the diffusion step is split into two substeps according to:

(a) expansion: $\sigma_{\tau+\Delta\tau}^2 = \sigma_\tau^2 + x(4\Delta\tau)$.

(b) redistribution over $(1-x)\Delta\tau$, with $\sigma = \sigma_{\tau+\Delta\tau}$.

An upper bound for the overlap is usually desired, σ_f , then the fraction x is set to zero once $\sigma = \sigma_f$.

The numerical solution, obtained using the vortex method, is compared to a converged numerical solution obtained using finite differences. To avoid confusion, we shall call the former the numerical solution and the later the exact solution. Comparison of vorticity and scalar between numerical and exact solution is done in terms of (i) contours at two times:

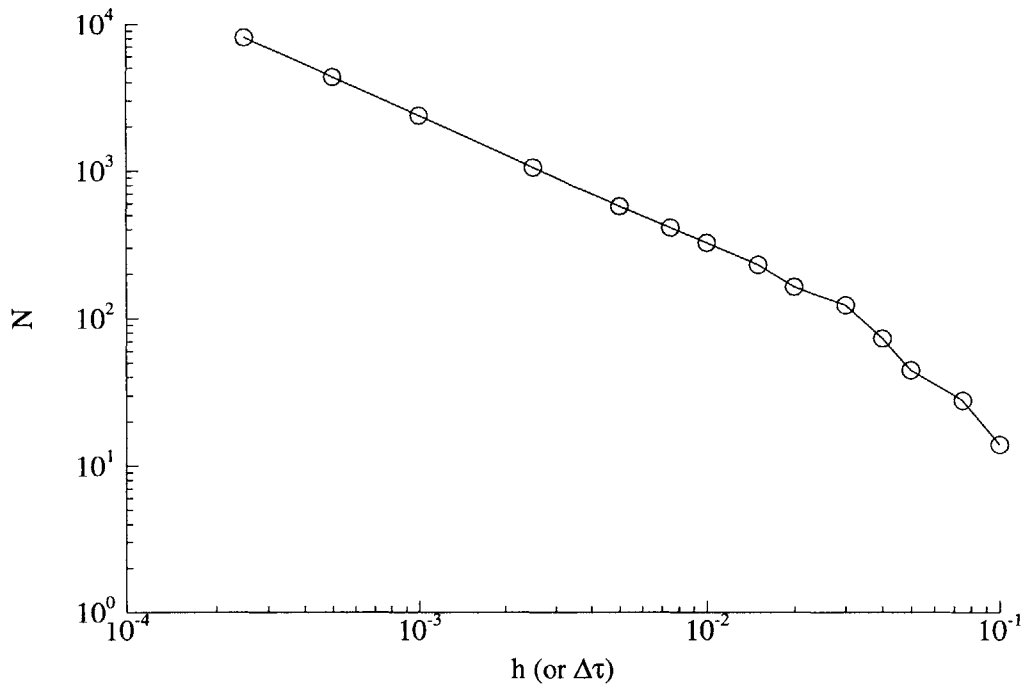


Figure 10-11: Number of elements as a function of time step.

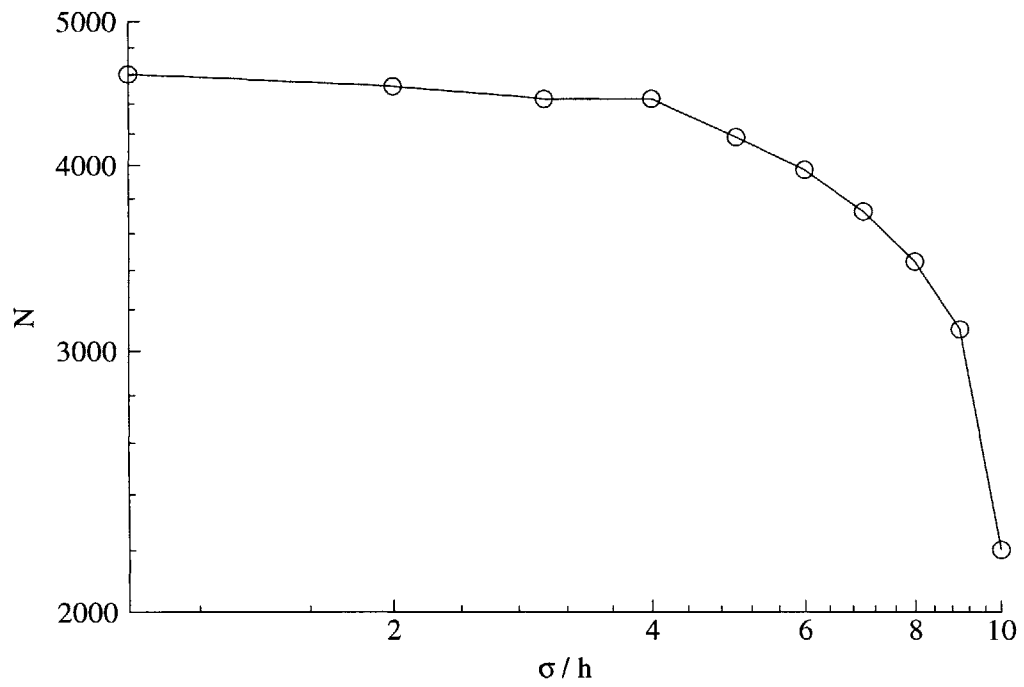


Figure 10-12: Number of elements as function of overlap ratio. $\Delta\tau = 0.0005$.

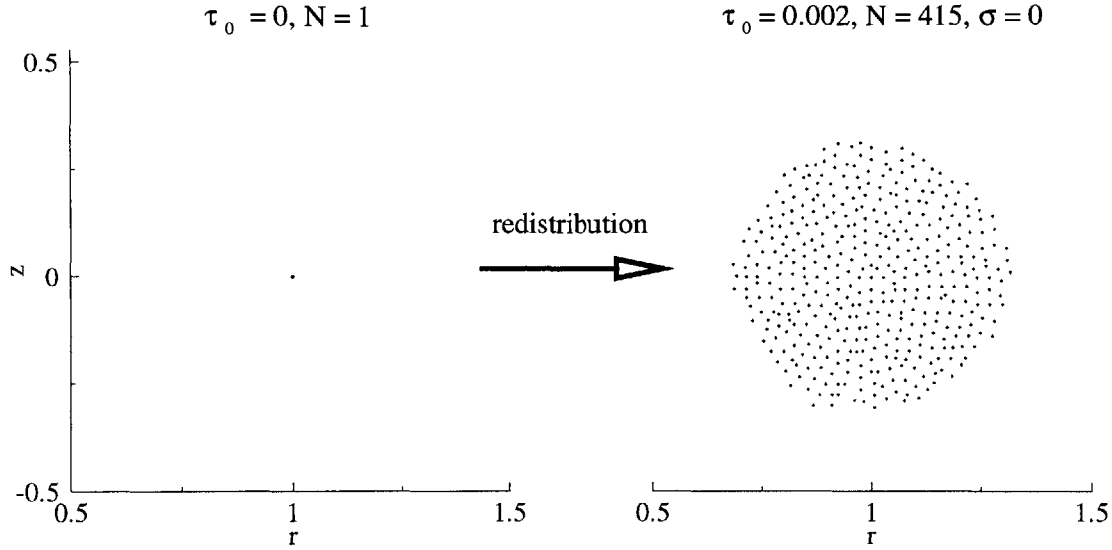


Figure 10-13: Initial elements distribution.

$\tau = 0.1$ and $\tau = 0.2$, (ii) radial and axial profiles at selected locations, (iii) global moments, and (iv) a measure of the global error.

The distribution of computational elements at different times is shown in Figure 10-14 for the case $\Delta\tau = 0.0005$, $\sigma_f = 2h_0$, $x = 0.1$. The distribution is characterized by denser and disordered elements near the center due to the straining effect of the flow. The two circles shown in the lower right are the initial elements spacing (h_0) and the final core radius (σ_f). The number of elements grows from 415 initially to 5720 at $\tau = 0.2$, the time at which 30% of the initial circulation has decayed across the axis of symmetry.

10.2.1 Vorticity and scalar

Figure 10-15 shows the vorticity and scalar at different times. The scalar contours are overlaid on top of the colored vorticity distribution. The contour values are the same for both vorticity and scalar. Notice that away from the axis, the scalar contours are close to the vorticity contours, which reflects that the solution is close to two-dimensional. However, near the axis, the vorticity and scalar behave differently. While the vorticity vanishes at the axis, the scalar does not, but alternatively, its radial gradient does. Note also that for the same reason the center of vorticity is farther from the axis than that of the scalar. At longer times, the vorticity at the center decays faster than the scalar due to the combined effect of spreading and axis cancellation of vorticity.

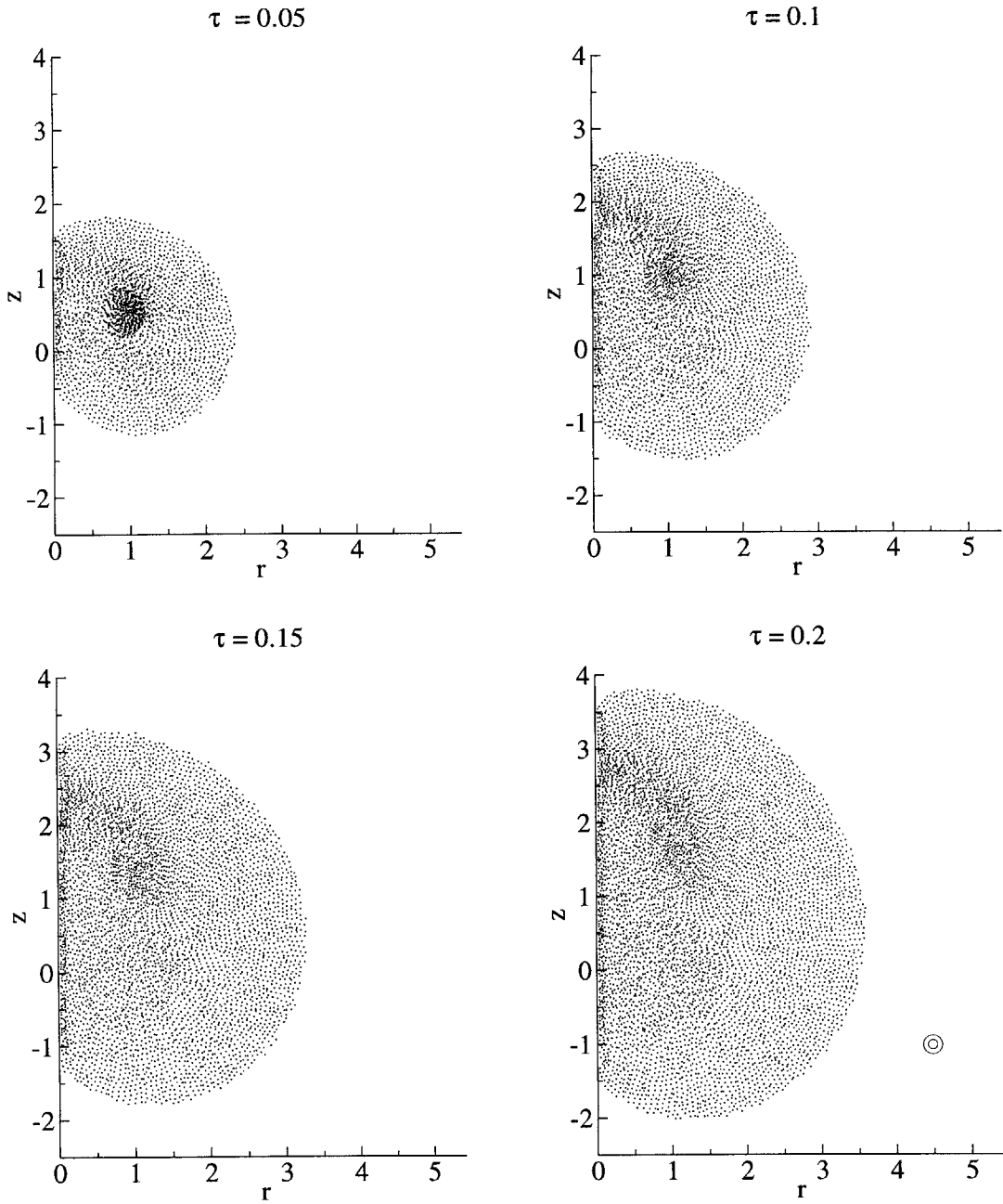


Figure 10-14: Computational elements distribution at different times.

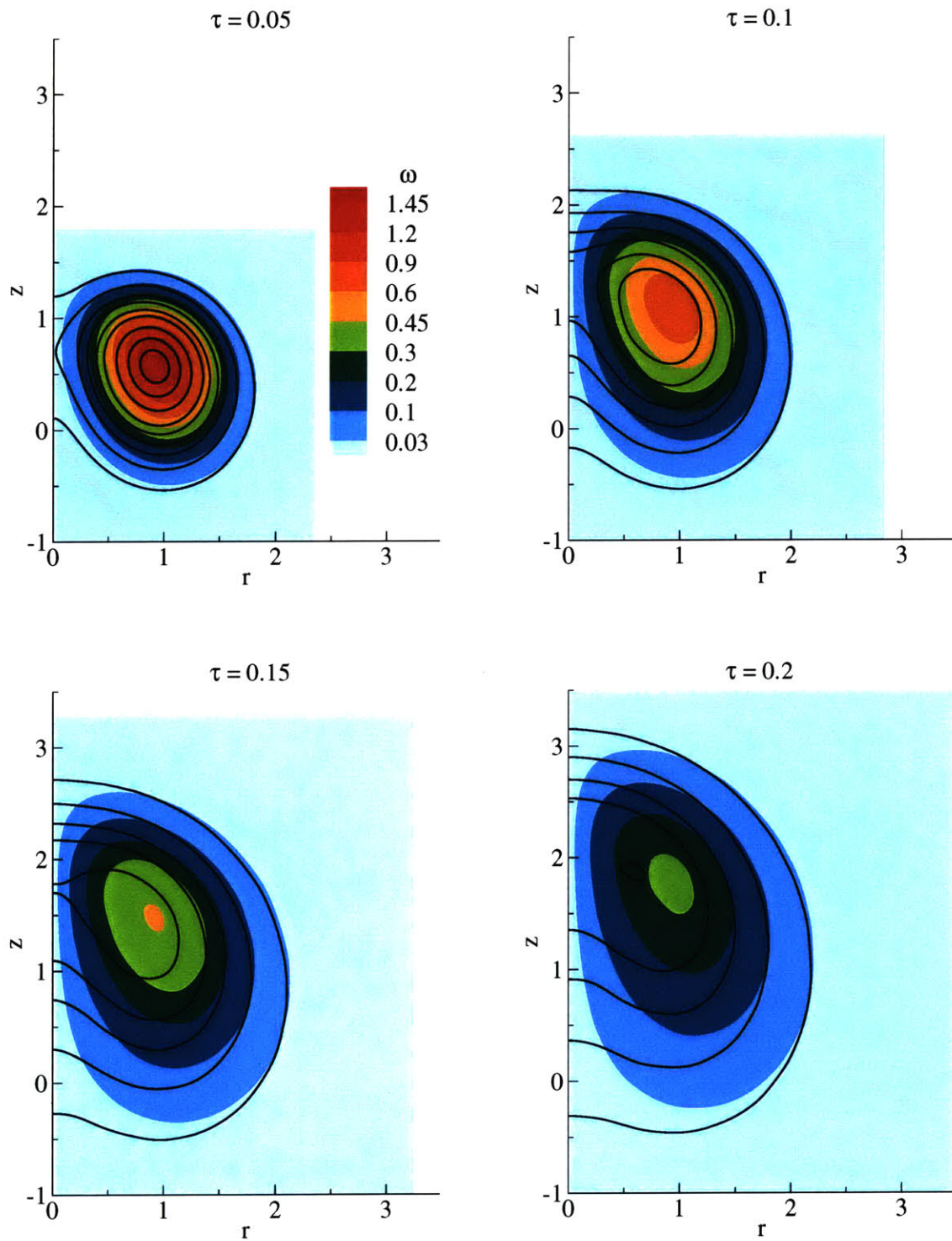


Figure 10-15: Scalar contours overlaid on top of vorticity colored distribution. Scalar contours (inwards) are 0.03, 0.1, 0.2, 0.3, 0.45, 0.6, 0.9, 1.2, and 1.45.

Moments of vorticity and scalar The decay of circulation for different spatial resolutions and fixed overlap ratio (set 2) is shown in Figure 10-16. The solid line is the exact solution. At early times, the flow, almost two-dimensional, is away from the axis. Later, at $\tau \sim 0.05$, the flow reaches the axis, and vorticity cancellation proceeds at larger rate. At large times, the solution approaches that of a stokes flow and the circulation decays as $O(\tau^{-1})$. Notice that for the three spatial resolutions tested the circulation decay is accurately computed with slight improvement for smaller $\Delta\tau$.

The average axial position for the vortex ring, based on the conservation of impulse, is defined as

$$\bar{z}_\omega \equiv \frac{\sum_{i=1}^N \Gamma_i r_i^2 z_i}{\sum_{i=1}^N \Gamma_i z_i}. \quad (10.8)$$

The axial mean position of vorticity for different spatial resolutions and fixed overlap ratio (set 2) is shown in Figure 10-16. Again improvement in the accuracy of the numerical solution is observed for smaller $\Delta\tau$.

The impulse of the vortex ring, $I_\omega \equiv \sum_{i=1}^N \Gamma_i r_i^2$, shown in Figure 10-17, is conserved with errors less than 7×10^{-5} , 3×10^{-5} and 10^{-5} for $\Delta\tau = 0.002$, 0.001 , and 0.0005 respectively. The axial expansion, defined as $\sum_{i=1}^N \Gamma_i z_i^2$ is shown in Figure 10-17.

The error in the total energy is shown in Figure 10-18. Conservation of energy is maintained with a relative error less than 8×10^{-5} , 4×10^{-5} and 2×10^{-5} for $\Delta\tau = 0.002$, 0.001 , and 0.0005 respectively. The mean axial position of the scalar, shown in Figure 10-18, follows that of vorticity. The improvement in the numerical solution for finer spatial resolution is still seen.

The radial expansion of the scalar is shown in Figure 10-19. Unlike the impulse, the scalar radial expansion is not conserved. Figure 10-19 shows the axial expansion of the scalar which follows that of vorticity. It is expected that the behaviour of axial moments is similar for both vorticity and scalar in view of the similarity in the corresponding term in the diffusion equation of each. Also differences in the radial moments is attributed to different radial terms in the diffusion equations for vorticity and scalar.

10.2.2 Convergence and accuracy

Convergence study is based on varying the spatial resolution $\Delta\tau$, overlap ratio σ_f/h_0 , and core expansion fraction x . Correspondingly, computations were conducted using the

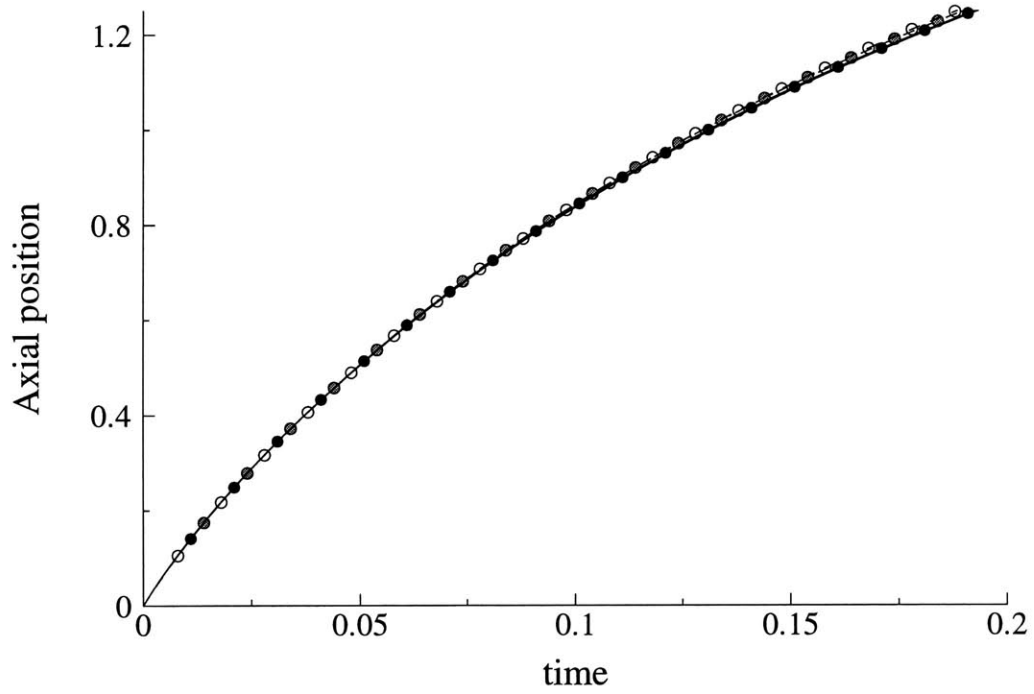
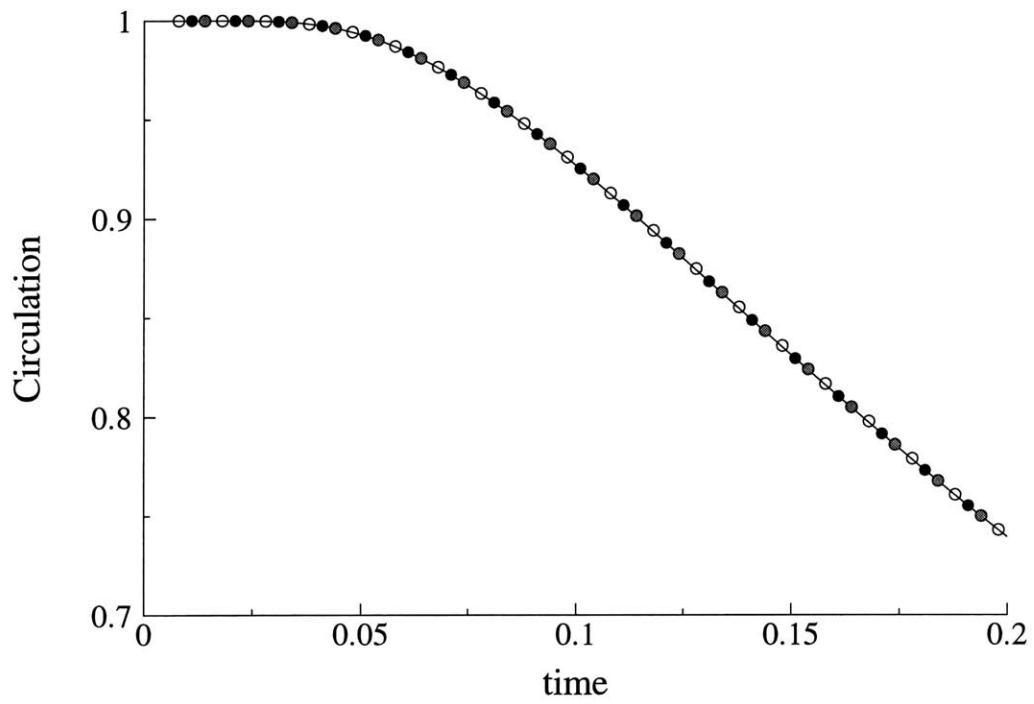


Figure 10-16: Upper figure: total circulation. Lower figure: mean axial position. Solid line is exact solution. Symbols are numerical solution: $\Delta\tau = 0.0005$: black circles, $\Delta\tau = 0.001$: grey circles, and $\Delta\tau = 0.002$: empty circles.

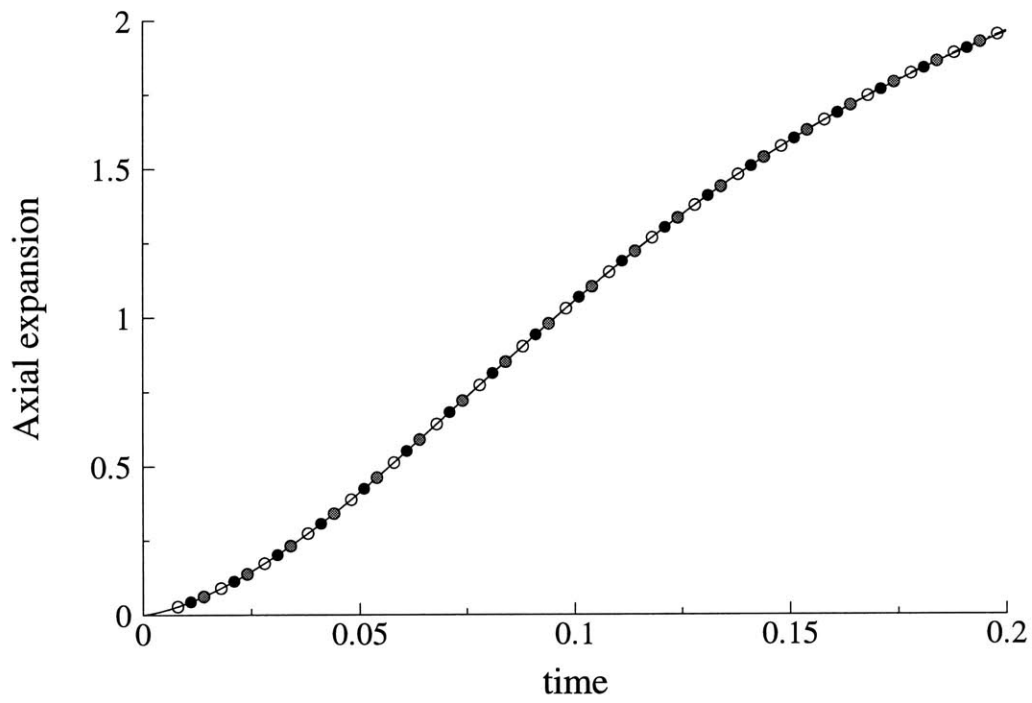
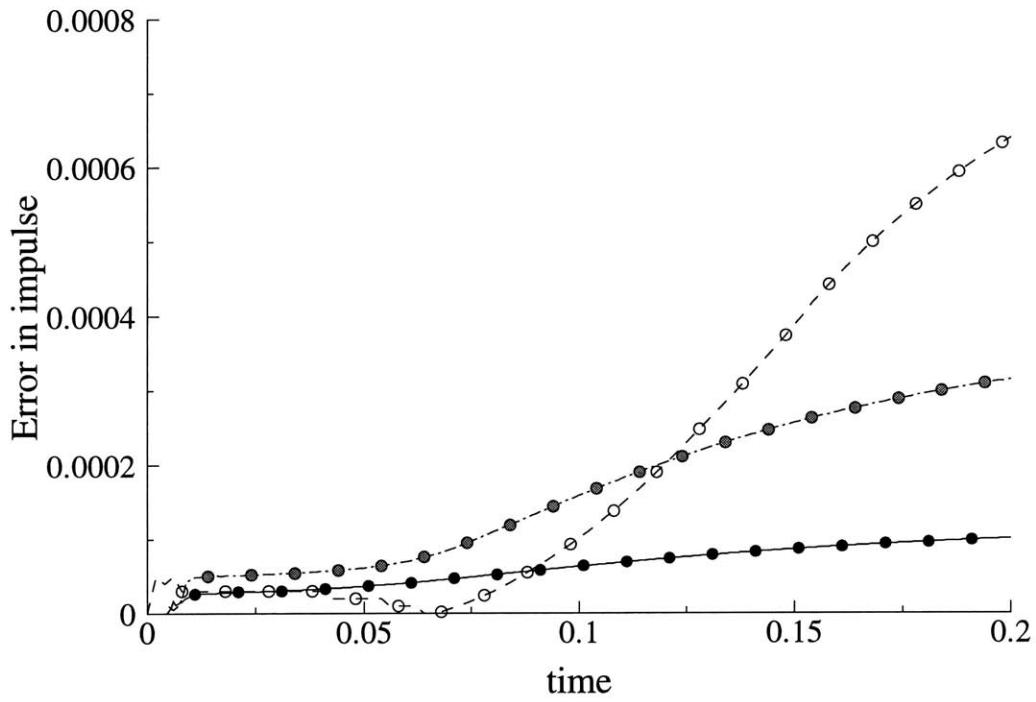


Figure 10-17: Upper figure: error in impulse. Lower figure: mean axial expansion. Solid line is exact solution. Symbols are numerical solution: $\Delta\tau = 0.0005$: black circles, $\Delta\tau = 0.001$: grey circles, and $\Delta\tau = 0.002$: empty circles.

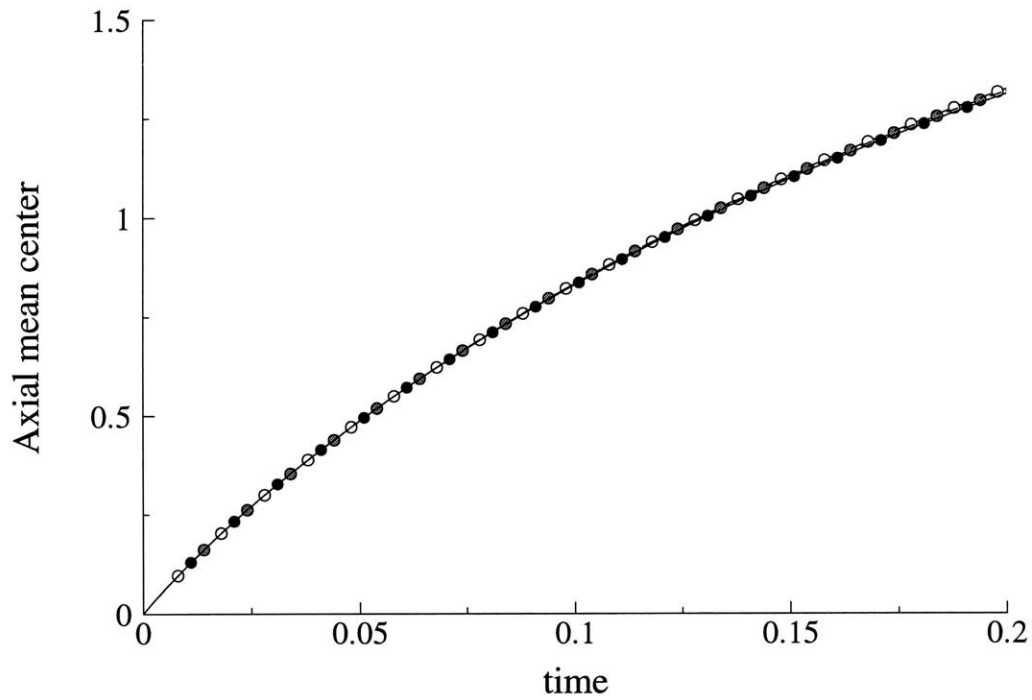
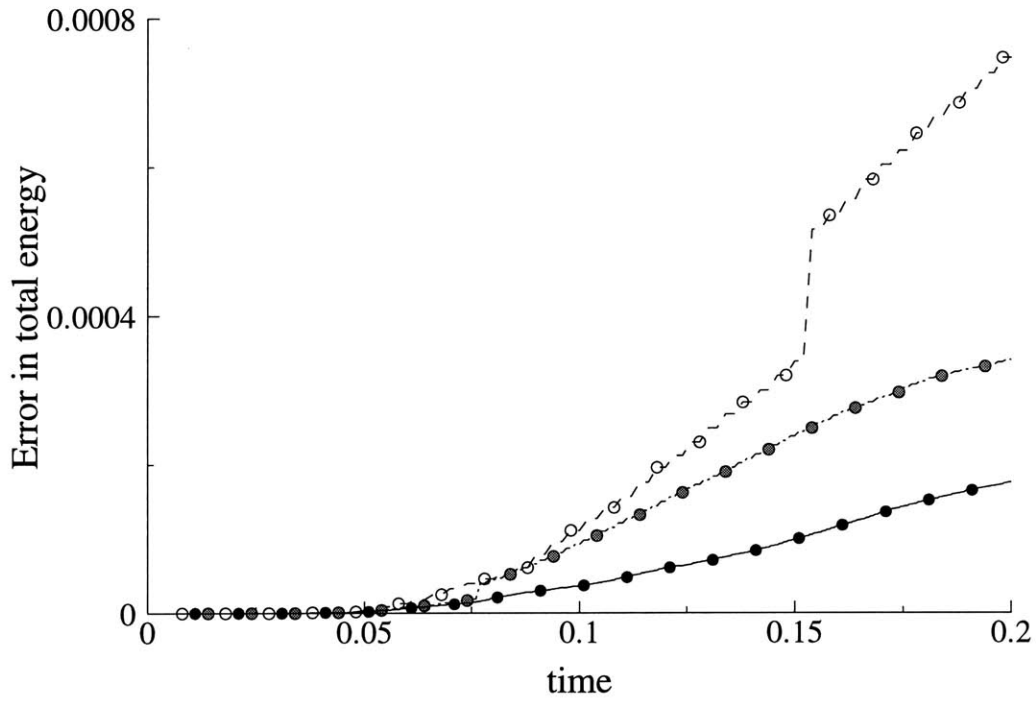


Figure 10-18: Upper figure: error in total energy. Lower figure: mean axial position. Solid line is exact solution. Symbols are numerical solution: $\Delta\tau = 0.0005$: black circles, $\Delta\tau = 0.001$: grey circles, and $\Delta\tau = 0.002$: empty circles.

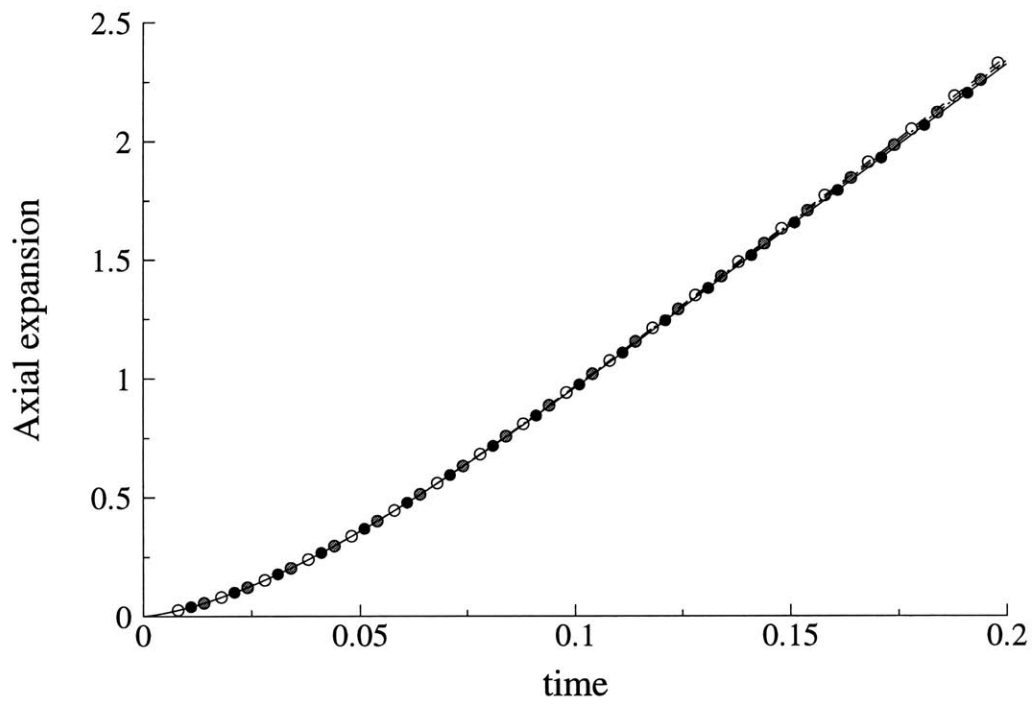
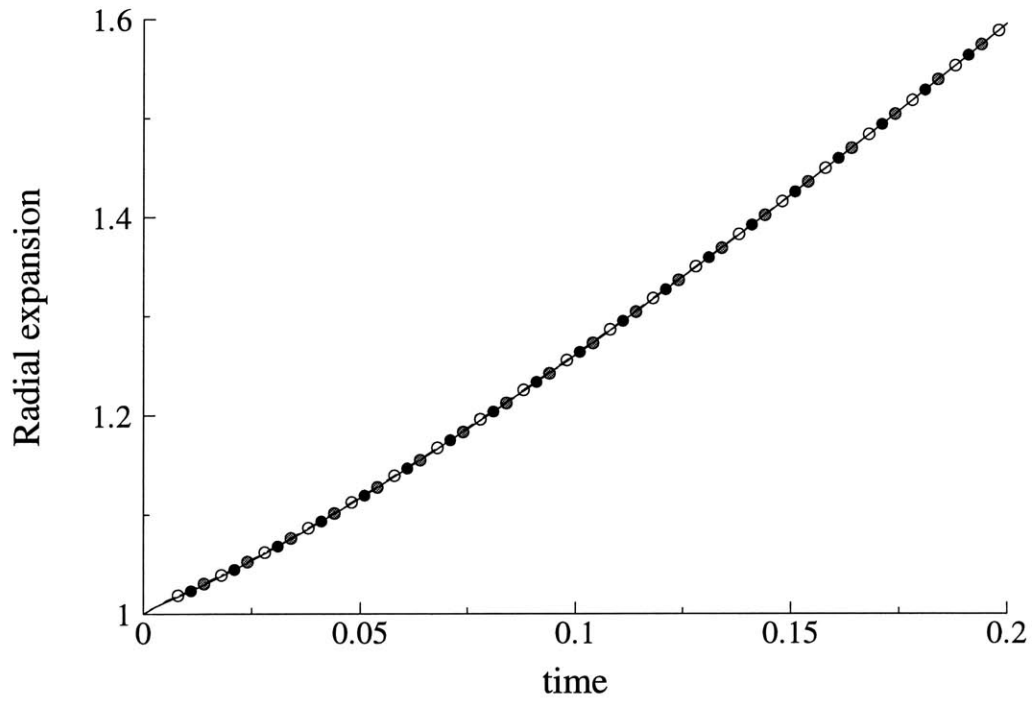


Figure 10-19: Upper figure: mean radial expansion. Lower figure: mean axial expansion. Solid line is exact solution. Symbols are numerical solution: $\Delta\tau = 0.0005$: black circles, $\Delta\tau = 0.001$: grey circles, and $\Delta\tau = 0.002$: empty circles.

$\Delta\tau$	h_0	σ_f	σ_f/h_0	x	N	$ \epsilon _{L_2}^{(\omega)}$	$ \epsilon _{L_2}^{(x)}$
0.0005	0.0632	0.245	3.873	0.075	7423	3.33×10^{-4}	2.46×10^{-4}
0.001	0.0894	0.245	2.738	0.075	3990	3.31×10^{-4}	2.46×10^{-4}
0.002	0.1265	0.245	1.936	0.075	2175	3.30×10^{-4}	2.55×10^{-4}
0.005	0.2000	0.245	1.225	0.075	1330	4.27×10^{-4}	4.33×10^{-4}
0.01	0.2828	0.245	0.866	0.075	910	7.27×10^{-4}	8.09×10^{-4}
0.0005	0.0632	0.1265	2.0	0.1	5720	1.82×10^{-4}	1.74×10^{-4}
0.001	0.0894	0.1789	2.0	0.1	3069	2.63×10^{-4}	2.34×10^{-4}
0.002	0.1265	0.2529	2.0	0.1	1688	3.91×10^{-4}	3.16×10^{-4}
0.0005	0.0632	0.0632	1.0	0.1	7047	3.61×10^{-4}	4.01×10^{-4}
0.0005	0.0632	0.0949	1.5	0.1	6926	3.77×10^{-4}	1.92×10^{-4}
0.0005	0.0632	0.1265	2.0	0.1	5720	1.82×10^{-4}	1.74×10^{-4}
0.0005	0.0632	0.1581	2.5	0.1	4674	2.21×10^{-4}	2.05×10^{-4}
0.0005	0.0632	0.2236	3.535	0.1	6159	3.52×10^{-4}	2.83×10^{-4}
0.0005	0.0632	0.1265	2.0	0.02	7315	1.64×10^{-4}	1.61×10^{-4}
0.0005	0.0632	0.1265	2.0	0.1	5720	1.82×10^{-4}	1.74×10^{-4}
0.0005	0.0632	0.1265	2.0	0.18	7567	7.20×10^{-4}	5.97×10^{-4}
0.0005	0.0632	0.1265	2.0	0.5	6961	5.29×10^{-4}	2.28×10^{-4}

Table 10.1: Parameters.

following sets of parameters:

1. $\Delta\tau = 0.0005, 0.001, 0.002, 0.005, 0.01, \sigma = \sigma_0 = 0.245, x = 0.075$.
2. $\Delta\tau = 0.0005, 0.001, \text{ and } 0.002, \sigma_f = 2h_0, x = 0.1$.
3. $\Delta\tau = 0.0005, \sigma_f/h_0 = 2, 2.5, \text{ and } 3.54, x = 0.1$.
4. $\Delta\tau = 0.0005, \sigma_f/h_0 = 2, x = 0.02, 0.1, 0.18, 0.5$.

The global errors in vorticity and scalar, as defined by equation (10.4), are presented in Table 10.1.

Variable h_0 , fixed σ_f , fixed x

For a fixed core size (σ_f) and expansion fraction (x), reducing the initial elements spacing h_0 (or $\Delta\tau$) results in smoother and more accurate solution for overlap ratio greater than two. Figure 10-20 shows vorticity and scalar contours at $\tau = 0.2$ for $\Delta\tau = 0.01, 0.002$, and 0.0005 respectively. While the solutions for $\Delta\tau = 0.0005$ and 0.002 are similar in terms of accuracy and smoothness, the solution for $\Delta\tau = 0.01$ is noisy with oscillations around the exact solution. This behaviour may be explained in terms of the overlap ratio. For

$\Delta\tau = 0.0005$ and 0.002 the overlap ratios, 3.873 and 1.936 respectively, are larger than one. On the other hand, the overlap ratio for $\Delta\tau = 0.01$ is $0.866 < 1$. This is in accordance with the behaviour witnessed in the stokes problem, as discussed in the previous section. The global error for vorticity and scalar is presented in Figure 10-21. For $\sigma_f/h_0 < 2$, the error decreases according to . Increasing the overlap ratio beyond two has little impact on the error. This may be explained in view of error bound, discussed in section 3.6, given by the expression

$$\|\text{error}\|_{L^1} \leq \text{constant} \cdot \left[\sigma^p + \left(\frac{h}{\sigma} \right)^L \sigma \right]. \quad (10.9)$$

Since $\sigma = \sigma_f$ is constant, its impact does not vary as $h = h_0$ varies. As h decreases, h/σ decreases, resulting in a decrease in the error until a point is reached where the discretization error due to overlap is smaller than the smoothness error due to core size at which the error is approximately only a function of σ .

Variable h_0 , fixed σ_f/h_0 , fixed x

Increasing the initial element spacing and core size such that the overlap ratio is kept fixed results in smoother less accurate solutions. This is due to the smoothness error associated with the core size. Notice that the discretization error is frozen due to the constant overlap ratio. The impact of using larger cores is shown in Figure 10-22 for $\sigma_f = 0.1265, 0.1789,$ and 0.2529 and $\sigma_f/h_0 = 2$. The corresponding global error in vorticity and scalar is shown in Figure 10-23.

Fixed h_0 , variable σ_f/h_0 , fixed x

Fixing the initial element spacing and varying the overlap ratio results in a variable core size. According to the inequality 10.9, this introduces both smoothness error and discretization error. For small overlap ratio the core size is small and consequently the discretization error is dominant. On the other hand, for large overlap ratio, the core size is large and consequently the smoothness error is dominant. Between these two extremes, one would expect moderate values of overlap ratio and core size that result in minimum error. Qualitatively, this is shown in Figure 10-24 where for $\sigma_f/h_0 = 1$, the discretization error is dominant and the numerical solution is noisy and oscillatory, whereas for $\sigma_f/h_0 = 3.535$, the smoothness error is dominant and the solution is smooth with a deviation from the exact solution. How-

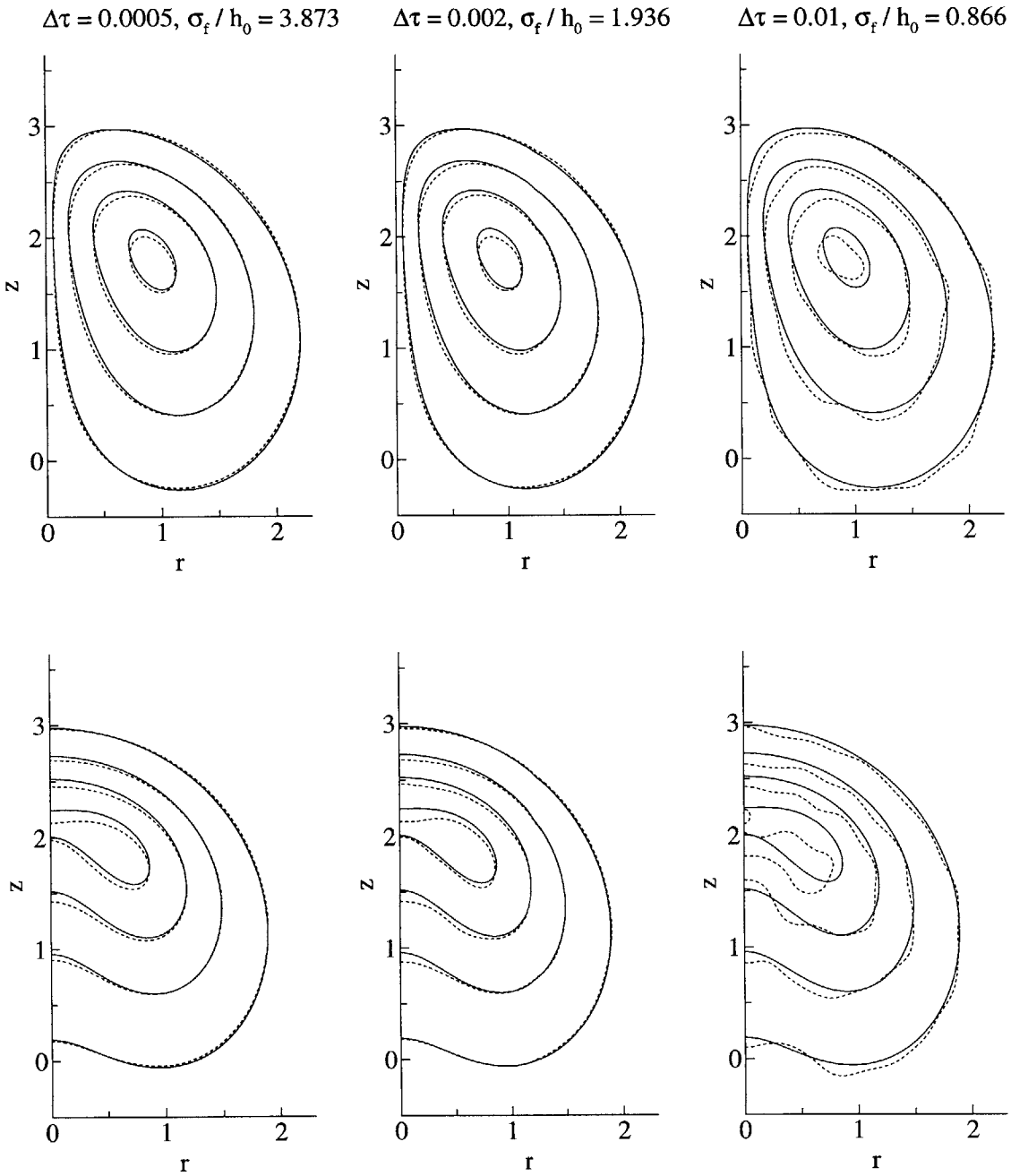


Figure 10-20: Vorticity (upper) and scalar (lower) contours at $\tau = 0.2$ for $\Delta\tau = 0.0005, 0.002,$ and 0.01 . Core size and core expansion fraction are fixed.

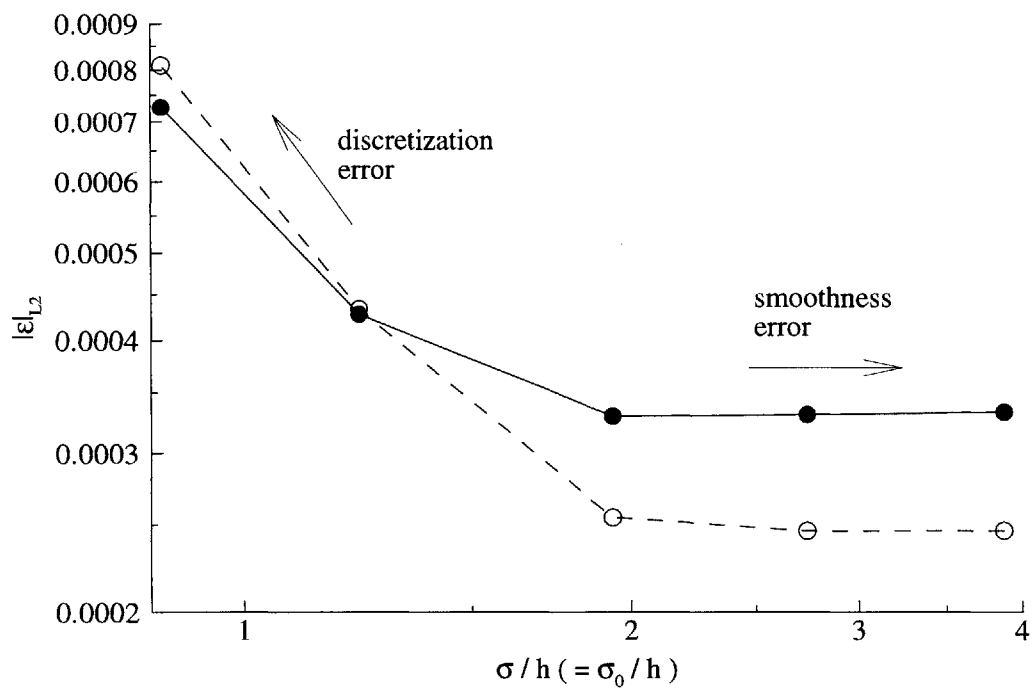


Figure 10-21: Global error as a function of overlap ratio. Core size and core expansion fraction are fixed. Vorticity: filled circles. Scalar: empty circles.

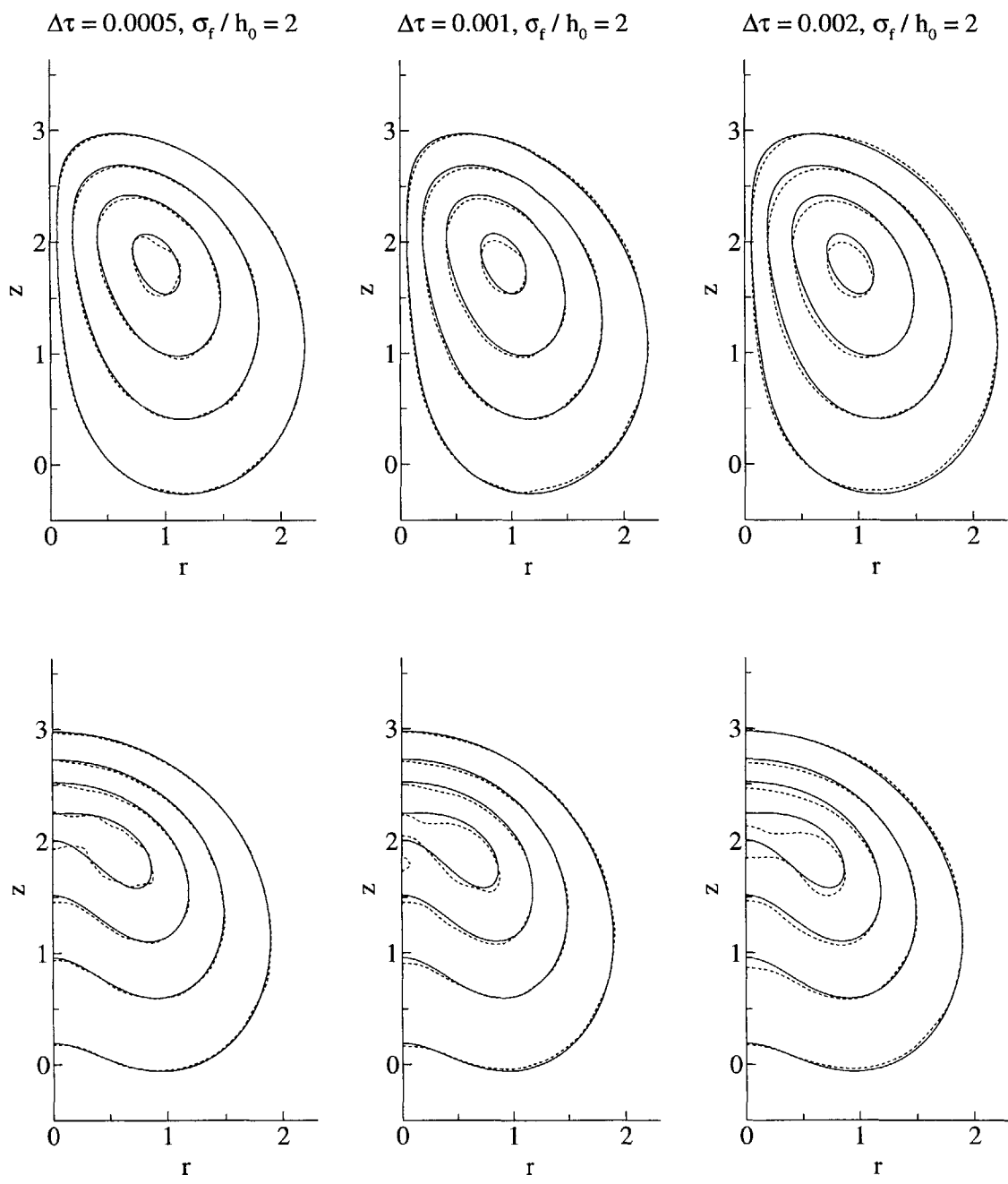


Figure 10-22: Vorticity (upper) and scalar (lower) contours at $\tau = 0.2$ for $\Delta\tau = 0.0005$, 0.001, and 0.002. Overlap ratio and core expansion fraction are fixed.

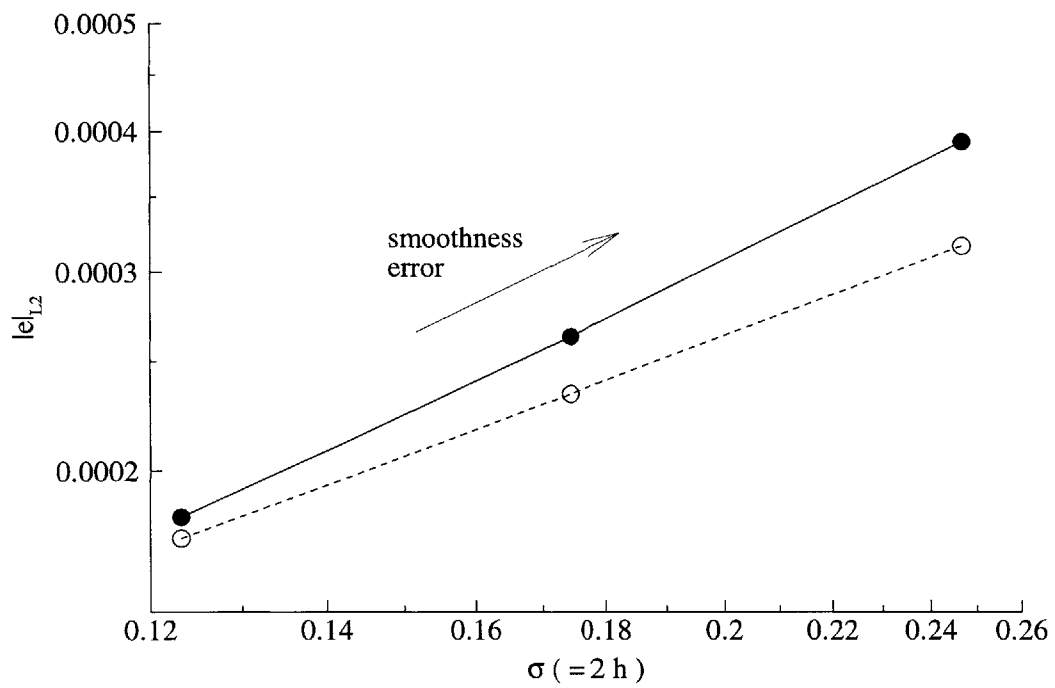


Figure 10-23: Global error as a function of core size. Overlap ratio and core expansion fraction are fixed. Vorticity: filled circles. Scalar: empty circles.

ever, for σ_f/h_0 , there is a balance between the two errors and the solution is most accurate. Quantitatively, this error behavior is shown in Figure 10-25, where for $\Delta\tau = 0.0005$, the optimal solution seems to lie in the neighborhood of $\sigma_f/h_0 = 2$.

Fixed h_0 , fixed σ_f/h_0 , variable x

Increasing the core expansion fraction, while fixing h_0 and σ_f , means that the core radius, initially zero, is increased at a larger rate until it reaches its desired upper bound σ_f . Thus, large values of x results in large cores and consequently introduction of error dominated by its smoothness component into the solution at early times. Consequently, this error propagates in time resulting in smooth numerical solution with large error. Smaller values of x may lead to the dominance of discretization error at early times. This is seen in the vorticity and scalar contours at $\tau = 0.2$ for $x = 0.02, 0.1$ and 0.5 shown in Figure 10-26. The values $x = 0.02$ results in a slight noisy solution, while the value $x = 0.5$ results in a smoother solution with larger error. The global error is presented in Figure 10-27.

10.2.3 Number of elements

The number of elements at $\tau = 0.2$ for all the cases considered is shown in Table 10.1. For constant initial element spacing, the number of elements does not vary much as the core size and/or the core expansion fraction vary. However, for variable initial element spacing (or time step), the number of elements increases linearly with the inverse of the square root of the initial element spacing (or the inverse of the time step.) This seems to be the case at early times as well, as shown in Figure 10-28, where the number of elements, as a function of time, is plotted for three different time steps. Notice that at early times the number of elements increases quadratically in time, whereas for longer times it increases linearly.

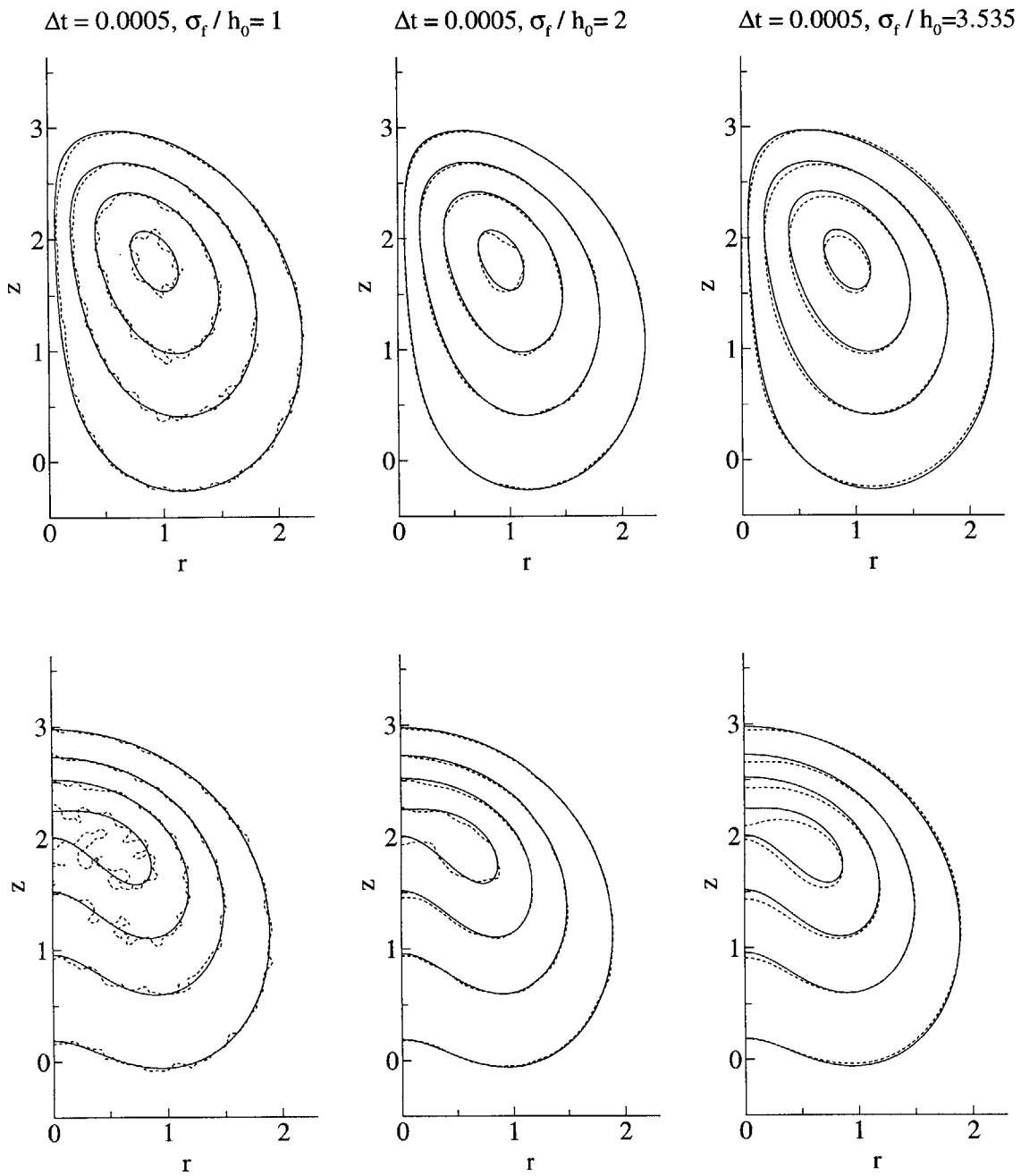


Figure 10-24: Vorticity (upper) and scalar (lower) contours at $\tau = 0.2$ for $\sigma_f/h_0 = 1, 2,$ and 3.535 . Core expansion fraction is fixed.

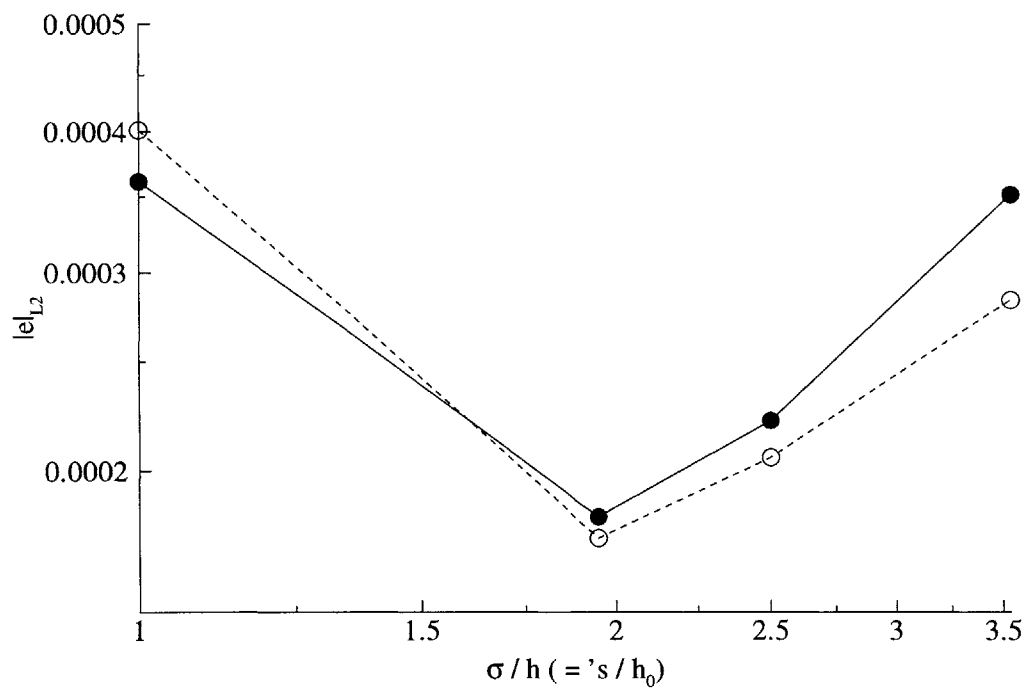


Figure 10-25: Global error as a function of overlap ratio. Core expansion fraction is fixed. Vorticity: filled circles. Scalar: empty circles.

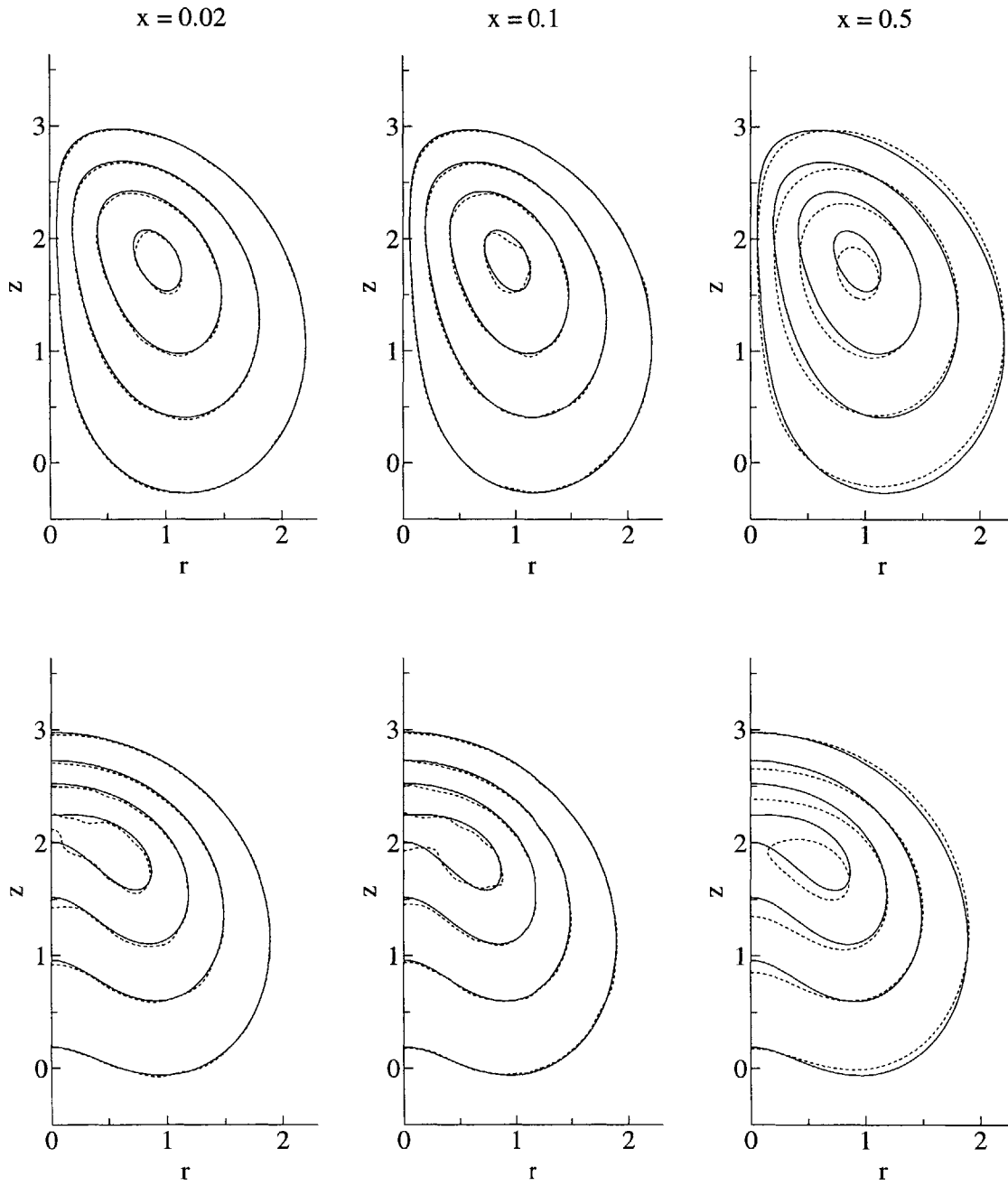


Figure 10-26: Vorticity (upper) and scalar (lower) contours at $\tau = 0.2$ for $x = 0.02, 0.1,$ and 0.5 . Final core size and initial element spacing are fixed.

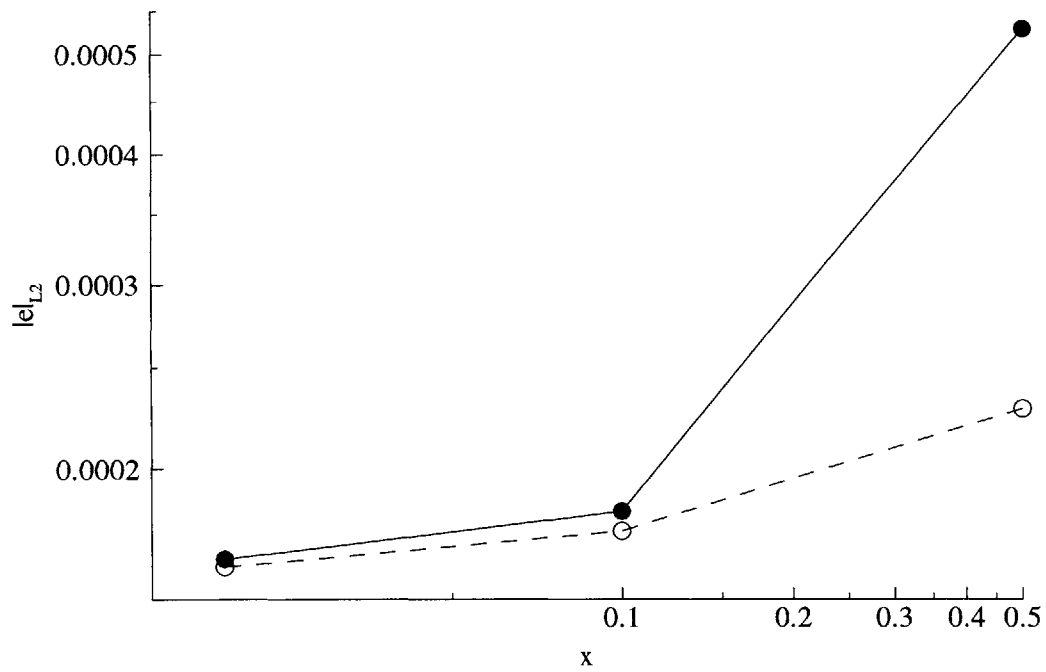


Figure 10-27: Global error as a function of core expansion fraction. Final core size and initial element spacing are fixed. Vorticity: filled circles. Scalar: empty circles.

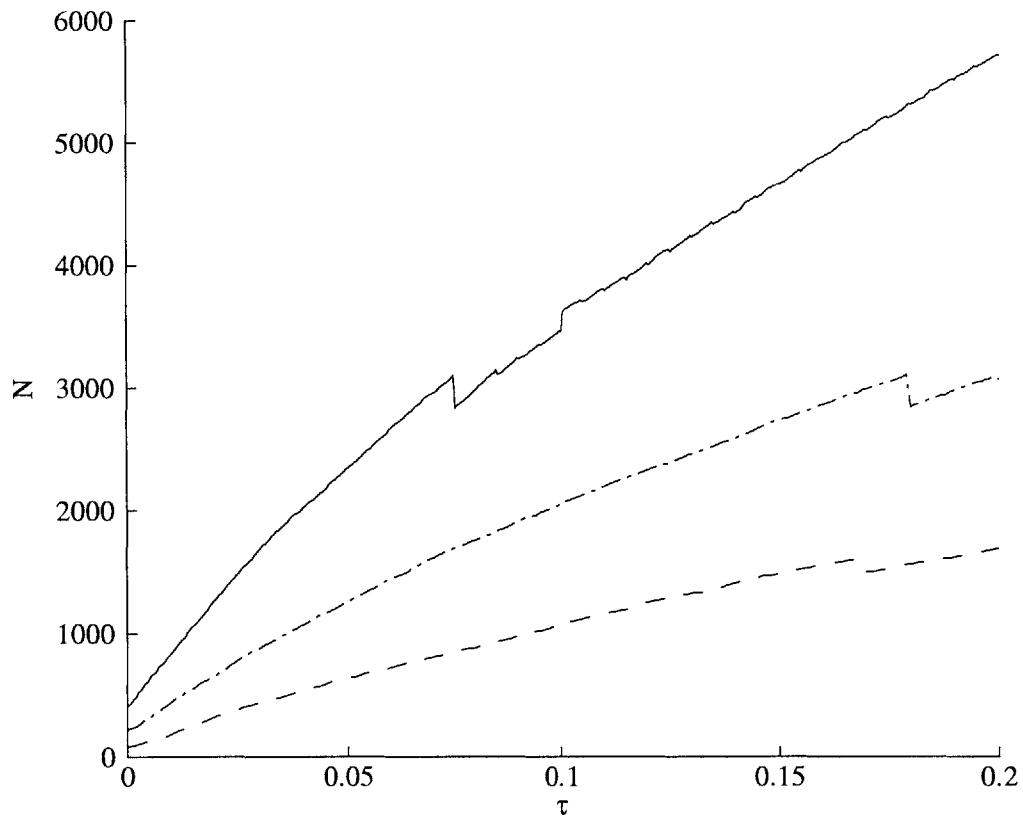


Figure 10-28: Number of elements as a function of time. Solid line: $\Delta\tau = 0.0005$, dash-dot line: $\Delta\tau = 0.001$, and dashed line: $\Delta\tau = 0.002$

Chapter 11

Solutions Using the Discrete Source Method

The example considered is that of an axisymmetric "ring" of methane reacting with air. The fuel ring consists initially of a region of fuel surrounded by air. Buoyancy is expected to play a dominant role since it is the major source of vorticity generation. The density change in time is also a source of volumetric expansion. The vorticity and energy equations are coupled via the density and its gradients. The chemical reaction across the flame produces sharp density gradients and products of lower density.

The objectives are to establish numerical convergence and to investigate the impact of radiation on a reacting buoyant flow.

11.1 Assumptions

1. Unbounded axisymmetric domain.
2. Reynolds number is constant.
3. Prandtl number is unity.
4. Lewis number of all species is unity.
5. Chemical reaction is single step, irreversible and of infinite rate.
6. Gases are ideal, gray and non-scattering.

11.2 Governing equations

The governing equations, in dimensionless form, are then given by

$$\frac{D\rho}{Dt} + \rho \nabla \cdot \mathbf{u} = 0, \quad (11.1)$$

$$\frac{D\mathbf{u}}{Dt} = -\frac{1}{\rho} \nabla p + \frac{1}{Re} \nabla^2 \mathbf{u} + (1 - \rho) \hat{\mathbf{z}}, \quad (11.2)$$

and

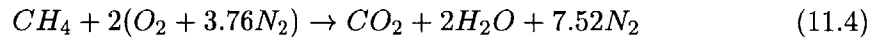
$$\frac{Ds}{Dt} = \frac{1}{Re} \nabla^2 s. \quad (11.3)$$

where s corresponds to a Shvab-Zel'dovich scalar.

11.3 Parameters

The parameters are:

- Reynolds number: $Re = 50$.
- The mass stoichiometric ratio: $\phi = 4.0$.
- Heat of reaction: $Q_f \equiv h_f^0 / c_{p0} T_0 = 80$, where h_f^0 is the heat of reaction of fuel per unit mass.
- The fuel is Methane.
- The chemical reaction is:



and the molar masses are: $M_f = 16$, $M_o = 32$, $M_d = 28$, and $M_p = 26.62$.

11.4 Initial conditions

The initial vorticity is zero. The initial temperature and species distributions, shown in Figure 11-1 correspond to diffusion of a Dirac delta source located at $r_0 = 1$, $z_0 = 0$ over a time $\tau_0 = 0.002$, where $\tau \equiv t/Re$. The initial distribution, consisting of 756 of elements,

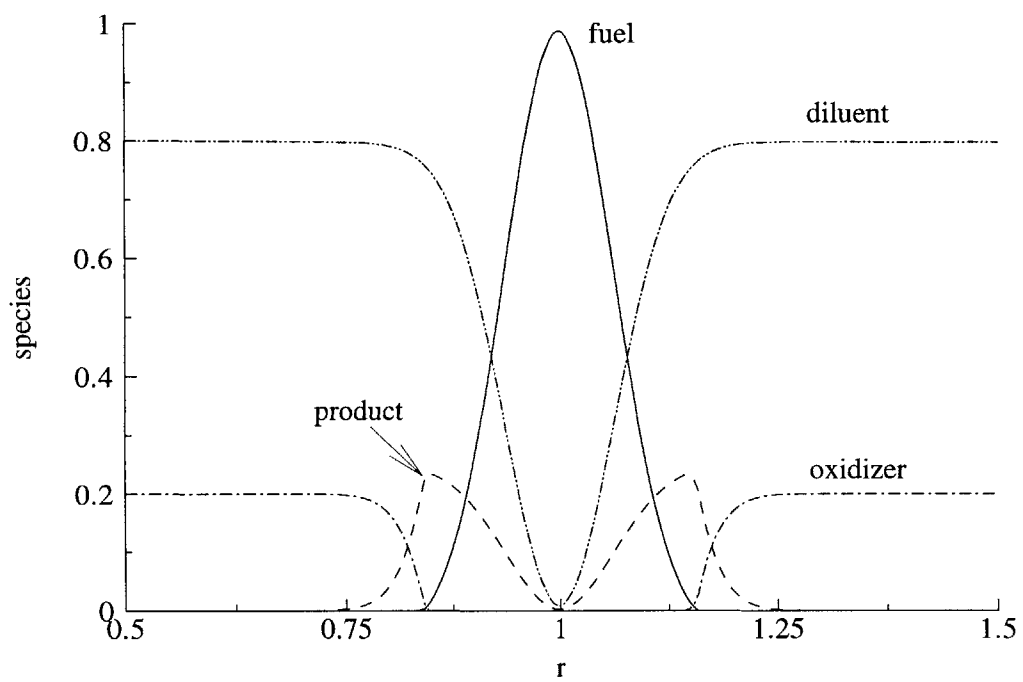


Figure 11-1: Initial species radial distribution at $z = 0$.

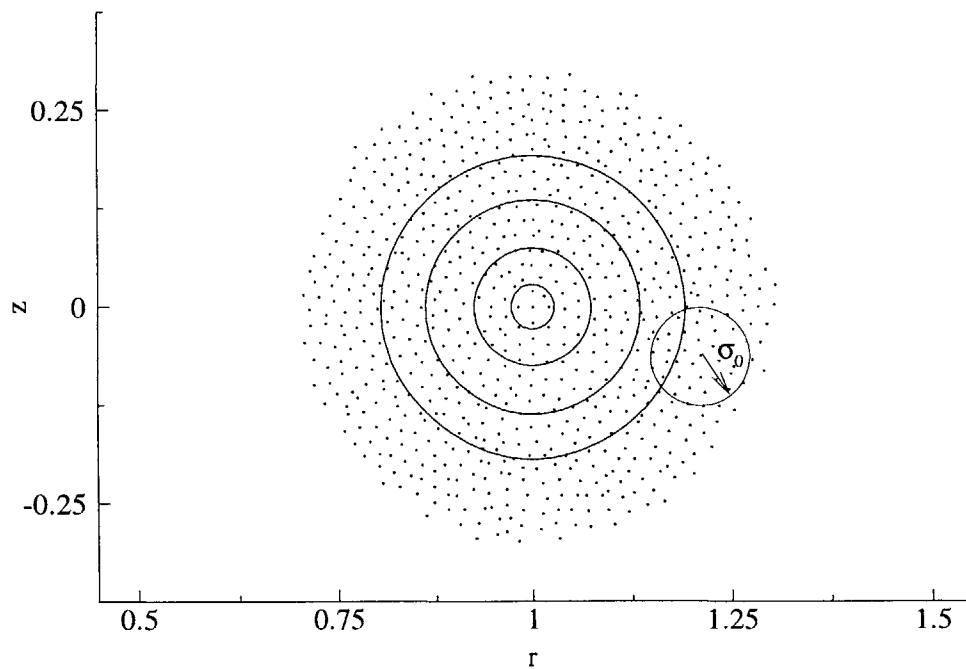


Figure 11-2: Initial elements distribution. Mixture fraction contours: 0.01, 0.1, 0.5, & 0.9.

shown in Figure 11-2, was obtained by diffusing the point source using the smoothed re-distribution method with $\Delta\tau_0 = 0.0002$, and the core radius was increased from $\sigma = 0$ to $\sigma_0 = \sqrt{20\Delta\tau_0}$. Contours of the mixture fraction are also shown in the figure. The mixture fraction varies from zero on the air side to one on the fuel side. The boundary conditions are:

on the fuel side: $Y_f = 1, Y_o = 0, Y_p = 0, Y_d = 0, T = 1$.

on the air side: $Y_f = 0, Y_o = 0.2, Y_p = 0, Y_d = 0.8, T = 1$.

11.5 Boundary conditions

- At infinity:

$$\omega_{\mathbf{r}\rightarrow\infty} = 0 \text{ and } s_{\mathbf{r}\rightarrow\infty} = s_0. \quad (11.5)$$

- At axis of symmetry:

$$\omega_{r=0} = 0 \text{ and } \left(\frac{\partial s}{\partial r}\right)_{r=0} = 0. \quad (11.6)$$

11.6 Numerical parameters

The computations were conducted with the following numerical parameters: $h = \sqrt{8\Delta\tau}$, $\Delta\tau = 0.0005, 0.001, 0.002, \text{ and } 0.005$, and the final time is $\tau_f = 0.2$, where h is the initial elements spacing. The core expansion fraction of the diffusion step and the upper bound of the core radius were chosen to be $x = 0.1$ and $\sigma_{max} = 4h$. Unless otherwise specified, results discussed correspond to $\Delta\tau = 0.0005$.

11.7 Results and discussion

The case of the reacting fuel ring without radiation is discussed first. The role of radiation is discussed next.

11.7.1 Vorticity

In the early stages, the temperature distribution resembles that of a two dimensional planar problem; it is symmetrical around the r and z axes passing through the ring center. The corresponding vorticity distribution, generated due to the interaction between temperature

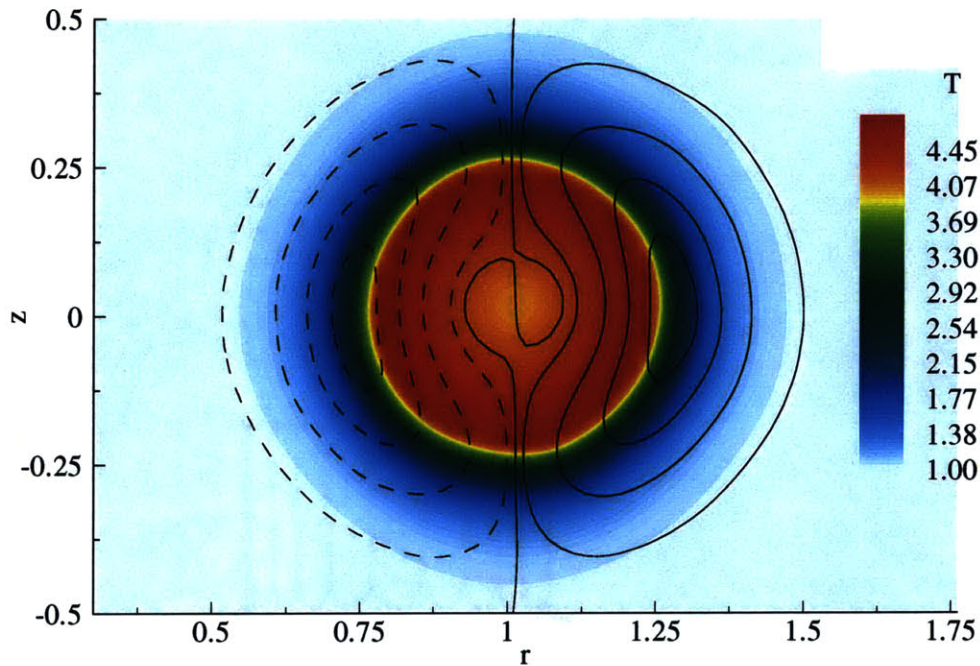


Figure 11-3: Vorticity contours at $\tau = 0.005$. Dashed contours (blue outwards): -1.4, -1, -0.5 & -0.1. Solid contours (red inwards): 0, 0.1, 0.5, 1 & 1.4. Temperature distribution is also shown.

gradients and gravity, is also symmetric. This is confirmed in Figure 11-3, where vorticity contours are overlaid on top of the temperature distribution. Note that positive vorticity is associated with negative temperature gradient and vice versa. These two symmetrical regions of opposite vorticity balance each other so that the flow is dominated by diffusion and convection plays a minor role. However, as the vorticity spreads, it starts dissipating across the z axis. Thus, diffusion across the axis causes the negative vorticity to decrease in absolute value, so that the net overall circulation is positive causing the overall structure to rotate clockwise. This is confirmed in Figure 11-4 where the vorticity contours are plotted at four times $\tau = 0.05, 0.1, 0.15$ and 0.2 . The symmetrical character of the vorticity at initial times can still be seen at $\tau = 0.05$. At later times, the structure rises and rotates clockwise. Assuming that diffusion is the dominant process initially, and knowing that vorticity is generated at the outer edge where products form, then according to the solution of the diffusion equation, it takes $\tau \sim 0.06$ for the negative vorticity region to reach the z axis and start decaying. Indeed, this is the case as can be seen in Figure 11-5, where the

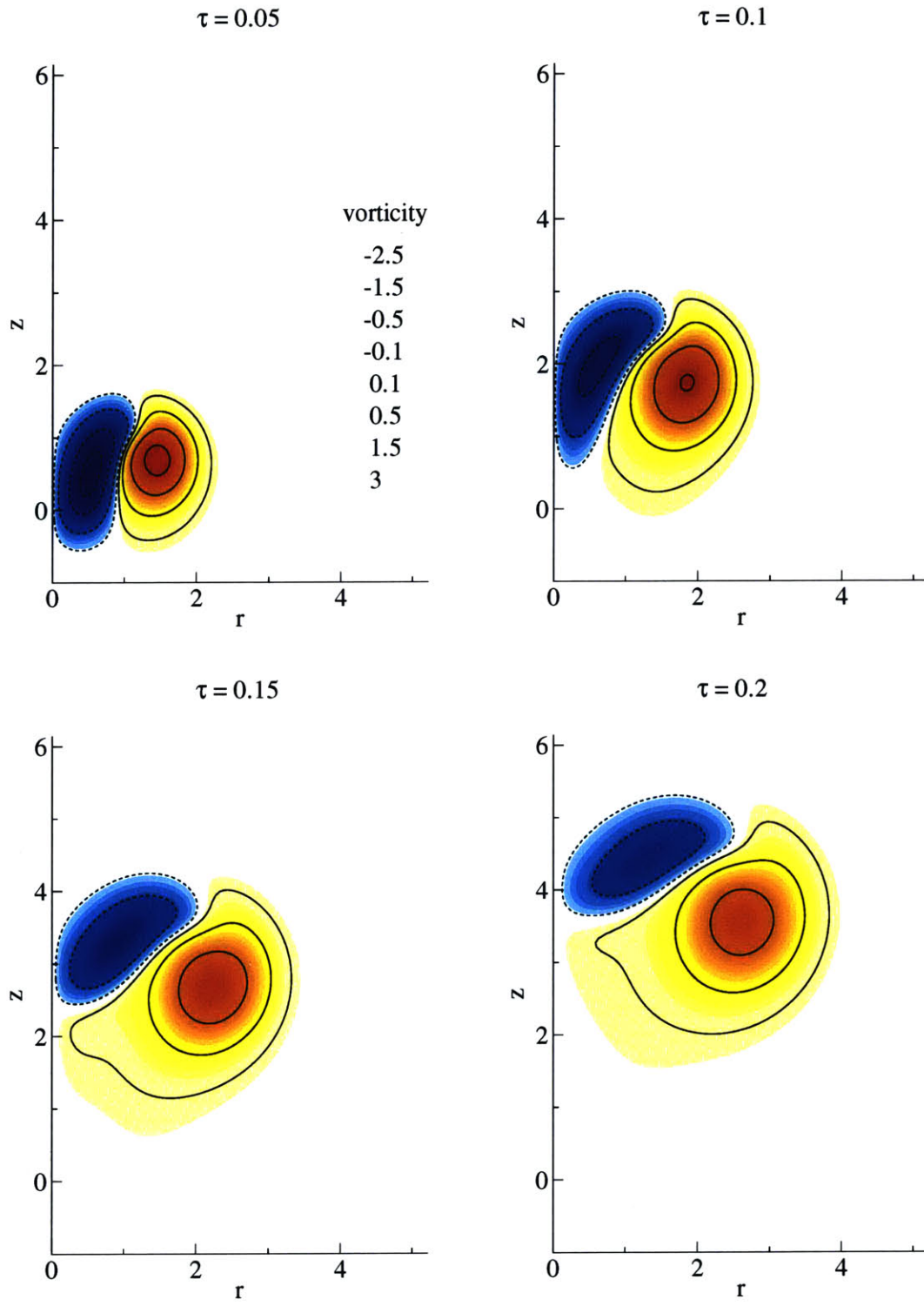


Figure 11-4: Vorticity contours at $\tau = 0.05, 0.1, 0.15,$ and 0.2 . Dashed contours (blue outwards): $-2.5, -1.5, -0.5$ & -0.1 . Solid contours (red inwards): $0.1, 0.5, 1.5$ & 3 .

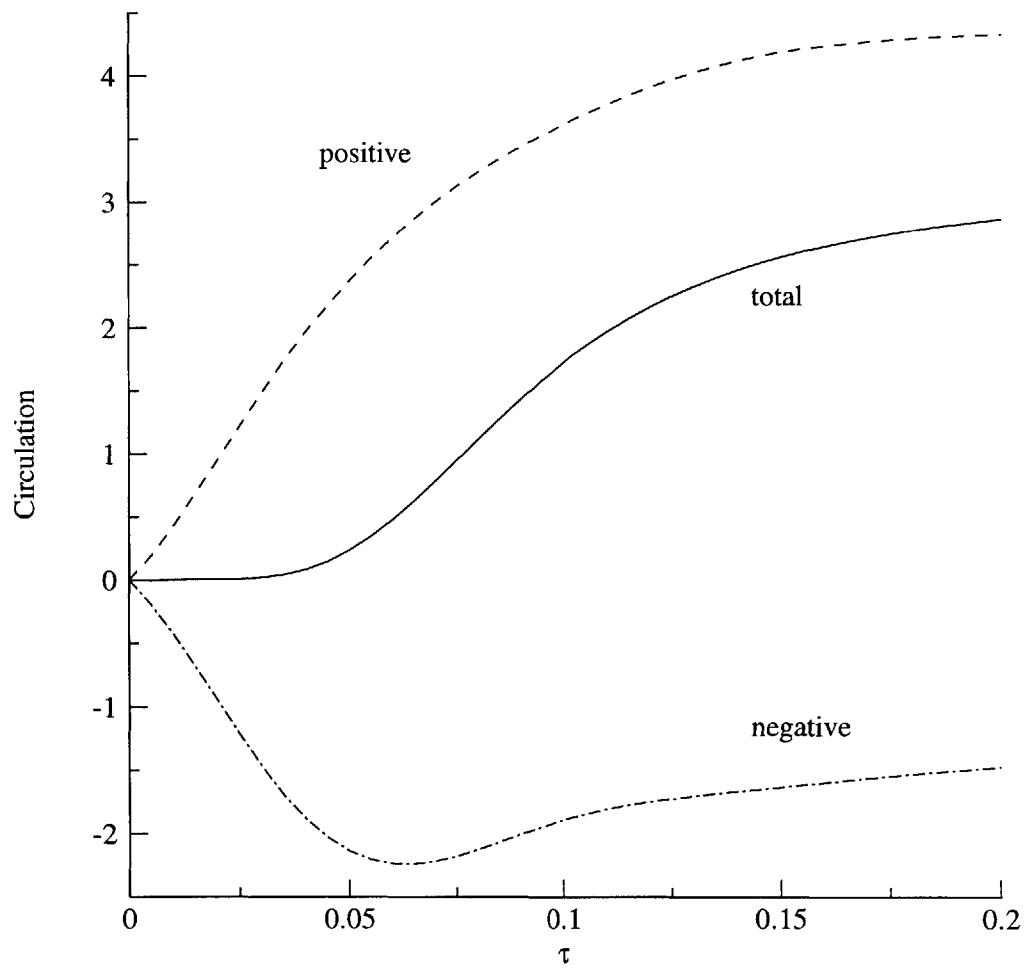


Figure 11-5: Total circulation versus time for $\Delta\tau = 0.0005$.

positive, negative, and total circulation (positive + negative) are plotted. The net total circulation stays close to zero until $\tau \sim 0.05$ after which it starts increasing.

11.7.2 Scalars

The fuel is consumed at the rate it diffuses to the reaction zone. At the early stages, the solution of the scalar diffusion equation is given by the Green's function

$$s(\mathbf{r}; \mathbf{r}_0, t) = \frac{2\pi E}{\pi^{3/2}\sigma^3} e^{-\frac{r^2+r_0^2+(z-z_0)^2}{\sigma^2}} I_0\left(\frac{2rr_0}{\sigma^2}\right), \quad (11.7)$$

where E is energy and I_0 is the modified Bessel function of the first kind and order zero. Starting with the initial scalar distribution, the scalar at the center of the ring, i.e. at $r = 1$, $z = 0$ decreases to 10 % of its initial value at $\tau = 0.015$. This is confirmed in Figure 11-6 where at $\tau = 0.015$, the fuel at the center of the ring is about 8 % of its initial value. The fuel mass fraction distribution presented in the figure shows that most of fuel consumption occurs at the early stages. This is reflected by the symmetry in the distribution that resembles the solution of the diffusion equation. The fact that the numerical value is less than obtained by pure diffusion may be attributed to the combined role of volumetric expansion and convection.

The temperature distribution at times $\tau = 0.05, 0.1, 0.15,$ and 0.2 are shown in Figure 11-7. As mentioned in the previous section, most of the fuel has been consumed before $\sim \tau = 0.02$, and consequently no chemical reaction occurs afterwards. The temperature distribution is then governed by diffusion and convection, the later due to vorticity and volumetric expansion. Contrary to the early stages where temperature is largest in the reaction zone as seen in Figure 11-3, large temperatures at later stages are associated with regions of high products concentration, as seen in Figure 11-7. Regions of large vorticity are associated with high temperature gradients as seen in vorticity and temperature distributions shown in Figures 11-4 and 11-7 respectively. Finally, the impact of volumetric expansion is manifested in larger volume of hot gas with a mean center moving away from the axis.

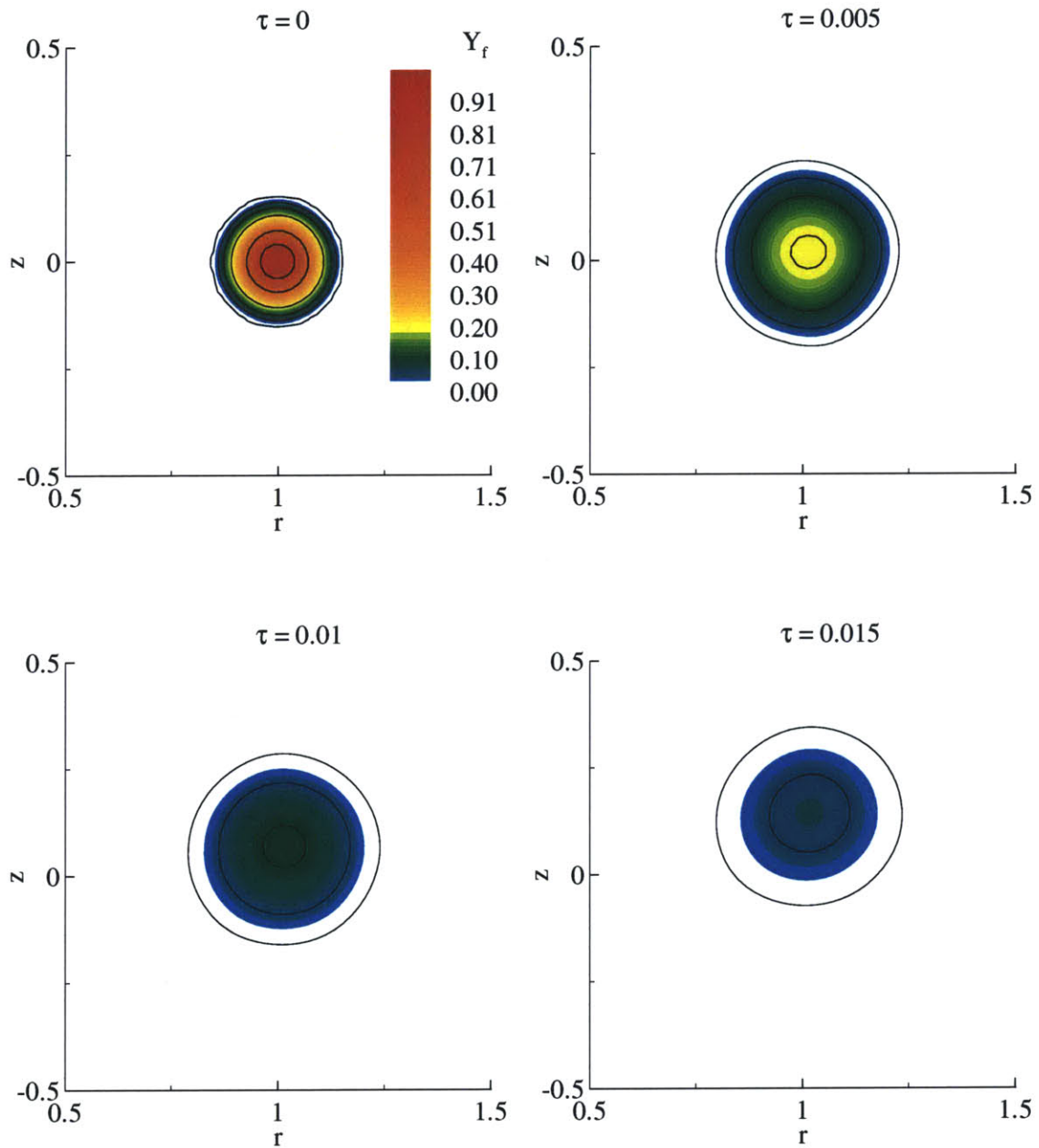


Figure 11-6: Fuel contours at $\tau = 0.05, 0.1, 0.15,$ and 0.2 . Contour values (inwards): 0.01, 0.05, 0.1, 0.2, 0.5, 0.8.

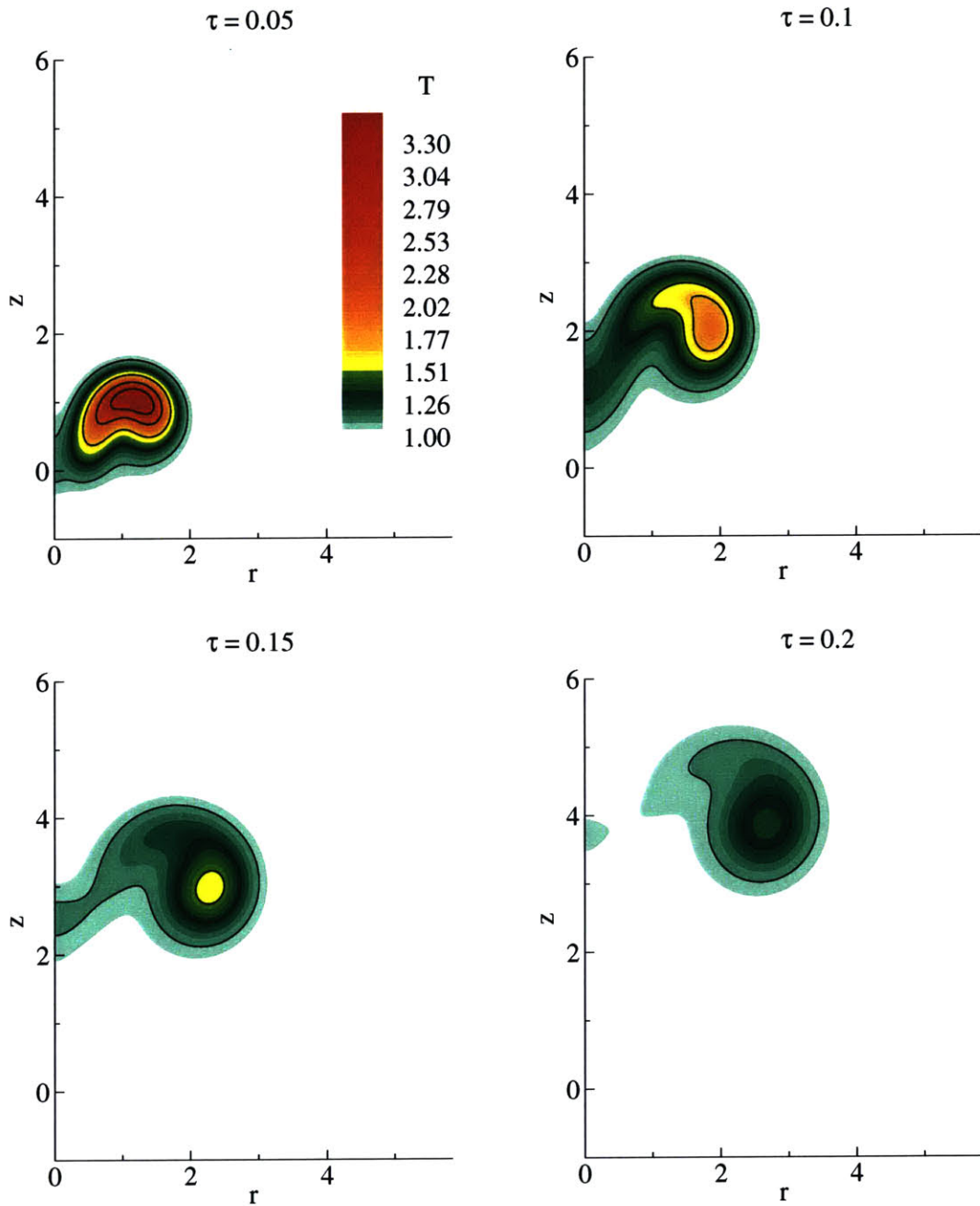


Figure 11-7: Temperature contours at $\tau = 0.05, 0.1, 0.15,$ and 0.2 . Contour values (inwards): 1.1, 1.3, 1.7, 2.35 & 3.

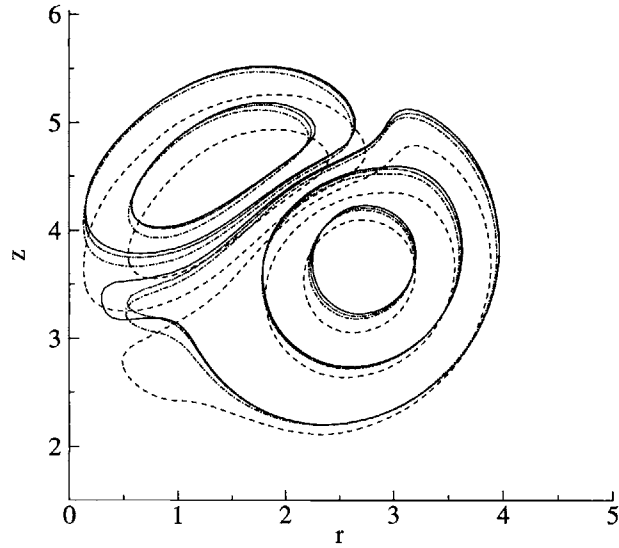


Figure 11-8: Vorticity contours at $\tau = 0.2$: -2.5, -1.5, -0.5, -0.1, 0.1, 0.5, 1.5, & 3. Solid line: $\Delta\tau = 0.0005$. Dash-dot-dot line: $\Delta\tau = 0.001$. Dash-dot line: $\Delta\tau = 0.002$. Dashed line: $\Delta\tau = 0.005$.

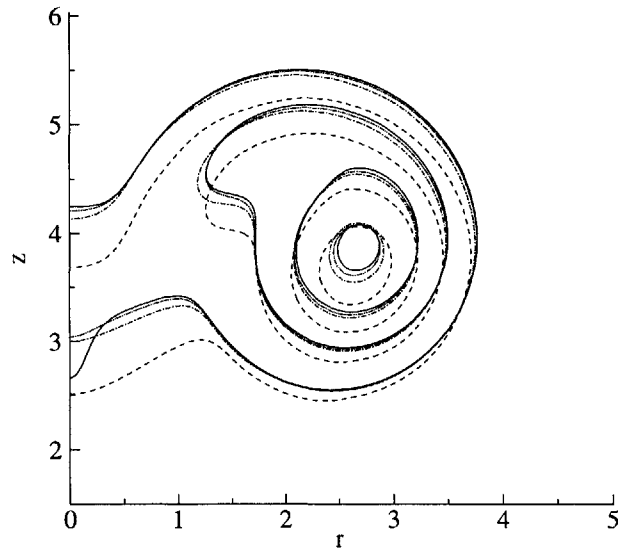


Figure 11-9: Scalar contours at $\tau = 0.2$: 0.00025, 0.001, 0.0025 & 0.0045. Solid line: $\Delta\tau = 0.0005$. Dash-dot-dot line: $\Delta\tau = 0.001$. Dash-dot line: $\Delta\tau = 0.002$. Dashed line: $\Delta\tau = 0.005$.

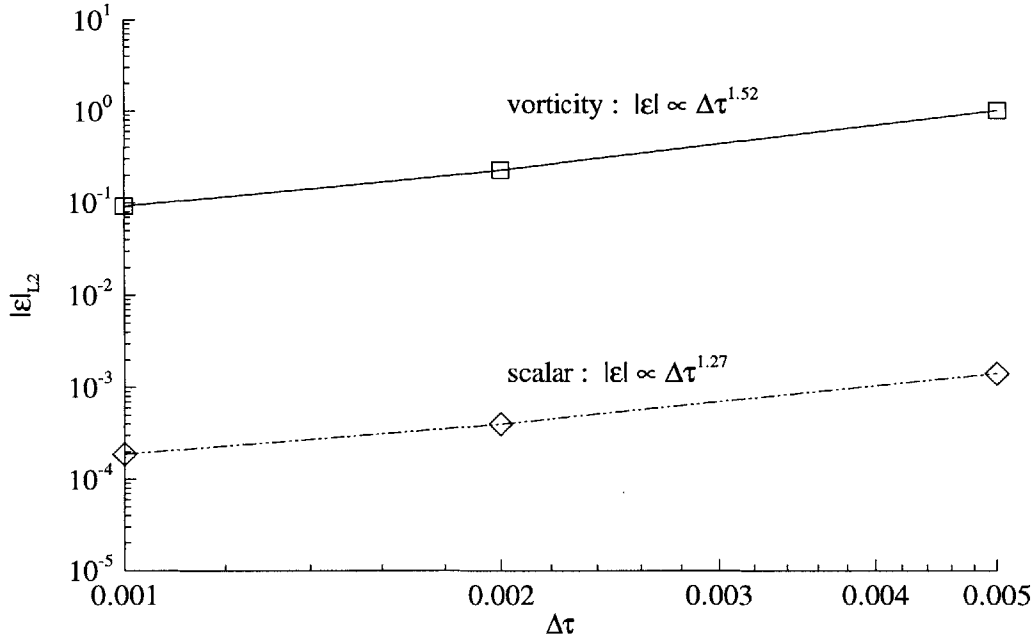


Figure 11-10: L-2 norm of error in vorticity and mixture fraction as a function of time step.

11.7.3 Convergence

To investigate numerical convergence the following time steps were used: $\Delta\tau = 0.0005$, 0.001, 0.002 and 0.005. The results are compared in terms of vorticity and scalar contours at the last time step, i.e. at $\tau = 0.2$. The vorticity contours presented in Figure 11-8 show that the numerical solution converges in a nonlinear fashion. This is confirmed in Figure 11-9 where the mixture fraction contours are shown. Using the solution with $\Delta\tau = 0.0005$ as a reference, the departure of the solutions for $\Delta\tau = 0.001$, 0.002 and 0.005 from this reference is measured in terms of an L-2 norm of the total error evaluated on a uniform mesh. The errors for both vorticity and scalar are presented in Figure 11-10 as a function of $\Delta\tau$. The error behaves as $\Delta\tau^m$, where $m = 1.52$ for vorticity and 1.27 for scalar.

The number of elements as a function of time is presented in Figure 11-11 for $\Delta\tau = 0.0005$. The increase in number of elements is linear. Further, it was observed that it decreases linearly with $\Delta\tau$. For example, the number of elements at $\tau = 0.2$ is 13368, 7764, and 4173 for $\Delta\tau = 0.0005$, 0.001 and 0.002 respectively.

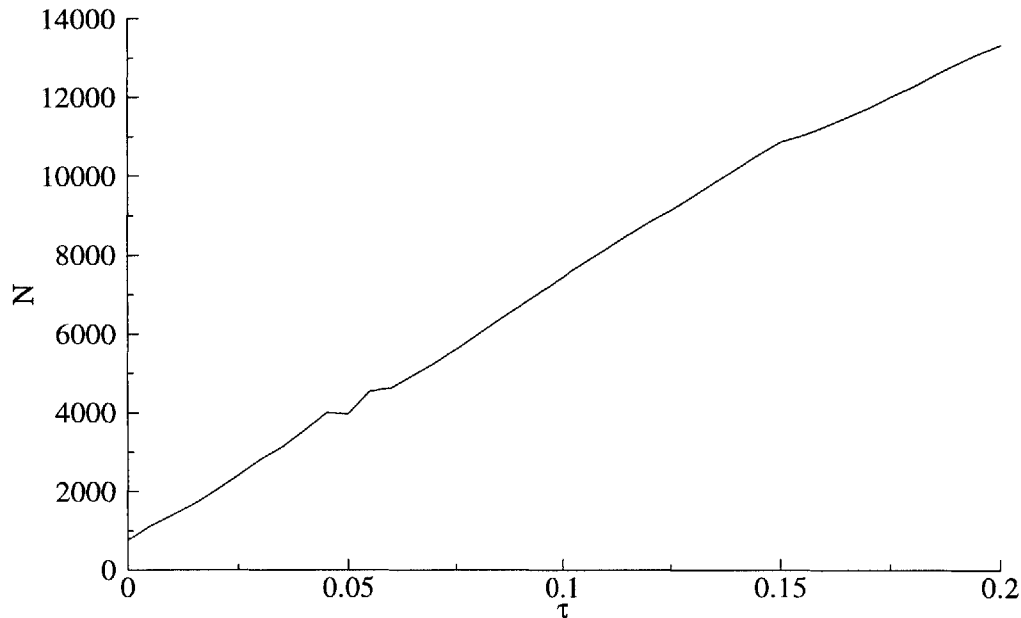


Figure 11-11: Number of elements versus time for $\Delta\tau = 0.0005$.

11.8 The role of radiation

In order to investigate the impact of radiation, the same example has been simulated, in which the radiation source term in the energy equation is determined according to the discrete source method described in the numerical methodology section. The medium is assumed to be gray, i.e. wavelength independent. The absorption coefficient is determined according to[70]

$$a = \sum a_{p,i}(T)p_i \quad (11.8)$$

where i corresponds to chemical species, and $a_{p,i}$ is the Plank-mean absorption coefficient of species i , and p_i is the partial pressure of the species. The temperature dependence of a_p for the various species, obtained using narrow band averaged values[91], is shown in Figure 7-14. The absorption coefficient of air is negligible for the range of temperature of interest.

The vorticity distribution, shown in Figure 11-12, resembles that of the non-radiating ring except that slightly lower values of vorticity are noticed. This is attributed to smaller vorticity generation associated with weaker temperature gradients. The temperature distribution is presented in Figure 11-13. Radiation contributes to the temperature field in two

ways: first it results in thermal energy loss to the surrounding and second it redistributes the thermal energy in an equilibrating manner, resulting in smaller temperature gradients.

A comparison of the time variation of the total circulation with and without radiation is shown in Figure 11-14. Radiation results in reduction in the absolute value of the total negative and positive circulation generation with a reduction in the net overall circulation. This may be thought of as a measure of the role of radiation in reducing vorticity generation via lower temperature gradients.

The total energy loss due to radiation is plotted as a function of time in Figure 11-15. During the stage where $\tau < 0.05$, the rate of energy loss is large as can be seen from the steep rate of energy lost. Later, for $\tau > 0.05$, energy loss approaches a steady state value reflecting the decaying role of radiation. This can be explained in terms of the corresponding fuel consumption. The maximum fuel mass fraction in the field is plotted as a function of time in the same figure. It can be noticed that the rate of energy loss due to radiation starts approaching zero by the time all the fuel has been consumed, represented by the dashed line in the figure. The shift in the radiation loss profile is due to the high thermal energy of the products of reaction right after the complete consumption of the fuel.

11.9 Conclusion

Grid-free Lagrangian computations of a reacting fuel ring with and without radiation have been presented. Radiation modeling is based on the discrete source method; a recent development in vortex methods. Radiation plays the roles of redistribution of thermal energy and losing part of it to the surrounding. Initially, the vorticity generated by buoyancy is symmetrical. Later diffusion causes the negative vorticity close to the axis to decay in absolute value resulting in rise and clockwise rotation of the structure. Radiation, via reducing temperature gradients, results in smaller generation (in absolute value) of positive, negative, and net overall circulation. Future works involves investigation of the impact of higher Reynolds number and heat release.

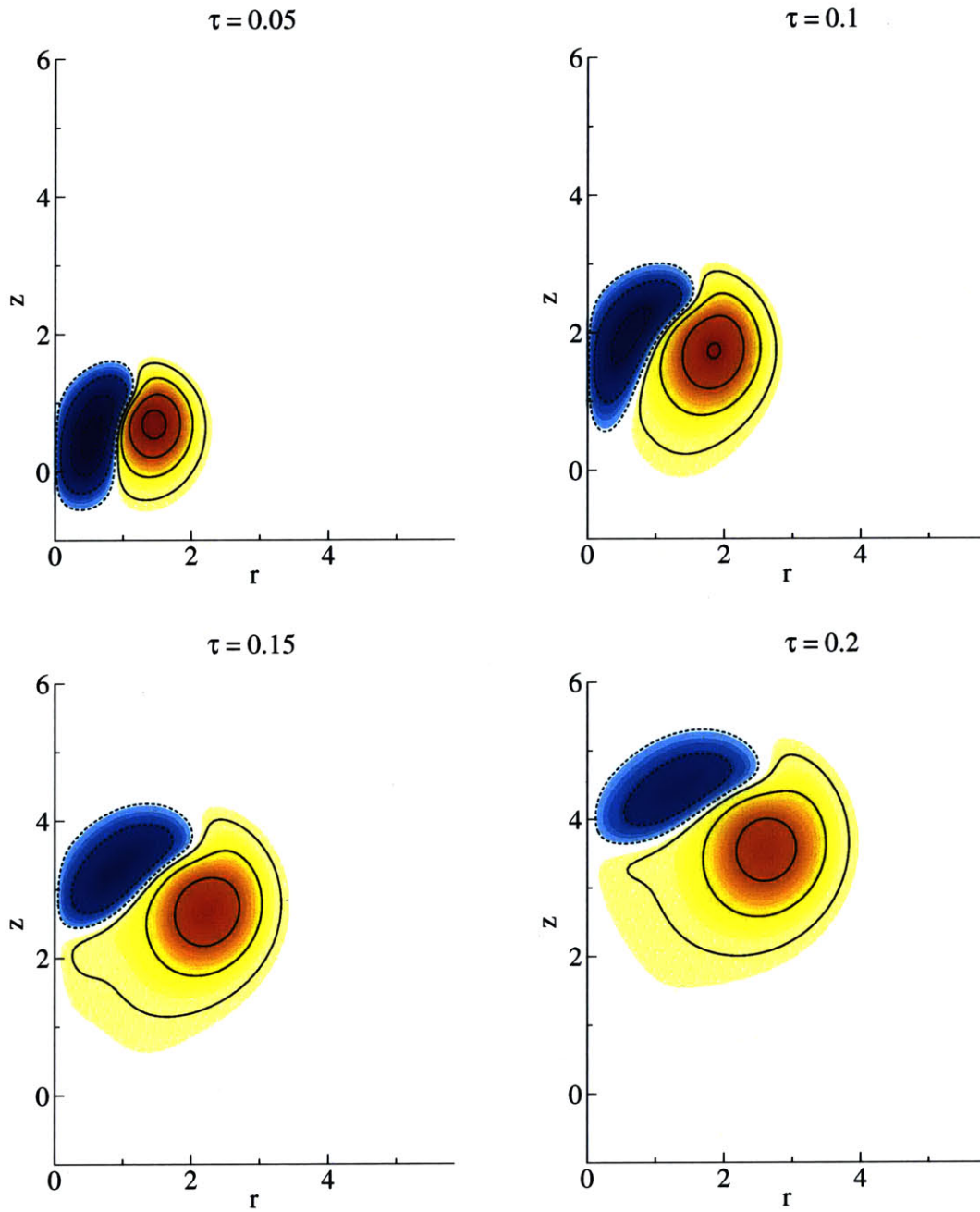


Figure 11-12: Vorticity distribution for the radiating case at $\tau = 0.05, 0.1, 0.15,$ and 0.2 . Dashed contours (blue outwards): $-2.5, -1.5, -0.5$ and -0.1 . Solid contours (red inwards): $0.1, 0.5, 1.5$ and 3 .

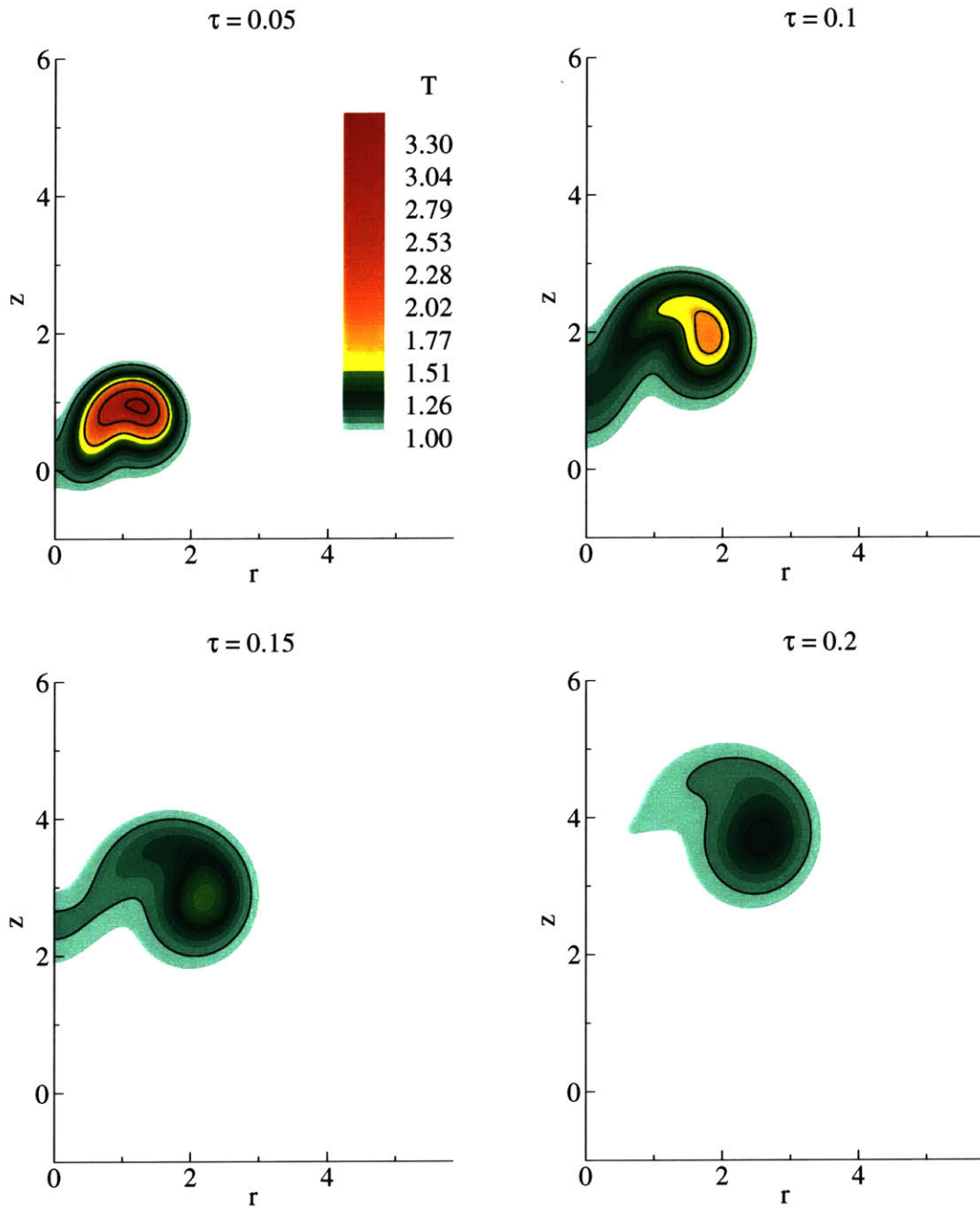


Figure 11-13: Temperature distribution for the radiating case at $\tau = 0.05, 0.1, 0.15,$ and 0.2 . Contour values (inwards): 1.1, 1.3, 1.5, 1.9, 2.35, and 3.

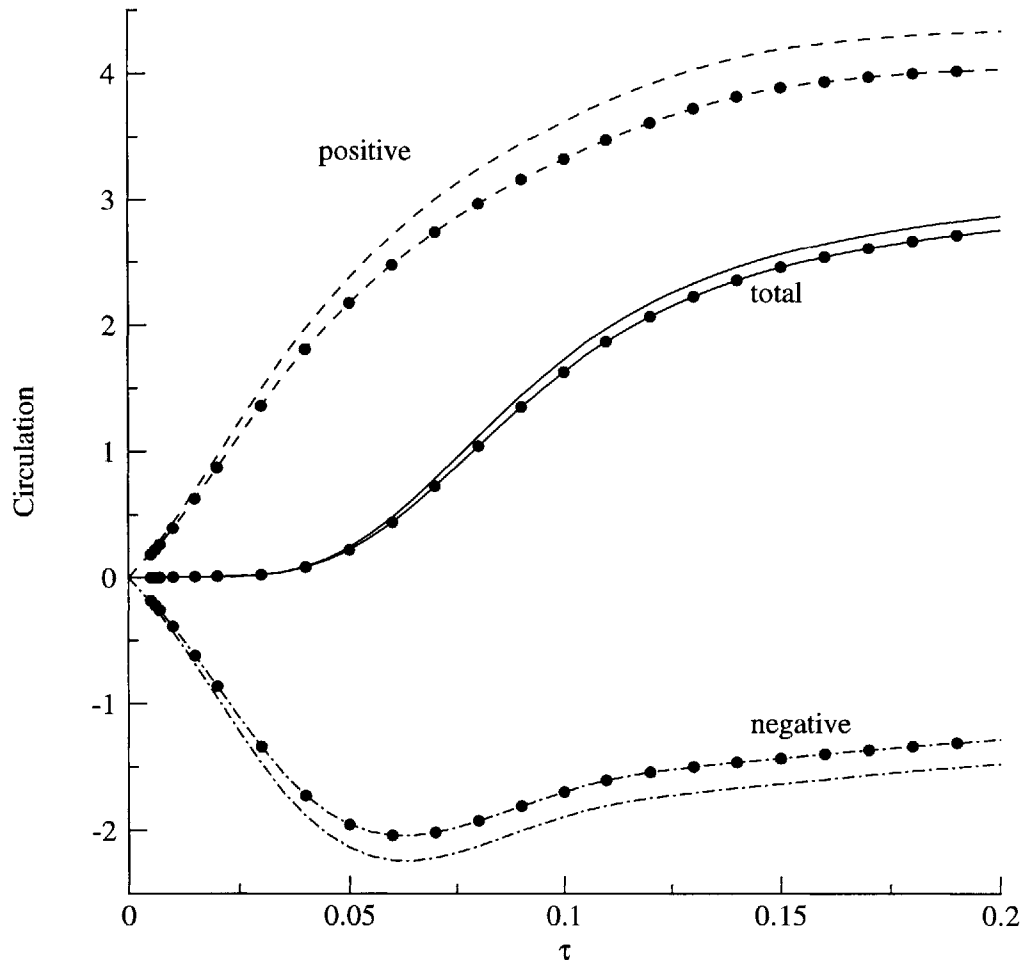


Figure 11-14: Total positive, negative, and net circulation as function of time with and without radiation. Symbols denote the case with radiation.

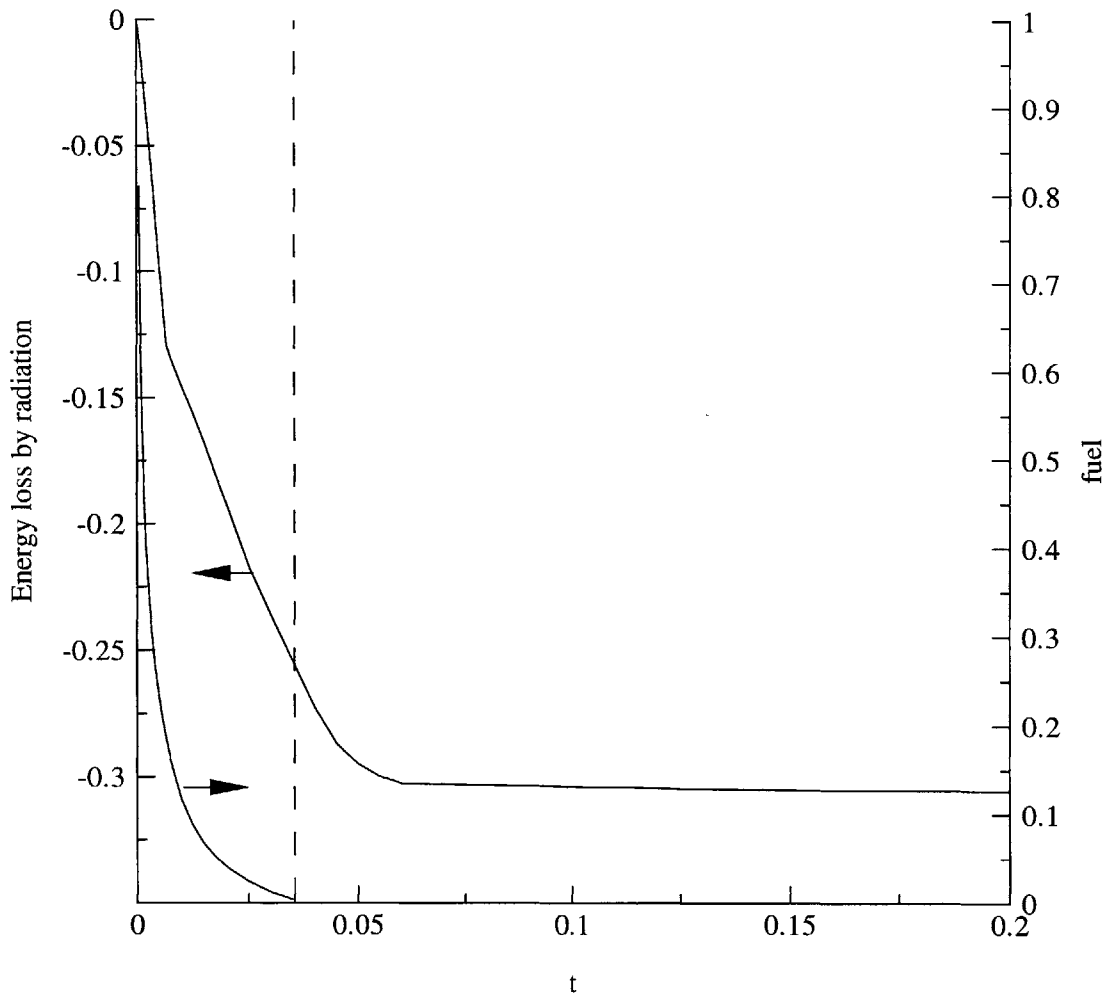


Figure 11-15: Ratio of thermal energy loss to energy generated by chemical reaction as a function of time. The maximum fuel mass fraction is also presented.

Chapter 12

Conclusion

In this thesis, we used available state of the art vortex methods to compute isothermal and reacting fire plumes. The results show agreement in the qualitative instantaneous and average behavior of the flow as well as quantitative parameters such as the puffing frequency, average plume height, and entrainment rates of air. The strengths and the weaknesses of the methodology used, which is based on the transport element method, have been pointed out. It has been concluded that further development is needed which objectives are accurate, grid-free, and flexible modeling of diffusion and grid-free modeling of radiative transfer. To meet these objectives, we have developed tools that are useful for numerical modeling of reacting flows in which radiative transfer plays a significant role. The major contributions are development of the smoothed redistribution method for accurate modeling of diffusion and the discrete source method for grid-free modeling of radiative transfer. We have also applied these tools to numerically compute various flows with the intent to validate the methodologies and investigate their convergence and accuracy.

The smoothed redistribution method is an extension of the redistribution method for a smooth representation of the vorticity field. The basis function assigned to each is the Green's function of the diffusion equation. Thus the method may be thought of as combination of the core spreading method and the redistribution method. It differs from the former in that instead of injecting new elements based on a predetermined geometrical pattern, it exploits the neighbors of the element to be diffused and injects a new element only in the presence of a gap (manifested by the impossibility to obtain a positive solution of the linear system). It differs from the redistribution method in terms of blob representation of the

field (as opposed to points), thus allowing smooth, accurate, and efficient recovery of the vorticity and scalar fields, and their gradients.

Accurate grid-free modeling of diffusion presents a challenge to vortex methods. Use of the core expansion method is not recommended since it introduces errors in convection. Accurate computation of the elements velocities required the field to be sufficiently resolved via enough overlap between the elements. The velocity field is determined using a Biot-Savart summation over all the elements. Essentially an integration, this summation provides an accurate approximation of the integral provided there are enough collocation points. Obviously, the uniformity plays an important role. For a uniform distribution of elements, the summation is very accurate. In grid-free methods, however, the elements are moved according to the velocity field and consequently controlling elements is out of question. Two exceptions arise, however. The first exception is periodic remeshing (particle to grid) of the field. This is a step that is needed in deterministic methods such as the PSE. The second exception is in the redistribution method, and more specifically in the injection step. As discussed before, the redistribution method injects elements in gaps which is manifested by the unsolvability of the linear system. It is how the element is injected that offers control on the location of this element location. The injection is implemented by promoting the uniformity of distribution of the elements by local search and optimization of the inter-elements distances. This feature endows the redistribution method with an advantage. Indeed, the method not only offers an accurate and efficient solution for diffusion, it also improves the accuracy of the convection step via promoting the uniformity of the elements distribution.

The discrete source method for grid-free numerical modeling of radiative transfer is novel. While current methods are tailored for a structured mesh, the discrete source method is designed to compute the divergence of the radiative heat flux based on Lagrangian distribution of computational elements, which renders the method compatible with vortex methods. The radiation source term in the energy is computed using a Biot-Savart summation over all the elements. Axisymmetric elements are rings of finite cores, two dimensional elements are infinite cylinders, and three dimensional elements are sphere. Accordingly, the method exploits fundamental solutions available or developed for these basic configurations. The introduction of the concept of the “effective attenuation coefficient” reduces the complexity and order of integration with insignificant loss in accuracy.

Suggested further work includes extending the smoothed redistribution method to account for variable diffusivity, numerical treatment of the source terms in a more accurate and robust manner, and applying this set of tools to more complicated problems.

Bibliography

- [1] M. Abramowitz and I. A. Stegun. *Handbook of Mathematical Functions*. Dover Publications, Inc., 1972.
- [2] C. Anderson and C. Greengard. *Vortex Methods*, volume 1360. Springer Verlag. Lecture Notes in Mathematics, 1988.
- [3] G. K. Batchelor. *An Introduction to Fluid Dynamics*. Cambridge University Press, 1999.
- [4] J. T. Beale and A. Majda. Rates of convergence for viscous splitting of the navier-stokes equations. *Math. Comp.*, 37(156):243–259, 1981.
- [5] J. T. Beale and A. Majda. Vortex methods. ii. higher order of accuracy in two and three dimensions. *Math. Comput.*, 39:29–52, 1982.
- [6] J. T. Beale and A. Majda. Higher order accurate vortex methods with explicit velocity kernels. *J. Comput. Phys.*, 58:188–208, 1985.
- [7] A. Bejan. Predicting the pool fire vortex shedding frequency. *J. Heat Trans.*, 113:261–262, 1991.
- [8] T. R. Blake and M. McDonald. An examination of flame length data from vertical turbulent diffusion flames. *Combust. Flame*, 94:426–432, 1993.
- [9] T. R. Blake and M. McDonald. Similitude and the interpretation of turbulent diffusion flames. *Combust. Flame*, 101:175–184, 1995.
- [10] B. M. Cetegen. *Entrainment and flame geometry of fire plumes*. PhD thesis, California Institute of Technology, Pasadena, CA, 1982.

- [11] B. M. Cetegen and T. A. Ahmed. *Fall meeting of Eastern States Section of The Combustion Institute*, (59), 1990.
- [12] B. M. Cetegen and T. A. Ahmed. Experiments on the periodic instability of buoyant plumes and pool fires. *Combust. Flame*, 157:184, 1993.
- [13] B. M. Cetegen, E. E. Zukoski, and T. Kubota. Entrainment in the near field and far field of fire plumes. *Comb. Sci. Tech.*, 39:305–331, 1984.
- [14] S. Chandrasekhar. *Radiative Transfer*. Dover Publications, 1960.
- [15] A. Cheer. Unsteady separated wake behind an impulsively started cylinder in slightly viscous flow. *J. Fluid. Mech.*, 201:485–505, 1989.
- [16] J. P. Choquin and S. Huberson. Particle simulation of viscous flow. *Comput. Fluids*, 17:397–410, 1989.
- [17] A. Chorin. Numerical study of slightly viscous flow. *J. Fluid Mech.*, 57:785–796, 1973.
- [18] A. J. Chorin. Vortex methods for rapid flows. *Proc. 2nd Int. Cong. Num. Meth. Fluid Mech.*, 1972.
- [19] A. J. Chorin. Vortex methods. Pam report 593, Department of Mathematics, University of Berkeley, 1993.
- [20] A. J. Chorin. *Vorticity and Turbulence*. Springer Verlag, 1994.
- [21] G.-H. Cottet. Particle-grid domain decomposition methods for the navier-stokes equations. *J. Comput. Phys.*, 89:301–318, 1990.
- [22] G.-H. Cottet and S. Mas-Gallic. A particle method to solve the navier-stokes system. *Numer. Math.*, 57:805–827, 1990.
- [23] G. Cox. *Combustion Fundamentals of Fire*. Academic Press, 1995.
- [24] B. Davison. *Neutron Transport Theory*. Oxford University Press, 1958.
- [25] P. Degond and F.-J. Mustieles. The weighted particle method for convection-diffusion equations part 1: The case of an isotropic viscosity. *Math. Comput.*, 53:485–507, 1989.

- [26] M. A. Delchatsios. Turbulent diffusion flames with large buoyancy effects. *Comb. Flame*, 70:33–46, 1987.
- [27] M. A. Delichatsios. Gravitational fluctuations in pool fires and pool buoyant plumes. *Comb. Sci. Tech.*, 1994.
- [28] M. A. Delichatsios and L. Orloff. Entrainment measurements in turbulent, buoyant jet flames and implications for modeling. *20-th Symp. (Int.) The Combustion Institute*, pages 951–960, 1984.
- [29] R. I. Emori and K. Saito. Study of scaling laws in pool and crib fires. *Combust. Sci. Tech.*, 31:217–231, 1983.
- [30] W. A. Fiveland. A discrete ordinates method for predicting radiative heat transfer in axisymmetric enclosures. *ASME*, 1982. Paper 82-HT-20.
- [31] W. A. Fiveland. Discrete ordinate methods for radiative heat transfer in isotropically and anisotropically scattering media. *ASME Journal of Heat Transfer*, 109:809–812, 1987.
- [32] J. A. Fleck. The calculation of nonlinear radiation transport by a monte carlo method. Technical report, Lawrence Radiation Laboratory., 1961. Report UCRL-7838.
- [33] A. Gharakani. *A 3-D vortex-boundary element method for the simulation of unsteady, high Reynolds number flows*. PhD thesis, Massachusetts Institute of Technology, 1995.
- [34] A. F. Ghoniem. Development and application of vortex methods; a review and some extensions. *1st National Fluid Dynamics Congress. AIAA*, pages 658–669, 1988.
- [35] G. Ghoniem, A. F. Heidarinejad and A. Krishnan. Numerical simulation of a thermally stratified shear layer using the vortex element method. *J. Comput. Phys.*, 79:135–166, 1988.
- [36] I. Ghoniem, A. F. Lakkis and M. Soteriou. Numerical simulation of the dynamics of large fire plumes and the phenomenon of puffing. *26th Symp. (Int.) Comb. The Combustion Institute*, pages 1531–1539, 1996.
- [37] V. N. Golubkin and G. B. Sizykh. Some general properties of plane-parallel viscous flows. *Izv. Akad. Nauk SSSr. Mekh. Zhidk. i Gaza*, 3:176–178, 1987.

- [38] L. Greengard and V. Rokhlin. On the efficient implementation of the fast multipole algorithm. Report yaleu/dcs/rr-602, Department of Computer Science, Yale University, 1988. Unpublished.
- [39] C. Greengrad. The core spreading method approximated the wrong equation. *J. Comput. Phys.*, 61:345–348, 1985.
- [40] O. H. Hald. Convergence of vortex methods. *Vortex methods and vortex motion*, pages 33–58, 1990.
- [41] J. C. Hamins, A. Yang and T. Kashiwagi. Entrainment measurements in turbulent, buoyant jet flames and implications for modeling. *24-th Symp. (Int.) Comb. The Combustion Institute*, pages 1695–1702, 1992.
- [42] M. A. Heaslet and R. F. Warming. Theoretical predictions of radiative transfer in a homogeneous cylindrical medium. *J. Quant. Spectrosc. Radiat. Transfer*, 6:751–774, 1966.
- [43] G. Heskestad. Peak gas velocities and flame heights of buoyancy-controlled turbulent diffusion flames. *18th Symp. (Int.) Comb. The Combustion Institute*, pages 951–967, 1981.
- [44] G. Heskestad. *Fire Safety J.*, 5:103, 1983.
- [45] G. Heskestad. A reduced-scale mass fire experiment. *Combust. Flame*, 83:293–301, 1991.
- [46] H. C. Hottel and E. S. Cohen. Radiant heat exchange in gas-filled enclosure: allowance for non-uniformity of gas temperature. *AIChE Journal*, 4:3–14, 1958.
- [47] H. C. Hottel and A. F. Sarofim. *Radiative Transfer*. McGraw-Hill, 1967.
- [48] J. R. Howell. *Application of Monte Carlo to heat transfer problems*, volume 5. Academic Press, 1968. in *Advances in Heat Transfer*,
- [49] J. R. Howell and M. Perlmutter. Monte carlo solution of thermal transfer through radiant media between gray walls. *ASME Journal of Heat Transfer*, 86(1):116–122, 1964.

- [50] F. Q. Hu, T. L. Jackson, D.G. Lasseigne, and C. E. Grosch. Absolute-convective instabilities and their associated wave packets in a compressible reacting mixing layer. *Phys. Fluids*, A5 (4):901–915, 1993.
- [51] J. H. Jeans. The equations of radiative transfer of energy. *Monthly Notices Royal Astronomical Society*, 78:28–36, 1917.
- [52] S. N. Kempka and Strickland J. H. A method to simulate viscous diffusion of vorticity by convective transport of vortices at a non-solenoidal velocity. Sand93-1763, Sandia National Laboratory, 1993.
- [53] O. Knio and Ghoniem A. F. Three-dimensional vortex simulation of rollup and entrainment in a shear layer. *J. Comput. Phys.*, 97:172–223, 1991.
- [54] O. Knio and Ghoniem A. F. Three-dimensional vortex simulation of rollup and entrainment in a shear layer. *J. Comput. Phys.*, 97:172–223, 1991.
- [55] V. Kourganoff. *Basic Methods in Transfer Problems*. Dover Publications, 1963.
- [56] A. Krishnan and A. F. Ghoniem. Simulation of the roll-up and mixing in rayleigh-taylor flow using the vortex/transport element method. *J. Comput. Phys.*, 99:1–27, 1992.
- [57] H. C. Kung and P. Stavrianidis. Buoyant plumes of large-scale pool fires. *19th Symp. (Int.) Comb. The Combustion Institute*, pages 905–912, 1983.
- [58] I. Lakkis and A. F. Ghoniem. Grid-free simulation of radiative transport in a participating medium. *Third Int. Workshop on Vortex Flows and Related Num. Meth.*, 1998.
- [59] I. Lakkis and A. F. Ghoniem. Lagrangian simulation of fire plumes. *7th AIAA/ASME Joint Thermo. and Heat Transf. Conf.*, 1:215–226, 1998.
- [60] I. A. Lakkis and A. F. Ghoniem. Development of a computational model for large fire plumes. Final report to nist, Massachusetts Institute of Technology, 1996.
- [61] M. E. Larson and H. C. Hottel. The exchange factor method: an alternative zonal formulation of radiating enclosure analysis. *ASME Journal of Heat Transfer*, 108(1):934–942, 1985.

- [62] C. L. Lawson and R. J. Hanson. *Solving Least Squares Problems*. Society for Industrial and Applied Mathematics, 1995.
- [63] A. Leonard. Vortex methods for flow simulation. *J. Comput. Phys.*, 37:289–335, 1980.
- [64] A. Neemann Lingen, J. K. Meyer, and M. Schriber. Instability of diffusion flames. vortex methods for flow simulation. *Twenty sixth Symp. (Int.) Comb. The Combustion Institute*, 1996.
- [65] V. C. Luu. *Numerical study of the reactive flow in a two-stream, coaxial-jet, axisymmetric bluff-body combustor*. PhD thesis, Massachusetts Institute of technology, 1996.
- [66] J. S. Marshall and J. R. Grant. Penetration of a blade into a vortex core: Vorticity response and unsteady blade forces. *J. Fluid Mech.*, 103:83–109, 1996.
- [67] L.-F. Martins and A.F. Ghoniem. Vortex simulation of the intake flow in a planar piston-chamber device. *Int. J. for Num. Meth. Fluids*, 12:237–260, 1991.
- [68] B. J. McCaffery. Purely buoyant diffusion flames: some experimental results. NBSIR 79-1910, National Bureau of Standards, Washington, DC, 1979.
- [69] W. E. Mell, K. B. McGrattan, and H. R. Baum. Numerical simulation of combustion in fire plumes. *26th Symp. (Int.) Comb.*, pages 1523–1530, 1996.
- [70] M. Modest. *Radiative Heat Transfer*. McGraw Hill, Inc., 1993.
- [71] B. R. Morton, G. I. Taylor, and Turner J. S. Turbulent gravitational convection from maintained and instantaneous sources. *Proc. Royal Soc.*, A234:1–23, 156.
- [72] R. L. Murray. *Nuclear Reactor Physics*. Prentice Hall, 1957.
- [73] Y. Ohami and T Akamatsu. Viscous flow simulation using the discrete vortex model-the diffusion velocity method. *Comput. Fluids*, 19:433–441, 1991.
- [74] International Standards Organization. Fire protection - vocabulary. Iso 8421-1, ISO, Geneva., 1987.
- [75] L. Orlof and J. de Ris. Froude modeling of pool fires. *19th Symp. (Int.) Comb. The Combustion Institute*, pages 865–895, 1982.

- [76] M. Perlman. On the accuracy of vortex methods. *J. Comput. Phys.*, 59:200–223, 1985.
- [77] P. A. Raviart. An analysis of particle methods. *Numerical Methods in Fluid Dynamics*, 1127:243–324, 1985. edited by F. Brezzi, (Springer-Verlag, New York/Berlin).
- [78] F. P. Ricou and B. P. Spalding. Measurements of entrainment by axisymmetric turbulent jets. *J. Fluid. Mech.*, 11:21–32, 1961.
- [79] P. G. Saffman. *Vortex Dynamics*. Cambridge University Press, 1995.
- [80] W. Schmidt. Turbulente ausbreitung eines stromes erhitzter luft. *Z. Angew. Math. Mech.*, 21(265-2178):356–363, 1941.
- [81] P. Shaenman. Estimated impact of the center for fire research program on the costs of fire. Report nist gcr, National Institute of Standards and Technology, 1991.
- [82] F. S. Sherman. *Viscous Flow*. McGraw Hill, 1990.
- [83] M. Soteriou and Ghoniem A. F. Effects of the free-stream density ratio on free and forced spatially-developing shear layers. *Phys. Fluids*, pages 2036,2050, 1995.
- [84] M. Soteriou and A. F. Ghoniem. On the application of the infinite reaction rate model in the simulation of the dynamics of exothermic mixing layers. *Combust. Sci. Tech.*, 105:377–397, 1995.
- [85] M. C. Soteriou. *Numerical study of turbulent combustion in a shear layer*. PhD thesis, Massachusetts Institute of Technology, 1993.
- [86] S. Subramaniam. *A New Mesh-Free Vortex Method*. PhD thesis, The Florida State University, 1996.
- [87] S. Subramaniam. Grid-free redistribution methods for axisymmetric and anisotropic diffusion. Technical report, Massachusetts Institute of Technology, 1999.
- [88] Z. Tan. Radiative heat transfer in multidimensional emitting, absorbing, and anisotropic scattering media - mathematical formulation and numerical method. *Journal of Heat Transfer*, 111, 1989.

- [89] P. H. Thomas, R. Baldwin, and A. J. M. Heselden. Buoyant diffusion flames: some measurements of air entrainment, heat transfer and flame merging. *10th Symp. (Int.) Comb. The Combustion Institute*, pages 983–996, 1965.
- [90] S. T. Thynell and M. N. Ozisik. Radiation transfer in an isotropically scattering homogeneous solid sphere. *J. Quant. Spectrosc. Radiat. Transfer*, 33(4):319–330, 1985.
- [91] C. L. Tien. Thermal radiation properties of gases. *Advances in Heat Transfer*, 5:253–324, 1968.
- [92] S. R. Tieszen and J. L. Moya. Vortical structures in pool fires: observations, speculation and simulation. Sandia report, sand96-2607.uc-722, Sandia National Labs, 1996.
- [93] J. S. Truelove. Discrete-ordinates solutions of the radiative transport equation. *ASME Journal of Heat Transfer*, 109(4):1048–1051, 1987.
- [94] J. S. Truelove. Three-dimensional radiation in absorbing-emitting-scattering media using the discrete-ordinates approximation. *Journal of Quantitative Spectroscopy and Radiative Heat Transfer*, 39(1):27–31, 1988.
- [95] J. S. Turner. Starting plume in neutral surroundings. *J. Fluid. Mech.*, 13:356–368, 1962.
- [96] S. Venkatesh, A. Ito, and K. Saito. Flame base structure of small-scale pool fires. *26th Symp. (Int.) Comb. The Combustion Institute*, 1:1437–1443, 1996.
- [97] D. V. Walters and R. O. Buckius. *Monte Carlo methods for radiative heat transfer in scattering media*, volume 5. Academic Press, 1992. in Annual Review of Heat Transfer,.
- [98] E. J. Weckman and A. Sobiesiak. Oscillation behavior of medium-scale pool fires. *22nd Symp. (Int.) Comb. The Combustion Institute*, pages 1299–1310, 1988.
- [99] F. Williams. *Combustion Theory*. Addison-Wesley, 1985.
- [100] B. D. Wood, P. L. Jr. Blackshear, and E. R. G. Eckert. Mass fire model: an experimental study of the heat transfer to liquid fuel burning from a sand-filled pan burner. *Combust. Sci. Technol*, 4:113–129, 1971.

- [101] X. C. Zhou and J. P. Gore. Air entrainment flow field induced by a pool fire. *Combustion and Flame*, 100:52–60, 1995.
- [102] X. C. Zhou and J. P. Gore. A study of entrainment and flow patterns in pool fires using image velocimetry. Final report, 1996.
- [103] E. E. Zukoski and G. Cox. *Combustion Fundamentals of Fire, Properties of Fire Plumes*, pages 101–219. Academic Press, s edition, 10 January 1995.
- [104] E. E. Zukoski, T. Kubota, and B. M. Cetegen. *Fire Safety J.*, 3:107, 1980.